Wind tunnel Investigation on Trailing Edge Noise Mitigation via Sawtooth Serrations

Customer
University of Twente

NLR-TR-2014-310

National Aerospace Laboratory NLR
Anthony Fokkerweg 2
1059 CM Amsterdam
The Netherlands
Tel +31 (0)88 511 3113
www.nlr.nl

EXECUTIVE SUMMARY

Wind tunnel Investigation on Trailing Edge Noise Mitigation via Sawtooth Serrations

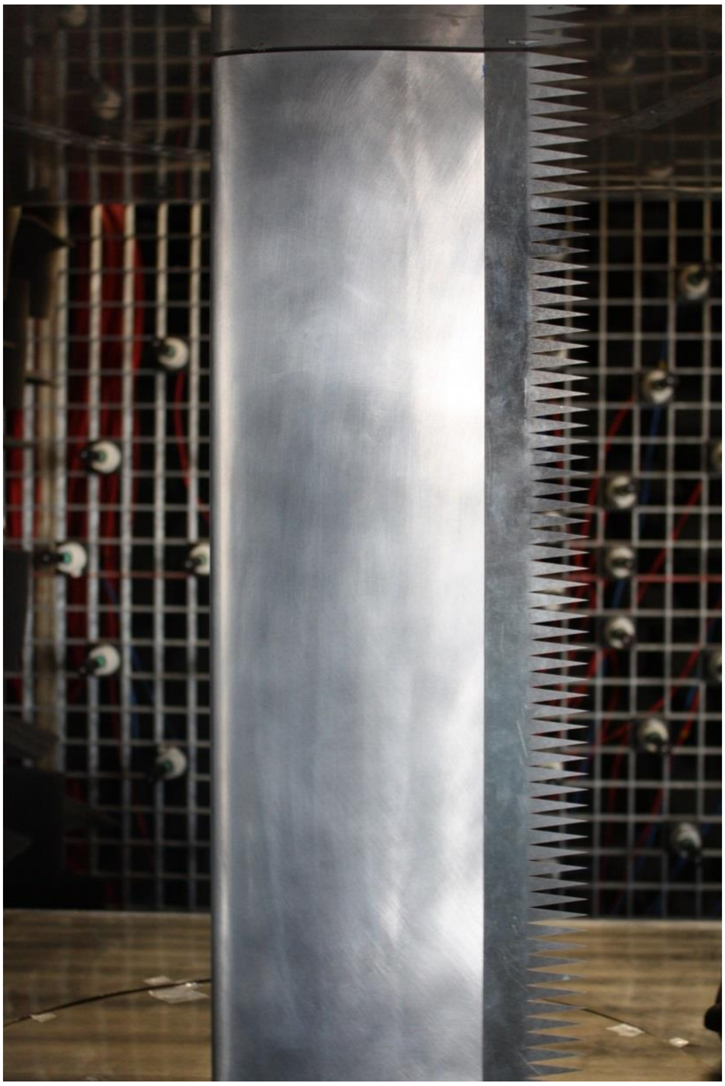

Report no.
NLR-TR-2014-310

Author(s)
D. Engler Faleiros

Report classification
UNCLASSIFIED

Date
13-10-2014

Knowledge area(s)
Aëro-akoestisch en experimenteel aërodynamisch onderzoek

Descriptor(s)
Serrations
Trailing
Noise
Acoustics

Problem area

Wind turbines noise production due to the interaction of the blades and the air.

Description of work

Enhance the potential of the use of sawtooth serrations on the trailing edge of wind turbine blades, in order to reduce noise at all frequency ranges, especially by investigating the influence of misalignment of the serrations with the flow.

Results and conclusions

Flexible serrations (FS) are more efficient than regular sawtooth serrations. Most of the high frequency noise previously reported in literature that was caused due to the application of serrations was eliminated. FS consistently showed great benefits with reductions up to 13 dB. Serrations, in general, decrease the aerodynamic efficiency and the pros and cons of using it need to be taken into account when considering full scale application.

Applicability

Serrations can be applied on wind turbine blades to decrease airfoil self-noise that occurs due to boundary-layer turbulence that passes over the trailing edge. This is the main noise mechanism of wind turbines, considering everything else is adequately treated.

Decreasing the noise from the blades would enable to install more wind turbines close to urban areas and open the possibility for harvesting sustainable energy. Furthermore, serrations can also be applied in airplane wings to help reduce the noise during the landing phase. Nevertheless, this application is not considered to be the focus of this report.

National Aerospace Laboratory NLR
Anthony Fokkerweg 2, 1059 CM Amsterdam,
P.O. Box 90502, 1006 BM Amsterdam, The Netherlands
Telephone +31 (0)88 511 31 13, Fax +31 (0)88 511 32 10, Website: www.nlr.nl

Wind tunnel Investigation on Trailing Edge Noise Mitigation via Sawtooth Serrations

D. Engler Faleiros

Customer
University of Twente

Customer	University of Twente
Contract number	
Owner	Not applied
Division NLR	Aerospace Vehicles
Distribution	Limited
Classification of title	Classified
Date	13-10-2014

Approved by:

Author	Reviewer	Managing department
David Engler Faleiros	Marthijn Tuinstra	Joost Hakkaart
Date	Date	Date

Summary

This report investigates the performance of sawtooth serrations in mitigating trailing edge noise from a DU-96-W-180 airfoil section, which is designed especially for wind turbines. The experiments were realized at NLR's Open-Jet Anechoic KAT wind tunnel. Acoustic measurements were performed with a 48-microphone array. Aerodynamic experiments were done via hot-wire traverses to obtain the boundary-layer and wake parameters.

The main conclusion of this work is that the use of a flexible mechanism, that allows the serrations to auto-align with the flow, makes them effective over almost the complete operational range. Furthermore, the high-frequency noise penalty that was often reported in literature, no longer occurs. The hinge mechanism that provides auto aligning with the flow should have a smooth surface. The removal of material by making cuts inside the serrations was also tested as a way of increasing flexibility. This concept however increased significantly the produced noise.

Lastly, the mounting strategy in case of retro-fitting of an existing wind turbine blade was investigated. Serrations fixed on the suction side of the airfoil performed better than serration mounted on the pressure side.

Key Words: Serrations, Flexible, Trailing Edge Noise, Wind Tunnel, Acoustics

Content

Abbreviations

Acronym	Description
NLR	National Aerospace Laboratory NLR
TE	Trailing Edge
LE	Leading Edge
BL	Boundary Layer
TBL	Turbulent Boundary Layer
LBL	Laminar Boundary Layer
VS	Vortex Shedding
SPL	Sound Pressure Level
AoA	Angle of Attack
Re	Reynolds Number
Ma	Mach Number
TBL-TE	Turbulent Boundary Layer – Trailing Edge Noise
TEB-VS	Trailing Edge Bluntness – Vortex Shedding Noise
PNS	Point of Noise Source
FS	Flexible Serration
US-TOP	Uncutted Serration fixed on the Suction Side (Top)
US-BOT	Uncutted Serration fixed on the Pressure Side (Bottom)
CS	Cutted Serration
SCP	Serration with Cutted Plate

List of Symbols

Symbol	Description
a	Axial Induction Factor
a'	Angular Induction Factor
α_{geo}	Geometric Angle of Attack
α_{eff}	Effective Angle of Attack
b	Half Width of the wake
B	Number of Blades
c	Chord Legth
c	Speed of Sound
C_l	Coefficient of Lift
C_d	Coefficient of Drag
C_p	Coefficient of Pressure
D'	Drag per unit span
δ	Boundary Layer Thickness
δ^*	Displacement Thickness
F_D	Drag Force
F_N	Normal Force
F_L	Lift Force
h	Half amplitude of the sawtooth serration
J'	Momentum per unit span
k	Trip Height
L	Wetted Span
$\mathcal{L}$	Correlation length of the turbulence
λ	Width of the sawtooth serration
λ_r	Ratio of local tangential velocity and wind free stream velocity
M_0	Mach Number of the undisturbed upstream flow
M_V	Component of the boundary layer Mach Number perpendicular to the edge
μ	Dynamic Viscosity
ν	Internal angle between height and side of the serration
ν	Kinematic viscosity
Ω or ω	Rotational Speed of the blade
$\langle \boldsymbol{p}^2 \rangle$	Mean-square sound pressure at the observer
ρ_0	Medium fluid density
ρ	Density of the fluid
φ	Angle of the serration with the chord line
φ	Relative Wind Angle
Ψ	Nondimensional edge noise spectrum

Ψ_0	Nondimensional edge noise spectrum in the absence of the serration
Q	Torque
r	Distance from the edge to the observer
r/R	Ratio of radius location at the blade an the total blade radius
t	Trailing Edge Thinkness
T	Thrust
θ	Pitch Angle
θ_{top}	Angle at the TE between the airfoil top surface and the chord line
θ_{bot}	Angle at the TE between the airfoil bottom surface and the chord line
u	Local velocity in stramwise direction
u_1	Velocity deficit
$\bar{u}$	Temporal mean velocity in streamwise direction
U	Velocity
U_c	Convection Velocity
$\mathbf{U}_\infty$	Free Stream Velocity
$\boldsymbol{U_e}$	Edge Velocity
v	Local velocity in transverse direction
v	Tangential Velocity
v’	Turbulent transverse velocity
v'^2	Mean-square turbulence velocity
V	Characteristic edge convection velocity

1 Introduction

On a wind turbine different noise sources can be identified, such as hub noise or the noise generated by the blades moving through the air. Studies performed by other authors showed that aeroacoustic noise is most relevant, provided that all the other ones are adequately treated (1). The aerodynamic sources are divided into two main groups: *inflow-turbulence noise,* which is caused by upstream turbulent flow around the Leading Edge (LE), and *airfoil self-noise* (2), which is caused by the interaction between the airfoil blade and the turbulence produced in its own boundary layer and near wake (3).

The airfoil self-noise mechanisms are (3):

- *Turbulent Boundary Layer – Trailing Edge (TBL-TE) Noise,* caused by the interaction between the TBL and the TE*;*
- *Laminar Boundary Layer – Vortex Shedding (LBL-VS) Noise*, which is caused by large LBL, whose instabilities result in Vortex Shedding (VS) at the Trailing Edge (TE);
- Flow separation close to the TE on the suction side for small angles of attack (AoA), producing noise due to shed turbulent vorticity;
- Deep Stall (high AoA), causing the airfoil to radiate low-frequency noise, similar to a blunt body;
- And *Trailing Edge Bluntness – Vortex Shedding (TEB-VS) Noise*, which is noise generated due to VS at a blunt TE.

Wind turbines extract power from the wind at relatively low wind velocities, from 7.5 m/s to 10 m/s in average. However, when taking into account the rotation of the blades, the relative velocity of the blades can become ten times higher or more, depending on the rotational speed and on the spanwise location at the blade. Thus, Reynolds Numbers based on chord length of O(10^6) are achieved and a TBL (Turbulent Boundary Layer) develops over the blade. Therefore, as long as separation does not occur and the TE is sufficiently sharp to avoid bluntness noise, TBL-TE noise is the dominant mechanism.

According to Howe (4), at right angles to the flow, the edge noise scales with $L\mathcal{L}V^5(1 - M_0 - M_{V1})$, where L is the wetted span, $\mathcal{L}$ the correlation length of the turbulence parallel to the edge, V the characteristic edge convection velocity, M_0 the undisturbed upstream flow Mach Number and M_{V1} the component of the boundary layer Mach Number perpendicular to the edge.

The attenuation of noise by serrations may be attributed to an effective reduction of the spanwise length at the trailing edge that actually contributes to the generation of sound, even though the physical wetted length increases with the serrations (5). It is derived in Howe (6) for sawtooth serrations that

$$\Psi(\omega) \approx \frac{\Psi_0(\omega)}{\left[1+\left(\frac{4h}{\lambda}\right)^2\right]}, \qquad \frac{\lambda}{h} < 1, \qquad \frac{\omega h}{U} \gg 1 \tag{1}$$

where $\Psi(\omega)$ is the nondimensional edge noise spectrum, $\Psi_0(\omega)$ is the noise in absence of the serration, ω the acoustic frequency, U is the main stream velocity and λ/h is the width over the half amplitude of the serrations (Figure 1). Therefore, if the ratio λ/h is reduced the attenuation of noise increases, i.e. slender serrations are more effective.

Nonetheless, experimental investigations show that Howe's prediction overestimates the amount of noise that can be reduced (7; 8) and that noise reductions are also obtained at low frequencies. According to these studies, sawtooth serrations presented low to mid frequencies moderate TBL-TE noise reduction up to 7dB and even increased the amount of TBL-VS noise at high frequencies. The misalignment of the serrations with the flow was suggested, e.g. by Braun (9), as a possible cause of noise level increase at high frequencies.

The objective of this report is to verify the impact of sawtooth serrations on TE noise mitigation on a wind turbine blade, with different configurations. The most important point of this study was to attempt to improve noise reduction via mechanisms that allow auto-alignment of the sawtooth serrations with the flow. Experimental investigations were carried out in the NLR's Small Anechoic Wind Tunnel (KAT) on a DU-96-W-180 airfoil, which is specifically designed for wind turbine applications (10).

1.1 Research Questions

The research questions that motivated this experimental investigation are:

1) How much noise can be mitigated from the airfoil DU-96-W-180 by the use of serrations?
2) Does the alignment of the serrations affect the amount of sound reduced?
3) Is the aerodynamic efficiency of the airfoil affected by the use of serrations?
4) Considering the application of serrations on existent wind turbines, what would be the best position to fix the serrations, on the top or on the bottom of the trailing edge?

Before starting the experiments, there were other definitions to be made in order to accomplish a relevant investigation:

a) Which part of the blade should be studied?
b) Is it necessary to apply trips in the airfoil?
c) What should be the dimensions of the serrations (λ/h) to maximize the noise reduction?
d) What mechanisms can be used to auto-align serrations with the flow?
e) How to evaluate the aerodynamic efficiency of the airfoil?

Chapter 2 discusses the presence of bluntness noise. Chapter 3 makes a comparison between the model scale and the full scale. Chapter 4 discusses the flow similarity at the trailing edge from an acoustic perspective. Chapter 5 show some literature review and simulations performed that led to the serration models to be tested. Chapter 6 explains how drag can be calculated from the wake, derive the equations and show some simulations of the wake development. Chapter 7 describes the experiments setup and test programs. In the Chapter 8, the results are presented. And finally, in Chapter 9 the conclusions and recommendations are presented.

2 Bluntness Noise

A description of the noise mechanisms was done in the introduction and a more detailed description was done by Brooks et al (3). With high wind tunnel speeds and small angles of attack, the presences of fully laminar BL or strong separation are not a concern. Turbulent boundary-layers are present in all conditions tested and are the dominant noise mechanism. Bluntness noise due to a TE with finite thickness is discussed in this section.

Empirical evidence (11) shows that for $t/\delta^* < 0.3$ bluntness noise can be neglected. The thickness of the TE is small ($t/c = 0.0027$) and its ratio with the displacement thickness δ^*at different conditions were simulated using Xfoil, which is an interactive program for the design and analysis of subsonic isolated airfoils (12). The results are shown in Table 1. Angles of attack were varied from 0° until 9° and the free stream velocities simulated are 70 m/s, 40 m/s and 20 m/s for an airfoil of 0.15 m chord. In this table only δ^*_{top} is considered. If δ^*_{bot} had been added to the total δ^* the ratios t/δ^* values would be even smaller.

TE thickness over displacement thickness (t/δ^*_{top})			
AoA	70 m/s	40 m/s	20 m/s
0°	0.28	0.24	0.18

1°	0.26	0.22	0.16
2°	0.24	0.20	0.15
3°	0.22	0.19	0.13
4°	0.20	0.17	0.12
5°	0.18	0.16	0.11
6°	0.16	0.14	0.09
7°	0.15	0.13	0.09
8°	0.13	0.11	0.09
9°	0.10	0.10	0.08

Table 1 – Bluntness Factor t/ δ simulated in the Xfoil*

These results show that bluntness noise can be neglected. However, during the experiments serrations were inserted in the trailing edge of the airfoils, which change the nature of the flow at that region. Thus, there is still a possibility that bluntness noise is present in the serrated configurations.

3 Full Scale to Wind Tunnel

Flow similarity is an important parameter in an experimental investigation, not only to translate the wind tunnel results into practical wind turbines conditions, but also to provide information on characteristics that must be present in the experiment. Two non-dimensional parameters define if one flow can be considered similar to another. The Re (Reynolds Number)

$$\mathrm{Re} = \frac{\rho U_\infty \mathrm{c}}{\mu} = \frac{inertial\ forces}{viscous\ forces} \tag{2}$$

where ρ is the density, μ is the dynamic viscosity U_∞ is the free stream velocity and c is the chord length. And the Ma (Mach Number)

$$\mathrm{Ma} = \frac{U_\infty}{\mathrm{c}} \tag{3}$$

where c is the speed of sound.

In typical wind turbines of 2MW, the Re would be one order of magnitude higher than what can be obtained at the limit velocity of 70 m/s of the Kat Wind Tunnel utilized, implying that flow transition occur closer to the leading edge in the full scale than in the prototype. As a result, the turbulence intensity and the boundary layer (BL) thickness are different at the TE in these two cases.

The Mach Number does not play a vital role here, since the velocities in the wind tunnel are not very different from the real flow condition and the rule of thumb for *Ma < 0.3* here applies and the assumption that the flow is imcompressible is used.

In the experiments a 2D situation is investigated (i.e. a section of an airfoil spanned across the wind tunnel section). On a wind turbine the flow is 3D and the cross sections of the blade vary in chord length and also in the twist angle. The relative wind speed and subsequently the Re also change through the blade as a function of span. Consequently, natural transition will be located in different points and the boundary layer characteristics will vary. Hence, when studying an airfoil for wind turbine purposes one region needs to be chosen that represents a section of the blade. Since most of the noise is produced on the 25% outer part of the blade (12), this is the focus here. Specifically it was chosen to work with a blade section at 90% span (*r/R = 0.9*).

Using generic design rules for a wind turbine blade the typical chord length and the relative velocity at that section was assessed. For this, it was used Blade Element Momentum (BEM) Theory, as it is described in the book 'Wind Energy Explained' (13). The following assumptions are made in order to simplify the calculations:

- No rotor plane deflection with the wind;
- Wake rotation is not considered (*a' = 0*);
- There is no drag, $C_d = 0$;
- Effects of tip vortices and downwash are not considered;
- The axial induction factor *a = 1/3*.

With the above assumptions the following relations are derived (13):

$$\varphi = \tan^{-1}\frac{2}{3\lambda_r} \tag{4}$$

$$Urel = 2/3\left(\frac{U}{\sin\varphi}\right) \tag{5}$$

$$c = \frac{8\pi r\sin\varphi}{3BC_l\lambda_r} \tag{6}$$

Where φ is the angle of relative velocity, $\lambda_r = \omega r/U$ is the ratio of tangential and free stream velocity, $Urel$ is the relative wind velocity, *c* is chord length and *B* is the number of blades (*B*=3).

Using data from a typical wind turbine of 2MW and the Equations 4, 5 and 6 the chord length and consequently the *Re* were determined. The data used and calculations are summarized at the Table 2.

Reference Reynolds Number at Wind Turbine Conditions	
Rotational Speed (rpm)	19.0
Rotational Speed - ω (rad/s)	2.0
Rotor Radius - R (m)	45.00
Local radius Position - r (m)	40.50
Tangential Velocity at r - v (m/s)	81.00
IEC Wind Class	IIA
Wind Average Speed - U (m/s)	8.5
Axial Induction factor - a	1/3
λr = v/U	9.53
Angle of relative wind φ (rad)	0.070
Angle of relative wind φ (degrees)	4.00
Relative Velocity - Urel (m/s)	80.39
Lift Coefficient - Cl	1
Number of Blades - B	3
Chord Length at r (m)	0.85
Density of Air - ρ (kg/m^3)	1.225
Dynamic Viscosity of Air - µ	1.8E-05
Reynolds Number at r	4.5E+06

Table 2- Chord Length and Reynolds Number Calculation for the airfoil section at r/R = 0.9

As it can be seen from the table, at full scale conditions it is obtained $Re = 4.5\times10^6$, which is around six times higher than the maximum $Re = 0.72\times10^6$ obtained at the wind tunnel, when operating at the maximum free stream velocity (70 m/s). Table 2 was used as an indicator of what to expect in a full scale flow. However, confidential data from Wind Turbine manufacturers, available at NLR's database was also verified, especially to determine boundary layer thickness to be investigated.

4 Flow Similarity at the TE from the Acoustic Perspective

As explained in the last section, it is not possible to achieve full similarity between model scale and full scale, since the maximum *Re* achieved at the wind tunnel is six times lower than required. Ffowcs Williams and Hall's theory (14) applied to the problem of turbulence convecting at low subsonic velocity U_c above a large plate and past the trailing edge into the wake yields as a primary result (3)

$$\langle p^2 \rangle \propto \rho_0^2 v'^2 \frac{U_c^3}{c} \left(\frac{L\mathcal{L}}{r^2} \right) \overline{D} \tag{6}$$

where ρ_0 is the medium density, v'^2 is the mean-square turbulence intensity velocity, *c* is the speed of sound, *L* is the spanwise extent wetted by the flow, $\mathcal{L}$ is a characteristic turbulence correlation scale, *r* is the distance from the edge to the observer and $\overline{D}$ is the directivity factor, which equals 1 for observers normal to the surface from the leading edge. The usual assumptions for the boundary layer flow (3) are that $v' \propto U_c \propto U_\infty$ and $\mathcal{L} \propto \delta \; or \; \delta^*$. Thus, trailing edge noise scales with $U_\infty^5 \delta^*$. Comparing noise emission between model and full scale, these two parameters should be similar in both flows. U_∞ is approximately the same at model and full scale and δ^* in both cases are compared in this section.

According to Boundary-Layer Theory (15) the BL thickness δ_x at a specific point *x/c* should grow while decreasing the Reynolds Number, given that in both situations they have the same nature (laminar or turbulent). This is because for lower *Re* the *viscous forces* start to play a more fundamental role than the *inertia forces* (Equation 2), causing the BL thickness to increase. A second effect on the BL thickness is that a TBL grows faster with *x* than a laminar one (15). For instance, a TBL thickness in a flat plate grows proportionally to $x^{0.8}$, while a LBL (laminar BL) grows proportionally to $x^{0.5}$. For higher Re transition occurs earlier and therefore δ_{TE} (BL thickness at the TE) increases with *Re*. With these two effects acting together, one increasing and the other decreasing δ with Re, it was uncertain whether the BL thickness would be smaller or bigger in the wind tunnel. Thus, simulations on the Airfoil DU-96-W-180 were required, which were performed using Xfoil.

Xfoil computes the displacement thickness δ*. This can be considered as a measure of the distance by which the external streamlines are shifted due to the BL (15). In Xfoil (16), the difference between the viscous *Cp* distribution and the inviscid *Cp* distribution is due to the modification of the effective airfoil shape by the boundary layers. The gap between these effective and actual shapes is equal to the local displacement thickness δ^*. This is only about 1/3 to 1/2 as large as the overall boundary layer thickness.

Figure 2 shows that for a fixed transition position and $AoA = 8.2°$, the displacement thickness δ^* (and consequently δ) reduces with Re. This plot was made for the suction side, where $Re = 0.72\times10^6$ corresponds to the situation in the wind tunnel ($c = 0.15\ m$ and $U = 70\ m/s$) and $Re = 4.5\times10^6$ to the wind turbine. Comparing these two cases, δ^* almost halved.

Figure 3 shows δ* when natural transition occurs. After $Re = 1.7\times10^6$, the effect of the boundary layer increasing due to turbulent flow starts to dominate. One can see in Figure 4 that the transition point on the suction side reduces with increasing Re, i.e. the transition occurs closer to the LE. Therefore, the higher the Re the bigger the turbulent region is.

In Figure 3, $\delta^* = 0.022$ for both Re of interest at $AoA = 8.2°$, which is the ideal case for flow similarity. Indeed, δ^* was first plotted for $Re = 0.72\times10^6$ (model scale) and $Re = 4.5\times10^6$ (full scale) at various AoA (Figure 5). There is a region between $AoA = 8.2°$ and $AoA = 10.5°$ where the δ^* is similar for both flows. Hence, working with $AoA = 8.2°$ provides the flow similarity required for the acoustic measurements. Moreover, $\delta^* = 0.02$ and $AoA = 8°$ are typical values found in wind turbines in the region closer to the blade tip, according to NLR's confidential database. Thus, working at this angle also provides insight on the region of interest ($r/R = 0.9$).

For angles below 8.2°, the boundary layer thickness is already thicker in the wind tunnel than in the full scale. The technique of tripping, used in other experiments (17) to force transition, would only increase δ^* even more. Going further than 8.2° (effective AoA) would be a problem in noise investigation because of the deflection of the jet by the airfoil in the open-jet wind tunnel outside the collector, which would cause an extra background noise. Finally, it is also important to realize that at $AoA = 8.2°$ and $Re = 0.72\times10^6$, natural transition on both sides of the airfoil occurs, which is crucial for the analysis of TBL-TE (Turbulent Boundary Layer - Trailing Edge) noise.

Lower velocities were also tested and they also showed good approximation at a region close to 8.2°.The possibility of using c = 0.20 m ($Re=0.96\times10^6$) was also verified, but yielded only a minor improvement. Since the lift increases, the flow deflection would increase, which could demand a reduction in flow velocity or angle of attack. Thus, chord length of 0.15 meters remained as the experimental choice. The graphs of this analysis are available in Appendix A.

5 Serrations Design

This section is divided in three parts. The first is a literature review on typical serrations that has been tested and the conclusions that were drawn by the authors. The second talks about hinge mechanisms, which were applied in the root of some serrations in order to enable auto-alignment with the flow. The third part presents the final models of the serrations which were selected for the experiments.

5.1 Literature Review on Serrations

Theoretical investigation pointed out that the serration geometry determines the magnitude of the noise reduction (6). In theory, noise reduction is expected to increase as λ/h (width over half length) decreases, meaning that narrow serrations are predicted to outperform wide serrations in terms of noise attenuation at all frequencies and flow speeds.

Moreau & Doolan (7) used a flat plate model at 0° AoA and with low and moderate Re in their study. Three configurations with 0.5 mm thick trailing edge plates were tested: a straight unserrated configuration, a narrow serration (λ/h = 0.2) and a wide serration (λ/h = 0.6). The frequency range in the analysis was separated using the non-dimensional Strouhal Number, based on the BL thickness, $St_\delta = f\delta/U$. The narrow serrations (Table 3) reduced noise up to 2.5 dB at region R1 ($St_\delta < 0.13$), increased the noise up to 3dB at region R2 ($0.13 < St_\delta < 0.7$) and reduced up to 10 dB of blunt vortex-shedding noise at R3 ($0.7 < St_\delta < 1.4$). The wide serrations (Table 4) reduced noise up to 3 dB at region R1 ($St_\delta < 0.2$), barely changed at region R4 ($0.2 < St_\delta < 0.7$) and reduced up to 13 dB of blunt vortex-shedding noise at R3 ($0.7 < St_\delta < 1.4$). In general, wider serrations outperformed the wider ones.

Serration	λ/h	λ (mm)	h (mm)	R1 ($St_\delta < 0.13$)	R2 ($0.13 < St_\delta < 0.7$)	R3 ($0.7 < St_\delta < 1.4$)
Narrow	0.2	3	15	↓2.5 dB	↑3 dB	↓10 dB

Table 3 – Narrow Serrations Results from Moreau & Doolan (2003)

Serration	λ/h	λ (mm)	h (mm)	R1 ($St_\delta < 0.2$)	R4 ($0.2 < St_\delta < 0.7$)	R3 ($0.7 < St_\delta < 1.4$)
Wide	0.6	9	15	↓3 dB	0 dB	↓13 dB

Table 4 – Wide Serrations Results from Moreau & Doolan (2003)

Gruber et al (8) did extensive work on sawtooth serrations applied to the airfoil NACA 651-210. First, tests were carried out at AoA = 5° and U = 40 m/s, varying λ (width) from 1.5 mm until 19 mm for both h = 10 mm and h = 15 mm (halve lengths). For this case, the narrowest serrations, with λ = 1.5 mm and λ = 3 mm, gave the best results at middle frequencies (300Hz < f < 7000Hz) with a reduction up to 5dB for h = 10 mm and 7dB for h = 15mm. For higher frequencies all serrations increased the noise levels, being higher for smaller *λ* and with maximum of 3dB. In the second part the authors fixed λ = 3 mm and varied *h* between 1 and 40 mm, building up a total of 27 sawtooth configurations. One important finding is that a sawtooth with root-to-tip distance smaller than the boundary layer thickness is inefficient in noise reduction, i.e. h/δ should be higher than 0.5. The frequency range where serrations were efficient to reduce noise was reported to be in the range $0.5 < St_\delta < 1$, where $St_\delta = f\delta/U$. Gruber et al agreed with Howe's theory in the sense that the sharper the serration, the more noise is reduced. Finally, they showed by flow visualization that there is crossflow within the teeth of the sawtooth serrations, which the authors considered to be the cause of high frequency noise generation.

Braun et al (9), realized experiments with sawtooth serrations in six different configurations which included λ/h of 0.33, 0.67 and 1 and serrations with different alignment angles with the suction side, which the authors called straight, bent and curved. For these configurations they tested AoA from 0 to 14°. The results found by Braun et al are summarized in the Table 5 considering AoA from 6° to 8°. The results are not discrete as presented here, since for a continuous range of frequencies and AoA it is difficult to summarize with a unique value. Nevertheless, the table gives a good summary, which helps to understand some important conclusions from Braun:

- A reduction from 2 to 3.5 dB was found to occur in low frequencies and medium AoA.
- Serrations aligned with the suction side of the airfoil increased the noise production in high frequencies.
- Aligning the serrations with the flow at the TE by curving or bending the serration, caused reduction of noise in high frequencies as well.

Serration*	λ/h	λ (mm)	h (mm)	Geometry	Low Freq. (0.63 -2 kHz)	Medium Freq. (2 - 4 kHz)	High Freq. (4 - 6 kHz)
Straight 2:1	1.00	20	20	Straight	↓2 dB	↑6 dB	↑8 dB
Straight 6:1	0.33	6.66	20	Straight	↓2 dB	↑6 dB	↑8 dB
Curved 2:1	1.00	20	20	Curved	↓3.5 dB	↓4 dB	↓2 dB
Bent 2:1	1.00	20	20	Bent	↓3 dB	↓3 dB	↓2 dB
Bent 3:1	0.67	20	30	Bent	↓3.5 dB	↓3 dB	↓3 dB

Table 5 - Results from Braun et al for different types of serrations
** the serration name as it was used by the author uses the ratio 2h/λ (length over width)*

One conclusion from Braun that is not apparent from the table is that in the range of frequencies around 1 kHz for almost all configurations, a tone appeared, reducing the absolute noise reduction benefit. Lastly, it is important to emphasize is that the work from Braun et al argues that the misalignment of the serration with the flow is what causes noise increase at high frequency. These findings support the idea for testing flexible serrations in this project.

5.1.1 Discussion on literature reviewed

Moreau and Doolan obtained significant reductions in high frequencies, however it should be noted that those were attenuations of bluntness noise, which apparently was not present in the other studies.

Moreau and Doolan found contradictory results compared to Gruber et al in respect to whether narrow or wide serrations perform better. Though, a possible reason is that the former used a flat plate and the latter analysed an airfoil. Besides, when looking into the whole data of Gruber et al, one can find trends and draw conclusions, however when comparing the serrations in pairs, it is sometimes unclear if a wide or a narrow serration performs better. As discussed by Gruber et al, it is uncertain if the ratio λ/h is the independent variable to be analysed or if h and λ should be verified separately. One guideline to be followed is that h should be bigger than δ. Another appears to be that sharper serrations gives better noise reduction until $St_\delta = 1$, at least for airfoils. However it should not be too sharp since in this case high frequency noise can be produced.

Finally, the ratio for the sawtooth serrations chosen for this experimental investigation is $\lambda/h = 0.5$. To support this decision Figure 6 from Gruber et al (8) is reproduced here. In the figure, it is shown the difference in sound power level ΔPWL in third octave bands and within limits of +- 2 dB. The experimental parameters are AoA = 5° and U = 60 m/s ($Re = 0.62\times10^6$). For $\lambda/h = 0.5$ ($h/\lambda = 2$ in the figure) reductions on the radiated sound are obtained in the range $0.3 < St_\delta < 0.8$, while for $St_\delta > 0.8$ noise increase is not relevant. Thus, $\lambda/h = 0.5$ appears to be an adequate choice. Besides, the investigation here reported focused on other aspects of the serrations than to find the most optimal ratio λ/h.

The sawtooth amplitude was calculated as $h = 5\delta^*$, in order to obtain $h/\delta \sim 1$, assuming that $\delta \sim 5\delta^*$. Therefore, the half length and width of the sawtooth used in the experiments are, respectively, $h/c = 0.1$ (15 mm) and $\lambda/c = 0.05$ (7.5 mm) (Figure 12).

5.2 Hinge Mechanisms

According to Braun (1998), aligning the serrations with the flow by bending them, can be a solution for the noise increase caused by serrations in high frequency band. However, only bending them would not completely solve the problem as the *AoA* is not always constant during the operation of a wind turbine. For instance, the blade is rotated around its own axis in order to apply pitch control for the purpose of adjusting the output power. The solution then appears to be increasing the flexibility of the serrations, allowing it to auto-align with the flow when a new *AoA* is imposed.

To define the initial bent position, Xfoil simulations were performed at $AoA = 8.2°$ and $Re = 0.72 \times 10^6$. In order to do so, first a 3 cm plate extension was included into the Airfoil geometry in Xfoil, aligned with the chord line $\varphi = 0°$, where φ is the angle between the serration and chord line. This is only an approximation method, since Xfoil only simulate 2D flow and does not consider 3D effects caused by a serrated profile. In this manner, a graph of C_p vs. x/c was obtained and the torque around the trailing edge was calculated.

Different angles φ were evaluated until the orientation where the torque equals zero was found at $\varphi = 2.1°$ (Figure 7). The pressure distribution on the 2D serration, obtained in the Xfoil can be seen in Figure 8. The same routine was realized for a second configuration, in which a plate length of 3.6 mm was added between the serrations and the airfoil TE, increasing the torque around the TE. The 3.6 mm length is part of one of the tested serrations which is explained later in this section in more details. For this new configuration, $\varphi = 2.3°$ was obtained. From these values the bent angles for pressure or suction side mounting were derived. In order to do so, the internal angles close to the trailing edge θ_{top} (top side) and θ_{bot} (bottom side) were taken into account (Figure 9).

In Table 6, the values for the bending angle between the serration and the chord line φ for the regular serration (φ_{ser}) and for the serration with a plate of 3.6 mm preceding the serration (φ_{pla}) are given.

θ_{top}	θ_{bot}	φ_{ser}	φ_{pla}	$\varphi_{ser} + \theta_{top}$	$\varphi_{pla} + \theta_{top}$	$\theta_{bot} - \varphi_{ser}$
13.0°	3.9°	2.1°	2.3°	15.1°	15.3°	1.8°

Table 6 – Bent Angles for the serrations

Bending the serrations only solves the misalignment with the flow for one specific design conditions, in this case an angle of attack of 8.2° and freestream velocity of 70m/s. If another angle is tested, such as AoA = 0°, a torque is experienced (Figure 10). The use of a serration that auto-aligns with the flow through a hinge mechanism is therefore considered.

Two different methods were used as a way of improving the flexibility of the serrations. One of them is a mechanical hinge mechanism created by laser cutting the sawtooth serrations, in such a way that separated small beams are shaped in the metal sheet, close to the root of the teeth. Through torsion these small bars twist and the serrations can pivot around the TE. This first technique is the basis of two different serrations, which will be referenced with the term *"cutted"*, to indicate that the laser cuttings are present. Another approach is to create a hinge by connecting the serrations to the trailing edge via a flexible material, such as adhesive tape. This latter method is referenced to as Flexible Serrations (FS).

In order to design the laser cuts, some basic solid mechanics modelling was performed. The Assumption is that the beam in which torsion occurs is only formed by the spring connection *l* between structural connections which would only act as links (Figure 11). The total torque acting on one spring connection is given by (18):

$$T = \frac{\theta G J'}{l} \tag{7}$$

Where θ is the angle which one spring connection turns when torque is applied, G is the torsional modulus for steel (~77 GPa) and J' the polar moment of inertia. For a solid rectangular section with side 2a and thickness 2b, J' is defined by (18)

$$J' = ab^3\left[\frac{16}{3} - 3.36\frac{b}{a}\left(1 - \frac{b^4}{12a^4}\right)\right] \tag{8}$$

in which a ≥ b. The total bent angle of the serration due to torsion is then defined as:

$$\Theta = \theta . n \tag{9}$$

The total torque due to the pressure distribution on the serration was simulated on Xfoil, as mentioned before. With φ = 2.1°, the torque is approximately zero for AoA = 8.2° and T = 0.0005 Nm in clockwise direction for AoA = 0°. This latter value was chosen as a representative torque experienced by the hinge mechanism resulting from the flow over the serrations. The torque experienced due to the weight of the serrations is not considered in the calculations because the experiments are performed with the serrations aligned vertically, i.e. perpendicular to the ground. Furthermore, the weight is one order of magnitude lower than that due the torque applied by the flow.

Using a Matlab program, predictions were carried out on the flexibility of each serration concept in order to design the hinge layout. The thicknesses (2b) of the material tested were 0.3, 0.4 and 0.5 mm. The distance between the cuts (2a) was set as 0.6 mm, because it was the maximum precision that could be obtained in the workshop. J' was then calculated for each half thickness b. Then, the number *n* of springs was plotted against the connection length *l* for each model of serration. The first prototype simulated was the one with laser cuts inside the serration. From now one, this model will be referenced here as *Cutted Serration (CS)* (Figure 13). In this case, the maximum spring beam size is determined by the width of the serration. Furthermore, the number of springs is restricted, because the surface of the serration cannot be completely covered with cuts. Therefore, a choice was made of n = 6, to provide a hinge that covers 14% of the surface of the serration at maximum.

The results for the Cutted Serration are plotted in Figure 16. The objective was to verify how much deflection could be obtained for the *l* and *n* parameters that are defined by the serration geometry. Notice that the spring length *l* is not constant for this concept and it is reduced when moving towards the tip of the sawtooth serration, because of its triangle shape. Therefore, in the Figure 16 the horizontal axis represents the average length of the connection, which for *n = 6* is *l = 1.4 mm*. Figure 16 shows that *t = 0.3 mm*, *l = 1.4 mm* and *n = 6* is a viable solution for a total bending of $\Theta = 0.8°$.

The second concept includes a small plate of 3.6 mm before the serrations to facilitate the hinge mechanism. The length of 3.6 mm was chosen in order to make it possible at least four springs. This way, the serration was freed from cuts in the triangle area. This model is referenced as *Serration with Cutted Plate (SCP) (Figure 14)*. In this case, *n = 4* and *l = 5.1 mm*. The maximum bending was $\Theta = 3.2°$ (Figure 17).

However, what is the required angle at which a serration should be able to bend as to fully align with the flow? Considering the range of AoA from 0° to 8.2°, this range of angles φ was estimated using Xfoil as follows:

- Applying AoA = 0° and U = 70 m/s, it was found that $\varphi_{CS/US,\ \alpha=0°}$ = -2° and $\varphi_{SCP,\ \alpha=0°}$ = -1.5° were the angles the serration should be bent to nullify the torque around TE for CS/US and SCP models, respectively.

- Comparing these neutral positions with the φ values found before for AoA = 8.2° ($\varphi_{CS/US,\alpha=8.2°}$ = 2.1° and $\varphi_{SCP,\alpha}$ = 2.3°) it was estimated that the serration should be able to pivot 4.1° and 3.8° around the TE for CS/US and for SCP models, respectively.

Therefore, the simulations show that SCP should be able to align with the flow in 85% of the range (3.1° of 3.8°) from 0° to 8.2°, while for CS only 20% (0.8° of 4.2°). Even though it is not as efficient as required, any gain in flexibility should represent some noise reduction, at least at angles close to 8.2°, which is the AoA in which the serrations are designed to be initially aligned.

The simulations done here have some limitations such as the fact that Xfoil is 2D flow simulator and also the fact that only torsion was considered and not bending. This latter phenomenon would probably help the serrations to better align with the flow, increasing the deflection and giving a slightly curved profile. However, it was assumed here that torsion is the most influent phenomena and responsible for most part of the serration rotation.

The reference torque values used in the simulations were also compared with the maximum torques supported by the internal beams and it was confirmed that the torsional stress caused by the air is below the maximum stress the material can handle without plastic deformation to occur. The maximum stress at the midpoint of one beam with a solid rectangular section is (18):

$$\tau_{max} = \frac{3T_{max}}{8ab^2}\left[1 + 0.6095\left(\frac{b}{a}\right) + 0.8865\left(\frac{b}{a}\right)^2 - 1.8023\left(\frac{b}{a}\right)^3 + 0.9100\left(\frac{b}{a}\right)^4\right] \tag{10}$$

So, using 58% of the yield stress (Von Mises Criterion) of stainless steel (~520Mpa) the maximum torque that one beam can hold depending on *b* (half thickness) and *a* (half distance between cuts) were calculated (Table 7).

Torque Simulated in Xfoil (Maximum at AoA = 0°)	
US or CS	0.0005 Nm
SCP	0.0016 Nm

Maximum Torque supported depending on thickness	
t = 0.3 mm	0.0040 Nm
t = 0.4 mm	0.0067 Nm
t = 0.5 mm	0.0099 Nm

Table 7 - Simulated and Maximum Torques

5.3 Sawtooth Serration Models

Until this section it was discussed all the theory used and simulations performed to define the serration models to be tested. In this section it is summarized the models to be tested:

- Clean Configuration (just the airfoil without serrations);
- Uncutted Serration fixed on the suction side (US-TOP) (Figure 12 A1);
- Uncutted Serration fixed on the bottom side (US-BOT); (Figure 12 A2);
- Cutted Serration (CS) (Figure 13);
- Serration with Cutted Plate (SCP) (Figure 14);
- Flexible Serration (FS) (Figure 15);

6 Drag in the Far Wake

This section explains how the drag on an airfoil is calculated in the far wake of an airfoil, which helps to answer the question: "Is the aerodynamic efficiency of the airfoil significantly affected by the use of serrations?" Moreover, the width increase of the wake moving downstream from the TE is estimated, to determine the measuring locations in the experiments.

A wake is a so-called free turbulent flow, because it is not confined by a solid wall. It is formed behind a body that is being dragged in a fluid at rest or behind a body which has been placed in a stream fluid. The velocities in the wake are smaller than the edge velocity, due to momentum losses, caused by airfoil drag. The width of the wake increases as it moves away from the body and the deficit velocity decreases. The drag in the body can then be calculated through the momentum equation (15).

The wake of an isolated airfoil, even at non-incidence is asymmetric, due to loading and different boundary layer developments on the suction and pressure sides. After a certain distance downstream from the body, the asymmetric behavior of the wake vanishes and the physical characteristics and aerodynamic loading have negligible effects. This region is referred to as "Far Wake". According to C. Hah and B. Lakshminarayana the asymmetry practically disappears after 1.5 chords downstream the TE of the airfoil (19). In this section, an expression for the velocity profile in the wake and its growth in the streamwise direction is derived, as it was done by Schlichting (15).

The velocity depression behind the wake is expressed as the difference between the stream velocity and the flow velocity, being the depression maximum at the center of the wake and zero in the half width b, where $u_1 = U_\infty$. Thus, the velocity depression is defined as

$$u_1 = (U_\infty - u) \tag{11}$$

where U_∞ is the free stream velocity and *u* the local velocity in the wake. Problems in free turbulent flow are of boundary-layer nature. This means that the region in the space where the solution is being pursued does not extend far in the transverse direction, as compared with the main direction of the flow and that transverse gradients are large compared to gradients in streamwise direction. Consequently it is permissible to study such problems using the boundary-layer equations. In two-dimensional motion, neglecting compressibility effects the momentum equation is then given by

$$\frac{\partial u}{\partial t} + u\frac{\partial u}{\partial x} + v\frac{\partial u}{\partial y} = \frac{1}{\rho}\frac{\partial \tau}{\partial y} \tag{12}$$

and continuity by

$$\frac{\partial u}{\partial x} + \frac{\partial v}{\partial y} = 0 \tag{13}$$

where *x* is the streamwise direction, *y* is the transverse direction and *u* and *v* the local velocities at x and y directions, respectively.

Prandtl's mixing-length hypothesis allows expressing the shear stress as follows

$$\tau = \rho l^2 \left|\frac{d\bar{u}}{dy}\right| \frac{d\bar{u}}{dy} \tag{14}$$

where $\bar{u}$ is temporal mean velocity in x direction, *ρ* is the density of the fluid and *l* is the so-called mixing length. Furthermore, in the far wake of 2D flow the term $v\partial u/\partial y$ is small and can be neglected. Hence, assuming steady flow and substituting (11) and (14) in (12) yields

$$-U_\infty \frac{\partial u_1}{\partial x} = l^2 \frac{\partial u_1}{\partial y}\frac{\partial^2 u_1}{\partial y^2} \tag{15}$$

When dealing with turbulent wakes it is usually assumed that *l* is proportional to the width of the wake 2*b*. Hence:

$$\frac{l}{b} = \beta = const.$$

Additionally the following rule endured with time:

$$\frac{Db}{Dt} \sim v'$$

This equation states that the rate of increase of the half width *b* is proportional to the transverse turbulent velocity *v'*. In Prandtl's mixing-length theory, it was derived that:

$$v' \sim l \frac{\partial u}{\partial y}$$

Thus:

$$\frac{Db}{Dt} \sim l \frac{\partial u}{\partial y}$$

The mean value of $\partial u/\partial y$ taken over half of the width of the wake is assumed to be proportional to u_1/b. So,

$$\frac{Db}{Dt} = const \times \beta u_1 \tag{16}$$

Now, using the definition of the material derivative:

$$\frac{Db}{Dt} = \frac{\partial b}{\partial t} + u_i \frac{\partial b}{\partial x_i}$$

Using assumption of steady state and since *b* is only function of *x*:

$$\frac{Db}{Dt} = u \frac{db}{dx} \tag{17}$$

So, because $u = (U_\infty - u_1)$ and under the assumption ($u_1 \ll U_\infty$):

$$\frac{Db}{Dt} = U_\infty \frac{db}{dx} \tag{18}$$

Equating (16) to (18):

$$U_\infty \frac{db}{dx} = const \times \beta u_1$$

Or

$$\frac{db}{dx} \sim \beta \frac{u_1}{U_\infty} \tag{19}$$

To calculate the drag from wakes, it is used a direct relation between momentum and the drag on the body. Considering the drag per unit span *D'* and *J'* the momentum per unit span, the following relation is used:

$$D' = J' = \rho \int u(U_\infty - u)dy \tag{20}$$

Equation 20 is valid, provided that the control surface has been placed so far behind the body that the static pressure has become equal to that in the undisturbed stream. This is equation is fundamental to determine the drag from the hot-wire experiments.

To determine the wake width and velocity deficit with distance, it is assumed that at a large distance behind the body, $u_1 = (U_\infty - u)$ is small compared to U_∞, and then it is possible to use the following simplification:

$$u(U_\infty - u) = (U_\infty - u_1)u_1 = U_\infty u_1$$

And equation (20) becomes:

$$D' = J' = \rho\, U_\infty \int u_1 dy \tag{21}$$

The drag per unit span can also be expressed in terms of the drag coefficient:

$$D' = ½\rho U_\infty^2 c c_d \tag{22}$$

where *c* is the chord of the airfoil. Equating (21) to (22) and using $J' \sim \rho\, U_\infty u_1 b$, it is thus obtained:

$$\frac{u_1}{U_\infty} \sim \frac{c_d c}{2b} \tag{23}$$

Then, inserting Eq. (20) into (23):

$$2b\frac{db}{dx} \sim \beta c_d c$$

or

$$b \sim (\beta x c_d c)^{0.5} \tag{24}$$

Inserting Eq. (24) back to (23), it is found the rate at which the depression in velocity curve decreases downstream to the TE:

$$\frac{u_1}{U_\infty} \sim \left(\frac{c_d c}{\beta x}\right)^{0.5} \tag{25}$$

The results from (25) and (24) show that the half width of the 2D wake increases with $\sqrt{x}$, while the velocity decreases with $1/\sqrt{x}$.

Equation 25 can also be expressed in the form:

$$u_1 \sim U_\infty \left(\frac{x}{c_d c}\right)^{-0.5} \left(\frac{l}{b}\right)^{0.5}$$

In the view of similarity of profiles the ratio $\eta = y/b$(x) is introduced as the independent variable and it is assumed that:

$$u_1 = U_\infty \left(\frac{x}{c_d c}\right)^{-0.5} f(\eta) \tag{26}$$

And from Eq. (24) it is assumed that:

$$b = B(x c_d c)^{0.5} \tag{27}$$

Inserting Eq. (26) and (27) into Eq. (15), it is obtained the following differential equation for the function *f(η)*:

$$\frac{1}{2}(f + \eta f') = \frac{2\beta^2}{B} f' f''$$

Integrating this equation with the boundary conditions

$$u_1 = 0$$
$$(\partial u_1)/\partial y = 0$$
$$at \;\; y = b$$

or

$$f = 0$$
$$f' = 0$$
$$at \;\; \eta = 1$$

It is obtained

$$\frac{1}{2}(\eta f) = \frac{2\beta^2}{B} f'^2$$

And integrating once again

$$f = \frac{1}{9}\frac{B}{2\beta^2}\left(1 - \eta^{\frac{3}{2}}\right)^2$$

Then, using $\int_{-1}^{1}\left(1 - \eta^{\frac{3}{2}}\right)^2 d\eta = 9/10$, one can obtain that B = $\sqrt{10}\beta$ and the final solution becomes:

$$b = \sqrt{10}\beta(xc_d c)^{0.5} \tag{28}$$

$$\frac{u_1}{U_\infty} = \frac{\sqrt{10}}{18\beta}\left(\frac{x}{c_d c}\right)^{-0.5}\left\{1 - \left(\frac{y}{b}\right)^{\frac{3}{2}}\right\}^2 \tag{29}$$

The use of equations (28) and (29) in practice has the inconvenient that *β* needs to be determined experimentally. To solve this problem, it was used data from Hah and Lakshminarayana (19), where it was available information about the wake width and velocity deficits at 3°, 6° and 9° angles of attack, $Re = 0.38 \times 10^6$ and $x/c = 1.5$ downstream the TE. Inputting this data into a Matlab program values for *β* were estimated. Interpolating and extrapolating the obtained values it was also determined *β* for 0° and 8.2° angle of attack. Moreover, *β* was considered to be the same at other free stream velocities, due to a lack of more precise values. The calculated values are shown in Table 8.

AoA	0°	3°	6°	8.2°
β	0.200	0.220	0.250	0.305

Table 8 – β values estimated for the wake simulations

With this, some simulations were done and the wake width 2b was found for all the conditions intended to be tested during the experiments, which are shown in Tables 9 and 10. One example of the simulations are shown in Figure 18, for U_∞ = 70 m/s and AoA = 8.2°. Notice however, that in the Figure 18 it is shown only the half width values.

x/c	Re 0.412				Re 0.514			
	A0	A3	A6	A8.2	A0	A3	A6	A8.2
0.94	0.125	0.143	0.171	0.209	0.118	0.135	0.160	0.199
1.5	0.158	0.181	0.216	0.264	0.150	0.170	0.203	0.252
1.75	0.171	0.195	0.233	0.285	0.162	0.184	0.219	0.272

Table 9 – Wake width simulated with Matlab for Re = $0.412{\times}10^{6}$ and $0.514{\times}10^{6}$

x/c	Re 0.617				Re 0.720			
	A0	A3	A6	A8.2	A0	A3	A6	A8.2
0.94	0.113	0.130	0.153	0.193	0.110	0.125	0.149	0.188
1.5	0.143	0.164	0.194	0.244	0.139	0.157	0.189	0.238
1.75	0.154	0.177	0.209	0.263	0.150	0.170	0.204	0.257

Table 10 – Wake width simulated with Matlab for Re = $0.617{\times}10^{6}$ and $0.720{\times}10^{6}$

7 Experimental setup and test programs

In September 2014, acoustic and aerodynamic measurements were performed on the TU-Delft airfoil DU-96-W-180 at the NLR's Small Anechoic Wind Tunnel KAT. The main goal was to observe the efficiency of sawtooth serrations on TE noise mitigation and also to verify how the aerodynamic properties of the airfoil are modified with them. The KAT is an open circuit, open jet wind tunnel, with a nozzle of 0.51 x 0.38 m, connected to two parallel end plates (0.90 × 0.70 m²), providing a semi-open test section. The airfoil was fixed in a vertical position, spanning between the plates (Figure 19). The anechoic room surrounding the test section is 5×5×3 m³, which was completely covered with 0.5 foam wedges (Figure 20) yielding more than 99% absorption above 500 Hz (17). First, balance measurements were carried out that allow for a correction of the effective angle of attack. Then hot-wire experiments were performed, followed by acoustic measurements using a 48-microphone phased array. The considered serration configurations are described in section 5.3.

7.1 Balance Measurements

Balance measurements were performed in order to compare the measured lift with Xfoil simulations to derive an effective angle of attack. The airfoil was mounted on a rotating balance, which allows remotely changing the AoA. The tests were performed within the range of -5° to 25° geometric angles of attack and for wind tunnel free stream velocities of 40, 50, 60 and 70 m/s. The measured lift force was non-dimensionalized as:

$$C_{l,meas} = \frac{L_{meas}}{\frac{1}{2}\rho U_{\infty}^{2} bc} \qquad (30)$$

The effective angles of attack are obtained by the following correction:

$$\alpha_{eff} = \frac{\alpha_t}{1.7523} \tag{31}$$

Where α_t is the geometrical AoA, and the value 1.7523, which is dependent on the chord length and the wind tunnel geometry, determined by a correction given by Brooks (1989).

7.2 Hot-wire

The probe was mounted on the AVHA 3-axis traversing system (AVHA-3ATS) (Figure 21). The support strut resembles a thick symmetrical airfoil (Figure 22). A single hot-wire was used that was orientated parallel to the spanwise direction (Figure 23), with a CTA (Constant Temperature Anemometry) system. In Figure 24 the coordinate system is shown. The origin is defined at the airfoil span centre, approximately 1.5 mm from the TE. A new origin was defined with respect to the varying TE position for each angle of attack.

7.2.1 Boundary-Layer Measurements

Boundary Layer measurements were obtained perpendicular to the camberline of the airfoil at 1% chord downstream the trailing edge. The data was obtained for the free stream velocities 40, 50, 60 and 70 m/s (Re 0.412, 0.514, 0.617 and 0.72×10^6) and for effective angles of attack 0°, 3°, 6° and 8.2° corresponding to geometric angles of attack 0°, 5.26°, 10.51° and 14.37°, respectively. The BL measurements were taken only for the Clean Configuration (without serrations). Each traverse consisted of 40 points, with 20 on each side of the airfoil.

7.2.2 Wake Measurements

Wake measurements were carried out for the clean configuration (no serration) in three downstream positions x/c = 0.94, 1.5 and 1.75 with respect to the TE to dermine the optimal location for drag dermination. For the serrated configurations only x/c = 1.75 was considered. The FS was only included in the acoustic measurements since this configuration was added on adhoc basis later in the test campaign. The traverses done for the clean configuration were realized at the center of the span (vertical position), with the points varying in the direction perpendicular to the airfoil surface. For the serrated configurations an H-shaped traverse was performed in a sequence of three steps. First, the wake was measured in the center of the span. Second, at another spanwise position, located at 0.15c below the first one. And third, the traverse was measured perpendicular to the first two (spanwisely), at roughly the center of the wakes (Figure 25). Note that the first two traverses are perpendicular to the wind tunnel axis and not the chordline or camberline. Besides, the center of the traverses does not coincide with the center of the wind tunnel it depends on the angle of attack.

The center and width of the wakes were approximately determined with the help of a HW connected to an oscilloscope, which enables to quickly visualize the turbulence of the flow at different positions of the wind tunnel. This way, it was guaranteed that the whole wake was measured and that the required precision was obtained, without oversetimating the wake width. The data was obtained for the free stream velocities 50 and 70 m/s (Re 0.514 and $0.72{\times}10^6$) and for the effective angles of attack 0°, 6° and 8.2°, corresponding to the geometric angles of attack 0°, 10.51° and 14.37°, respectively. The same traverses were used for the measurements in 50 and 70 m/s, since the differences in wake size or location with U_∞ were found to be negligible.

7.3 Acoustic Measurements

Acoustic Measurements were realized using a microphone array with 48 microphones located at the suctions side of the model at a distance of 0.6 m from the center of the Small Anechoic Wind Tunnel KAT from NLR (Figure 26). To obtain good resolution at low frequencies the array had 0.6 × 0.8 m^2 (Figure 27). The coordinate system used for the microphone array (Figure 28) had its center located at mid span and in the rotating axis of the airfoil, which is 31.3% c from the leading edge. The y-axis here is positive in the opposite direction in comparison with the hot-wire coordinates, i.e. in the direction of the microphone array.

The acoustic measurements were performed for the six configurations mentioned in section 5.3 at four different wind tunnel speeds 40, 50, 60 and 70 m/s (Re 0.412, 0.514, 0.617 and $0.72{\times}10^6$) and at geometric angles of attack ranging from -4° to 20° with steps of 2°.

Figure 29 shows an example of one acoustic source map obtained through the experiments for the clean configuration with $\mathbf{U}_\infty$ = 40 m/s, α_{eff} = 6° at f = 3150 Hz. The grey rectangle represents the airfoil model. The colour graph represents the SPL (Sound Power Level) in dB, while the range was always 12 dB. The flow goes from left to right. It is clear from this graph that noise is emitted from the trailing edge.

In order to perform balance measurements the profile should be mounted clear of any obstruction and not clamped between the side plated. The airfoil span was approximately 0.3 mm smaller than the distance between the plates, which leaves an air gap between the airfoil and the upper end plate. On the lower part there is also small gaps on the junction between the lower plate and the airfoil, where the airfoil is fixed. However, they are smaller than at the upper part. When the wind tunnel is running, air flows through these gap and tip vortices are created, increasing significantly the turbulence at these locations. With this, noise sources are created close to the plates, the so-called "corner-sources", which are stronger than the acoustic disturbances at other regions of the airfoil. This way, the acoustic source maps cannot show clearly the noise sources of interest, such as at the TE of the airfoil middle span. To fix this problem, these gaps need to be treated, which was done using silicone (Figure 30).

Figure 31 shows the effectiveness of the treatment via the acoustic source maps at $\mathbf{U}_{\infty}$ = 40 m/s, AoA = 10.5° (α_{eff} = 6°) and f = 2000 Hz, with the US-BOT serration installed. In this figure it is shown the situations before (LEFT) and after (RIGHT) the gap between the airfoil and the wind tunnel plate has been filled with silicone. The corner-source on the upper part of the airfoil before the treatment was 60 dB, which after the treatment reduced to approximately 58 dB (note that the figures are not in the same scale). This two dB reduction enables other noise sources to become clearer in the graph, which has a maximum of 12 range dB. One can see that filling the gaps with silicone, provided a better visualization (RIGHT) showing also noise in the range of 46 to 49 dB that was hidden before. Also, the silicone increased leading edge noise on the upper part, which changed to around 51 dB (light green) and it was less than 49 dB (white) before. This side effect does not influence the results, since the noise in the trailing edge is still much higher and around 56 dB. The important outcome of this treatment is that the middle span-trailing edge noise becomes easier to distiguish.

8 Results

8.1 Lift Coefficients

Figures 32 to 35 show the Cl-α curves for the Clean Configuration plotted together with the Xfoil Simulations. The experimental values are plotted in two ways: *Cl* vs. the geometrical angle of attack α_{geo} and *Cl* vs. the effective (corrected) angle of attack α_{eff}. The measured lift approximates to Xfoil predictions when plotted against effective angle of attack, in particular in the region where the Cl-α curve is linear. A shift of approximately one degree to the right is found when compared with simulations. Furthermore, stall starts earlier in the wind tunnel (α_{eff} ~ 9.1°) than in simulations (AoA ~ 10°). The Brooks correction proved to be a good approach to relate the experiments performed in an open jet environment with infinite free flow.

The balance measurements were realized several times and presented good repeatability. Figure 36 shows six different measurements for the clean configuration at 70 m/s, where *F* stands for Forward (increasing AoA) and *R* stands for Reward (decreasing AoA), indicating which direction the balance was being turned. No hysteresis effect was found. The only case that measurements presented some difference was in the stall region for the US-TOP, when comparing two different measurements days. Because of this, two curves for the US-TOP are presented in the general comparison amid all configurations (Figure 37 and 39).

Figure 37 shows the balance measurements for all configurations (section 5.3), with exception of the FS. In the first figure, the Cl values were normalized taking into account also the area provided by the serration. Neglecting the small angle of 2.1° between the serration and the chord line, the new surface area, projected on the plane z =0, becomes

$$A_{surface} = A_{airfoil} + A_{serration}$$

$$A_{surface} = (b \times c) + (½ \times b \times l_{serration})$$

where *b* is the span and *l* the length of the serration. And because $l_{serration} = 0.2c$:

$$A_{surface} = b \times 1.1c \qquad (32)$$

This is equivalent to say that a new chord 10% higher is being used. For the SCP, however, because of the extra 3.6 mm plate $l_{SCP} = 0.224c$ and $A_{SCP} = b \times 1.112c$.

Figure 38 shows the *Cl-α* curve with *Cl* values normalized with the airfoil chord only. In both Figures 37 and 38, the measured *Cl-α* curves in the linear region (before stall) are parallel to each other, with a slightly difference in slope compared to the Xfoil curve. Also in the linear region, independently of the normalization method, the *Cl* is highest for the clean configuration, followed by (in order) SCP, CS, US-TOP, US-TOP (2) and US-BOT. Also interesting to note is that the stall region starts later for the serrated configurations, with a maximum lift around α_{eff} ~ *10.3°*, while it was α_{eff} ~ *9.1°* for the clean configuration. Finally the biggest difference between both normalization methods is that if the first one is considered (Figure 37), then the clean configuration has a higher maximum lift than all the serrated configuration, while for the second method (Figure 38) the serrations have comparable maximum lift coefficients, with SCP and US-TOP (1) being even higher. A better way to compare would be to use *Cl/Cd* curves. However, because the drag is not sufficiently accurate measured by the balance, due to the precision of the machine, the drag coefficient must be deduced from the momentum deficit in the far wake.

8.2 Hot-wire

This section presents the results obtained for the Hot-wire measurements for the Boundary Layer (4.2.1) and for the Wake (4.2.2).

8.2.1 Boundary-Layer

Figures 39 to 42 show a comparison among the velocity profiles in the Boundary Layer of different free stream velocities and Figures 43 to 46 compare the turbulence profiles. The pressure side is represented by the positive part of n/c (normal coordinates to the camber line over chord length), while the suction side is represented by the negative axis.

For $\alpha_{eff} = 0°$ (Figure 39) the profiles are similar, not varying much with velocity. Figure 43 shows the turbulence graphs for the same angle. The turbulence intensity is lower and returns to free stream levels faster for higher U_∞, that is, in a smaller transverse distance. Hence, the boundary layer is thinner for higher U_∞.

For $\alpha_{eff} = 3°$ (Figure 40), at lower U_∞ the velocity profiles are less full and takes longer in the transverse direction to reach the edge velocity. This also indicates bigger boundary layer thicknesses for lower U_∞. Figure 44 shows the turbulence once again returning faster to free stream levels for higher U_∞.

For $\alpha_{eff} = 6°$ (Figure 41) again the velocity profiles are fuller for higher U_∞. However, in the pressure side an exception to this trend occured, in which the 70 m/s velocity profile is the least full. This difference also is noted in the turbulence intensity graph (Figure 45), where the 70 m/s turbulence profile takes to return to free stream levels than the 60 m/s profile.

For $\alpha_{eff} = 8.2°$ (Figure 42), the deficit in velocity for 60 m/s and 70 m/s are more intense in the center and the velocity profiles are less full on the suction side. This indicates that the flow is either separated or close to separation. In the pressure side for U_∞ = 70 m/s the velocity profile is less full than the trend. In Figure 46, the turbulence levels for U_∞ = 60 m/s and U_∞ = 70 m/s on the suction side and U_∞ = 70 m/s on the pressure side are also higher than the trend.

The Local Turbulence Profiles are plotted in Figure 47 for all free stream velocities, but only for = α_{eff} = 0° and α_{eff} = 8.2° to retain clarity. One can see that the local turbulence increases with AoA and that achieves a peak for U_∞ = 70 m/s and α_{eff} = 8.2°. This is unexpected, since the local turbulence at other angles (0°, 3° and 6°) decrease with higher U_∞ (see also Figures 48 and 49), while for *AoA = 8.2°* the trend is opposite. This is indicates that flow separation might be occuring for this condition and causing the local turbulence to increase abruptly. As it was shown in the Lift Coefficient Curves, *AoA = 8.2°* was close to the maximum lift point (~9.1°) in the wind tunnel. It should also be noted that in the regions where the local turbulence is bigger that 0.5 the measurements might not be accurate anymore.

Lastly, the behavior of the BL measurements with different AoA was also investigated. Figures 50 to 53 show a comparison among the velocity profiles in the BL of different AoA, at constant U_∞. On the suction side, increasing AoA the velocity profiles become less full and the turbulence intensity becomes higher and takes longer to return to free stream levels. On the pressure side, increasing AoA the velocity profiles become fuller and the turbulence intensity lower, returning to free stream values in shorter distances. This contrast between suction and pressure sides is related to the shifting transition location. Increasing the angle of attack, transition occurs closer to the Leading Edge on the suction side and farther from it in the pressure side. Therefore, while on the suction side the BL thickness increase with AoA, on the pressure side it decreases.

Figures 54 to 57 show the turbulence intensity profiles. It is noted that in the positive axis of the graph, there is a peak close to n/c = 0, decreasing gradually to the right. This peak is believed to be releated with the wake of the airfoil due to the finite thickness of the trailing edge, that lies between the boundary layers. In this region after the TE, within the 0.4 mm thickness, may be some back flow, increasing turbulence levels.

The displacement thickness δ*, the momentum thickness θ and the shape factor H were calculated and plotted in Figures 58 to 63 together with Xfoil simulations. The equations used to calculate these parameters in incompressible flow are:

$$\delta^* = \int_{-\infty}^{\infty} \left(1 - \frac{u(y)}{Ue}\right) dy \tag{33}$$

$$\theta = \int_{-\infty}^{\infty} \frac{u(y)}{Ue} \left(1 - \frac{u(y)}{Ue}\right) dy \tag{34}$$

$$H = \delta^*/\theta \tag{35}$$

The data shows that, in general, increasing angle of attack, δ^*_{top} and θ_{top} increase, δ^*_{bot} and θ_{bot} decrease and the shape factors do not vary much, with exception of H_{top} for α_{eff} = 8.2°, that is higher than at lower angles. Increasing U_∞ results in decreasing δ^*_{top}, δ^*_{bot} , θ_{top} and θ_{bot}, while the shape factors remains unchanged. Comparison with Xfoil simulations shows a good agreement on the suction side, especially for the displacement thickness. On the pressure side they were underpredicted by Xfoil in about 37%. One possible reason for that might be that the wake related to the finite thickness (0.4 mm) of the TE is not excluded from the calculations., . Some particular cases of interest are that show a deviation from general trends:

- **A** - δ^*_{top} and θ_{top} for:
  - A1 - U_∞ = 40 m/s and α_{eff} = 3.0°
  - A2 - U_∞ = 60 m/s and α_{eff} = 8.2°
  - A3 - U_∞ = 70 m/s and α_{eff} = 8.2°

- **B -** δ^*_{bot} and θ_{bot} for:
  - B1 - U_∞ = 70 m/s and α_{eff} = 6.0°
  - B2 - U_∞ = 70 m/s and α_{eff} = 8.2°

- **C -** H_{top} and H_{bot} for:
  - C1 - U_∞ = 70 m/s and α_{eff} = 8.2°

A1 is yet unclear and still there are no conclusions drawn from this behavior. On the suction side at α_{eff} = 8.2° for U_∞ = 60 and 70 m/s the hypothesis is that the flow might be separated or close to it. On the pressure side it is not very likely that the flow is separated. Therefore, for U_∞ = 70 m/s at α_{eff} = 6° and 8.2° it might be that the flow from the suction side is interfering with the flow on the pressure side throught the TE region, causing the deviations. Still, a more comprehensive analysis needs to be done to confirm that.

8.2.2 Wake

Figures 64 to 67 show the wake velocity and turbulence intensity profiles for the Clean Configuration at the *x/c* positions 0.94, 1.5 and 1.75, α_{eff} 0°, 6° and 8.2° and for U_∞ 50 m/s and 70 m/s. Since the experiments are performed in an open-jet wind tunnel the airfoil loading causes the jet potential core to be deflected. From the velocity profiles, one can see indeed that the center of the wakes (minimum U/U_∞) are significantly shifted from the wind tunnel center (n/c

=0). Even at α_{eff} = *0°* the center of the wake is slightly out of center. This is due to non-zero lift of the cambered airfoils at 0° angle of attack.

Only for the Clean Configuration the wake was measured at three *x/c* positions. At x/c = 1.75 the velocity and the turbulence intensity profiles were more symmetric. This is a good indication that the traverse is closer to the far wake, where the drag can be calculated by momentum difference (Equation 20). It is obvious that the farther downstream the wake is measured, the closer to the far wake it gets, however, because of the jet deflection the quality of the data could be reduced and that was the point of first measuring in three different positions. As no quality loss was observed, the experiments for the serrated configurations followed only at x/c = 1.75.

The results show that the position of the wake is not significantly dependent on U_∞, but mostly on the AoA. Moreover, increasing the free stream velocity, U/U_∞ decreases. However, if the velocity deficits are normalized with U_e (edge velocity), then the velocity profiles become more independent of U_∞ (Figure 68).

Figures 69 to 71 compare the velocity profiles in the wake at x/c = 1.75 and in the middle span (z/c =0) of all measured configurations at 70 m/s for α_{eff} = 0°, 6° and 8.2°. The serrated configuration display a change in the wake position, shifting them a little bit to the left, closer to the wind tunnel axis. Also, apparently the serrations caused an impact on the local velocities, increasing them in comparison to U_∞, leading to higher U_e as well. Though, it is difficult to make a fair comparison among the performance of the different configurations through these pictures.

Figures 72 to 74 show the same results as before, however with the wakes normalized and with their centers aligned. The normalization was carried out by dividing all local velocities from the left side of the wake by the left U_e, while all local velocities from the right of the wake by the right U_e, and the center local velocity by the highest Ue between values. This way, U/U_∞ = 1 in both sides for all velocity profiles. For α_{eff} = 0°, adding serrations cause drag to increase, especially when mounted on the pressure side, with exception of US-TOP. For α_{eff} = 6° one can see that if one serration has more momentum deficit on one side it compensates decreasing in the other and it only becomes clear that they are increasing drag when the center region is observed, where the velocity deficit in the clean configuration is smaller. For α_{eff} = 8.2° the only clear case that is increasing the momentum deficit is the SCP configuration. Following, the drag coefficients are calculated from the wake momentum deficit.

Equation (20) calculates the drag per unit span in the far wake. This can be rewritten as

$$D = \rho\, U_\infty{}^2 bc \int \frac{u}{U_\infty}\left(1 - \frac{u}{U_\infty}\right)\frac{dy}{c} \tag{36}$$

The drag coefficient is defined as

$$C_d = \frac{D}{½\, \rho U_\infty{}^2 bc} \tag{37}$$

Substituting equation (36) in (37) yields:

$$C_d = 2\int \frac{u}{U_\infty}\left(1 - \frac{u}{U_\infty}\right)\frac{dy}{c} \tag{38}$$

Here, as it was done for the lift coefficients, two methods for calculating C_d are used. First method by considering the surface area of the serration, leading to

$$c_{serration} = 1.1c$$

$$c_{SCP} = 1.112c$$

In the second method, it is considered *c* as the reference chord for all configurations, i.e. neglecting the serrations surface area in the Drag Coefficient calculations. Figures 75 and 76 show the drag for the different configurations at U_∞ = *50 m/s* and U_∞ = *70 m/s*, respectively, according to first method, and Figure 77 and 78 according to the second method.

The Xfoil predictions showed in average 24% lower drag than the experiments for the clean configuration, which might be due to the fact that the measurements were done in an open-jet wind tunnel. Brooks and Marcolini (20), for instance, argued that this might be due to an induced drag caused by the streamlines deflection. However, the implementation of this correction did not show good results and further discussions about drag correction are not in the scope of this report. The serrations increased the drag coefficients (see Figures 75 to 78), with exception of α_{eff} = 6° and 8.2°, with U_∞ = 70 m/s, when Method 1 is considered.

Finally, to answer research question number 3, “Is the aerodynamic efficiency of the airfoil affected by the use of serrations?”, Cl/Cd is compared, which incorporates both lift and drag forces and is independent of any definition with respect to the surface area considered. Figures 79 and 80 show the aerodynamic efficiency at 50 and 70 m/s, respectively. In Figure 79 some configurations are missing, because Lift was not measured at 50 m/s for those types.

The results before showed that Xfoil had higher Lift and smaller Drag, thus obviously it has also a higher L/D than the measured values. Comparing the Clean Configuration and the Serrations, there were some doubts, depending on the method. Now it becomes clear that the aerodynamic performance L/D is reduced, with exception at 70 m/s and α_{eff} = 8.2°, which might be due to a stronger separation in the case of the clean type, reducing L/D. It appears that separation influenced less the performance of the serrated configurations.

The wake width was also compared with predictions that are described in chapter 6 for α_{eff} = 0°, 6° and 8.2° at U_∞ = 50 m/s (Figure 81) and U_∞ = 70 m/s (Figure 83). To calculate the wake widths it was considered the wake limits to be where the local velocity is equal to 99% of the edge velocity (U = 0.99 $U_{e)}$. The prediction for α_{eff} = 0° matched well, whereas for higher angles of attack the wake width increased less than predicted. For all measurements, the wake clearly increases with streamwise position, with exception of U_∞ = 70 m/s and α_{eff} = 6°, where it remains approximately constant.

Lastly the spanwise variations in the wake are evaluated for the serrated TE configuration. When measured the velocities at the center of the wake, it was not found any significant variation and it was not found interesting to further comment about it in the results part. The wakes measured at z/c = 0.15 below the middle span were also similar to the wakes measured at middle span as one can see in Figures 83 and 84 for the US-TOP and CS configurations, respectively.

8.3 Acoustics

In Appendix B, Figures 132 to 179 show the acoustic source maps for each of the configurations (Clean, US-TOP, US-BOT, CS, SCP and FS) at the free stream velocities 40, 50, 60 and 70 m/s and for the effective angles of attack 0°, 3.4°, 6° and 8.2°, divided into low (1250 Hz, 1600 Hz and 200 Hz), middle (2500 Hz, 3150 Hz and 4000 Hz) and high frequencies (5000 Hz, 6300 Hz and 8000 Hz). These figures are disposed in the end of this report, in order to show the quality of the data obtained and for completeness. However, since the interest here is the noise emission of the airfoil's TE, spectra are plotted that were extracted from the source plots at the mid span of the airfoil (Figures 85 to 128). These data were used to assess the effectiveness of the serrations.

8.3.1 Flexible Serrations

The flexible serration showed the most noise reductions in almost all cases. Moreover, no increase in noise levels was observed for this configuration. FS presented a maximum reduction of 13 dB for U_∞ = 50 m/s, α_{eff} = 3.4° and f = 8000 Hz. Comparing the averages over the whole spectra the maximum was 8.5 dB also for U_∞ = 50 m/s and α_{eff} = 3.4°. The total average reduction was 4.6 dB.

Figures 85 to 92 show a comparison between flexible serrations and clean configuration. In Figures 85 to 88 the spectra are given for all velocities separated per AoA. First of all, independently of the configuration, one can see that the noise levels are higher for lower frequencies, higher velocities and higher angles. Second, the FS decreased noise almost everywhere, with a few exceptions where the SPL are the same. The biggest reductions occurred for lower velocities. With highest reductions at 40 m/s for α_{eff} = 0° and 6° and at 50 m/s for α_{eff} = 3.4° and 8.2°.

In Figures 89 to 92 noise differences with respect to the reference Clean Configuration are plotted for all α_{eff} with one graph per free stream velocity. In these figures one can clearly see how reduction in noise levels is dependent on the frequency and how the optimal frequency for noise reduction via sawtooth serrations is dependent on the free stream velocity. The noise reduction is composed by peaks and valleys in noise reduction, intercalated between certain frequency limits. For U_∞ = 40 m/s (Figure 89), the peaks in noise reduction occur at f = 3150 Hz and f = 8000 Hz, with the exception of α_{eff} = 8.2° that has his second peak in f = 6300 Hz. For U_∞ = 50 m/s (Figure 90), the peaks in noise reduction occur at f = 2000 Hz and f = 4000 Hz with a high slope at f = 8000 Hz, meaning a possible peak at an even higher frequency. Though, these peaks of reduction look also to be dependent on AoA, since the curves of different angles are not completely “in phase” with each other. For U_∞ = 60 m/s and 70 m/s (Figures 91 and 92) the highest noise reduction is at f = 6300 Hz for all AoA with exception of α_{eff} = 0° and U_∞ = 60 m/s which has a higher reduction at f = 8000 Hz.

In general α_{eff} = 8.2° shows the highest noise reduction for frequencies up to 4000 Hz, with the exception of α_{eff} = 3.4° at U_∞ = 50 m/s which presents high noise reduction in all frequencies.

8.3.2 Uncutted Serration Mounted on the Suction Side (US-TOP)

US-TOP presented the best results after FS, with a maximum reduction of 9.5 dB for U_∞ = 70 m/s, α_{eff} = 8.2° and f = 3150 Hz. Comparing the averages over the whole spectra the maximum was 5.4 dB also for U_∞ = 70 m/s and α_{eff} = 8.2°. The total average reduction was 2.6 dB.

Moreover, the condition for U_∞ = 70 m/s and α_{eff} = 8.2° was the only case for a specific angle and velocity, in which the average reduction was higher (0.8 dB more) for US-TOP than for the FS. This is understandable since the angle φ between the serration and the chordline for the US-TOP of 2.1° was designed to be the most efficient at this condition. This result confirms that the simulation done in Xfoil was effective in determining the bent angle of the serration and also that the flexibility provided by the FS helped the serration to align with the flow and provide better results in all the other angles different from 8.2°. The only situation that US-TOP increased the average noise was for U_∞ = 70 m/s and α_{eff} = 0°.

Figures 93 to 100 show a comparison between US-TOP and the clean configuration. Figures 93 to 96 display the SPL (Sound Power Level) curves plotted vs. frequency (Hz), for all velocities in one graph per AoA. Notice in Figure 93 that, unfortunately, there was a problem while gathering data for U_∞ = 40 m/s and α_{eff} = 0° and this data is missing. For other U_∞, the results show that at α_{eff} = 0°, the US-TOP configuration is not effective. Especially at 70 m/s, where for almost all frequencies noise generation of due to the serrations are found. At α_{eff} = 3.4°, this scenario already changes and US-TOP was effective in reducing noise also for α_{eff} = 6° and 8.2°. For U_∞ = 70 m/s, which are closer to the real flow situation, the noise increased up to 2 dB at α_{eff} = 0°, reduced up to 3 dB at α_{eff} = 3.4°, reduced up to 4.5 dB at α_{eff} = 6°, and reduced up to 9.5 dB at α_{eff} = 8.2°.

Figures 97 to 100 show the noise difference curves for US-TOP in comparison to the clean configuration. In Figure 97 (U_∞ = 40 m/s), one can notice the highest noise reductions at the band f = 3150 Hz at all α_{eff}, as it was observed for the FS configuration, and at f = 6300 Hz for α_{eff} = 6° and 8.2. As the velocity increase though, the curves for the smaller α_{eff} start to lose their peak and valley formats becoming more of a straight line with some parts above the zero point, showing some noise increase. For α_{eff} = 8.2° it remains similar to what was observed for the FS configuration and also with the noise reduction maxima occurring at the same frequencies as before f = 3150 Hz and f = 6300 HZ. With all these differences between US-TOP and FS occurring specially for smaller α_{eff}, the alignment of the sawtooth serrations with the flow is concluded to be a crucial characteristic to be taken into account while aiming for noise reduction.

Finally, Figures 101 to 104 show a direct comparison between US-TOP and Flexible Serrations, where it becomes clear that the FS configuration achieves more noise reductions and in all conditions, while US-TOP is effective only close to angle that it was designed (8.2° in this case).

8.3.3 Uncutted Serration Mounted on the Pressure Side (US-BOT)

The US-BOT provided an overall noise reduction of around 1 dB and was less effective than the US-TOP. It increased overall noise for all free stream velocities at α_{eff} = 0° and also for U_∞ = 60 m/s and U_∞ = 70 m/s at α_{eff} = 3.4°. It was most effective at α_{eff} = 8.2°, where the serration bent angle was designed to align with the flow direction.

Figures 105 to 108 show a comparison between US-BOT and the clean configuration. The serration generated spurious noise for α_{eff} = 0°, increasing the average noise for all free stream velocities. For α_{eff} = 3.4°, it was only effective at U_∞ = 50 m/s, which was also the best condition for FS. Figures 107 and 108 show that US-BOT was effective for α_{eff} = 6° and 8.2°.

In Figures 109 to 112 the noise difference curves for the US-BOT are shown in comparison to the clean configuration. In this case the US-BOT configuration causes an increase of noise levels for α_{eff} = 0° at all velocities and at α_{eff} = 3.4° for U_∞ = 60 and 70 m/s. For U_∞ = 40 m/s one can see that for α_{eff} = 6° and 8.2° the peak in noise reduction that was found for US-TOP and FS at f = 3150 Hz is shifted to 2500 Hz. For U_∞ = 60 m/s the reduction in low frequency is less pronounced than for US-TOP and that the peak in reduction at f = 6300 Hz is gone, giving a more smooth shape to the curves.

Figures 113 to 117 show a direct comparison between US-BOT and US-TOP. The unique condition at which US-BOT was more effective was at U_∞ = 50 m/s and α_{eff} = 3.4°. All the other results show that mounting of the serration on the suction side is superior. The hypothesis is that the step created by the thickness of the serration (in this case 0.3 mm) has less impact on the suction side, where the boundary layer is an order of magnitude thicker than the on the pressure side. Comparison of both configurations at U_∞ = 70 m/s, which are closest to flow conditions occurring on an actual wind turbine blade, show that for α_{eff} = 6° the difference becomes more pronounced ($\sim 2\ dB$) for frequencies higher than 2500 Hz. For α_{eff} = 8.2°, on the other hand, the differences concentrate more on the peaks of noise reduction observed before (f = 3150 Hz and f = 6300 Hz), where US-TOP reduces 5 dB more noise than US-BOT.

8.3.4 Cutted Serration (CS) and Serration with Cutted Plate (SCP)

The Cutted Serration (CS) and the Serration wit Cutted Plate (SCP) did not work as expected. It is not clear if the cuts gave the flexibility predicted, since there was no easy way of measuring the angle of the serration, while the wind tunnel was running. However, the cuts increased noise considerably and the serrations became even worse than compared to the clean configuration.

Figures 117 to 120 compare CS versus Clean and Figures 121 to 124 compare SCP versus Clean. The curves apparently have a similar format, in the way that their peaks in noise normally occur in the same frequencies. Both serration configurations increased significantly the noise, especially at high frequencies. The maximum noise increase occurred in most cases at f = 8000 Hz and highest for 40 m/s. In this latter condition CS increased up to 10 dB at α_{eff} = 0°, 11 dB at α_{eff} = 3.4°, 11.5 dB at α_{eff} = 6° and 9.5 dB at α_{eff} = 8.2°. The SCP configuration on the same conditions increased the noise levels up to 12 dB at α_{eff} = 0°, 12 dB at α_{eff} = 3.4°, 11.5 dB at α_{eff} = 6° and 10 dB at α_{eff} = 8.2°. A peak of 12 dB was also noted for SCP at U_∞ = 40 m/s, α_{eff} = 0° and f = 2500Hz. Overall CS and SCP configurations showed similar trends. However, the SCP configuration did in general create a higher level of spurious noise. This is highlighted in Figures 125 to 128 which show a comparison between SC and SCP.

A general conclusion is that the concept of cutted serrations was not successful. The gaps generate spurious noise, overshadowing any benefit that can be obtained from the serration in reduction of TE noise. From this it is concluded that the serration surface should be smooth to avoid spurious noise (as is the case for the FS configuration). The hinge mechanism concept study could be more successful in case the gaps are filled with a flexible material to avoid spurious noise.

9 Conclusions and Recommendations

9.1 Conclusions

This experiment campaign provided data, from which it was possible to reinforce concepts of previous experiments on serrations as well as to draw new conclusions. These are summarized below:

- A flexible serration with smooth surface proved to be efficient in reducing sound levels in all frequencies, angles and velocities;
- The misalignment with the flow is likely one of the causes for the generation of spurious noise at high frequencies;
- Suction side mounted serrations gave higher noise reductions than pressure side mounted serrations. The hypothesis is that the interaction of the thin boundary-layer on the pressure side with the step caused by the thickness of the serration generates additional spurious noise;
- Cuts on the serration surface increased noise overshadowing any potential benefit from serration and must be avoided;

- Serrations with ratio $\lambda/h = 0.5$ reduced noise as long as they were not too misaligned with the flow and had a smooth surface;
- Serrated configurations reduced the aerodynamic efficiency of the airfoil compared to the clean configurations and presented similar results among themselves;
- Spanwise variations in the wake along the teeth of the serrations are small.

9.2 Recommendations

Recommendations for further analysis are listed below:

- Perform experiments with PIV (Particle Image Velocimetry) to characterise the flow topology, and to check the wake measurements used to calculate drag;
- Carry out aerodynamic measurements for the FS, which was not yet performed;
- Perform oil-flow visualization to determine the transition and separation regions on the airfoil surface;
- Use improved acoustic processing algorithms for the noise analysis to determine absolute noise levels per unit span;
- Improve the calculations of boundary-layer thickness, excluding the contribution from the wake aft the blunt TE;
- Attempt to separate contributions from different noise mechanisms such as TBL-TE, TBE-TE and boundary layer separation noise through application of scaling laws;
- Further improve the Flexible Serration concept, e.g. by testing other hinge materials and lengths ;
- Apply the flexible serration concept on full-scale wind turbines.

Figures

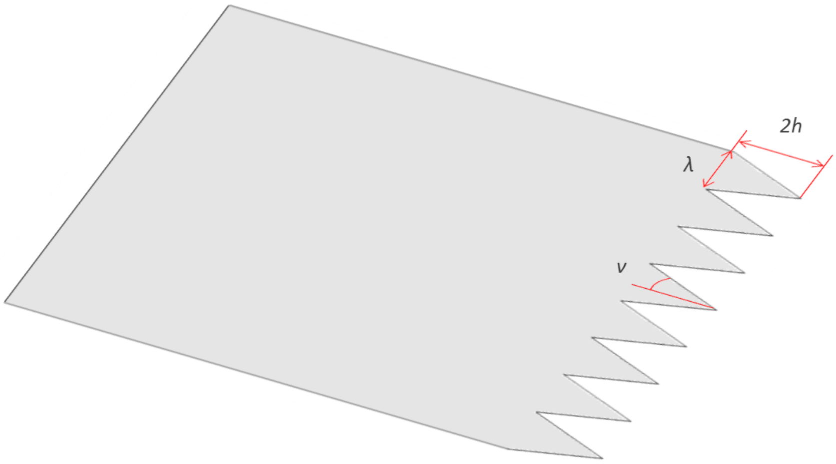

Figure 1– Sawtooth Serration Geometry

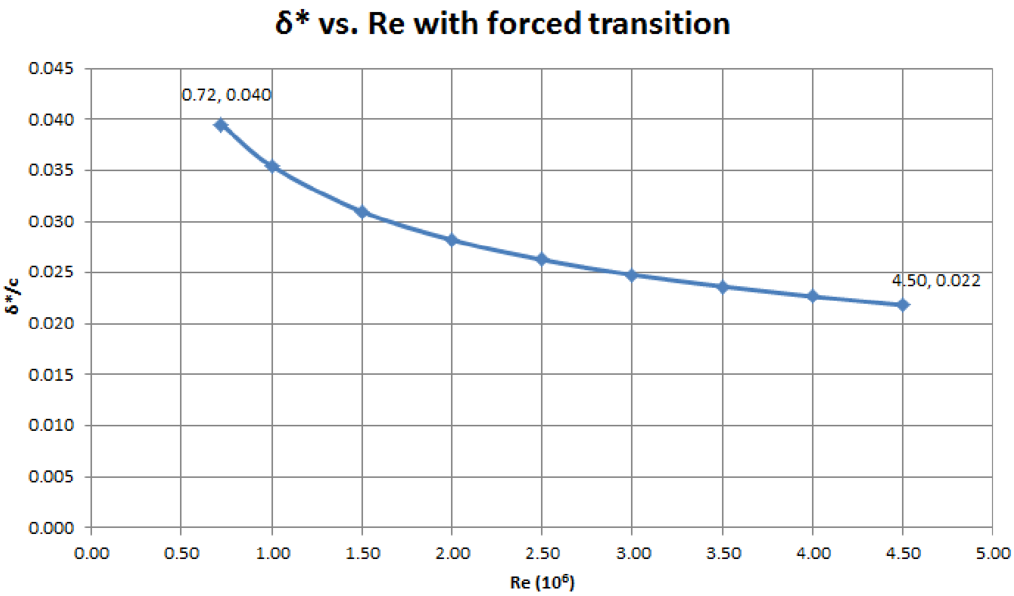

Figure 2 - Displacement Thickness vs. Re (Forced Transition), AoA = 8.2°

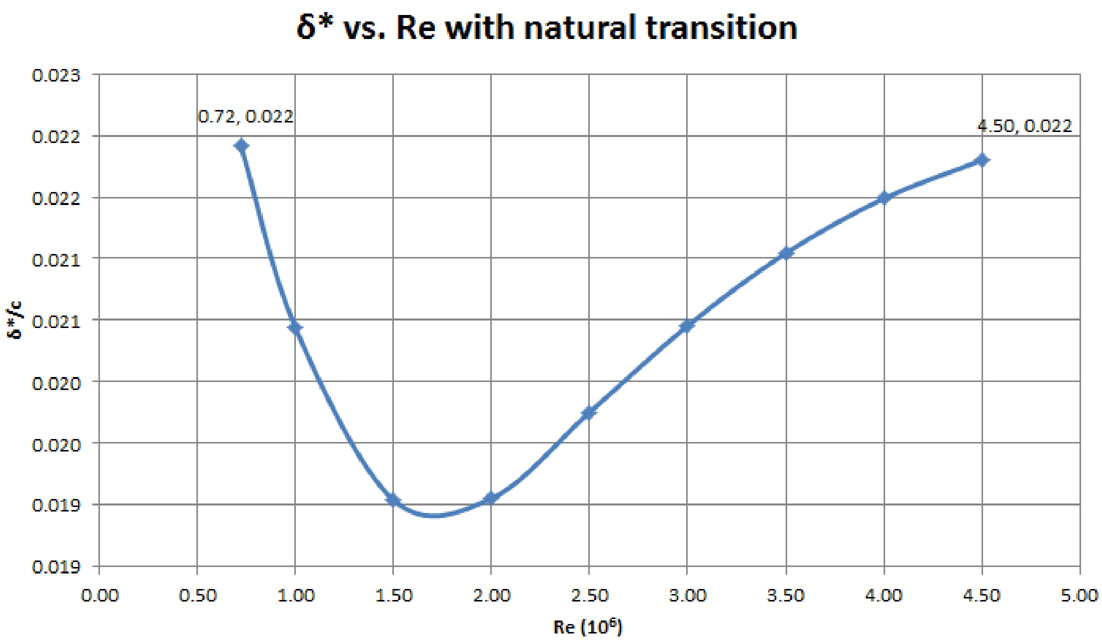

Figure 3 - Displacement Thickness vs. Re (Natural Transition), AoA = 8.2°

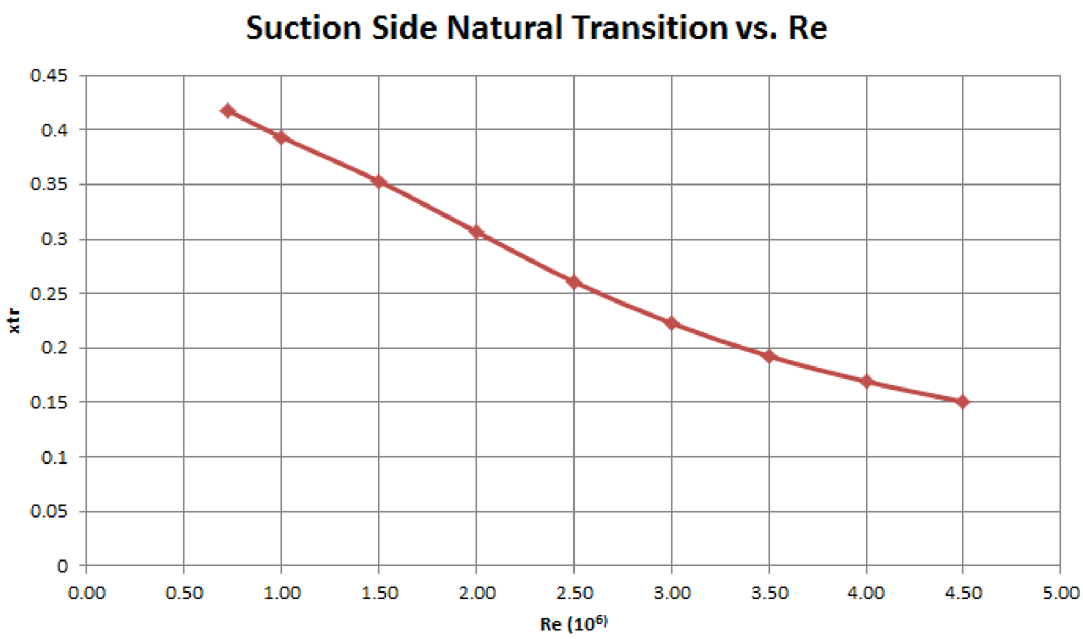

Figure 4 - Suction Side Natural Transition vs. Re

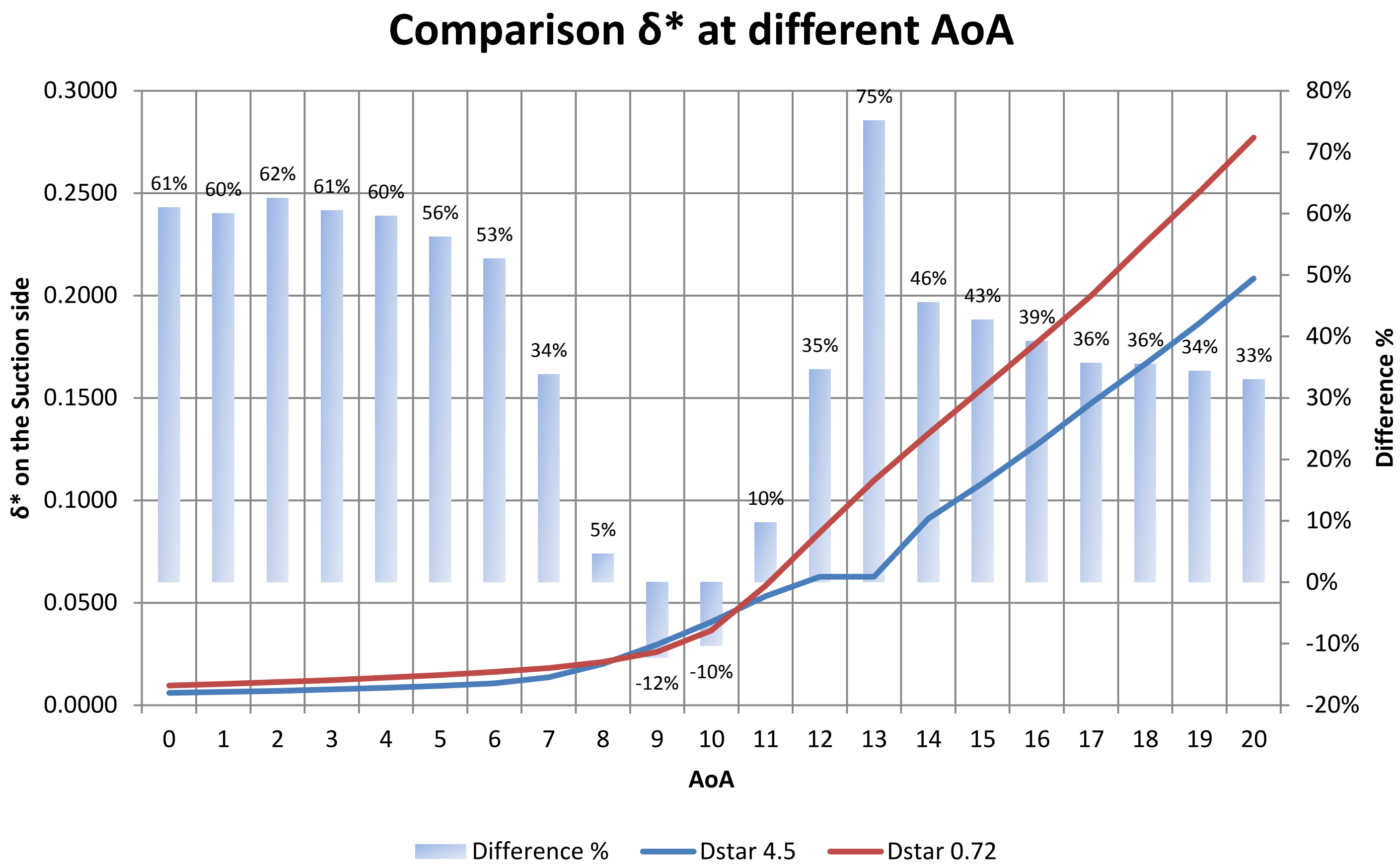

Figure 5 – Comparison δ at different AoA*

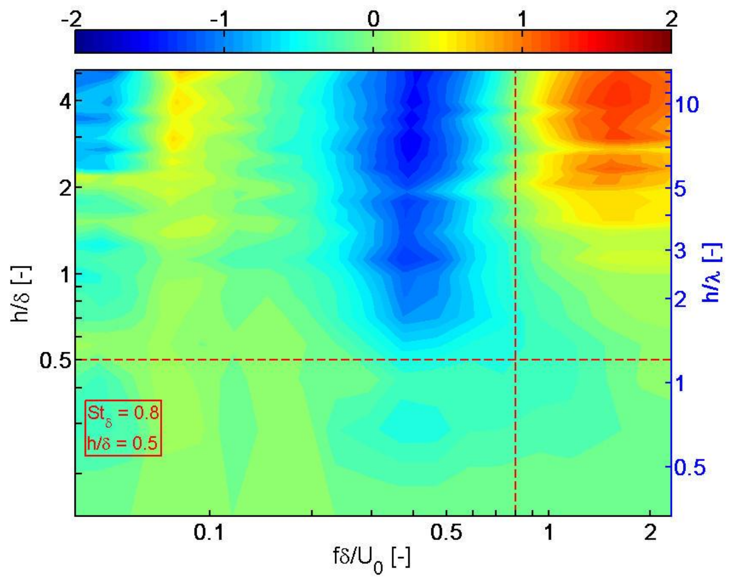

Figure 6 – Non-dimensional sawtooth amplitudes h/δ and h/λ vs. Strouhal Number St_δ. U_0 = 60 m/s, AoA = 5°. (8)

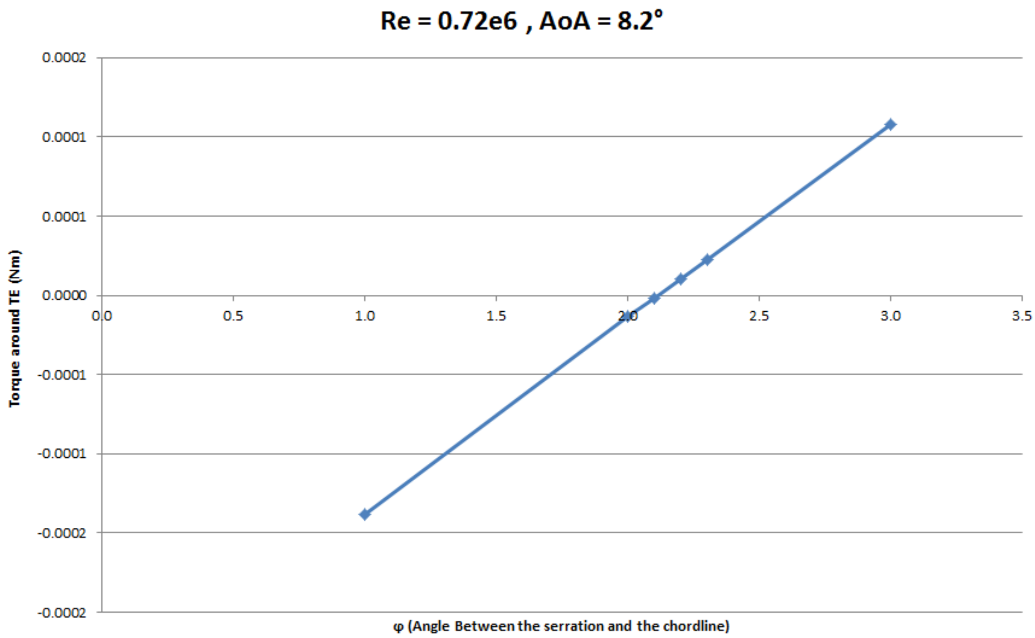

Figure 7 - Torque around the TE experienced by the serration, with different angles between the serration and the chordline

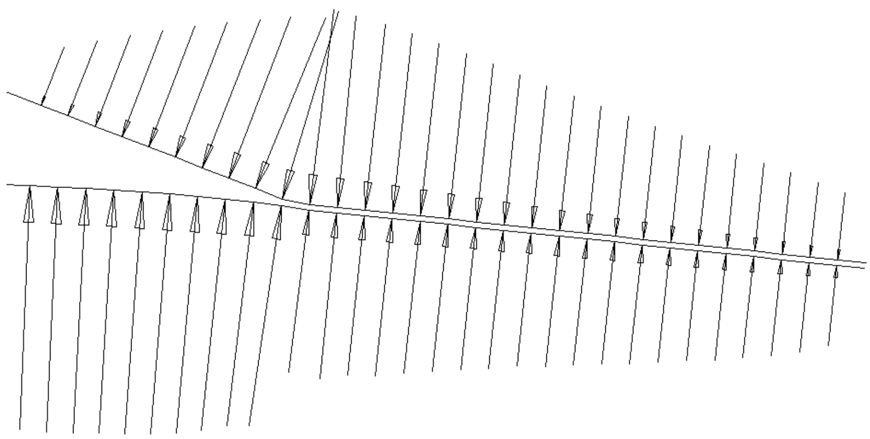

Figure 8 – Pressure Distribution in the 2D Serration, obtained in the Xfoil for Re = 0.72×10^{6}, AoA = 8.2° and φ = 2.2°. The position of the chord line is not shown in the figure, but the serrations located 2.2° counter clockwise from the chordline.

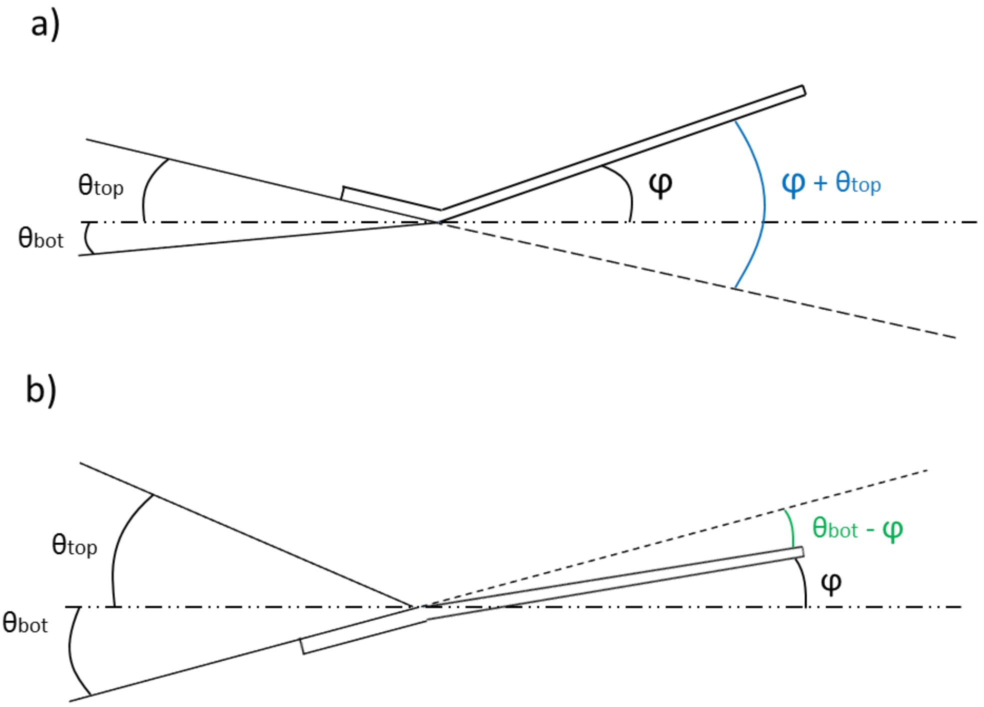

Figure 9 – Fixation of the Serrations on a) suction side of the airfoil or b) pressure side of the airfoil. This figure is not on scale.

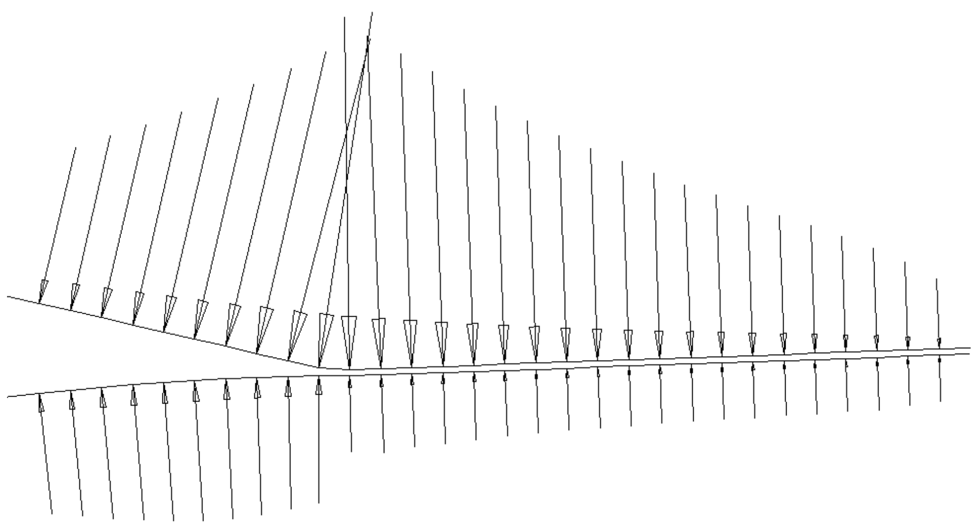

Figure 10 – Pressure Distribution in the 2D Serration, obtained in the Xfoil for Re = 0.72×10^{6}, AoA = 0° and φ = 2.2°. The position of the chord line is not shown in the figure, but the serrations located 2.2° counter clockwise from the chordline.

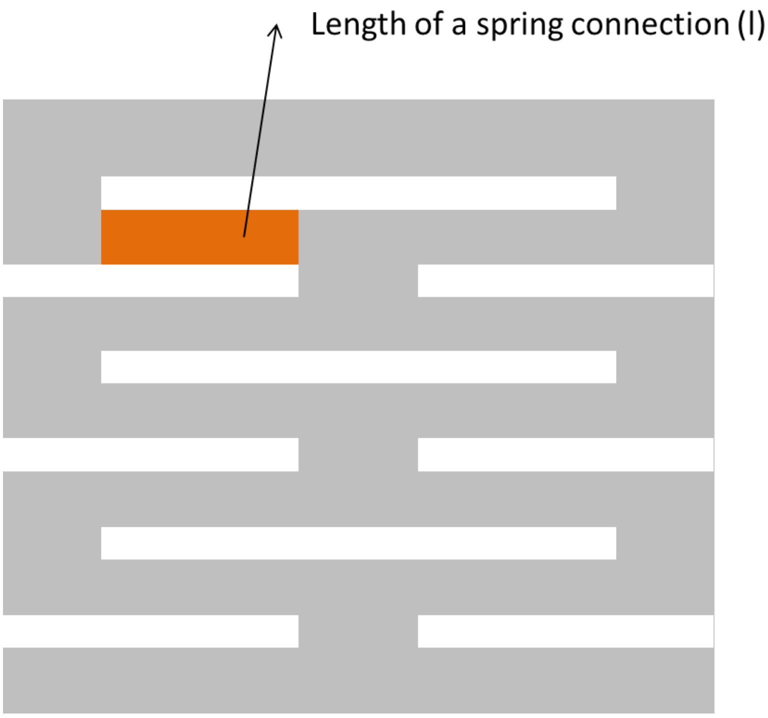

Figure 11 – Laser-Cut Hinge Mechanism

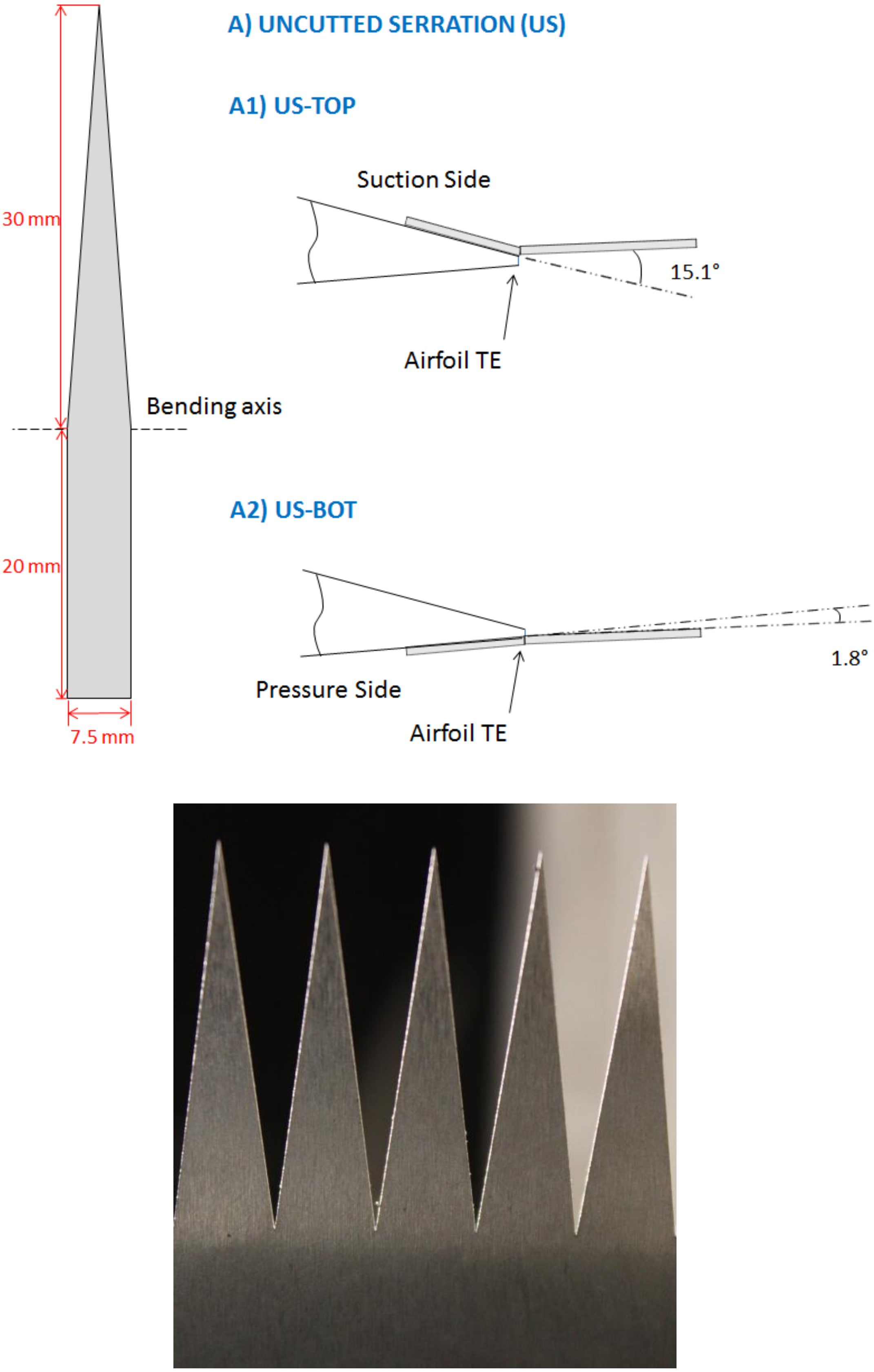

Figure 12 – Uncutted Serration (US)

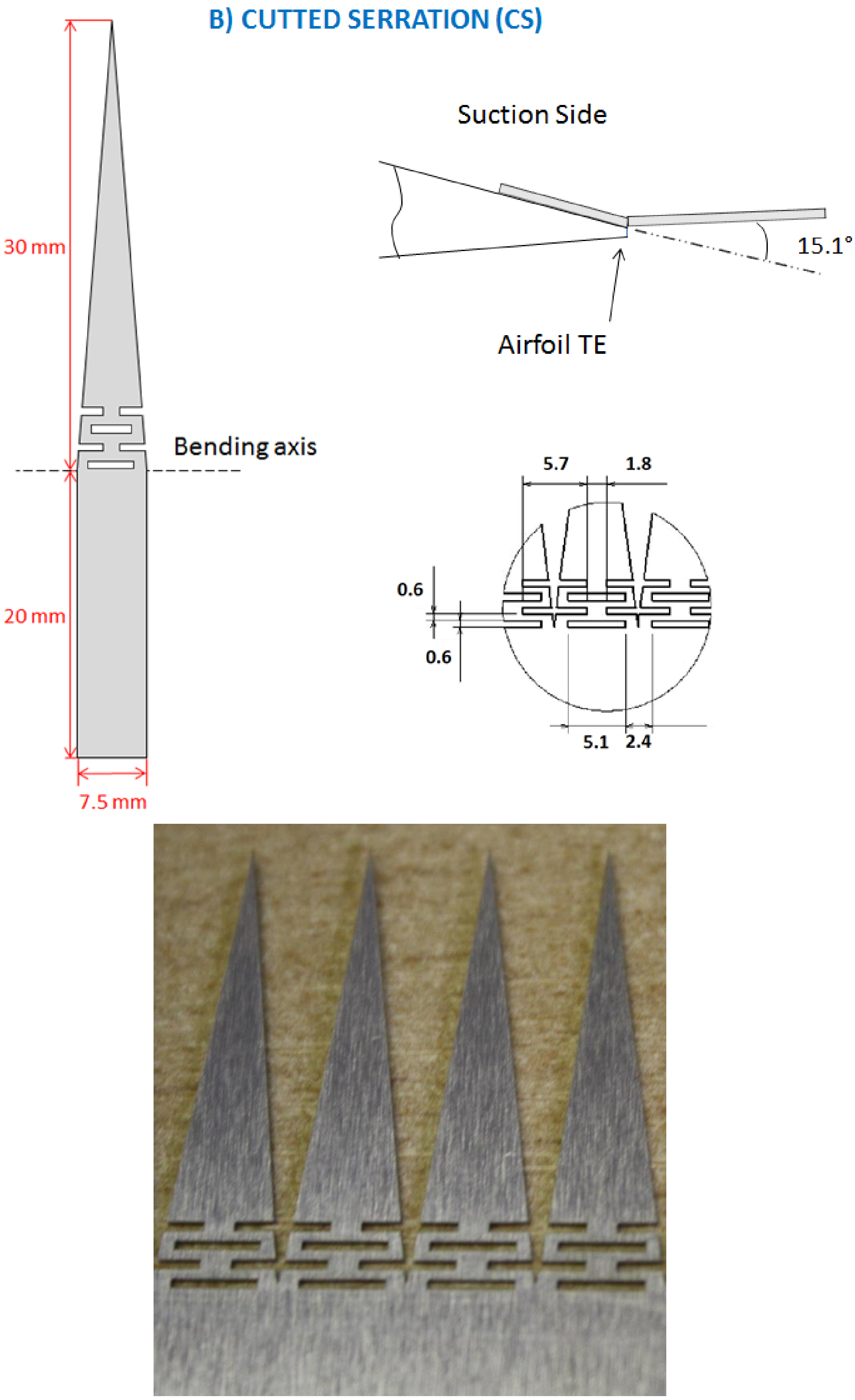

Figure 13 – Cutted Serration (CS)

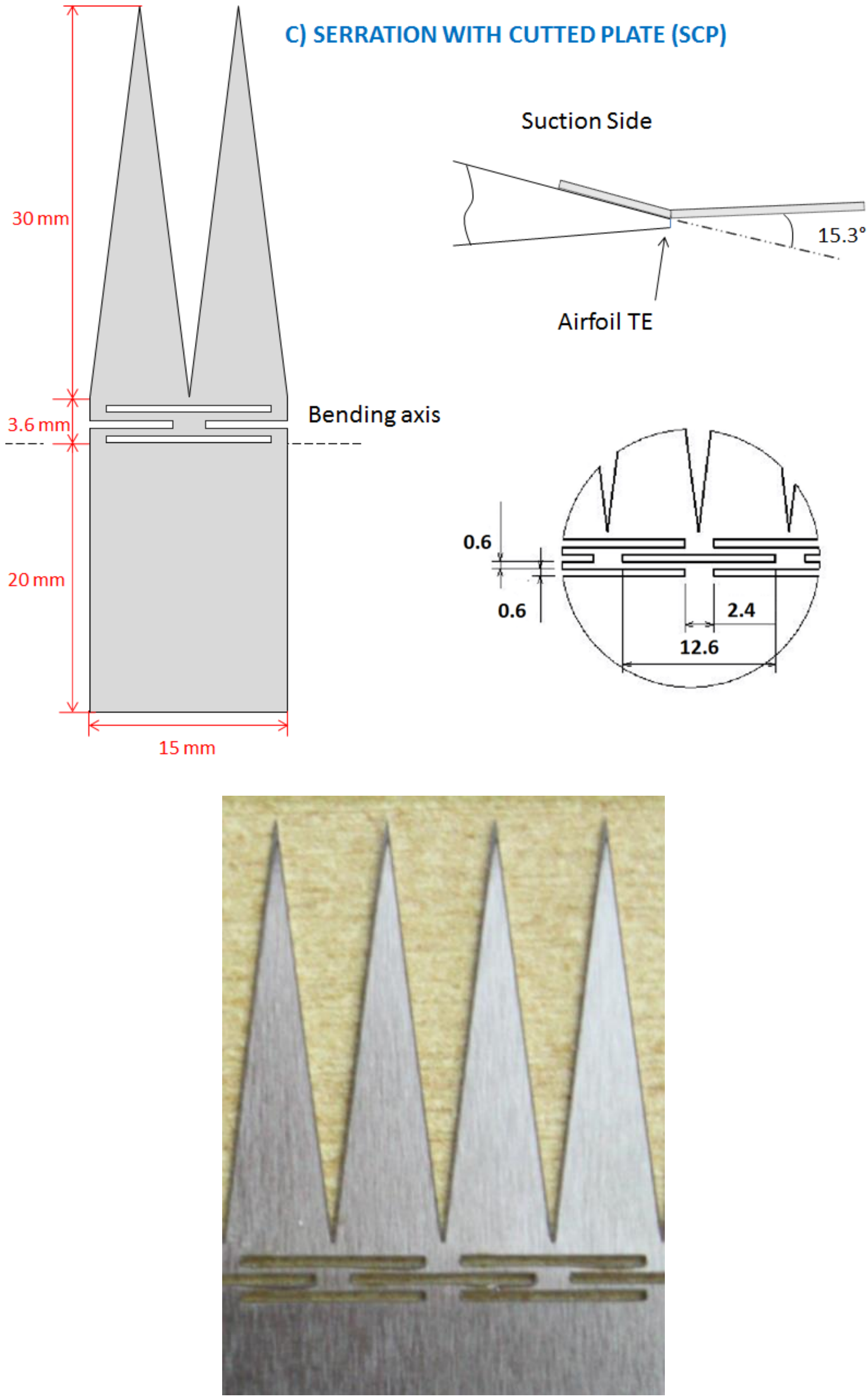

Figure 14 – Serration with Cutted Plate (SCP)

D) FLEXIBLE SERRATION (FS)

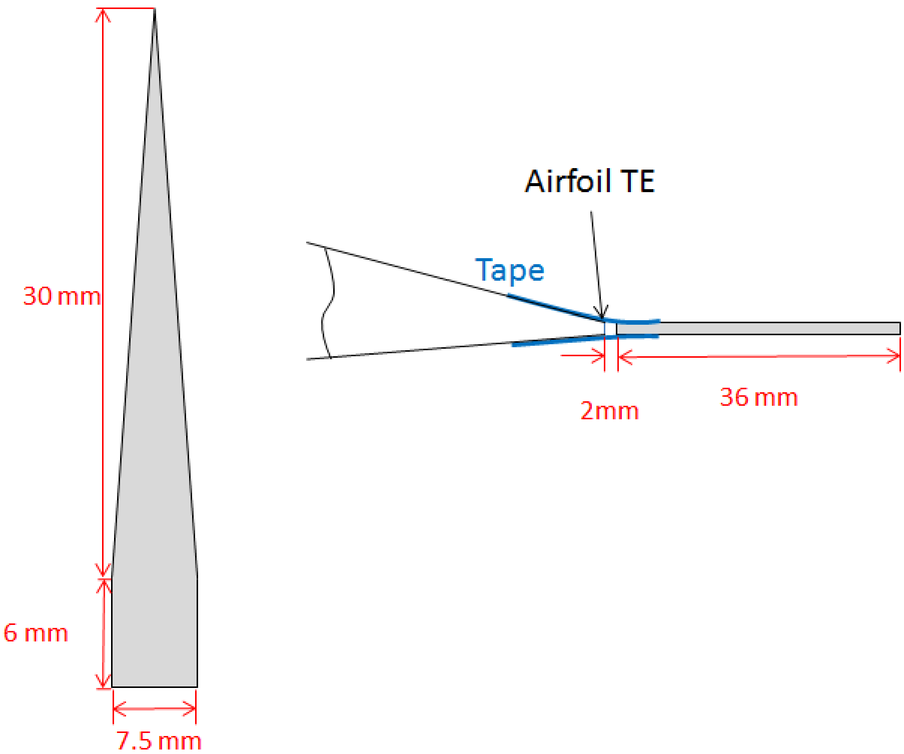

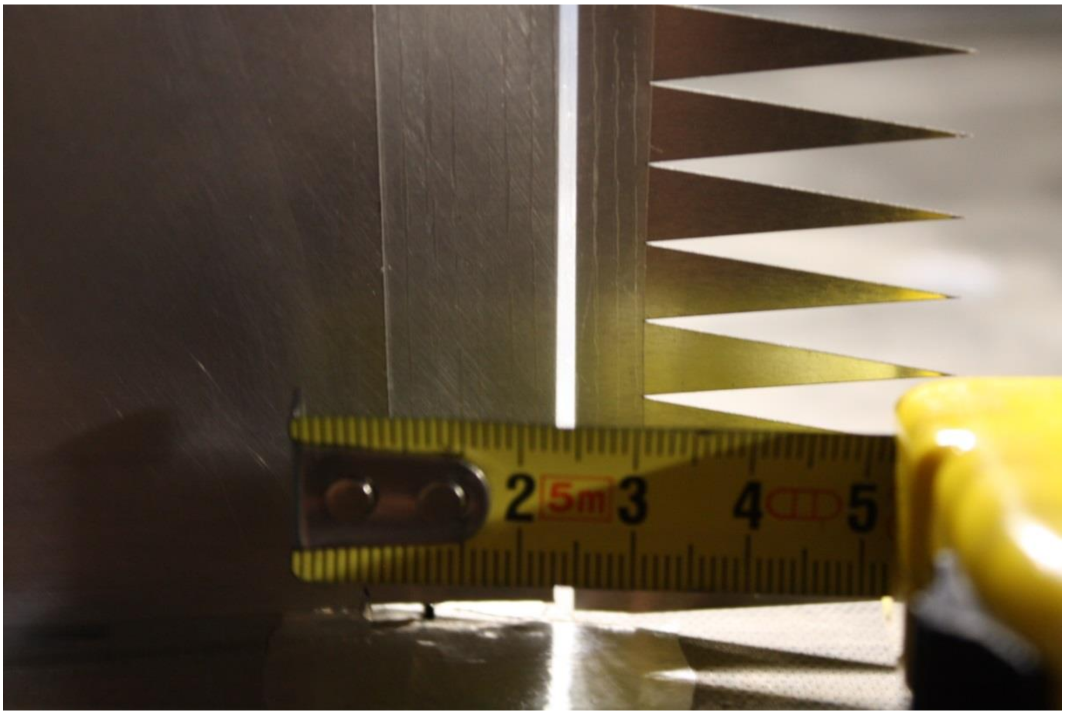

Figure 15 – Flexible Serration (FS)

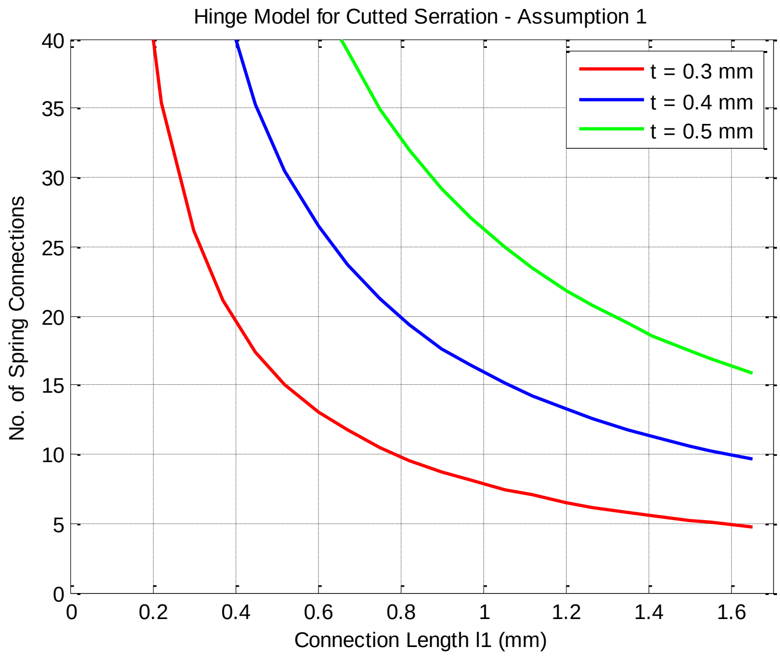

Figure 16 – Number of springs vs. connected length for the Cutted Serration (ϴ=0.8°)

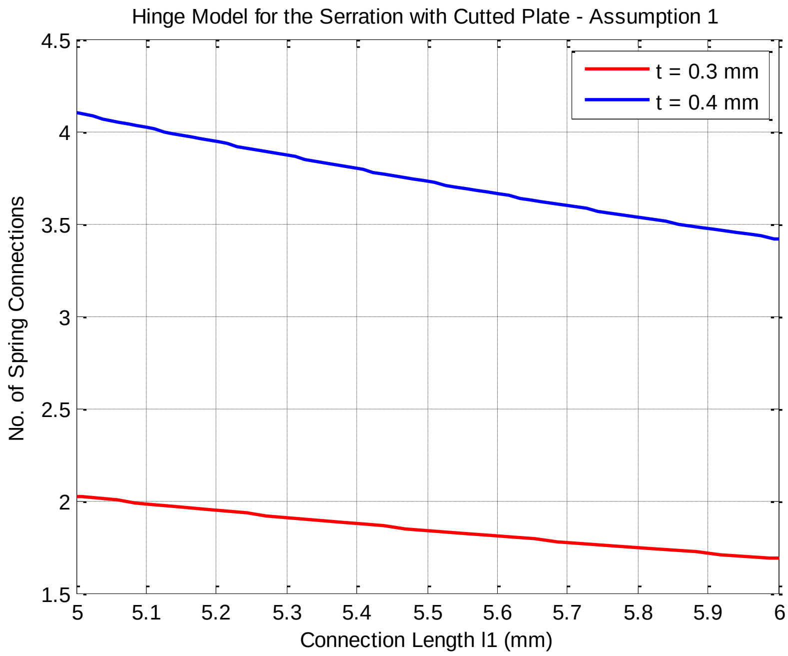

Figure 17 - Number of springs vs. connected length for the Serration with Cutted Plate (ϴ=3.2°)

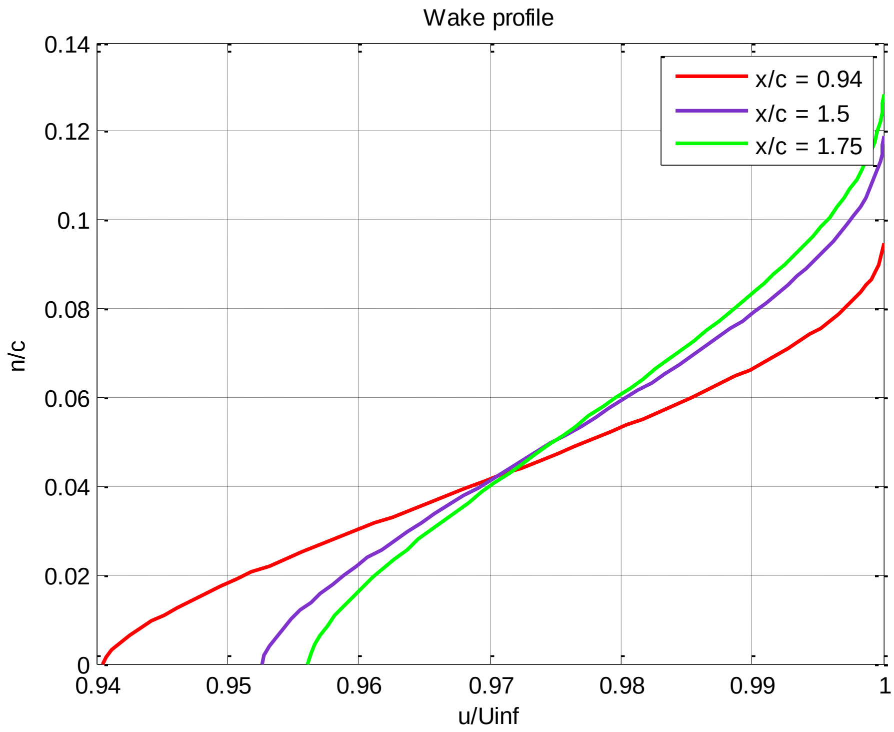

Figure 18 – Simulation for the half wake width and velocity deficit at U_∞ = 70 m/s and AoA = 8.2° for three different downstream x/c positions.

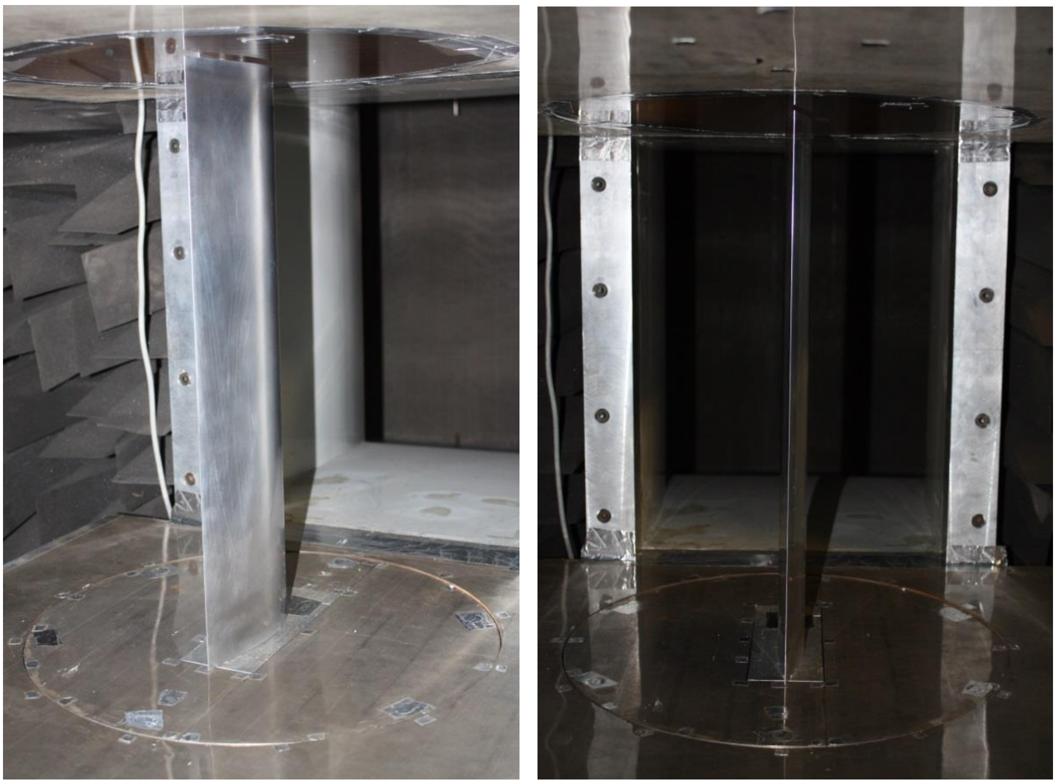

Figure 19 – DU-96-W-180 Airfoil, spanned between the end plates on the rotating balance, which sets different AoA automatically. The 0.38 × 0.51 m nozzle is shown behind the airfoil.

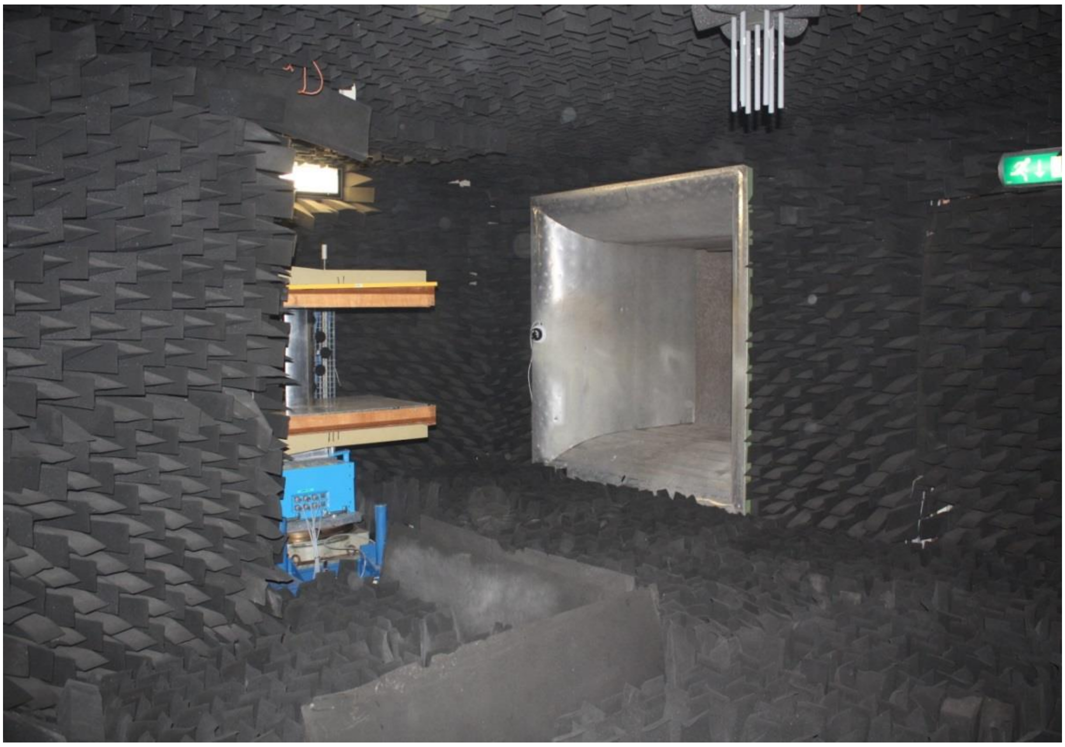

Figure 20 – Anechoic Room with 0.5 m foam wedges

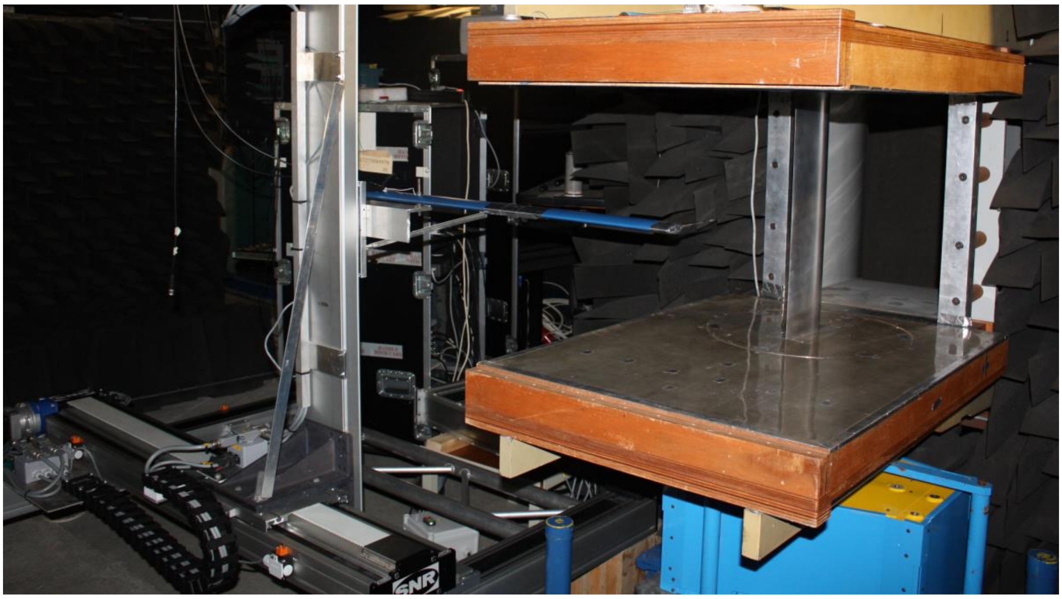

Figure 21 – Traversing System AVHA-3ATS with a support strut

Figure 22 – Support Strut used to hold the Hot-Wire Probe

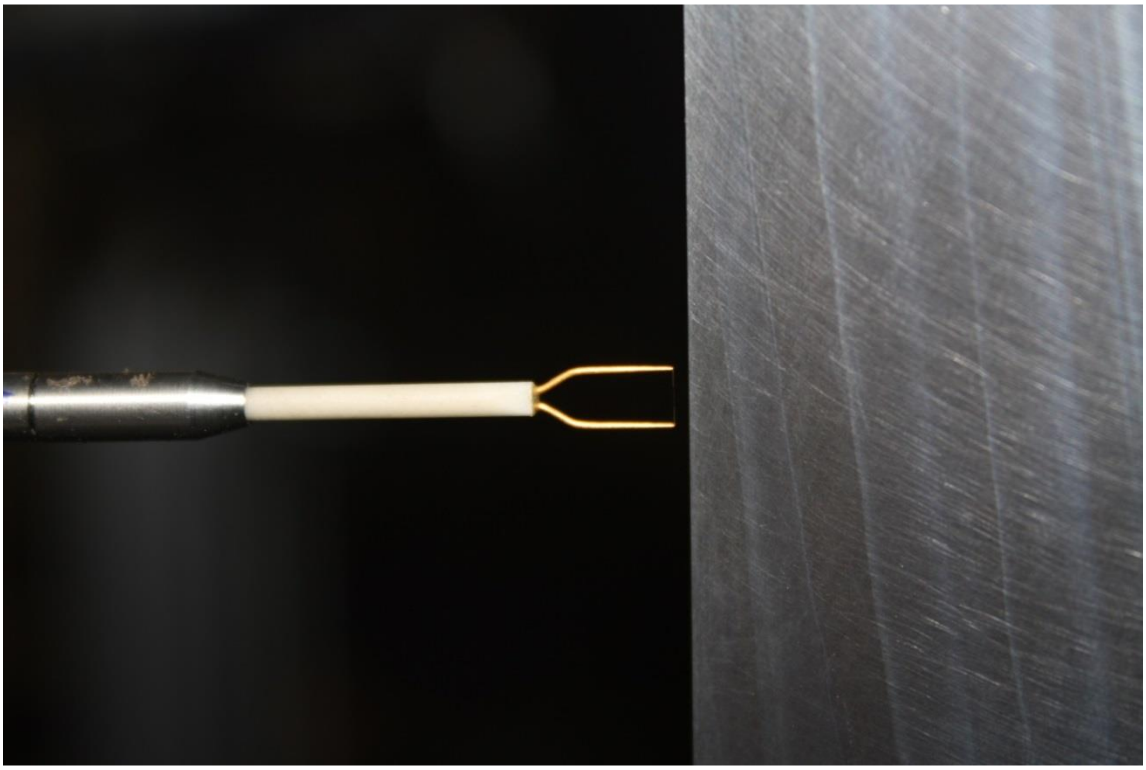

Figure 23 – Single Wire Probe close to the Trailing Edge

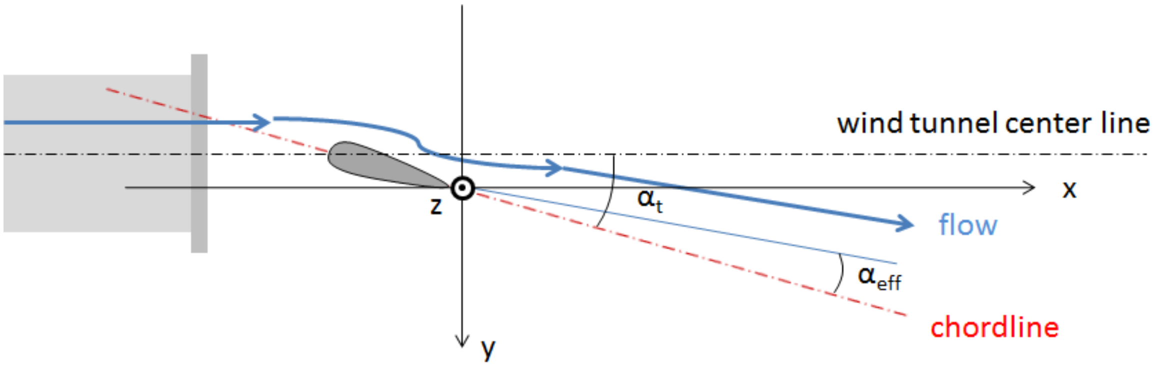

Figure 24 –Coordinates used for the Hot-wire transverse system (upper view on mid-span plane). The origin was located at 1.5 mm downstream the TE of the airfoil. A new origin was taken for different AoA. The z axis is in the direction coming out of the paper. The y- axis is positive in the pressure side direction.

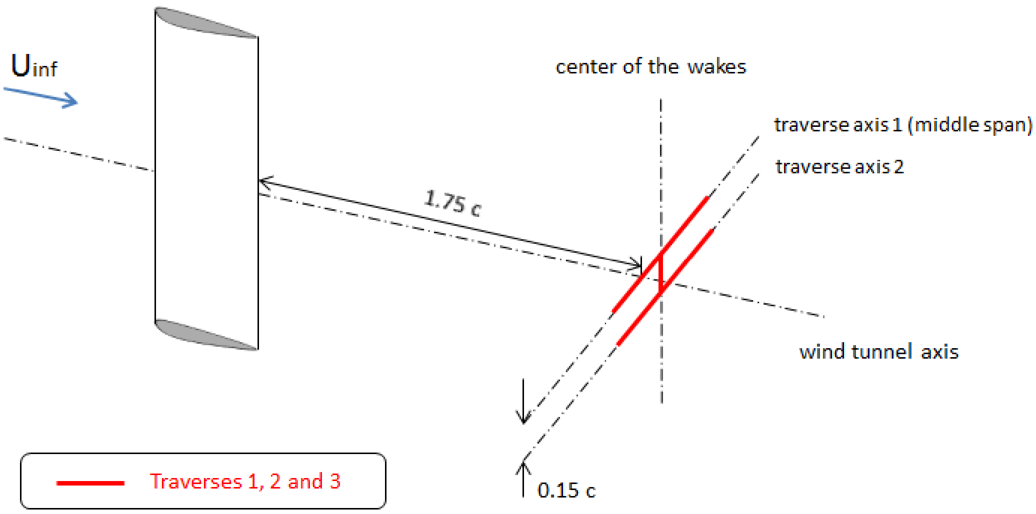

Figure 25 - Wake Measurements for the serrated configurations

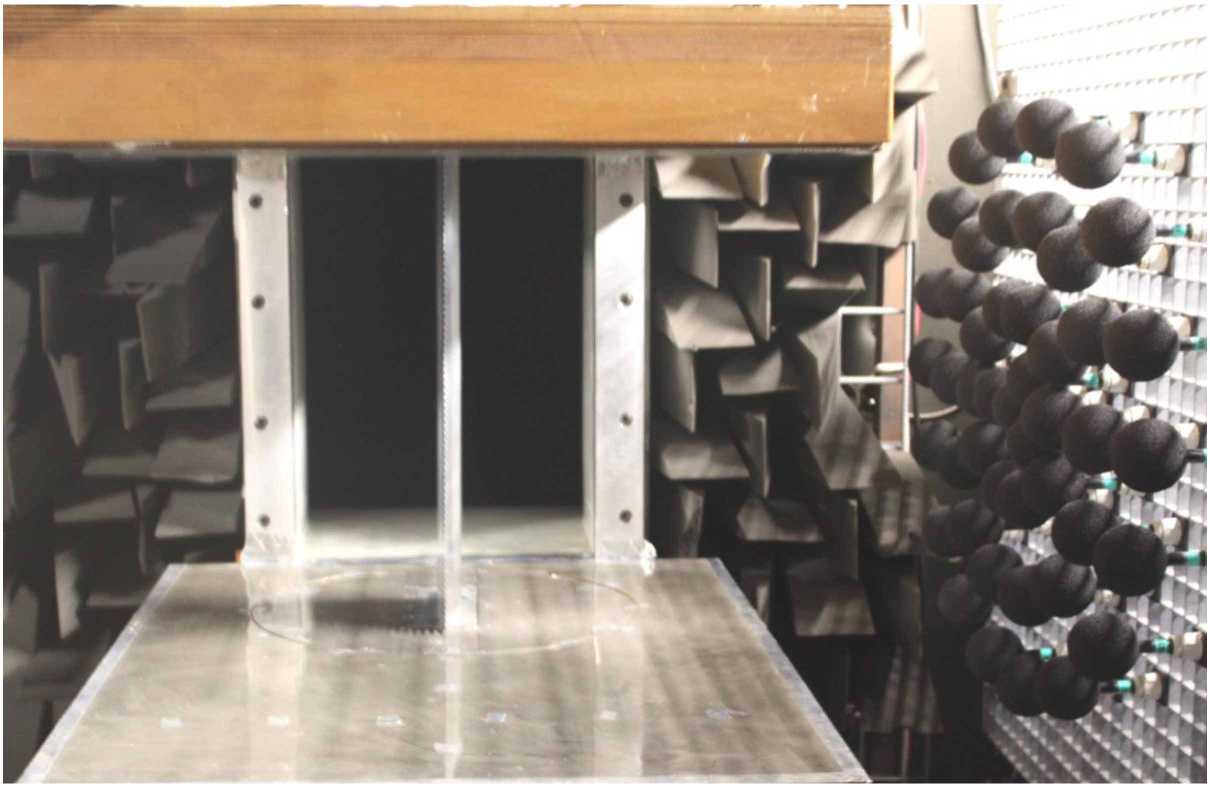

Figure 26 – Microphone Array on the Suction Side of the Airfoil (0.6 m from the wind tunnel Axis)

Figure 27 - Microphone Array on the Suction Side of the Airfoil (0.6 × 0.8 m²)

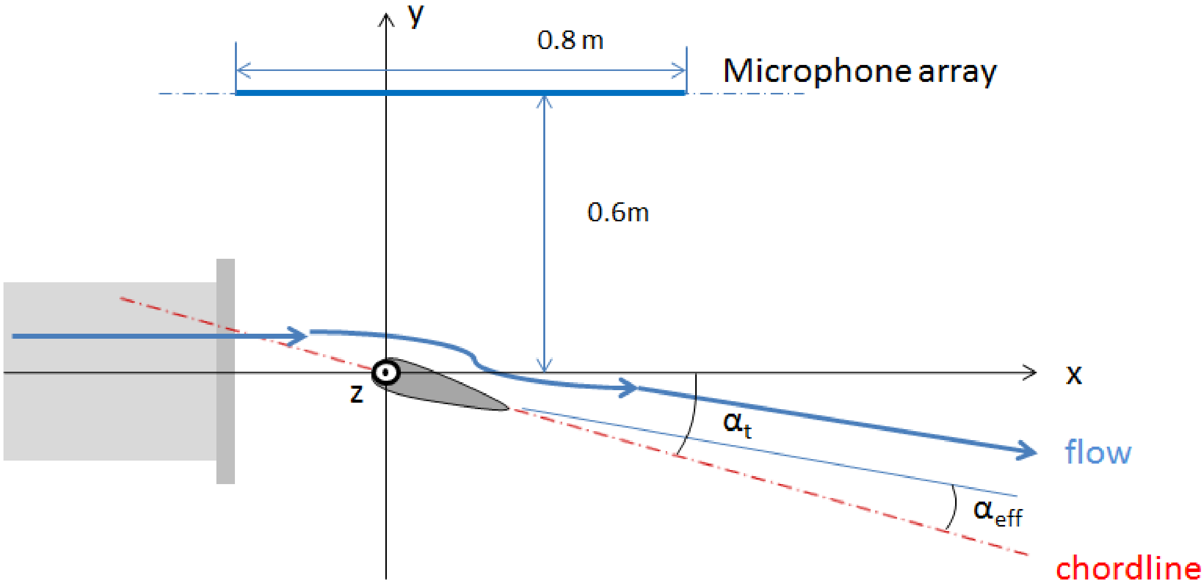

Figure 28 – Coordinate System for Acoustic Measurements (Not on Scale)

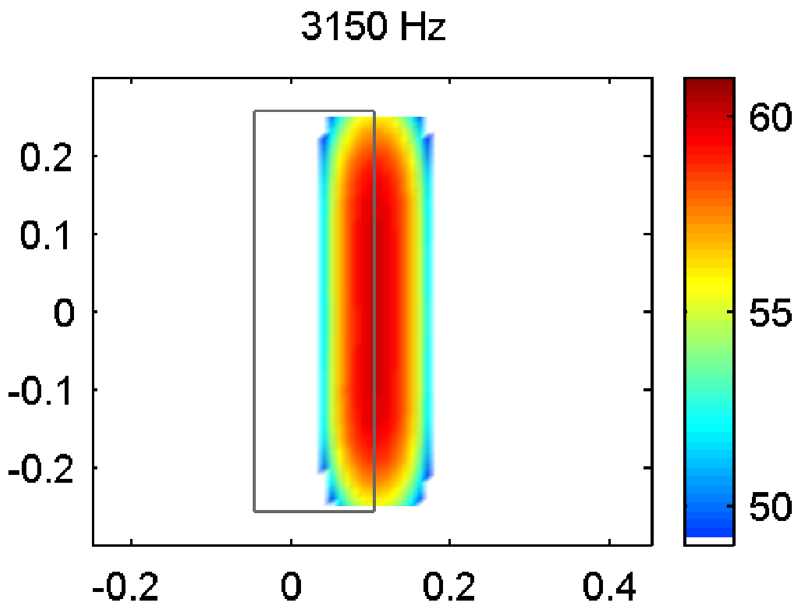

Figure 29 – Acoustic Source map at U_{∞} = 40 m/s, α_{eff} = 6° and f = 3150 Hz

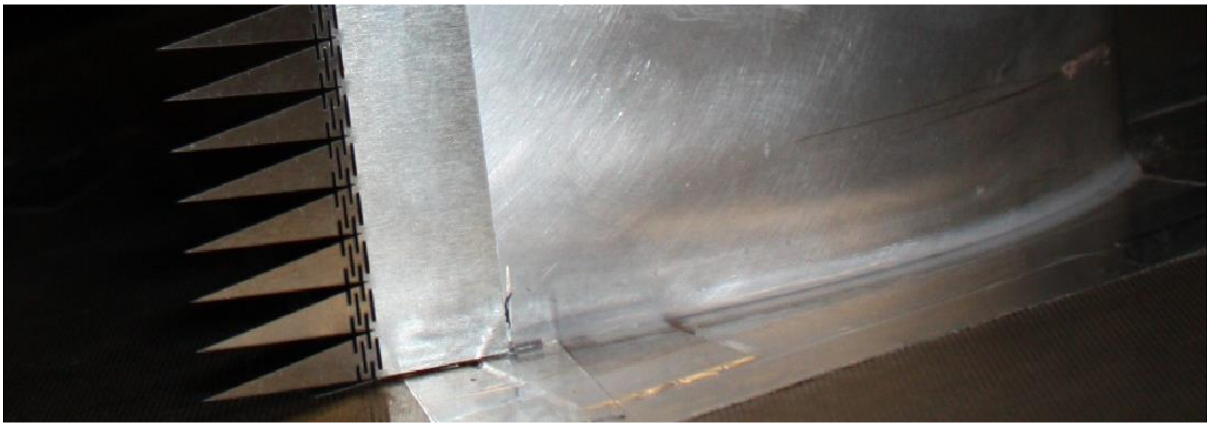

Figure 30 –Silicone applied between the gap of the airfoil and the plate (In this picture the Cutted Serration was mounted).

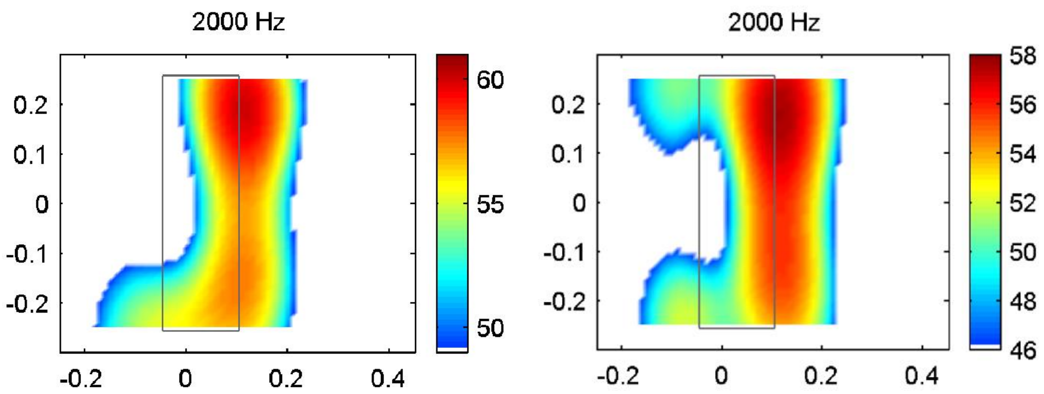

Figure 31 –Acoustic Source Maps at U_∞ = 40 m/s, AoA = 10.5° (α_{eff} = 6°) and f = 2000 Hz, with the US-BOT serration installed, before (LEFT) and after (RIGHT) the gap of the airfoil and the wind tunnel plate has been filled with silicone.

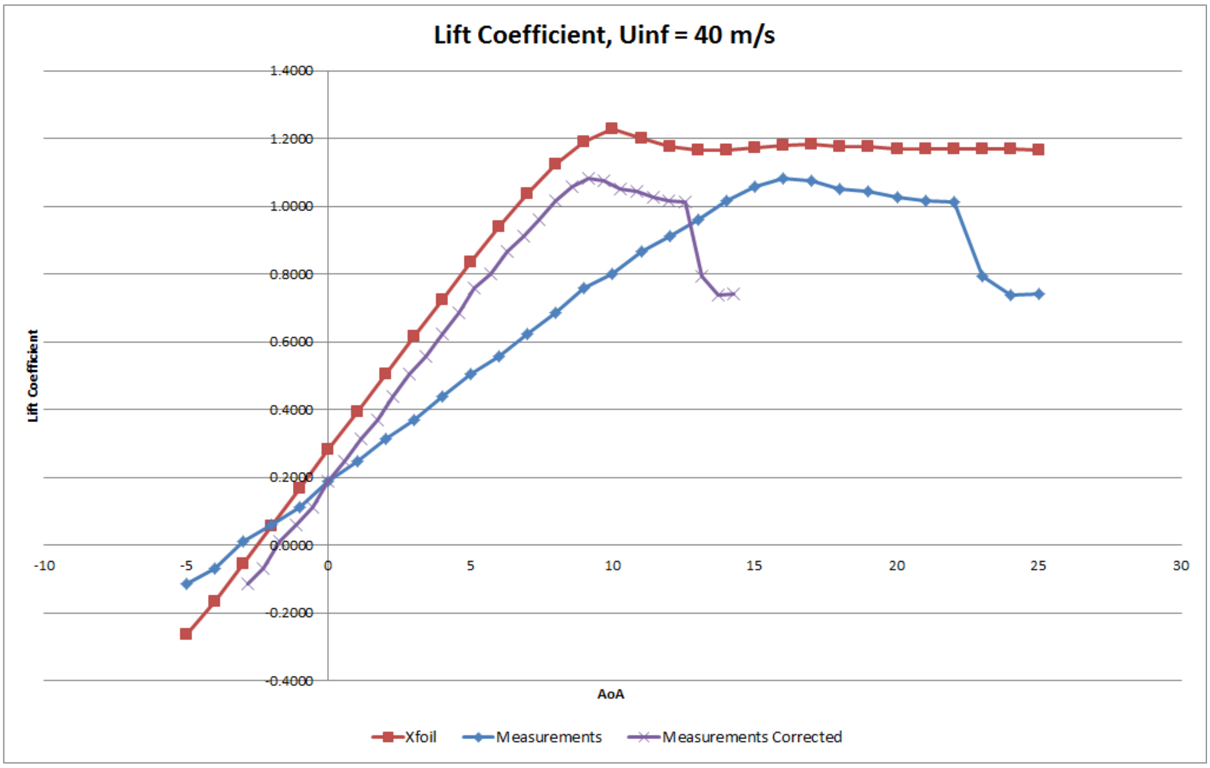

Figure 32- Lift Coefficient measure at wind tunnel velocity of 40 m/s within the range of -5° and 25°, compared with Xfoil simulations

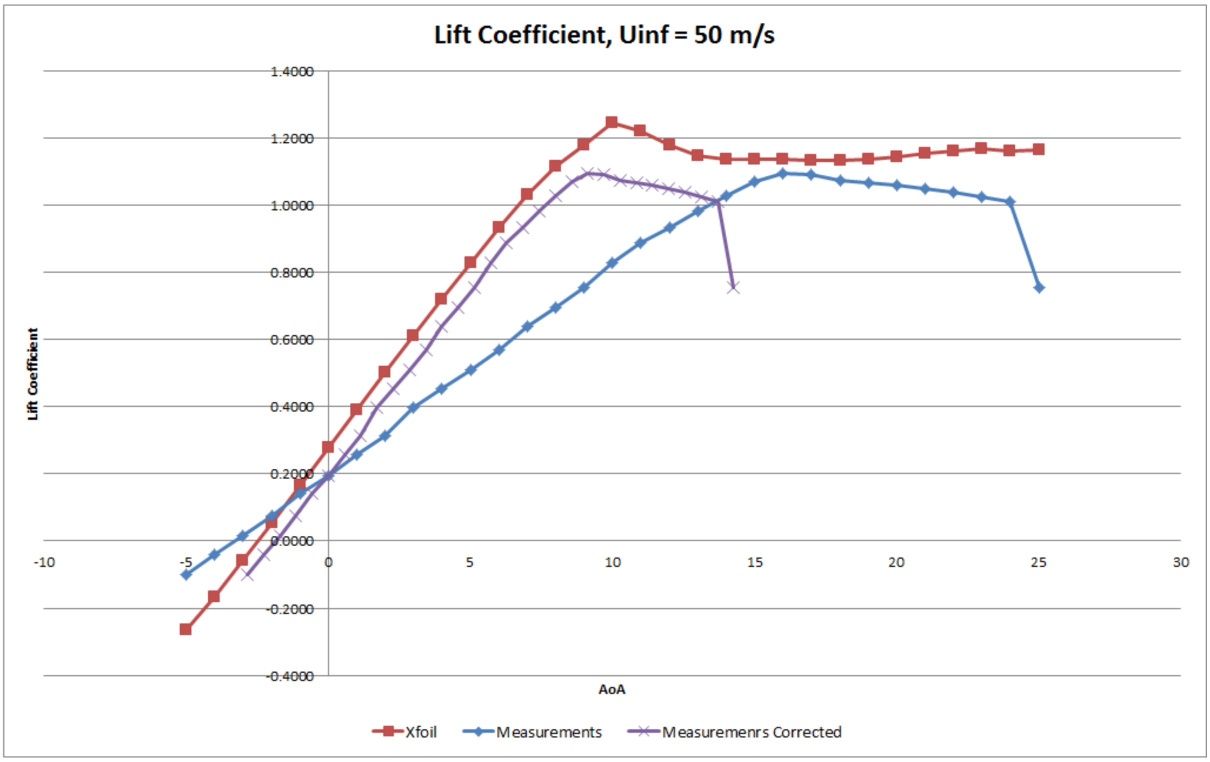

Figure 33 - Lift Coefficient measure at wind tunnel velocity of 50 m/s within the range of -5° and 25°, compared with Xfoil simulations

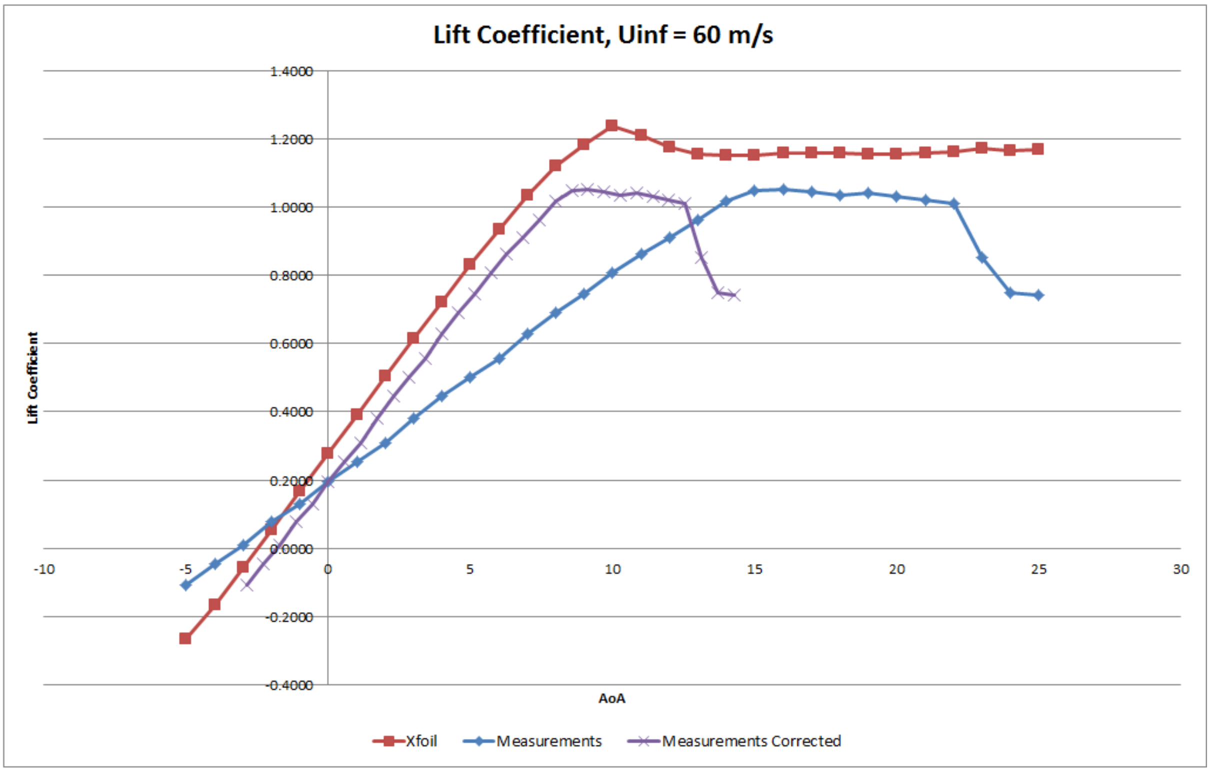

Figure 34 - Lift Coefficient measure at wind tunnel velocity of 60 m/s within the range of -5° and 25°, compared with Xfoil simulations

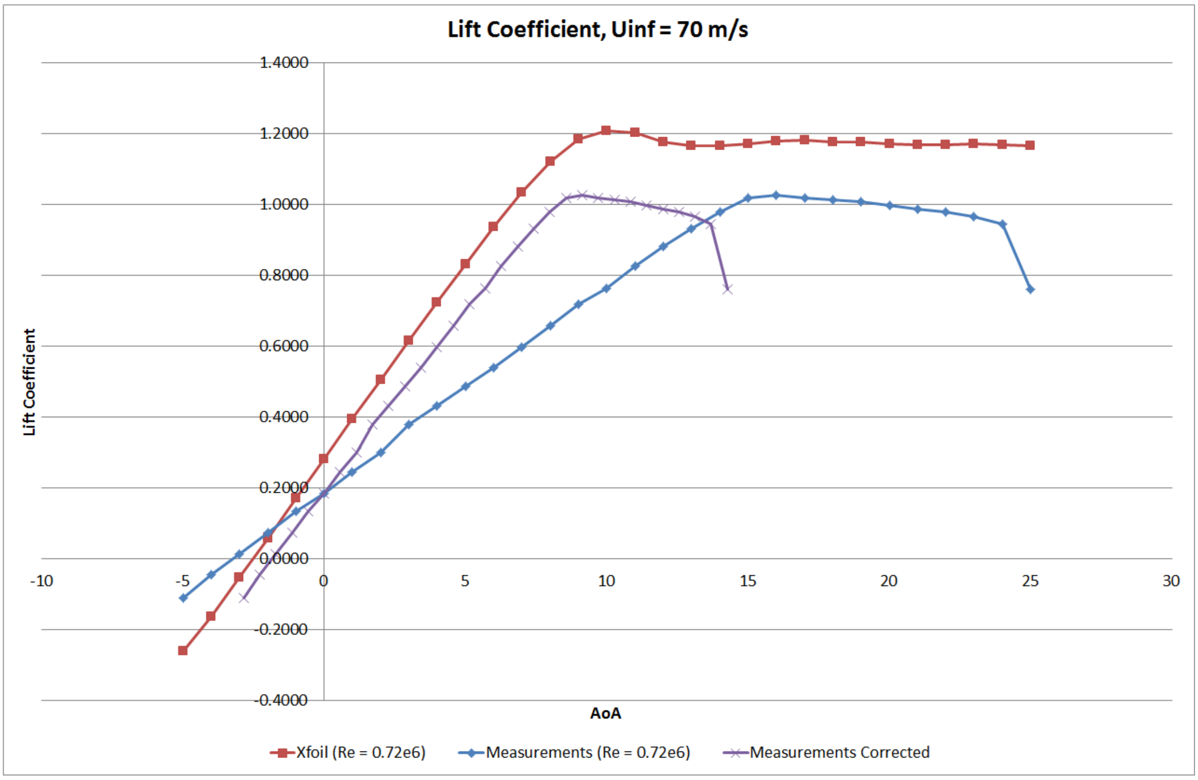

Figure 35 - Lift Coefficient measure at wind tunnel velocity of 70 m/s within the range of -5° and 25°, compared with Xfoil simulations

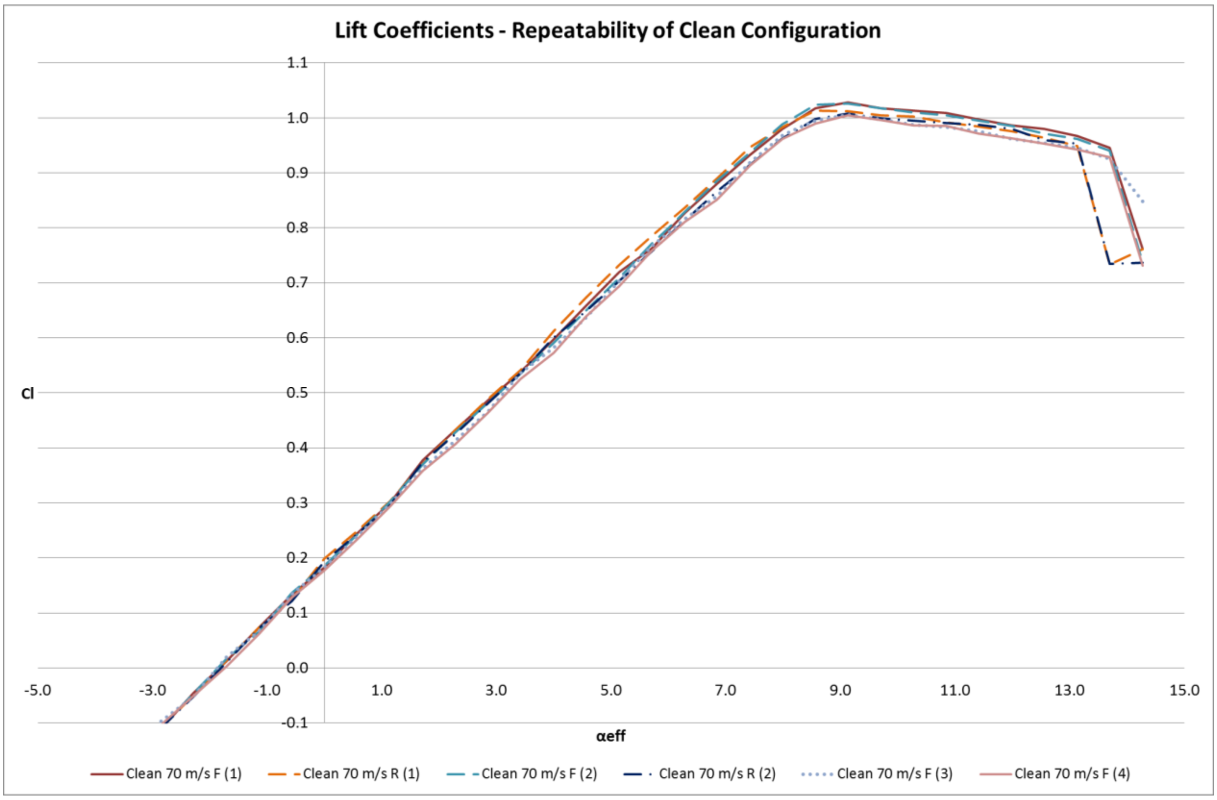

Figure 36 – Repeatability of Balance Measurements

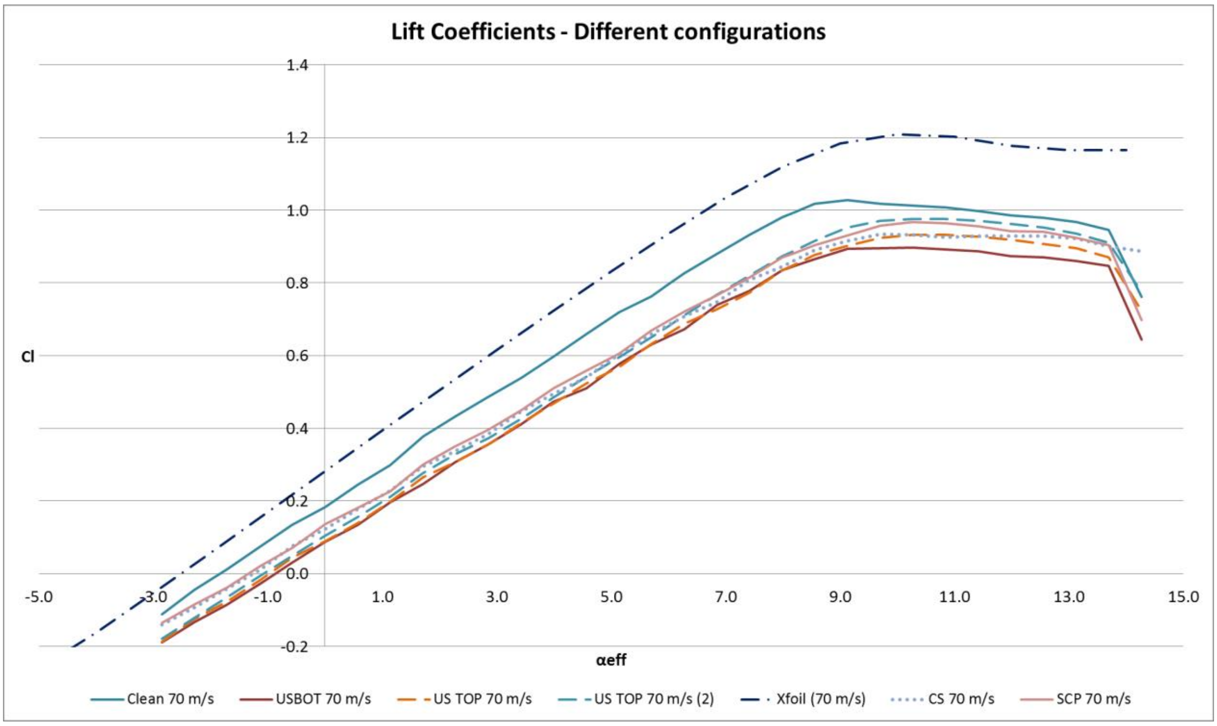

Figure 37 – Lift Coefficients with the extra area due to the serrations included in the normalization

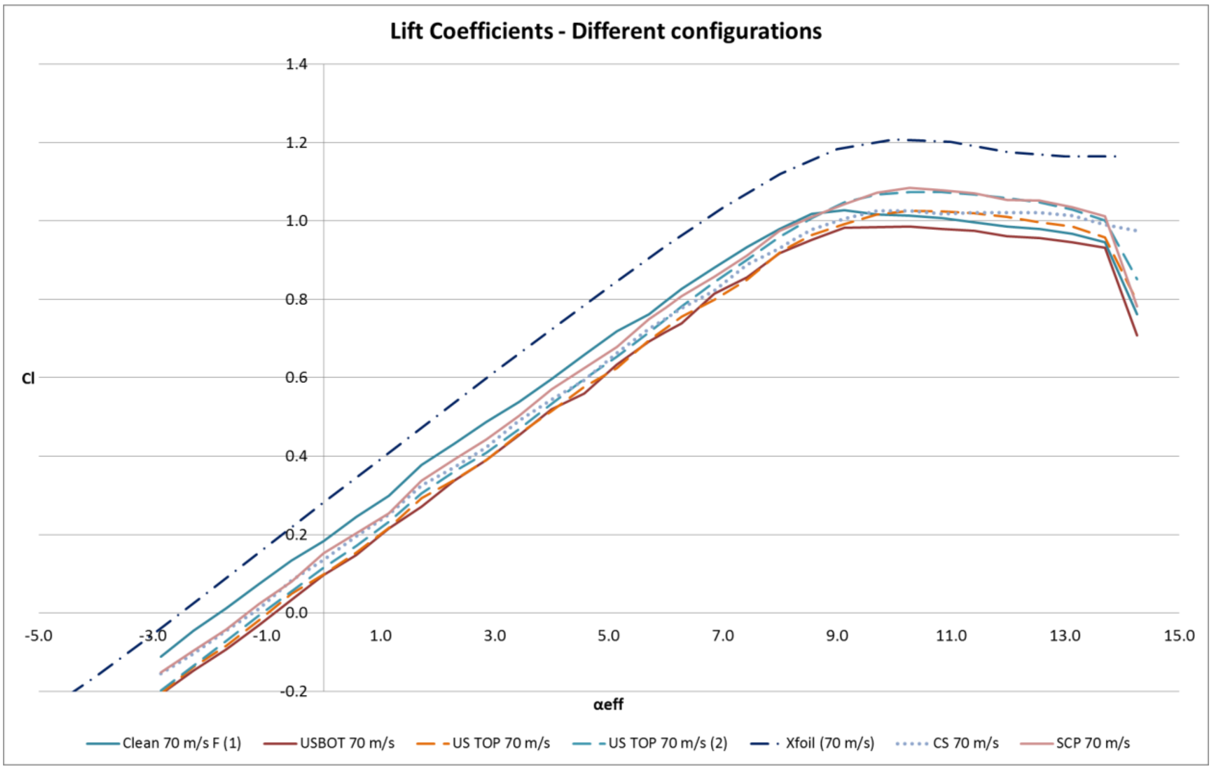

Figure 38 – Lift Coefficients with all Cl curves normalized with only the surface area of the airfoil

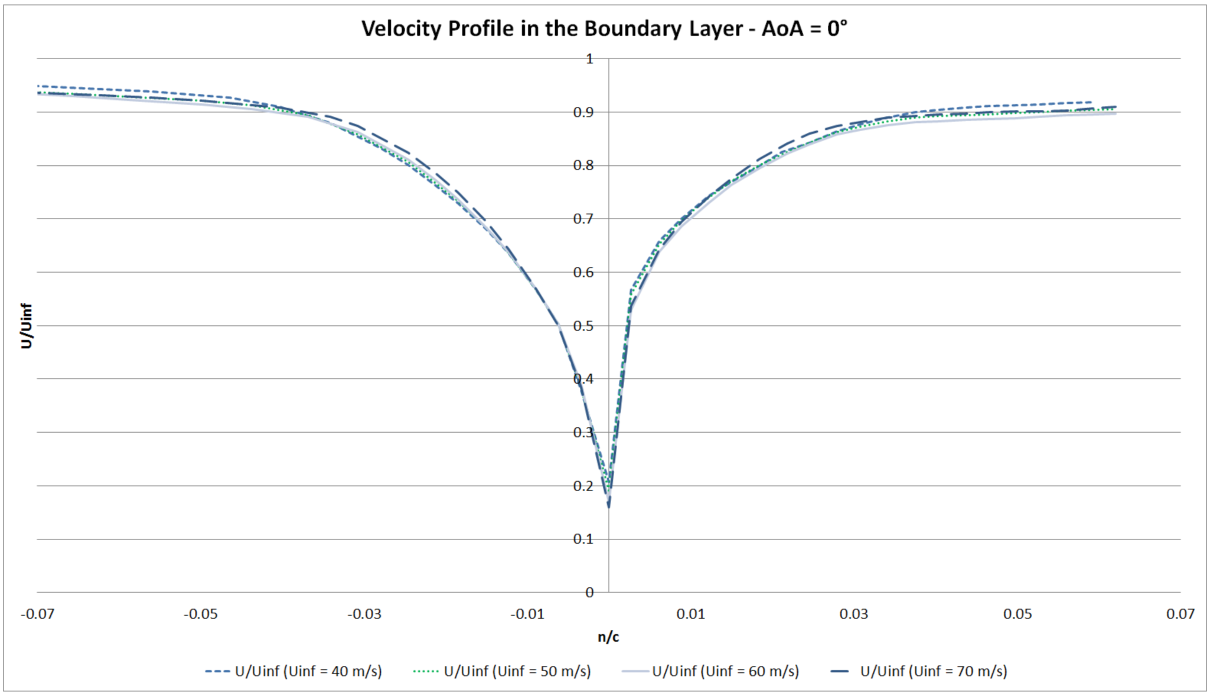

Figure 39– Velocity Profile in the Boundary Layer for different free stream velocities at AoA = 0° (effective angle of attack)

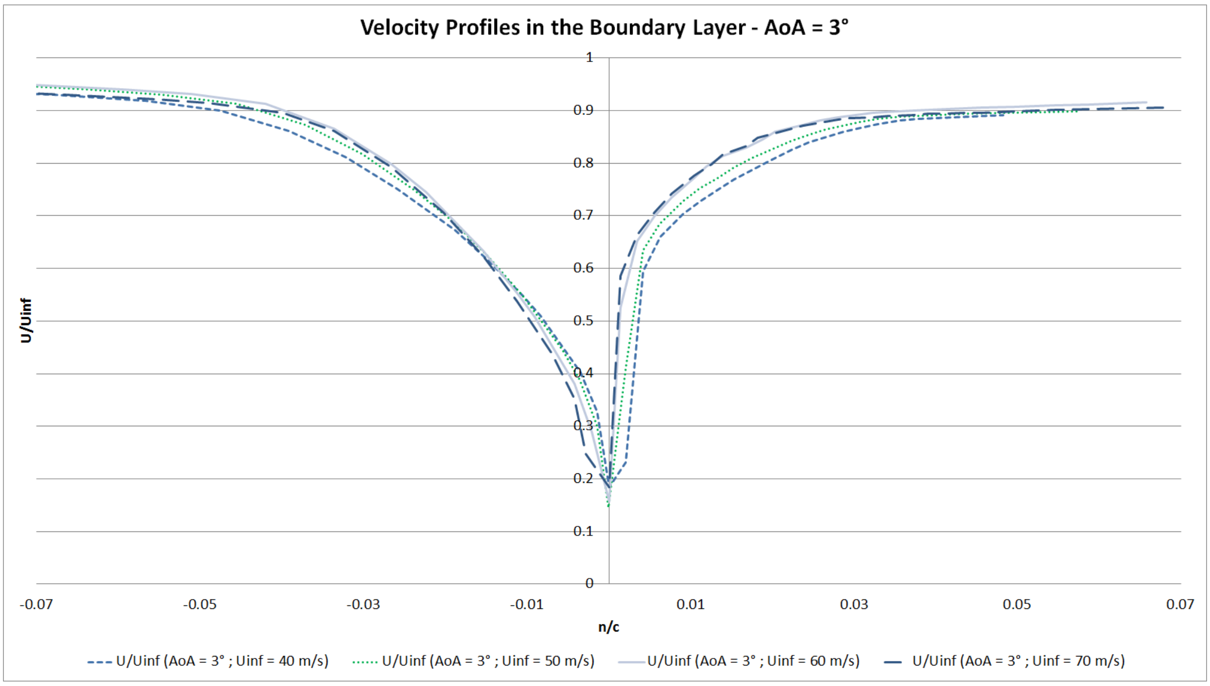

Figure 40 – Velocity Profile in the Boundary Layer for different free stream velocities at AoA = 3° (effective angle of attack)

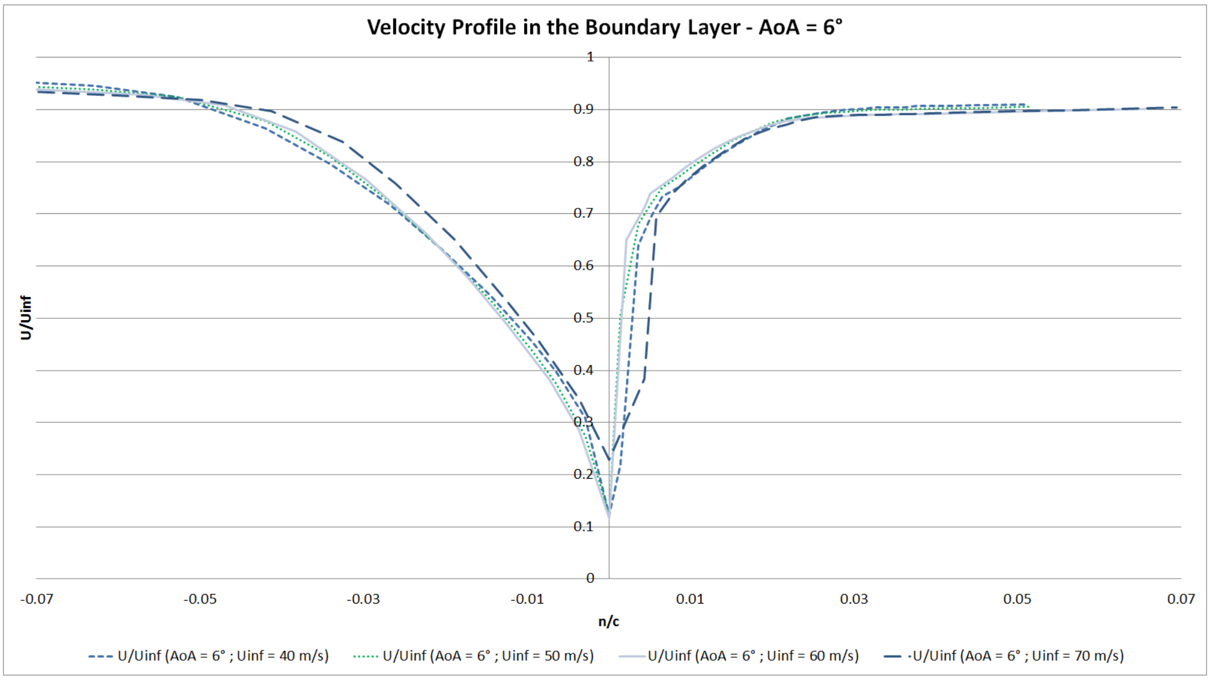

Figure 41 – Velocity Profile in the Boundary Layer for different free stream velocities at AoA = 6° (effective angle of attack)

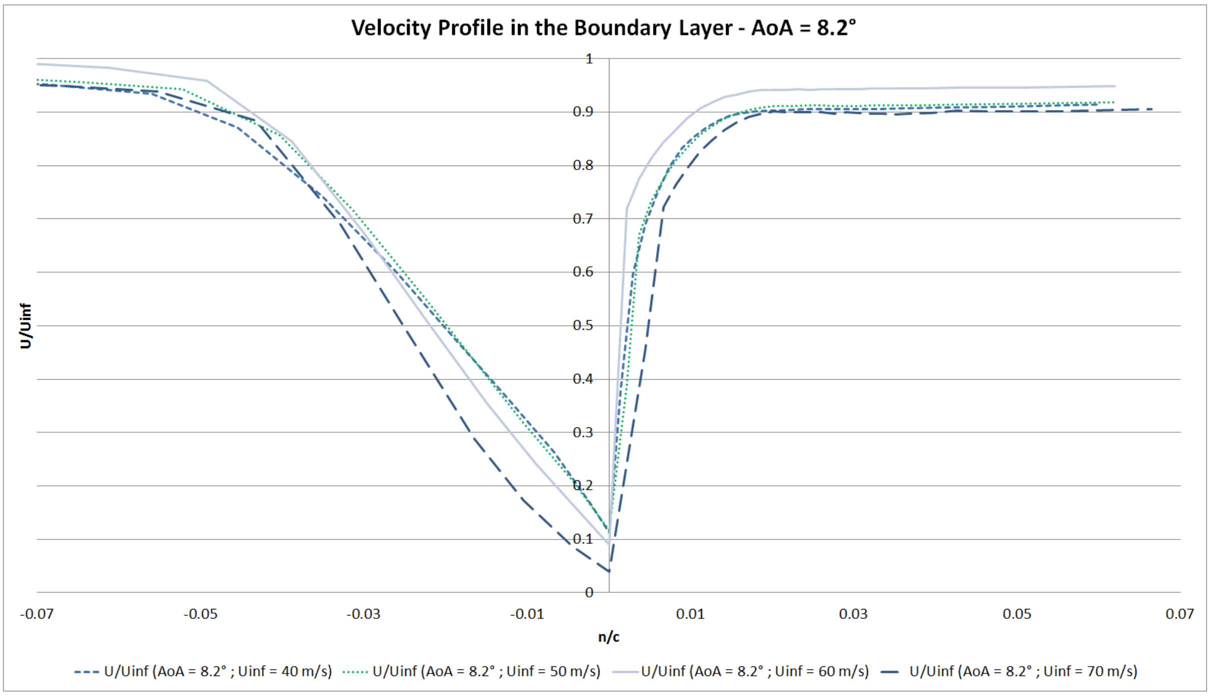

Figure 42 – Velocity Profile in the Boundary Layer for different free stream velocities at AoA = 8.2° (effective angle of attack)

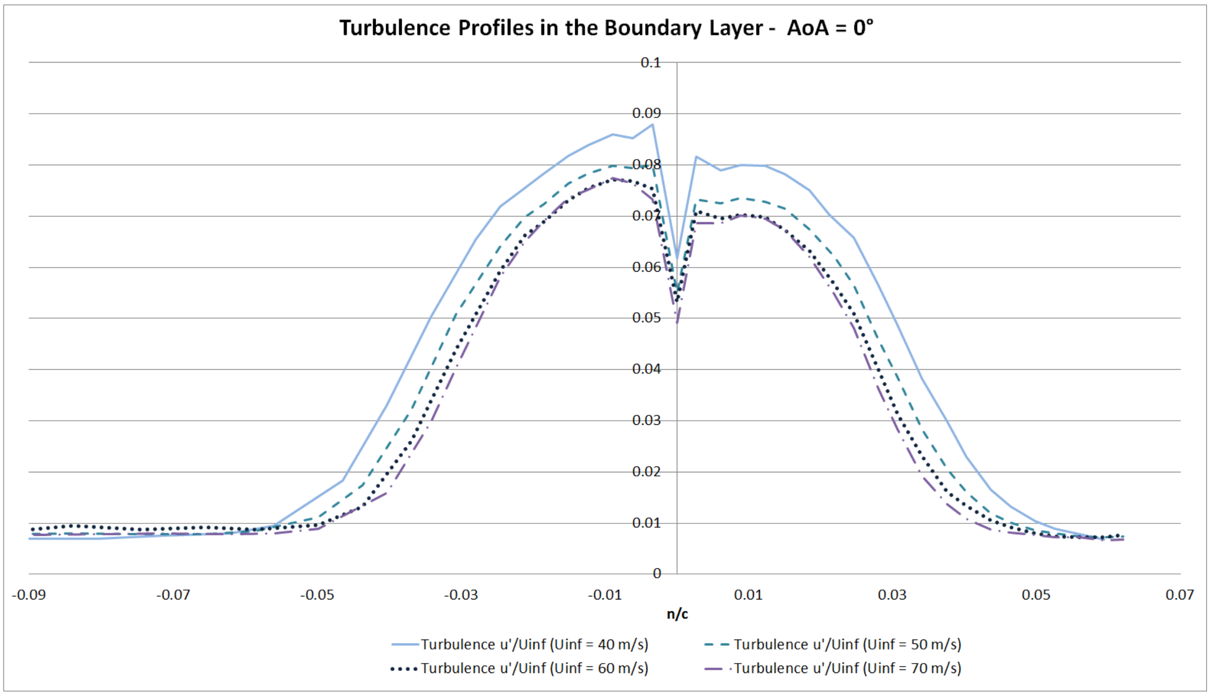

Figure 43 – Turbulence Profile in the Boundary Layer for different free stream velocities at AoA = 0° (effective angle of attack)

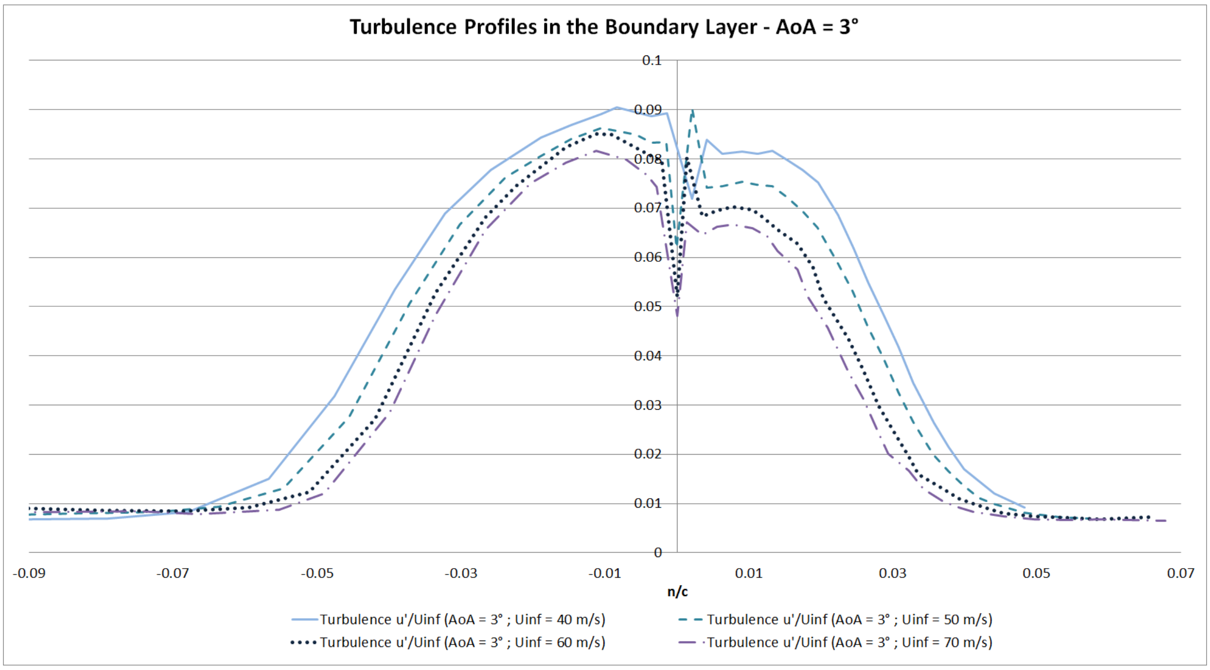

Figure 44– Turbulence Profile in the Boundary Layer for different free stream velocities at AoA = 3° (effective angle of attack)

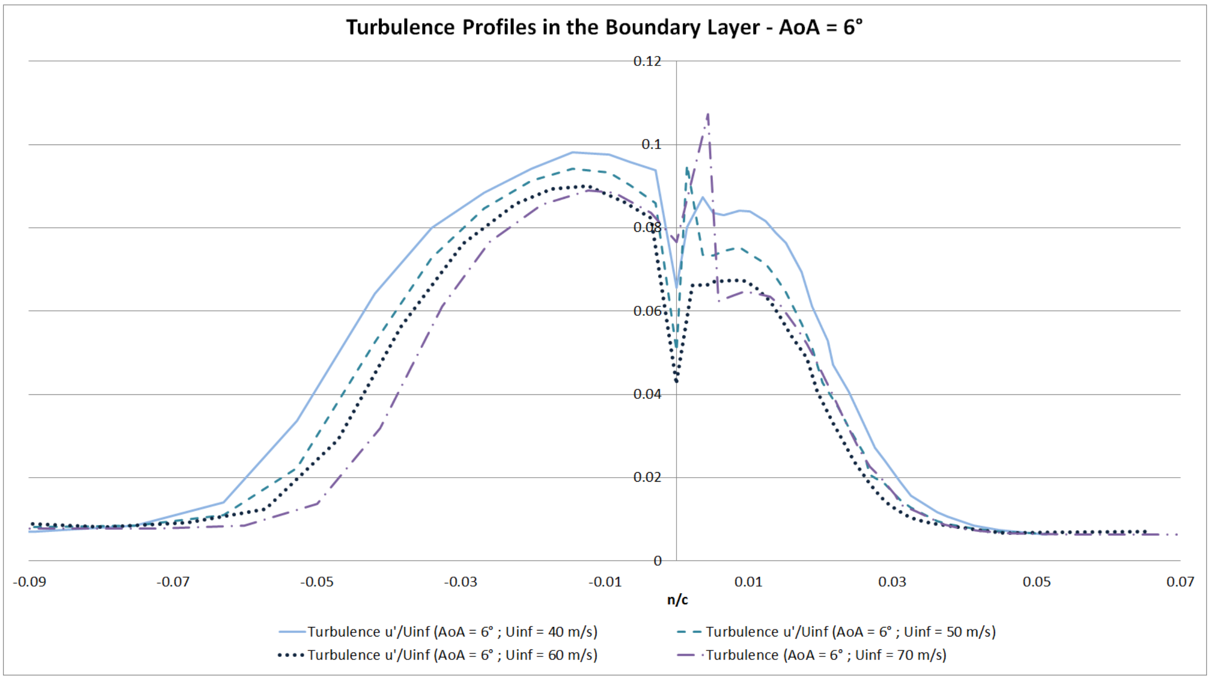

Figure 45 – Turbulence Profile in the Boundary Layer for different free stream velocities at AoA = 6° (effective angle of attack)

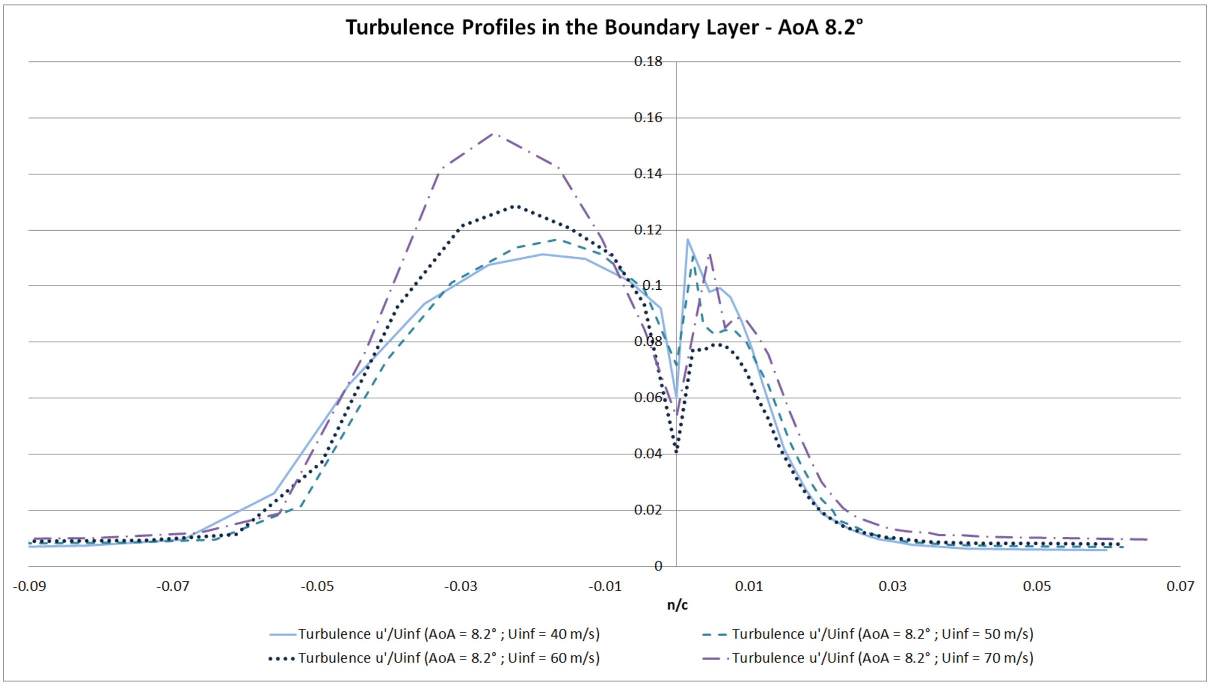

Figure 46– Turbulence Profile in the Boundary Layer for different free stream velocities at AoA = 8.2° (effective angle of attack)

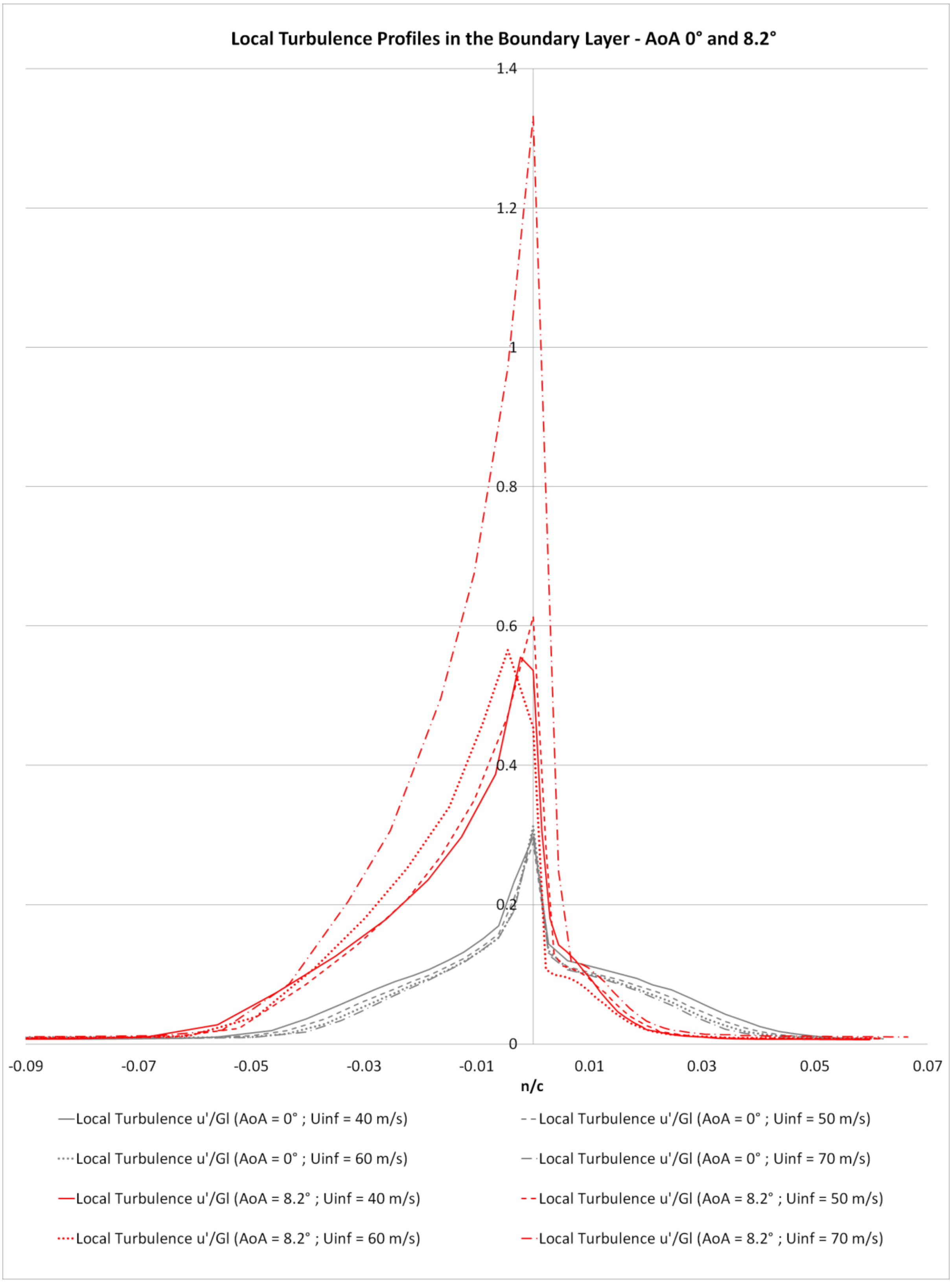

Figure 47– Local Turbulence Profiles in the Boundary Layer for different free stream velocities at AoA = 0° and 8.2°

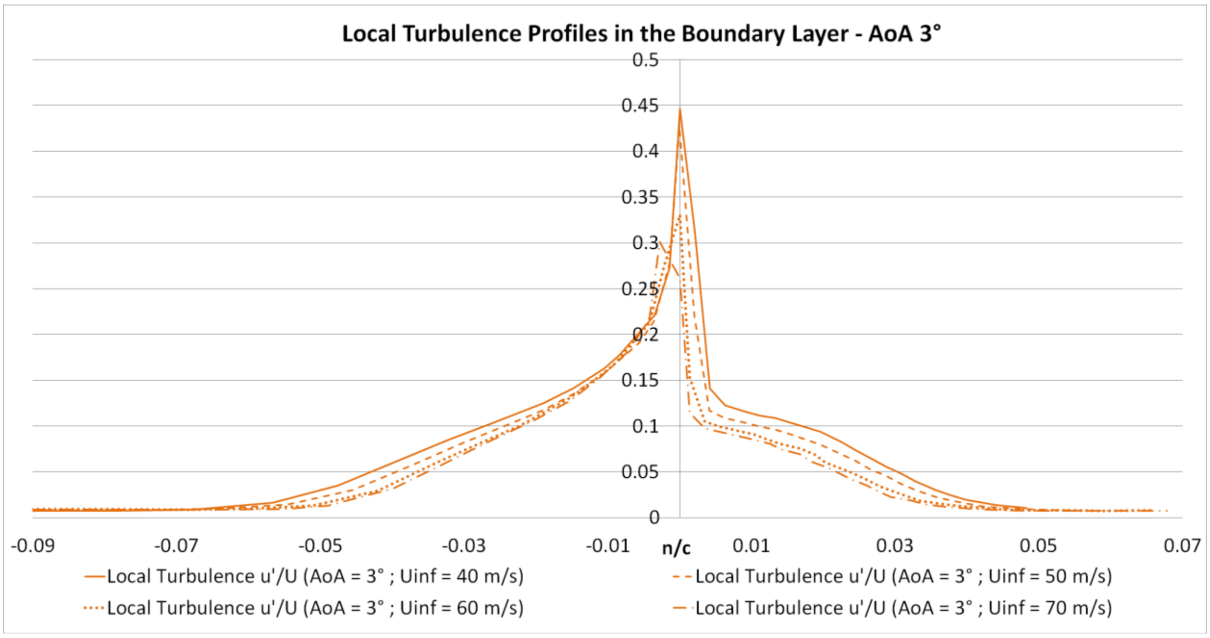

Figure 48 – Local Turbulence Profiles in the Boundary Layer for different free stream velocities at AoA = 3°

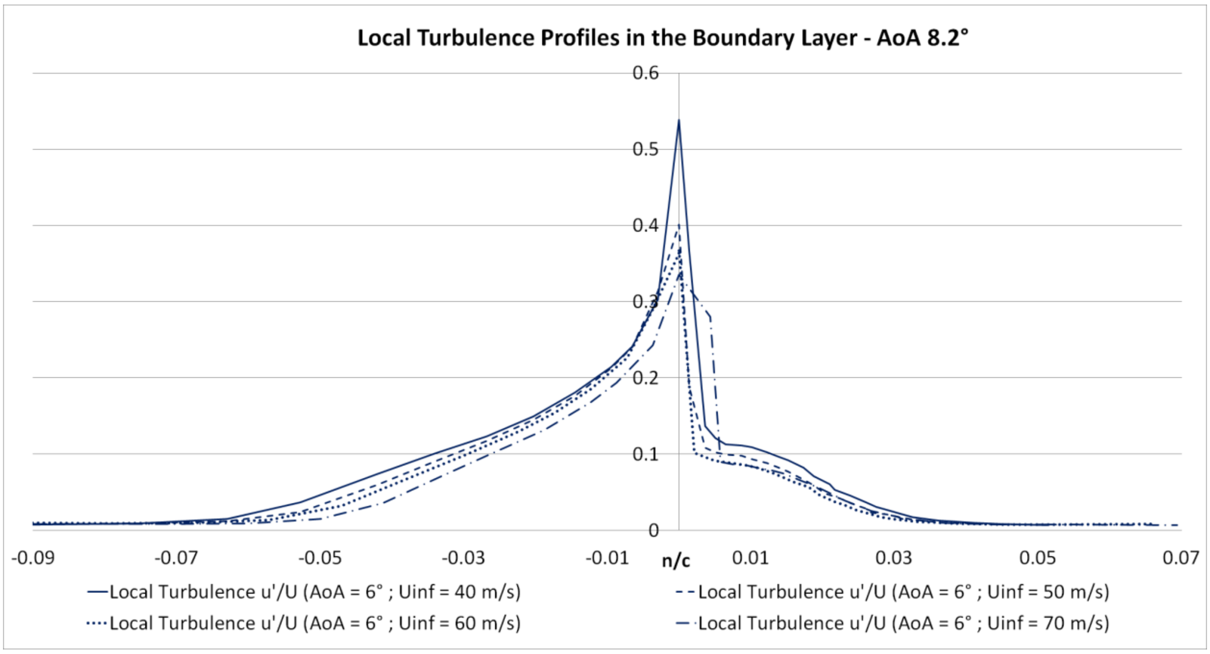

Figure 49– Local Turbulence Profiles in the Boundary Layer for different free stream velocities at AoA = 3°

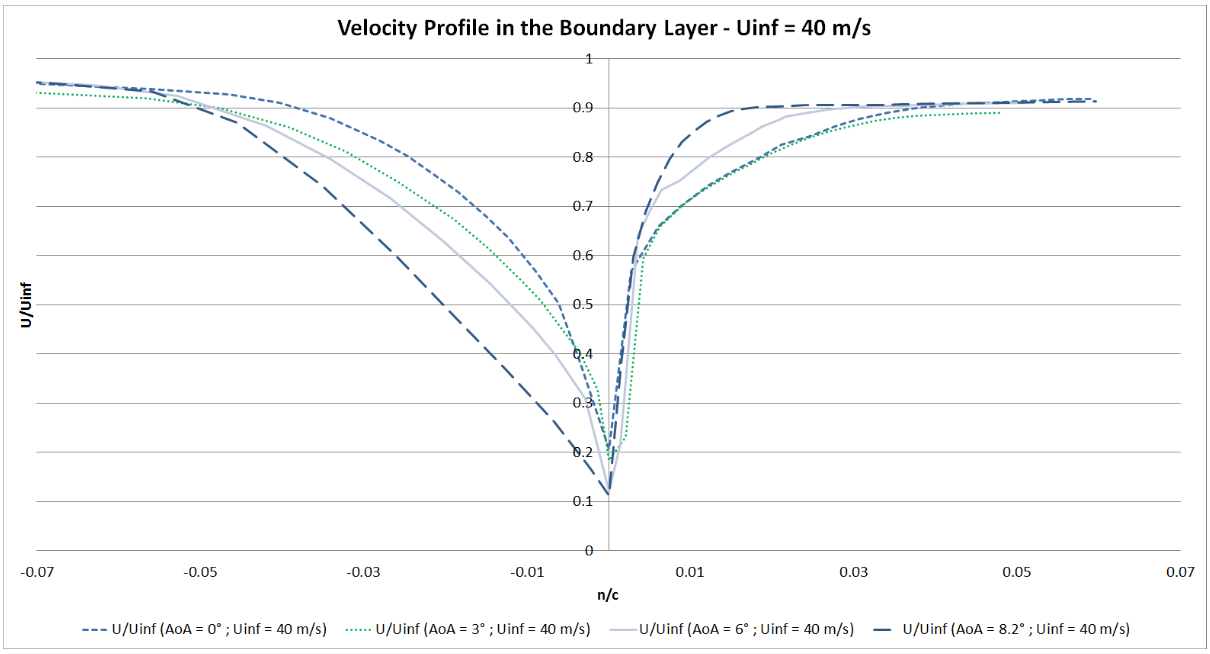

Figure 50– Velocity Profile in the Boundary Layer for different effective angles of attack at U_∞ = 40 m/s

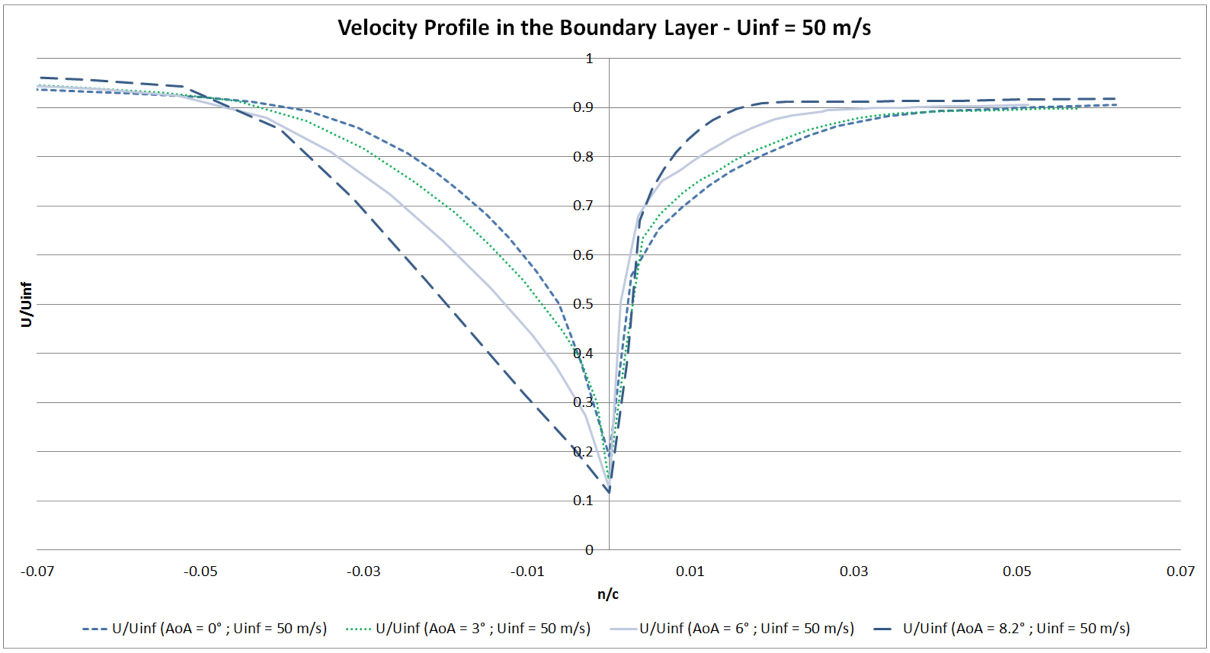

Figure 51– Velocity Profile in the Boundary Layer for different effective angles of attack at U_∞ = 50 m/s

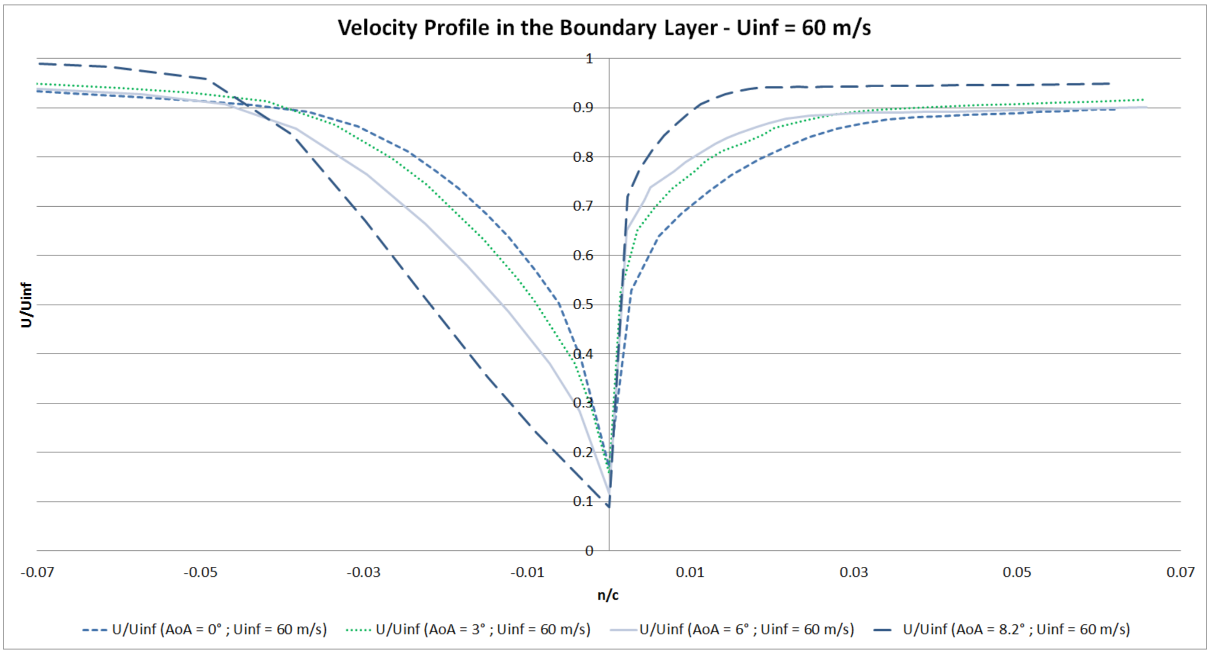

Figure 52 – Velocity Profile in the Boundary Layer for different effective angles of attack at U_∞ = 60 m/s

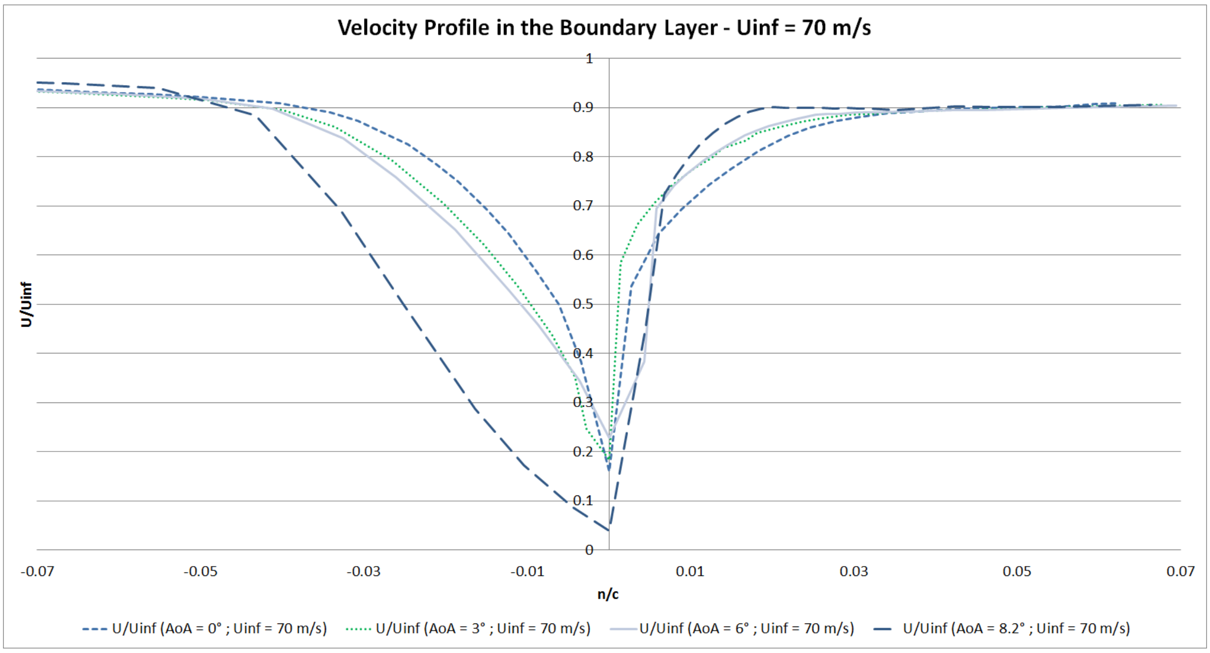

Figure 53– Velocity Profile in the Boundary Layer for different effective angles of attack at U_∞ = 70 m/s

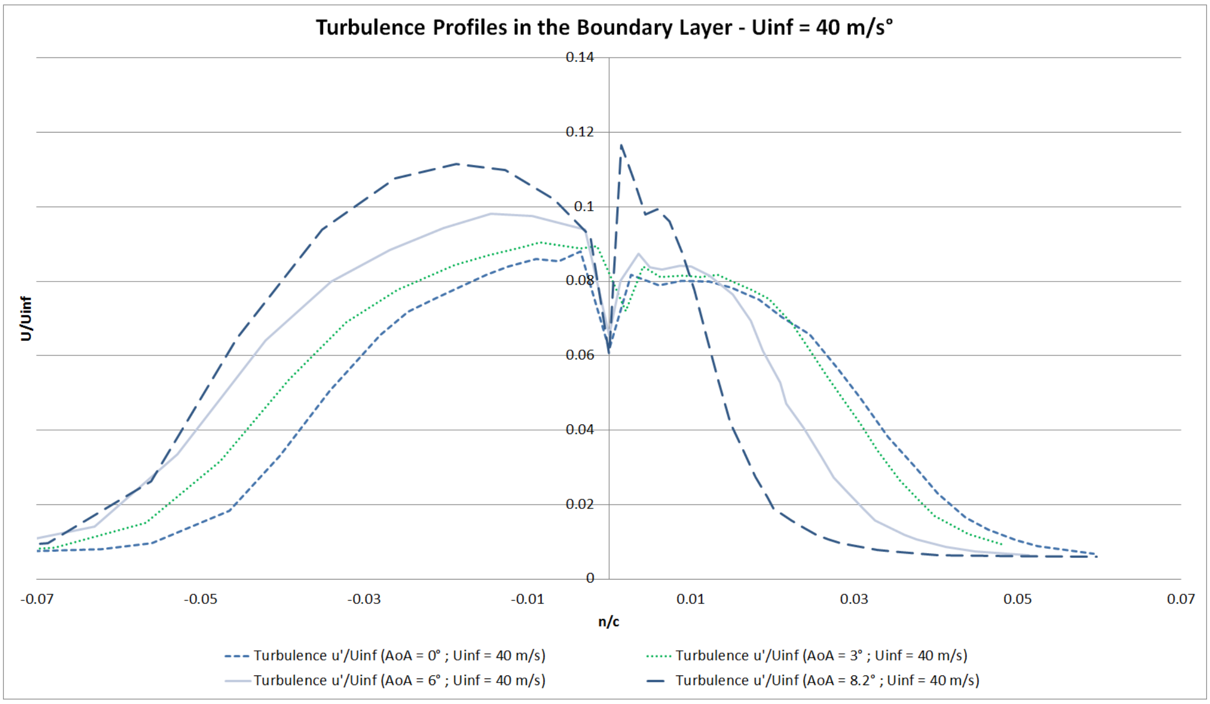

Figure 54– Turbulence Profile in the Boundary Layer for different effective angles of attack at U_∞ = 40 m/s

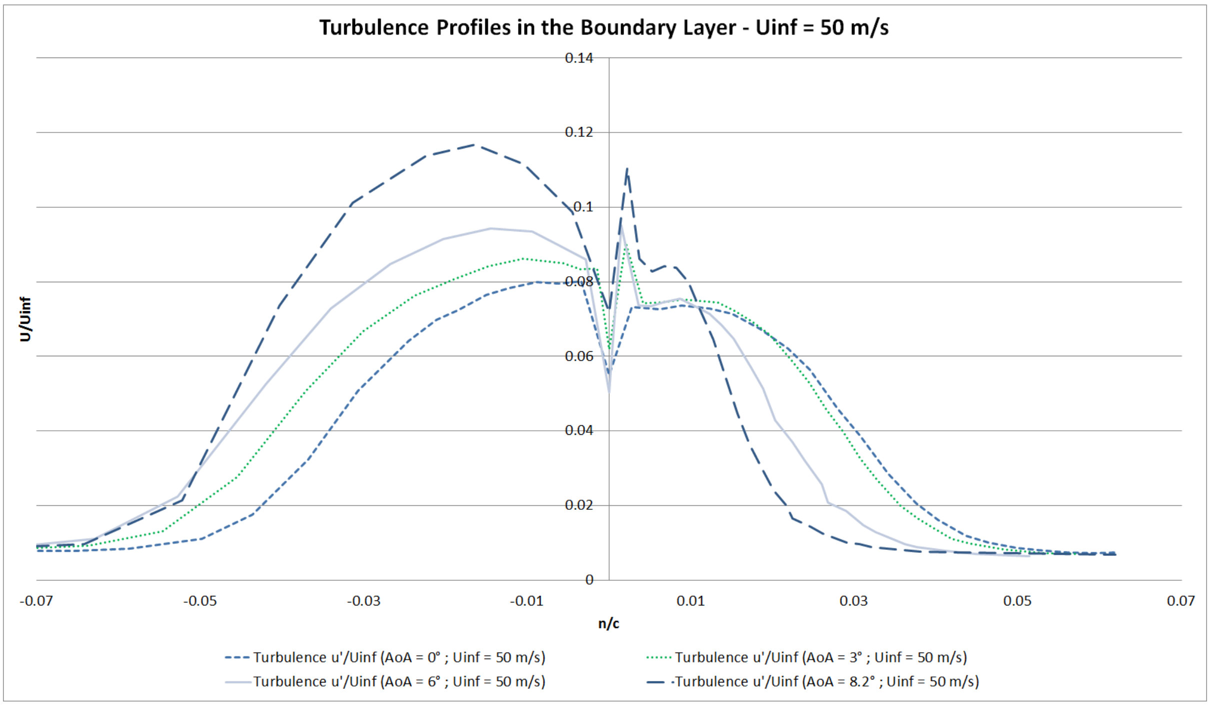

Figure 55– Turbulence Profile in the Boundary Layer for different effective angles of attack at U_∞ = 50 m/s

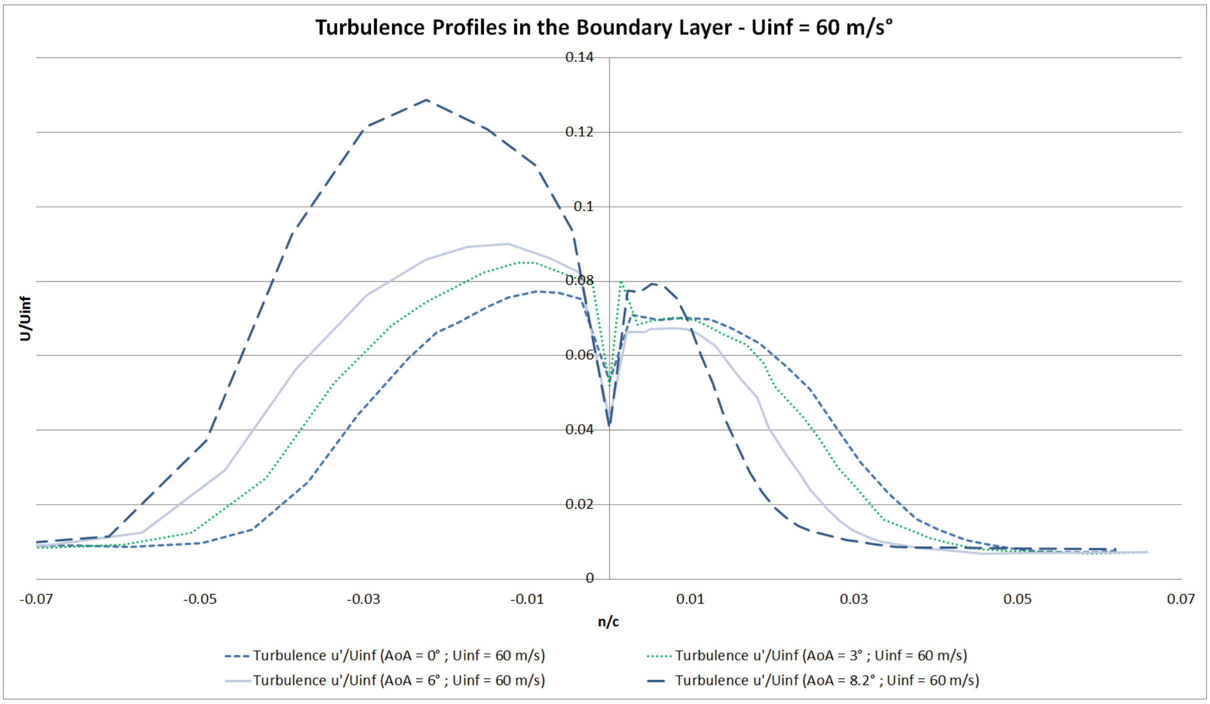

Figure 56– Turbulence Profile in the Boundary Layer for different effective angles of attack at U_∞ = 60 m/s

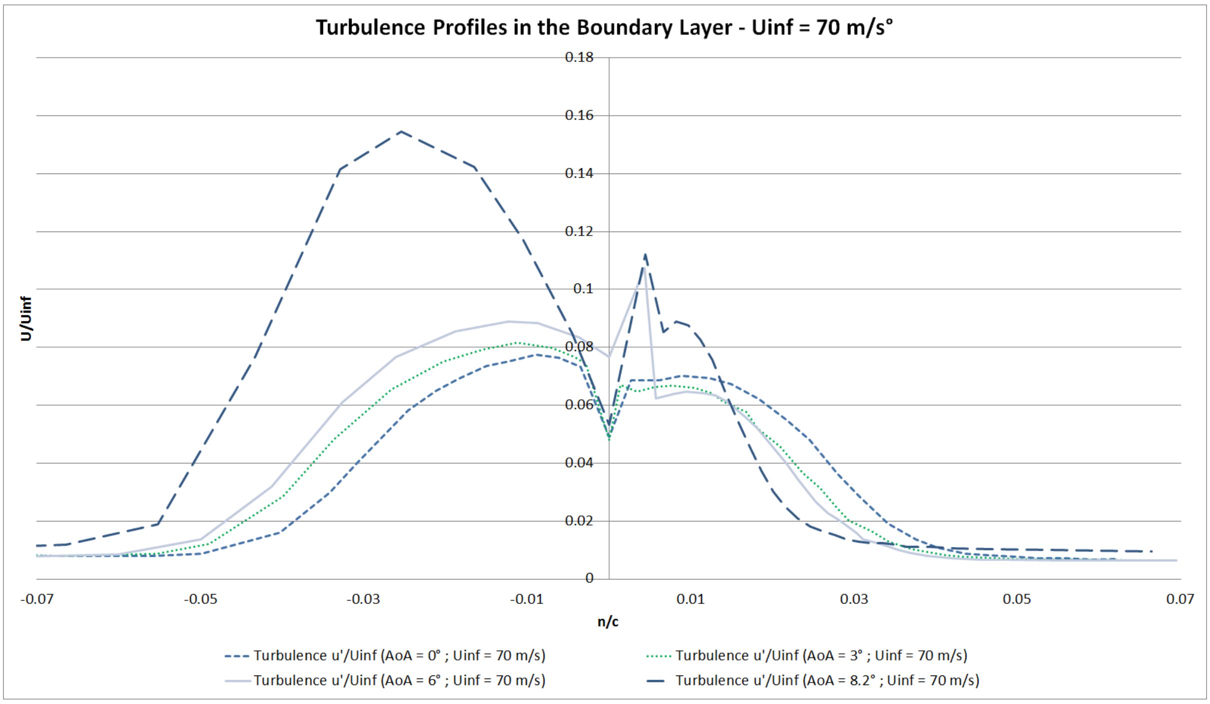

Figure 57– Turbulence Profile in the Boundary Layer for different effective angles of attack at U_∞ = 70 m/s

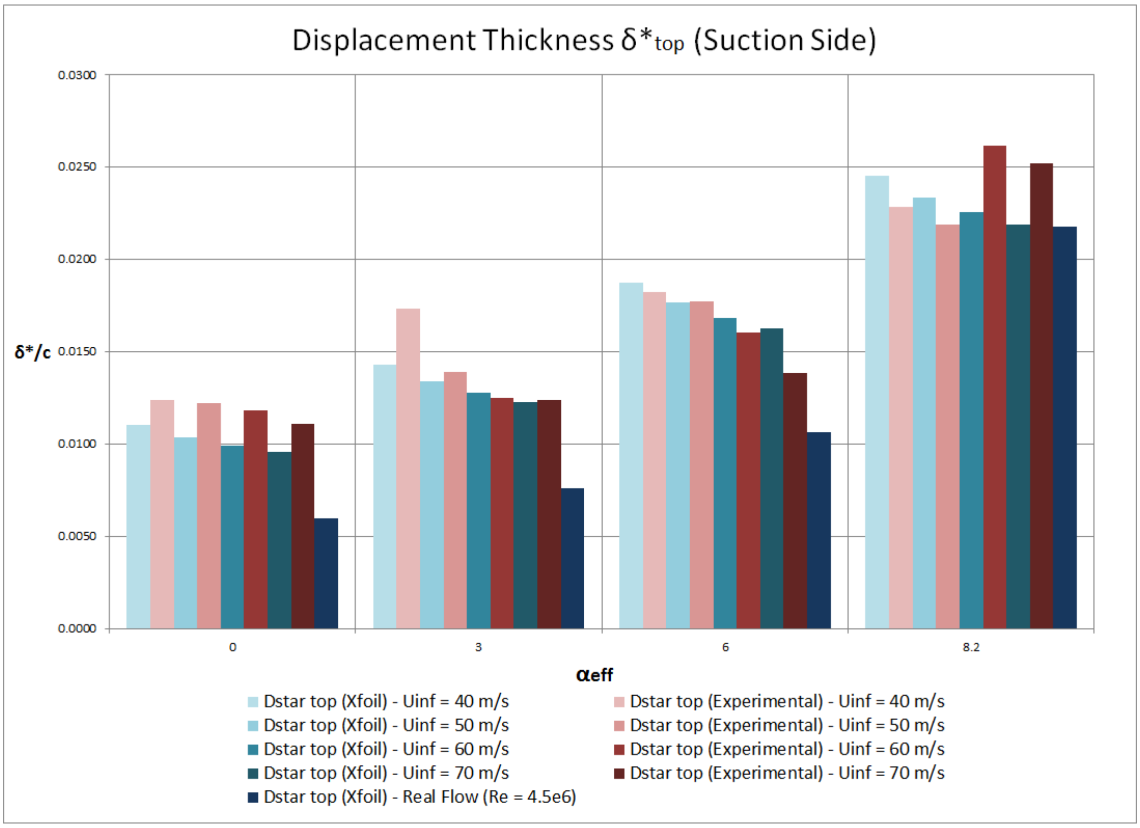

Figure 58 – Displacement Thickness on the Suction Side

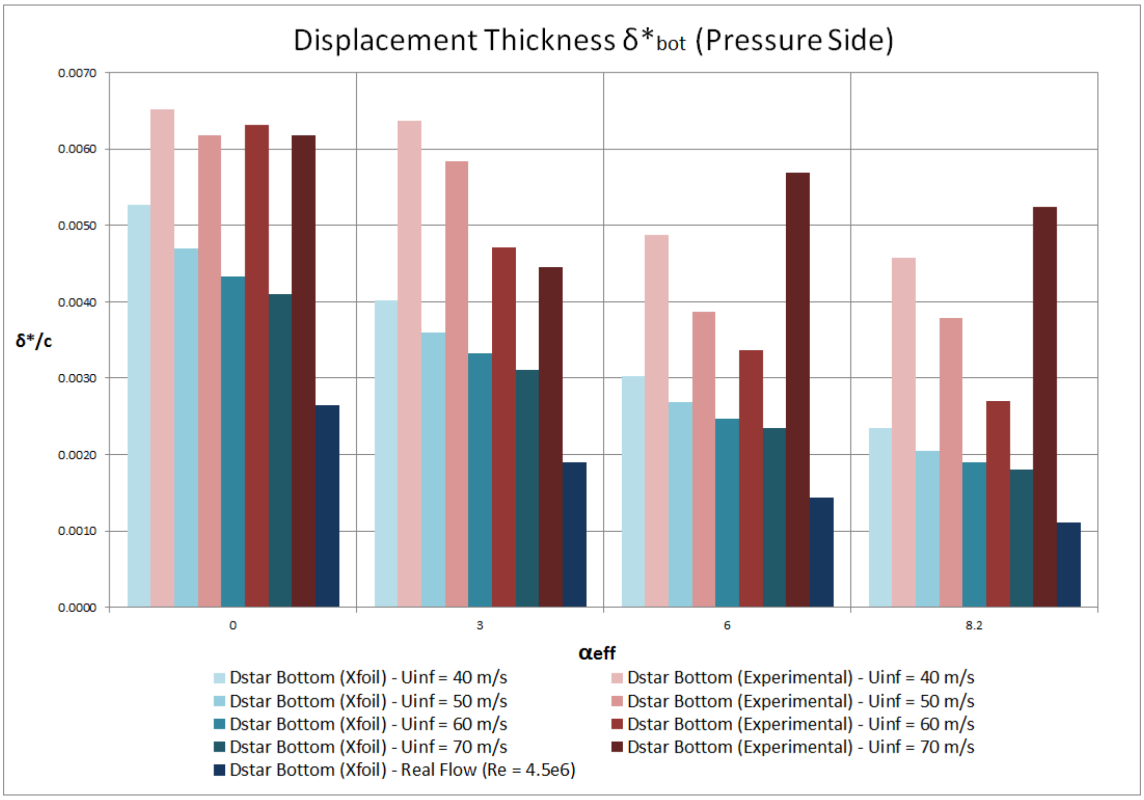

Figure 59 – Displacement Thickness on the Pressure Side

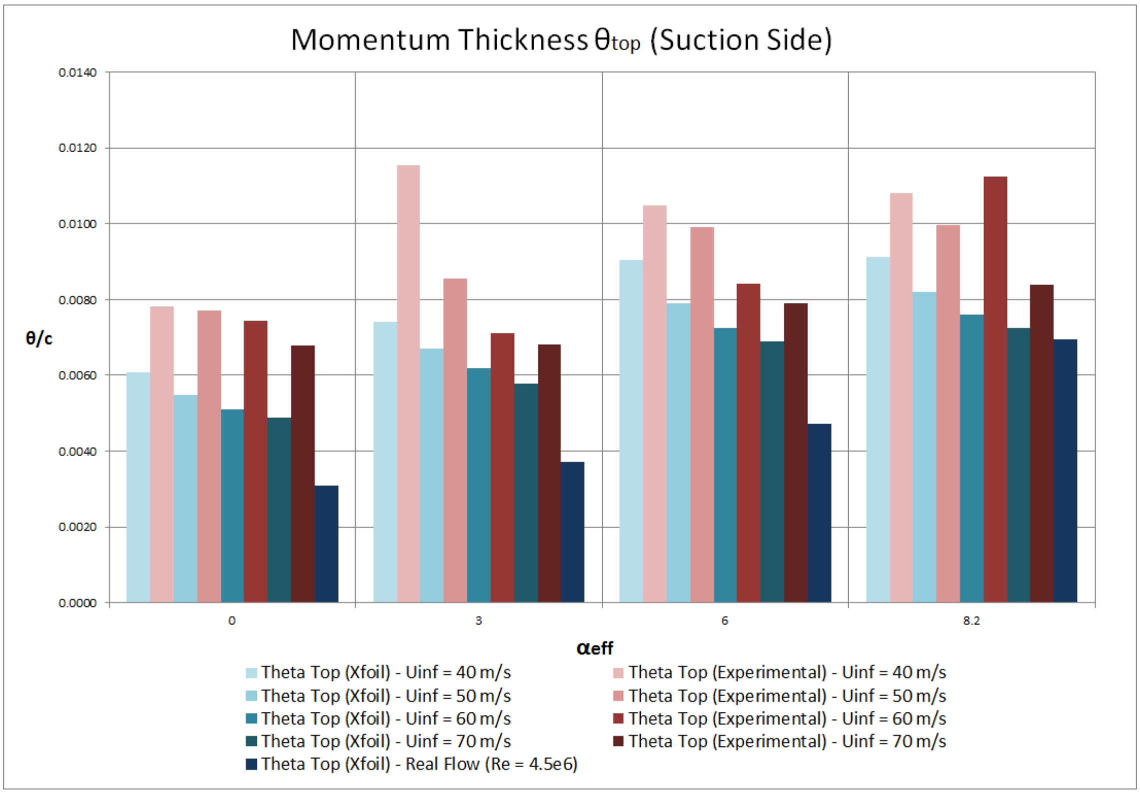

Figure 60 - Momentum Thickness on the Suction Side

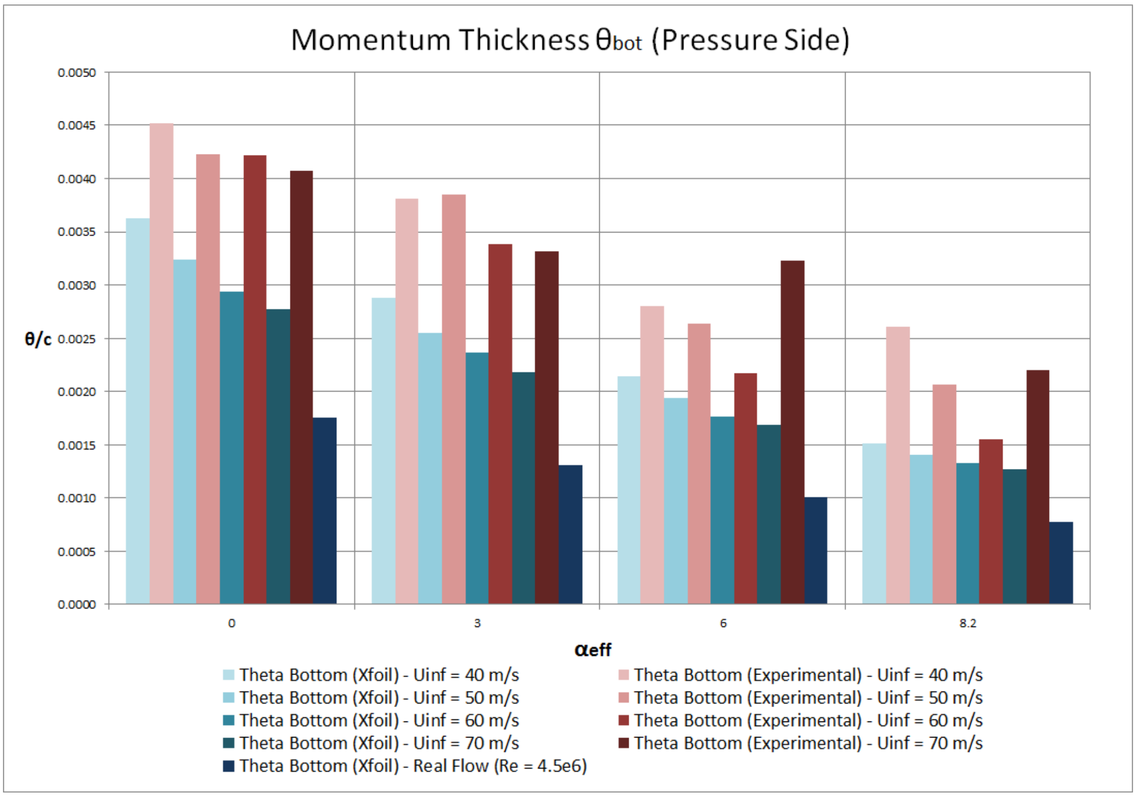

Figure 61 - Momentum Thickness on the Pressure Side

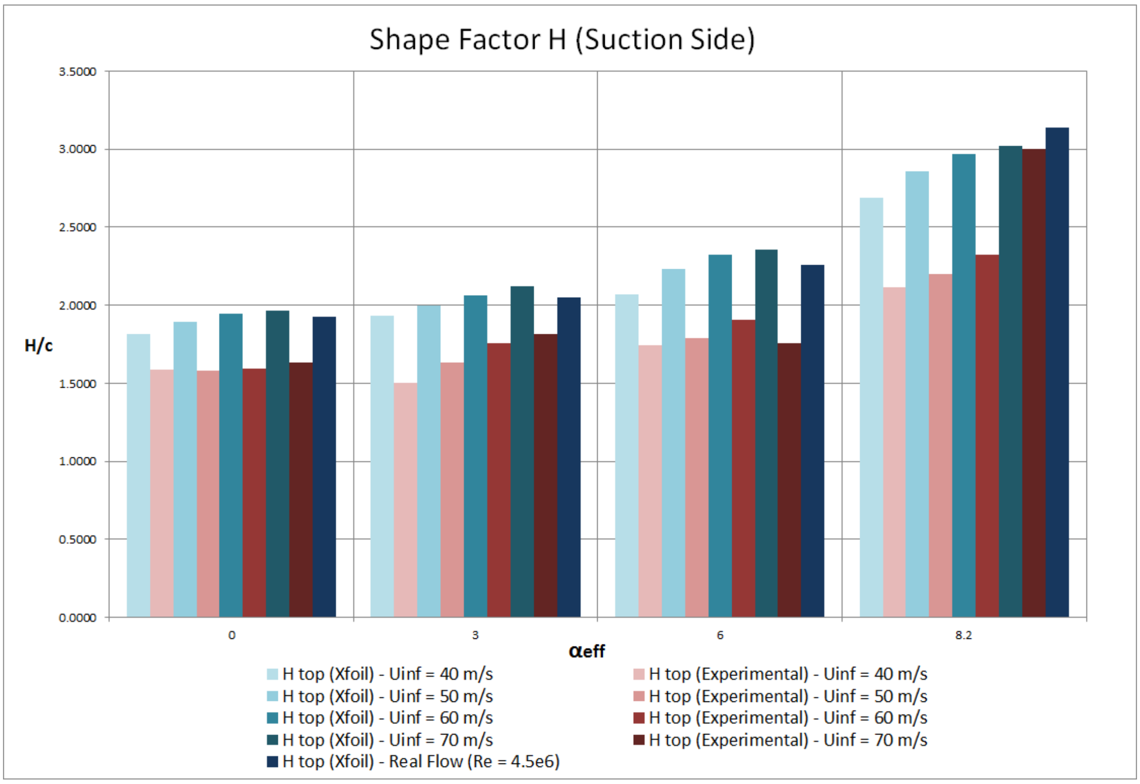

Figure 62 – Shape Factor on the Suction Side

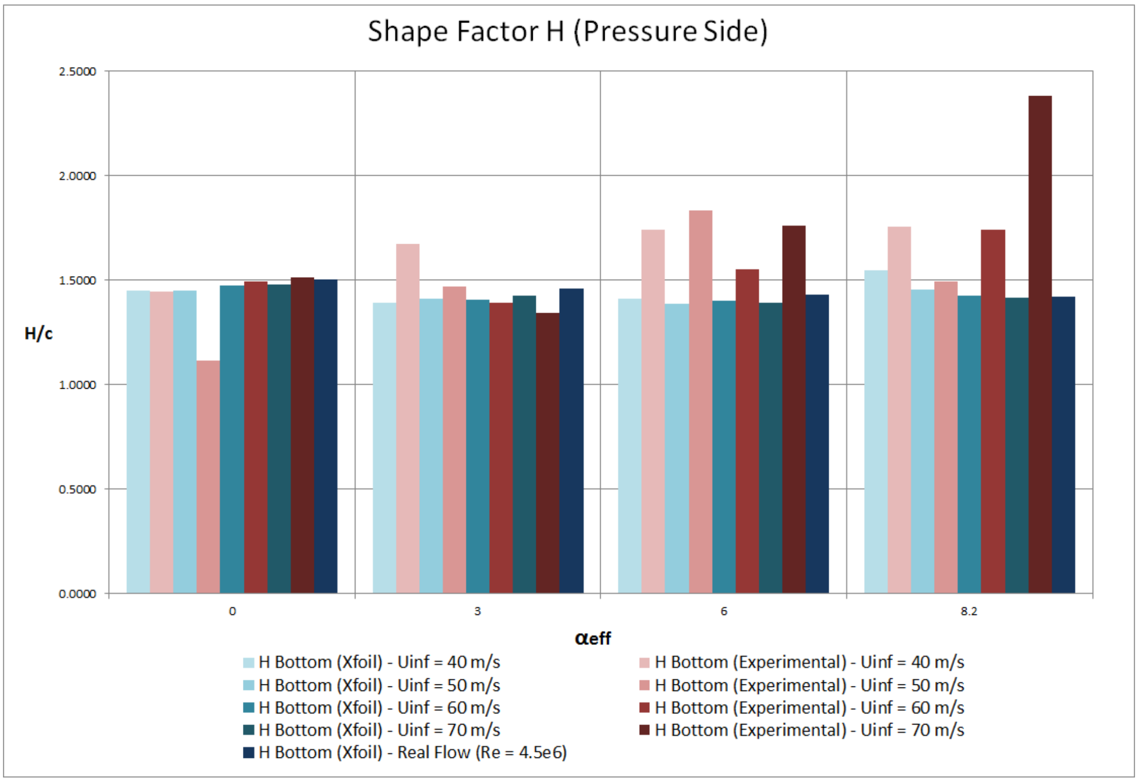

Figure 63 - Shape Factor on the Pressure Side

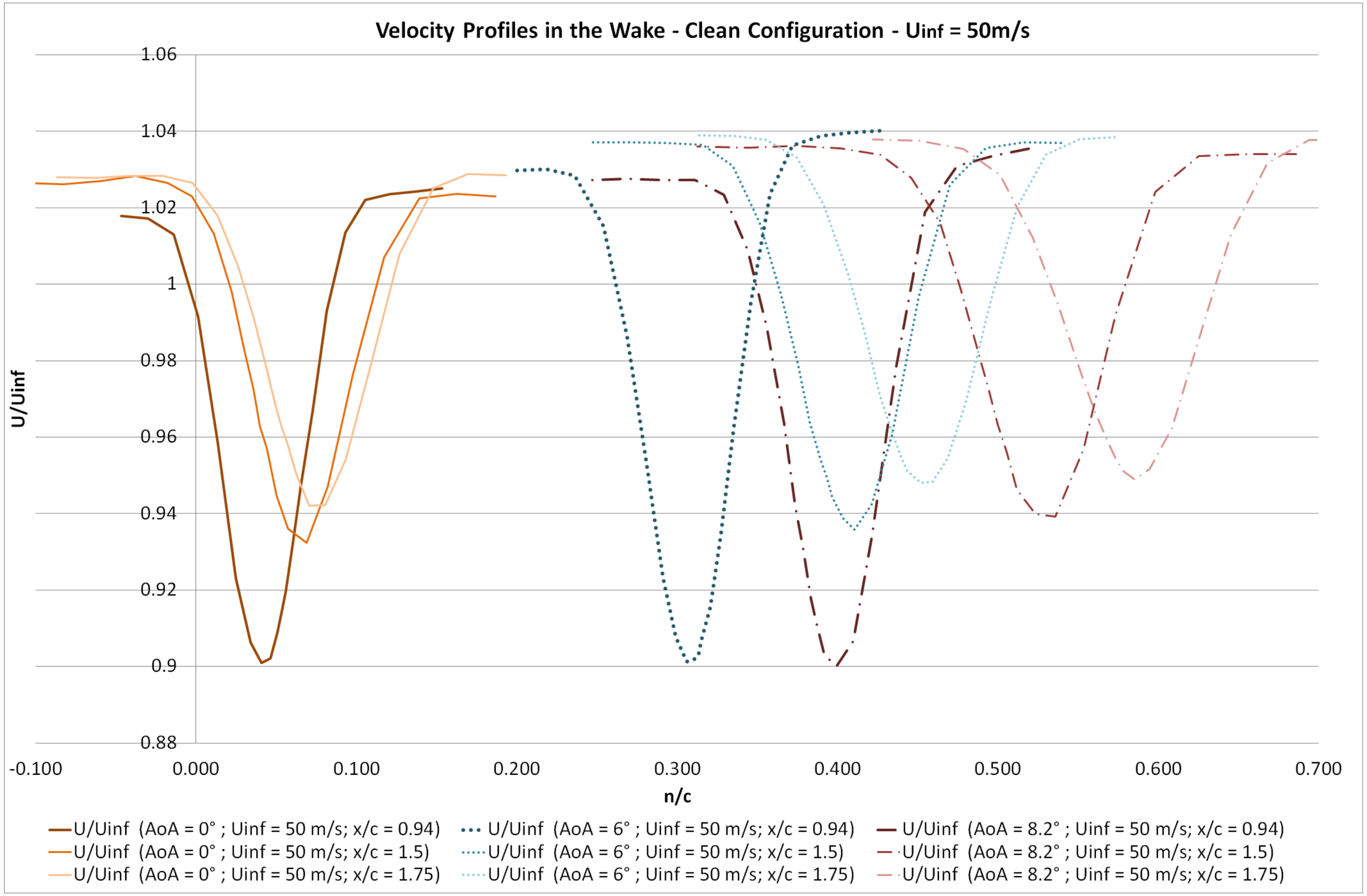

Figure 64 – Velocity Profiles in the Wake – Clean Configuration – U_∞ = 50 m/s

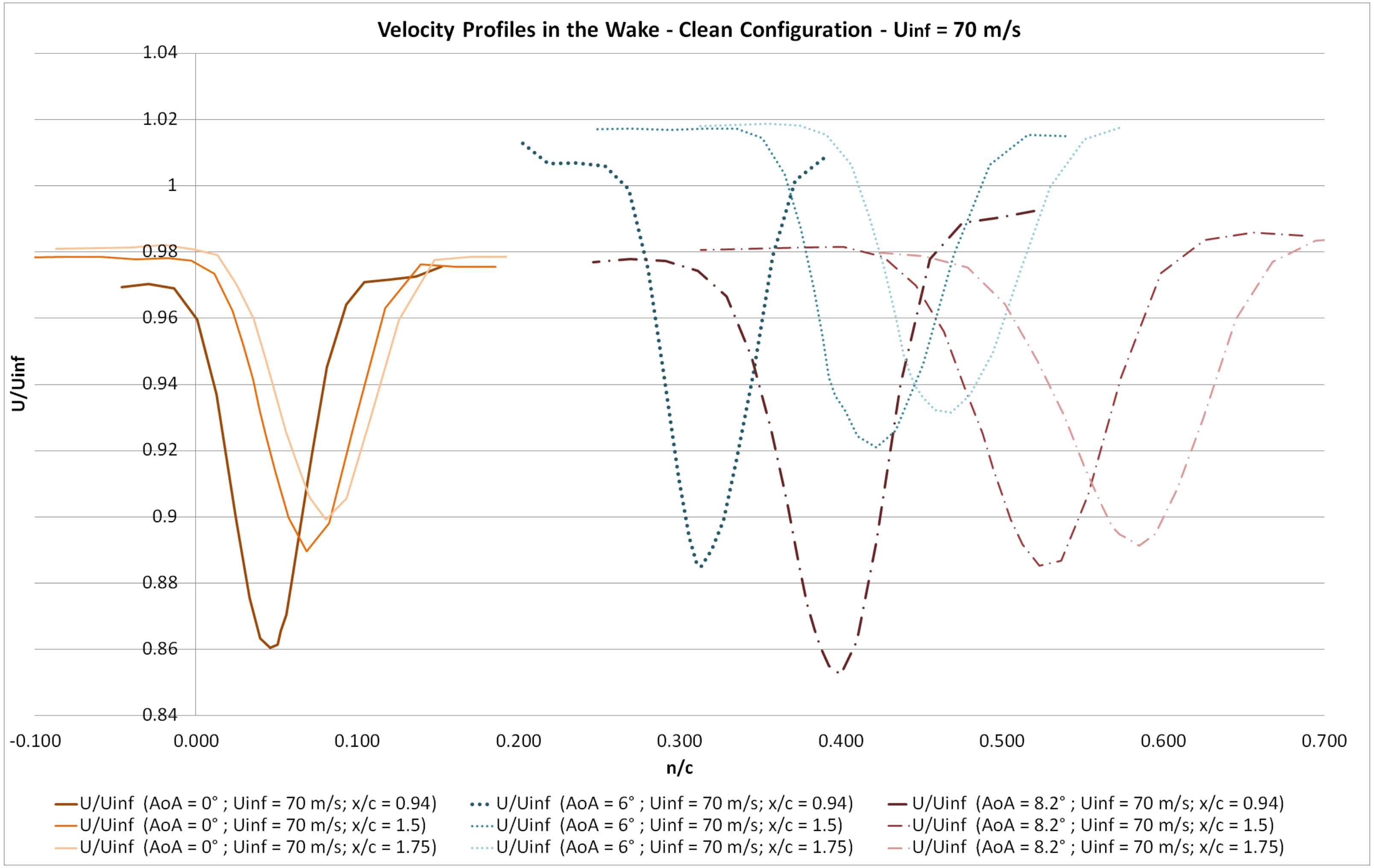

Figure 65 – Velocity Profiles in the Wake – Clean Configuration – U_∞ = 50 m/s

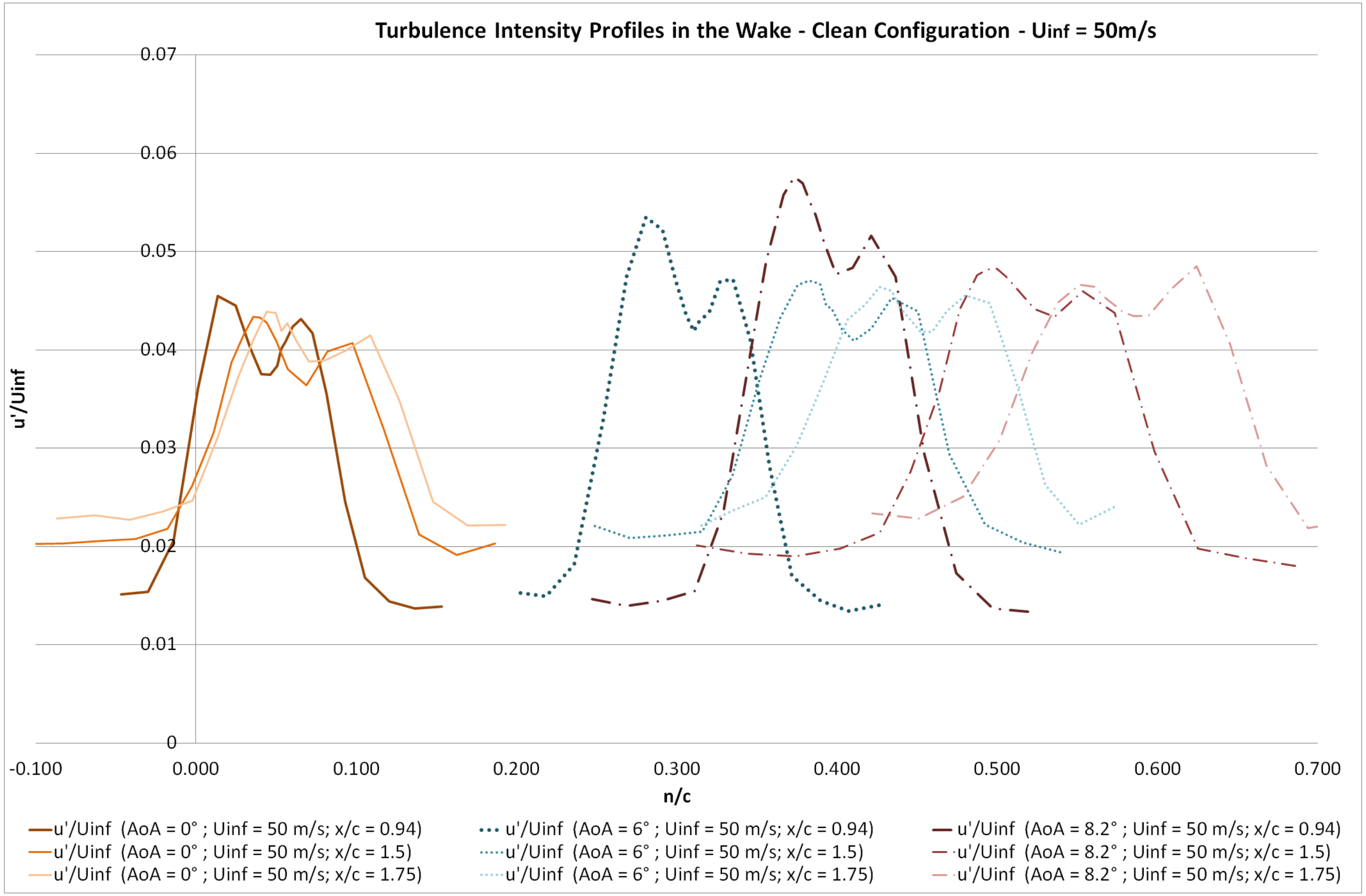

Figure 66 –Turbulence Intensity Profiles in the Wake – Clean Configuration – U_∞ = 50 m/s

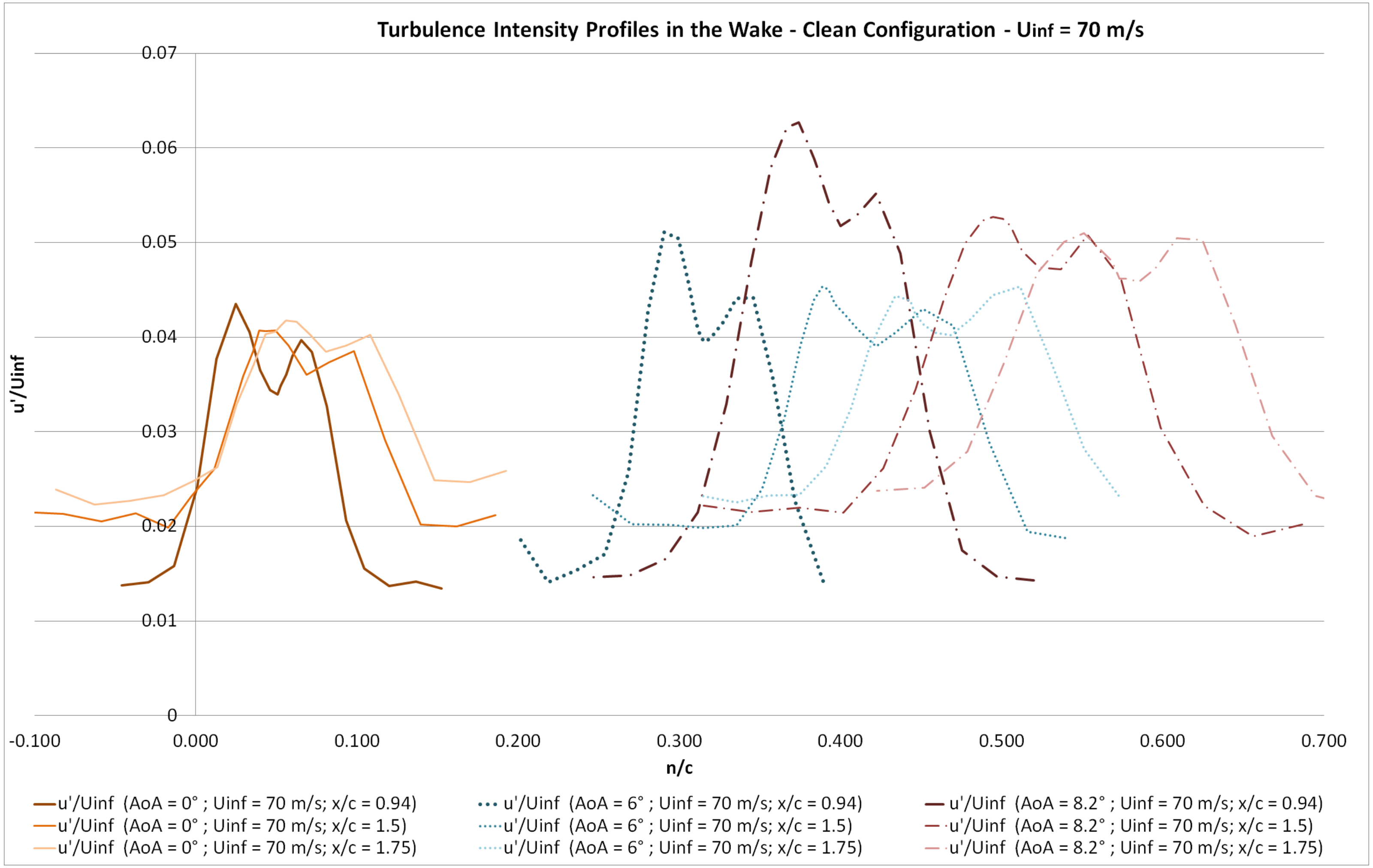

Figure 67 –Turbulence Intensity Profiles in the Wake – Clean Configuration – U_∞ = 70 m/s

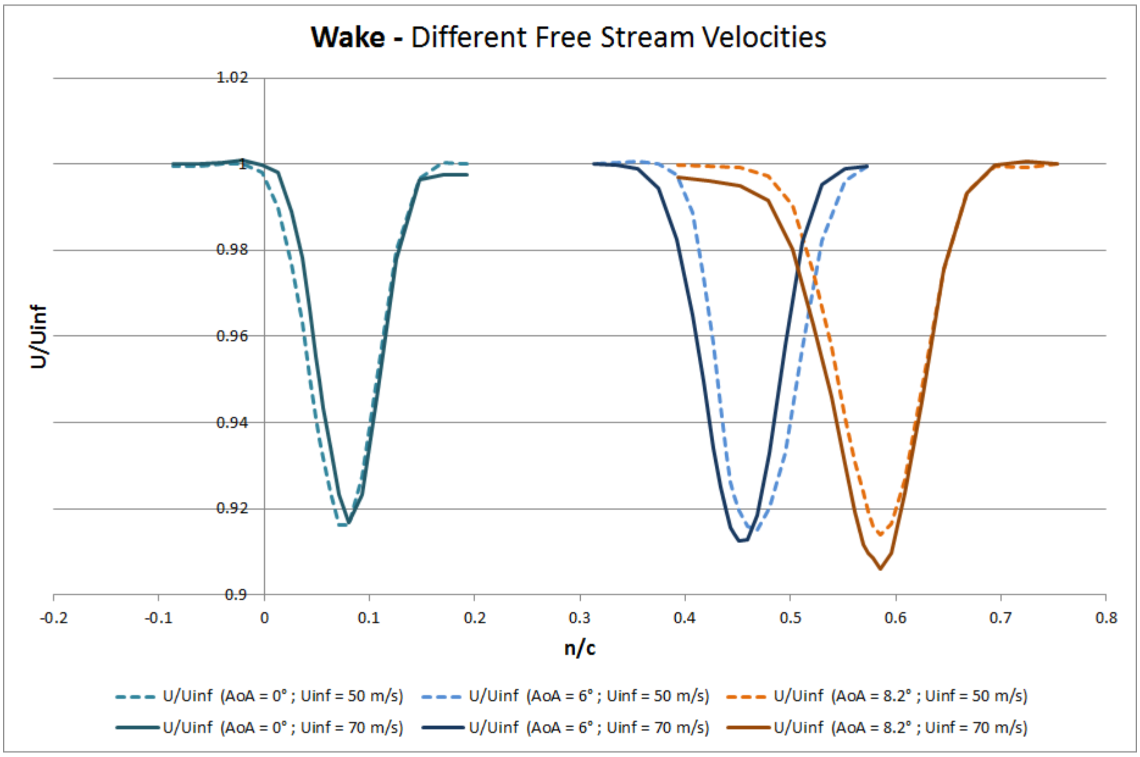

Figure 68 – Wake comparison between different U_∞

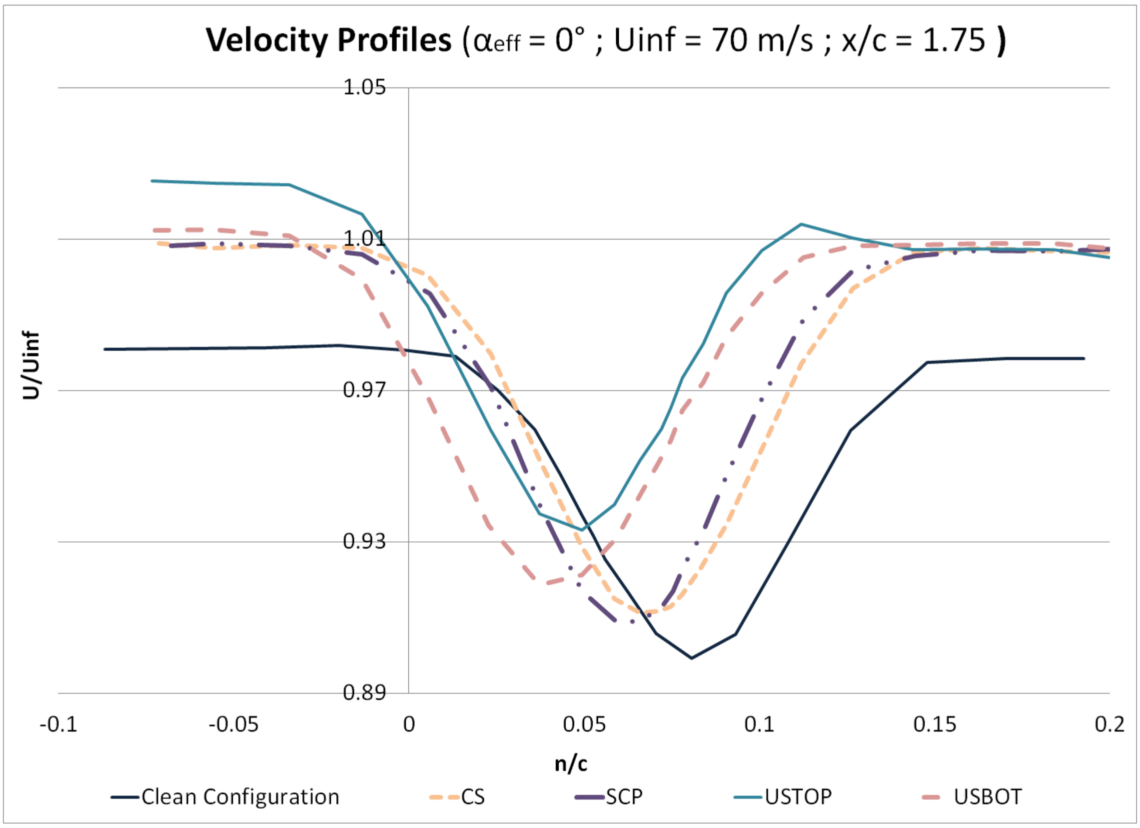

Figure 69 –Velocity Profiles of Different Configurations (αeff = 0°, U_∞ = 70 m/s, x/c = 1.75, z/c =0)

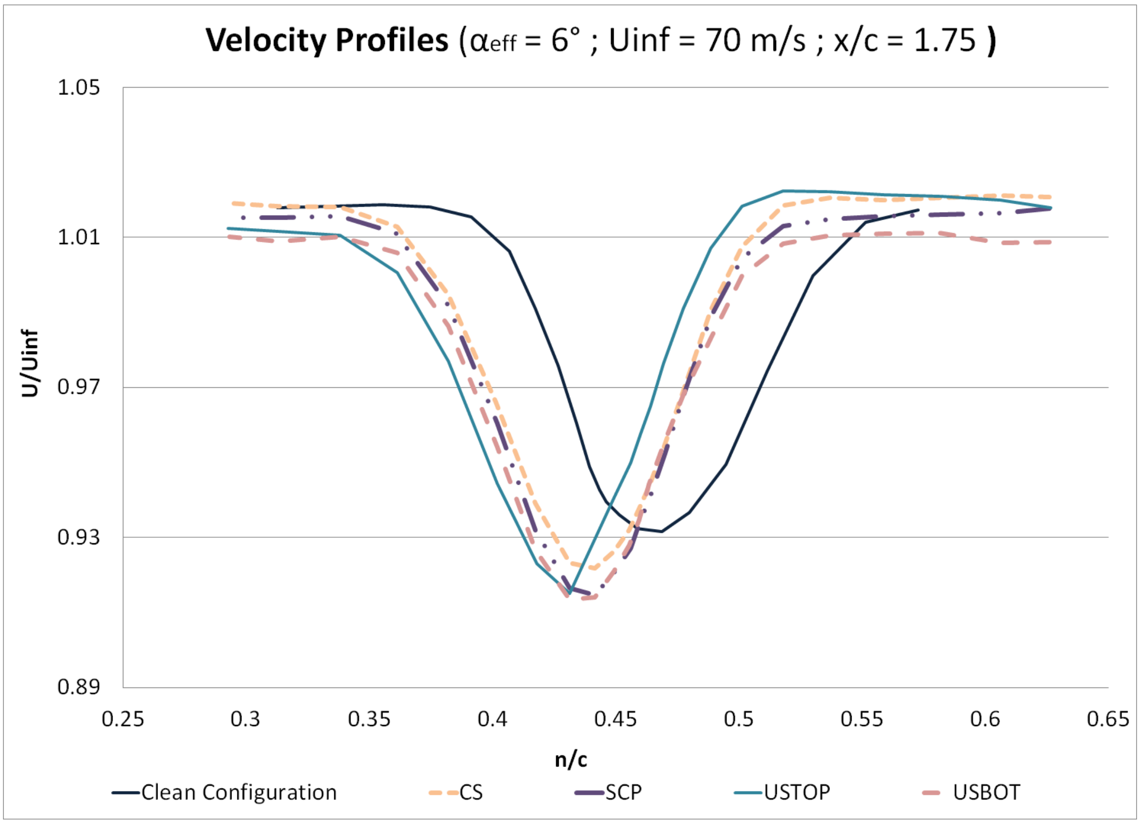

Figure 70 –Velocity Profiles of Different Configurations (αeff = 6°, U_∞ = 70 m/s, x/c = 1.75, z/c =0)

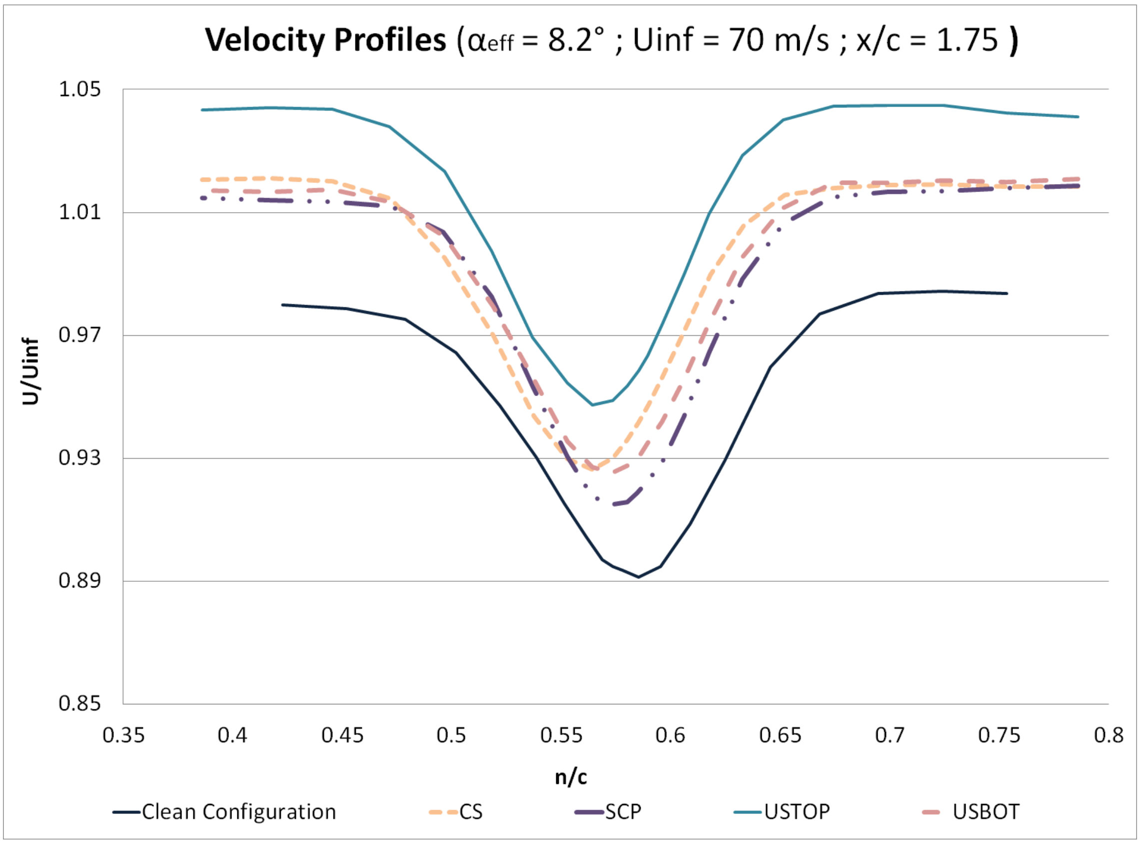

Figure 71 –Velocity Profiles of Different Configurations (αeff = 8.2°, U_∞ = 70 m/s, x/c = 1.75, z/c =0)

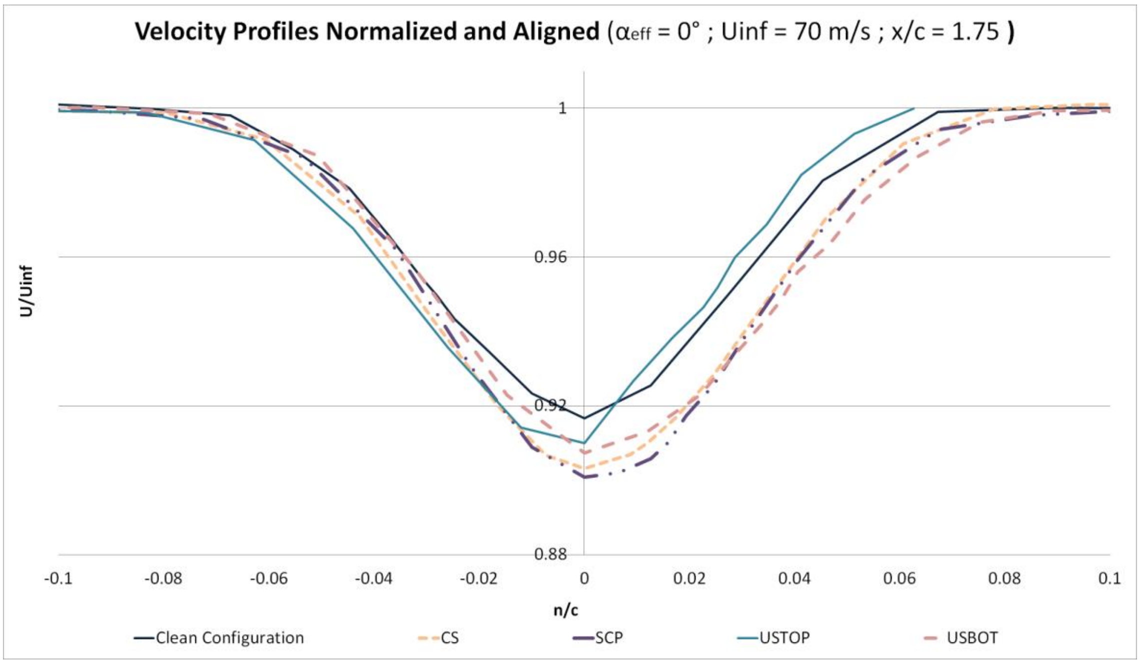

Figure 72 –Velocity Profiles of Different Configurations Normalized and Aligned (αeff = 0°, U_∞ = 70 m/s, x/c = 1.75, z/c =0)

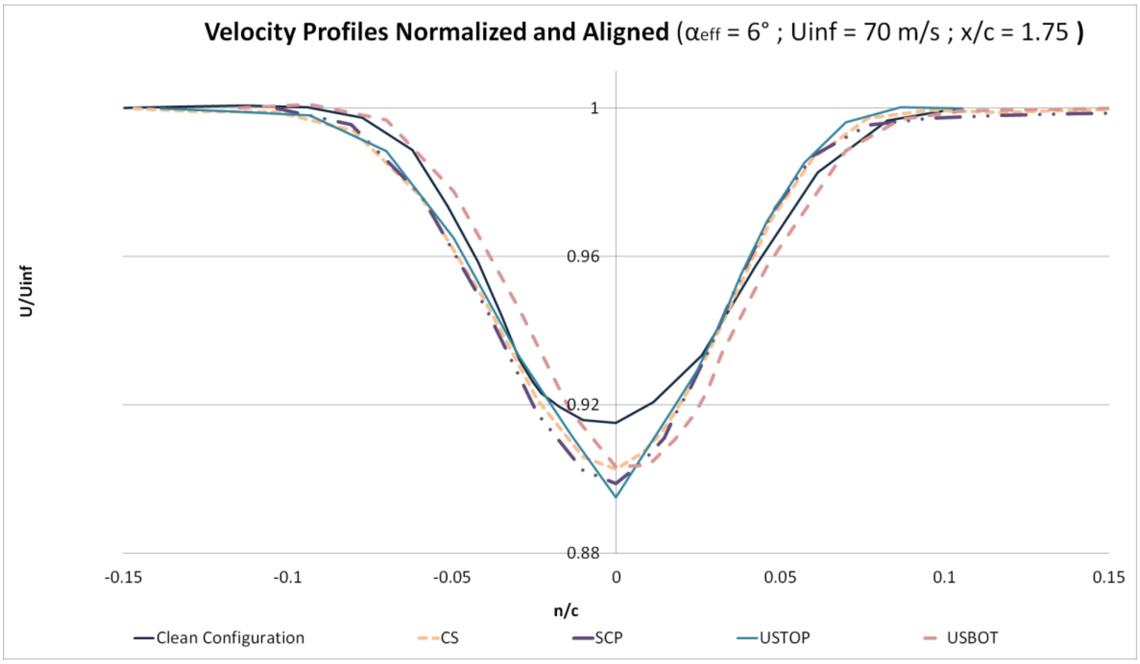

Figure 73 –Velocity Profiles of Different Configurations Normalized and Aligned (αeff =6°, U_∞ = 70 m/s, x/c = 1.75, z/c =0)

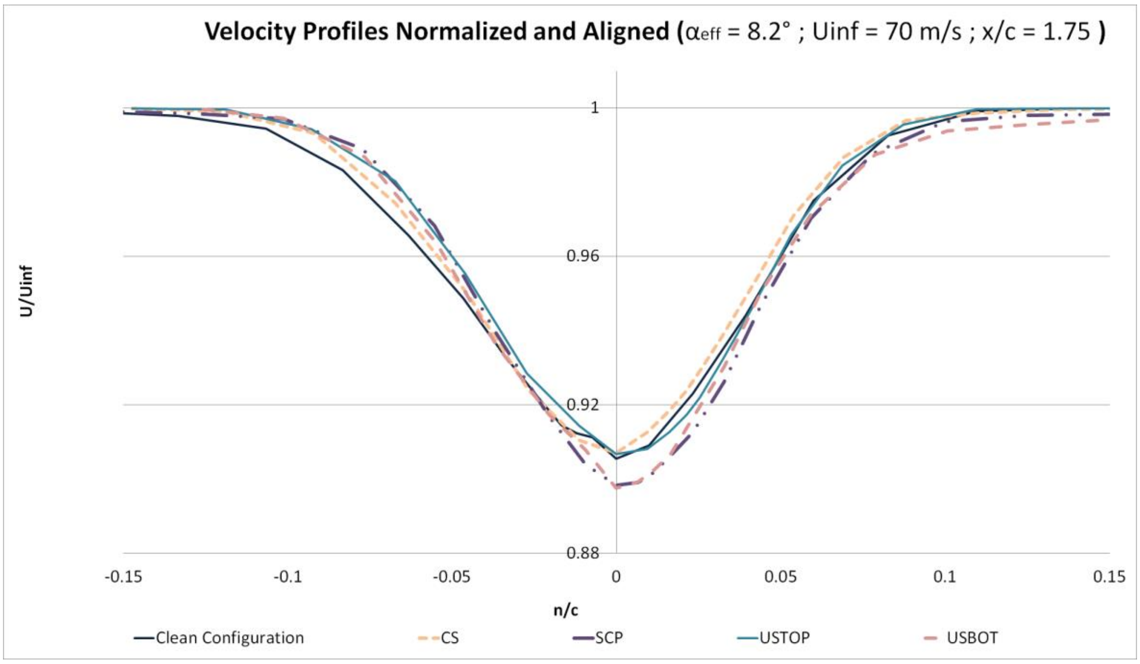

Figure 74 –Velocity Profiles of Different Configurations Normalized and Aligned (αeff = 8.2°, U_∞ = 70 m/s, x/c = 1.75, z/c =0)

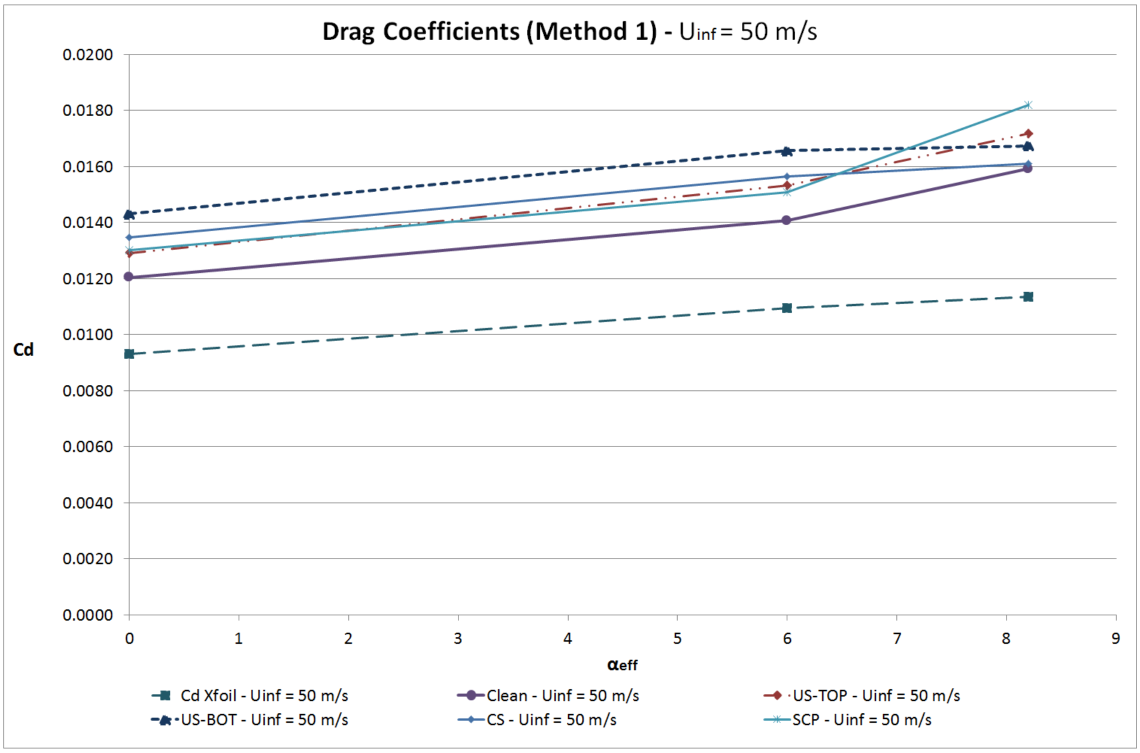

Figure 75 - Drag Coefficient (Method 1) - U_∞ = 50m/s

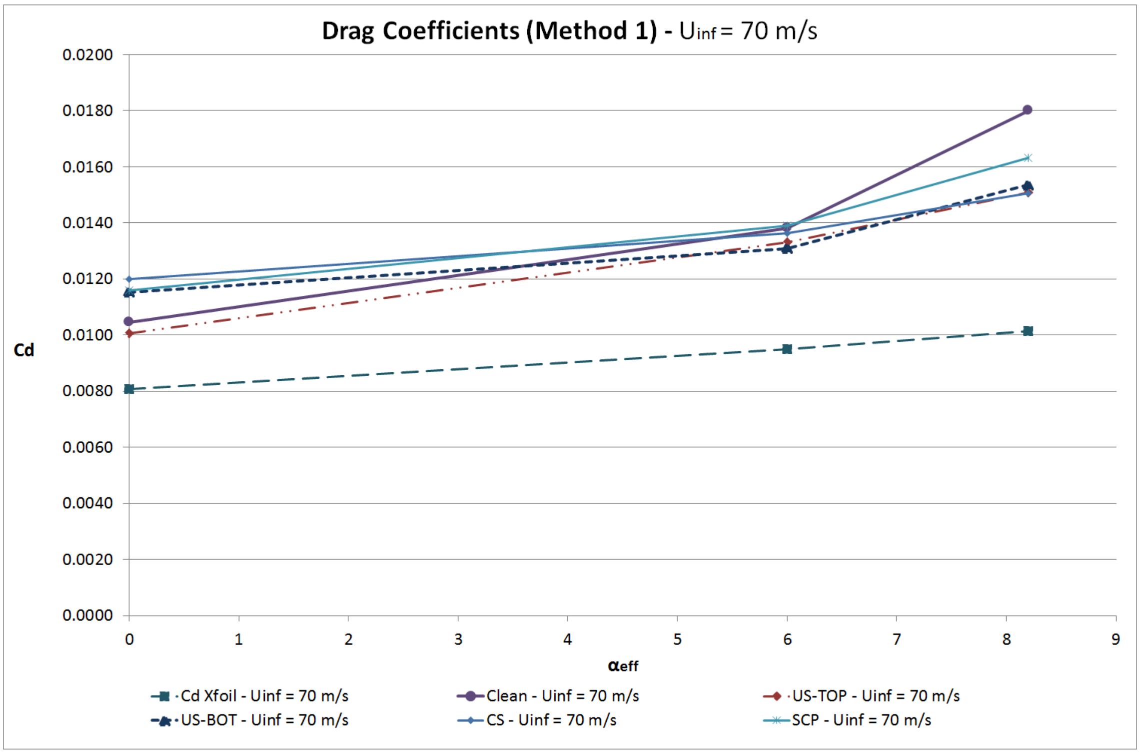

Figure 76 - Drag Coefficient (Method 1) - U_∞ = 70m/s

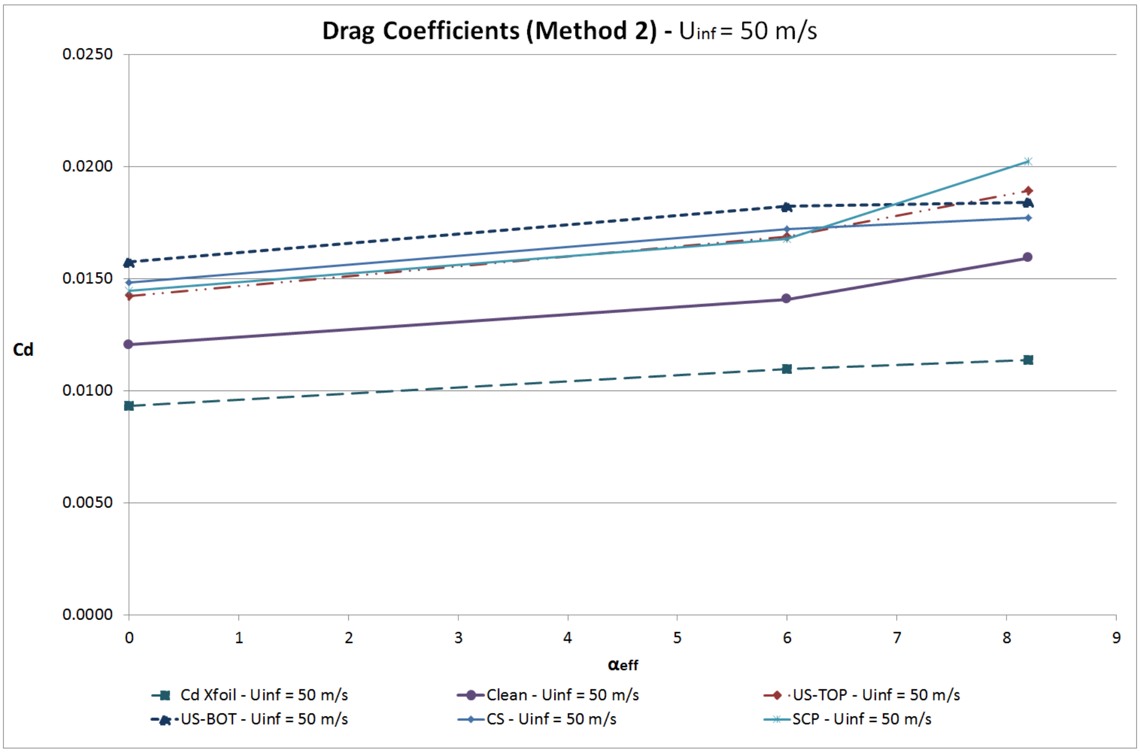

Figure 77 - Drag Coefficient (Method 2) - U_∞ = 50m/s

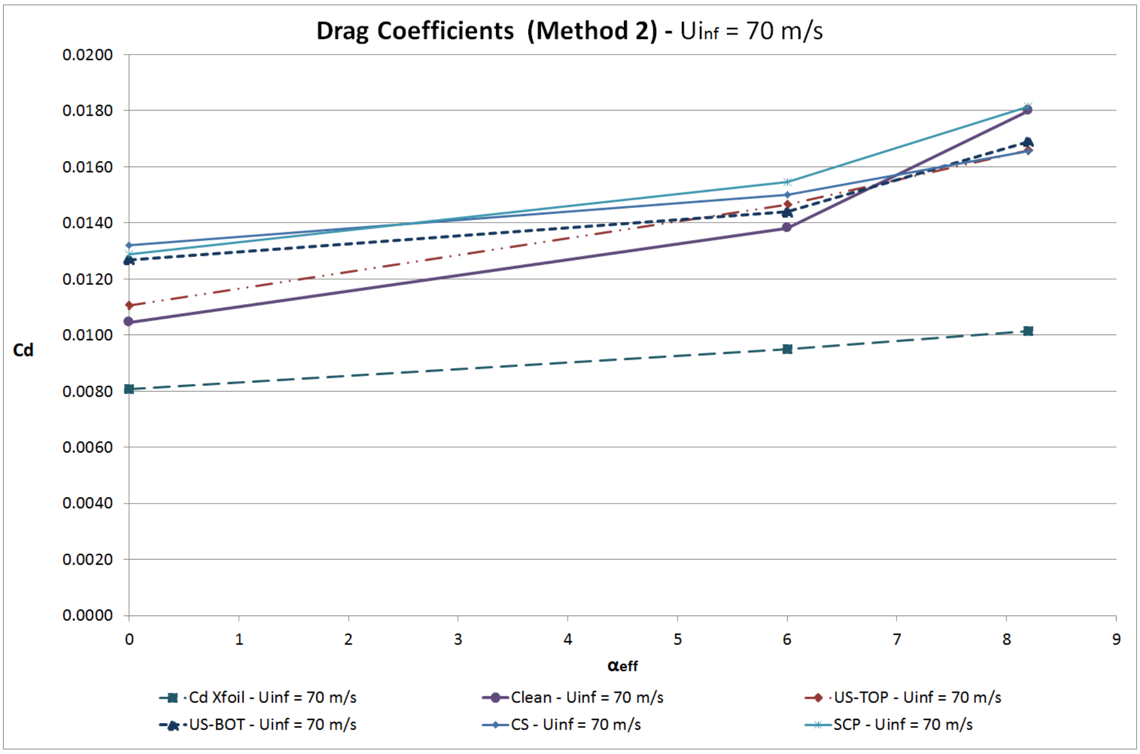

Figure 78 - Drag Coefficient (Method 2) - U_∞ = 70m/s

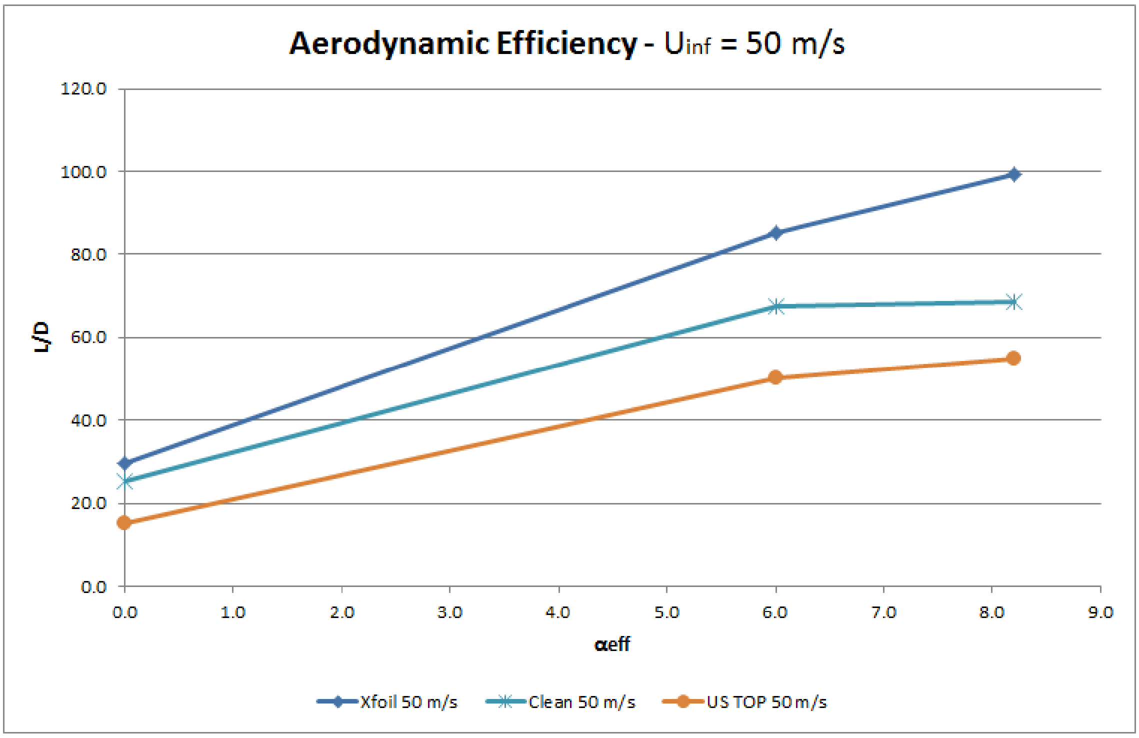

Figure 79 – Aerodynamic Efficiency (L/D) – U_∞ = 50 m/s

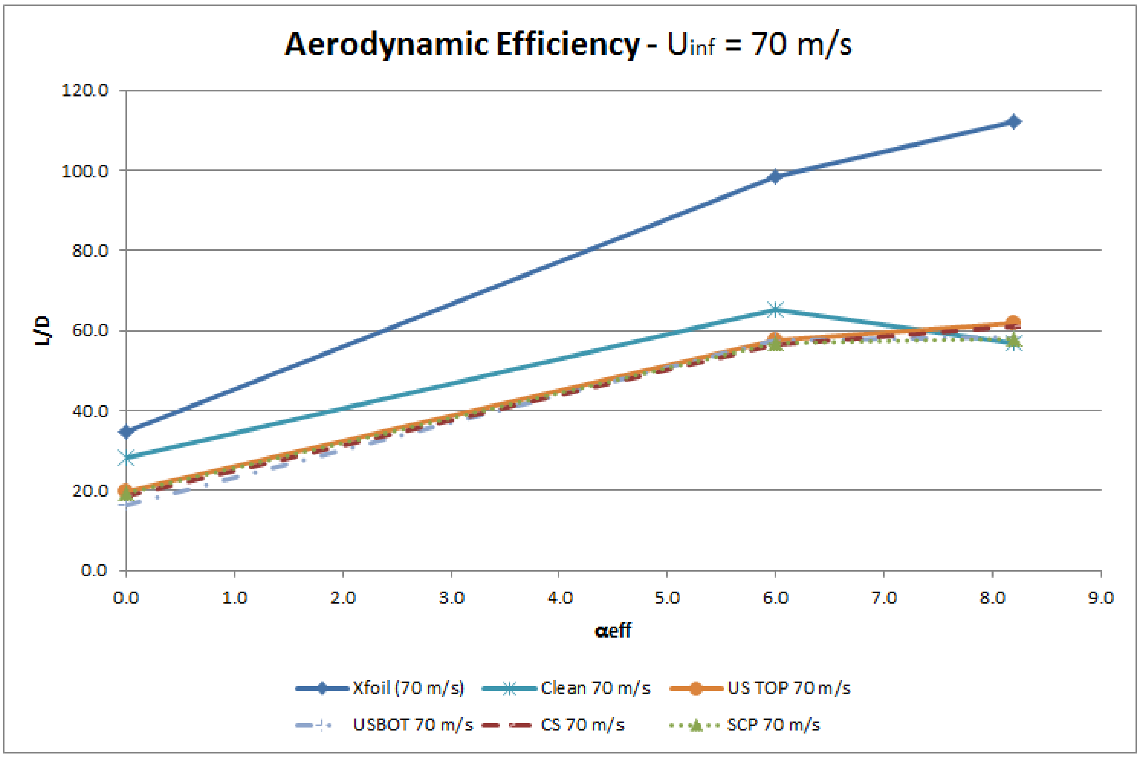

Figure 80– Aerodynamic Efficiency (L/D) – U_∞ = 70 m/s

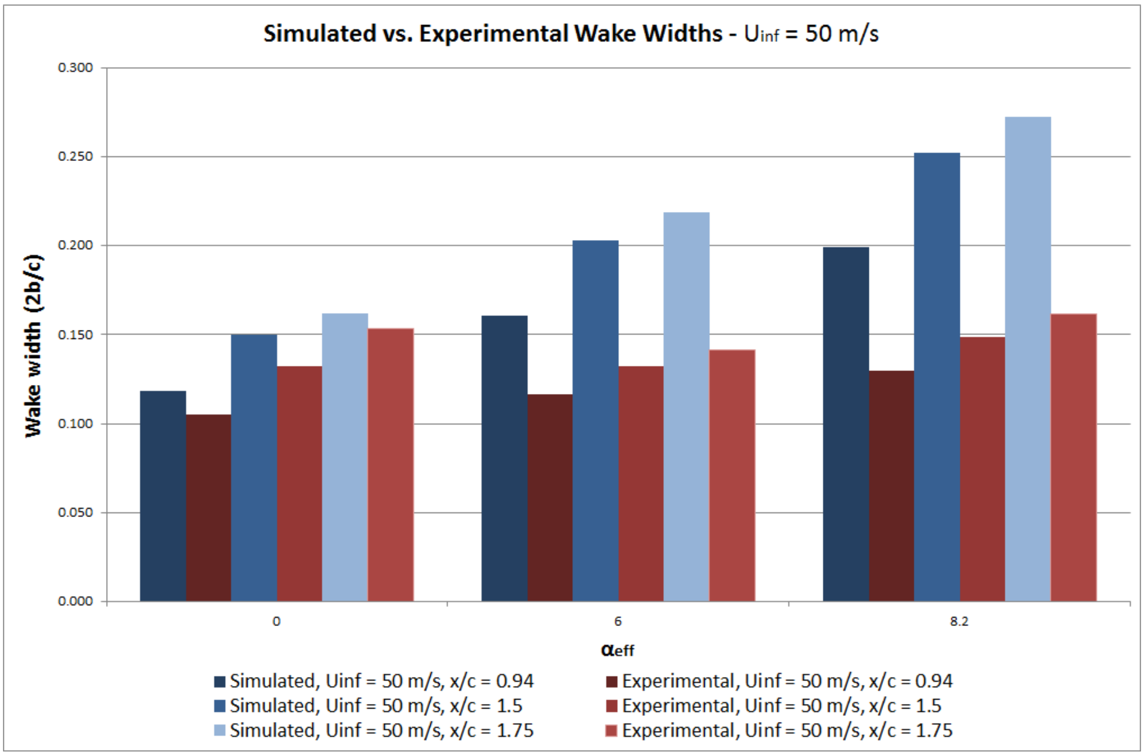

Figure 81- Simulated vs. Experimental Wake Widths – U_∞ = 50 m/s

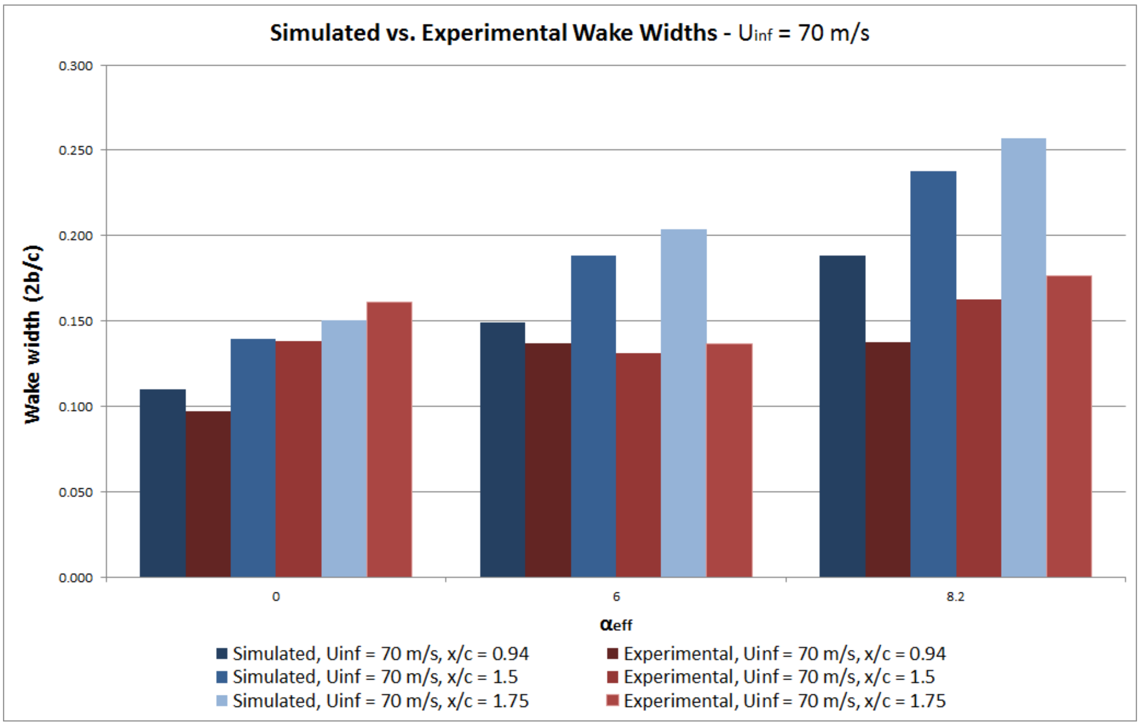

Figure 82 - Simulated vs. Experimental Wake Widths – U_∞ = 70 m/s

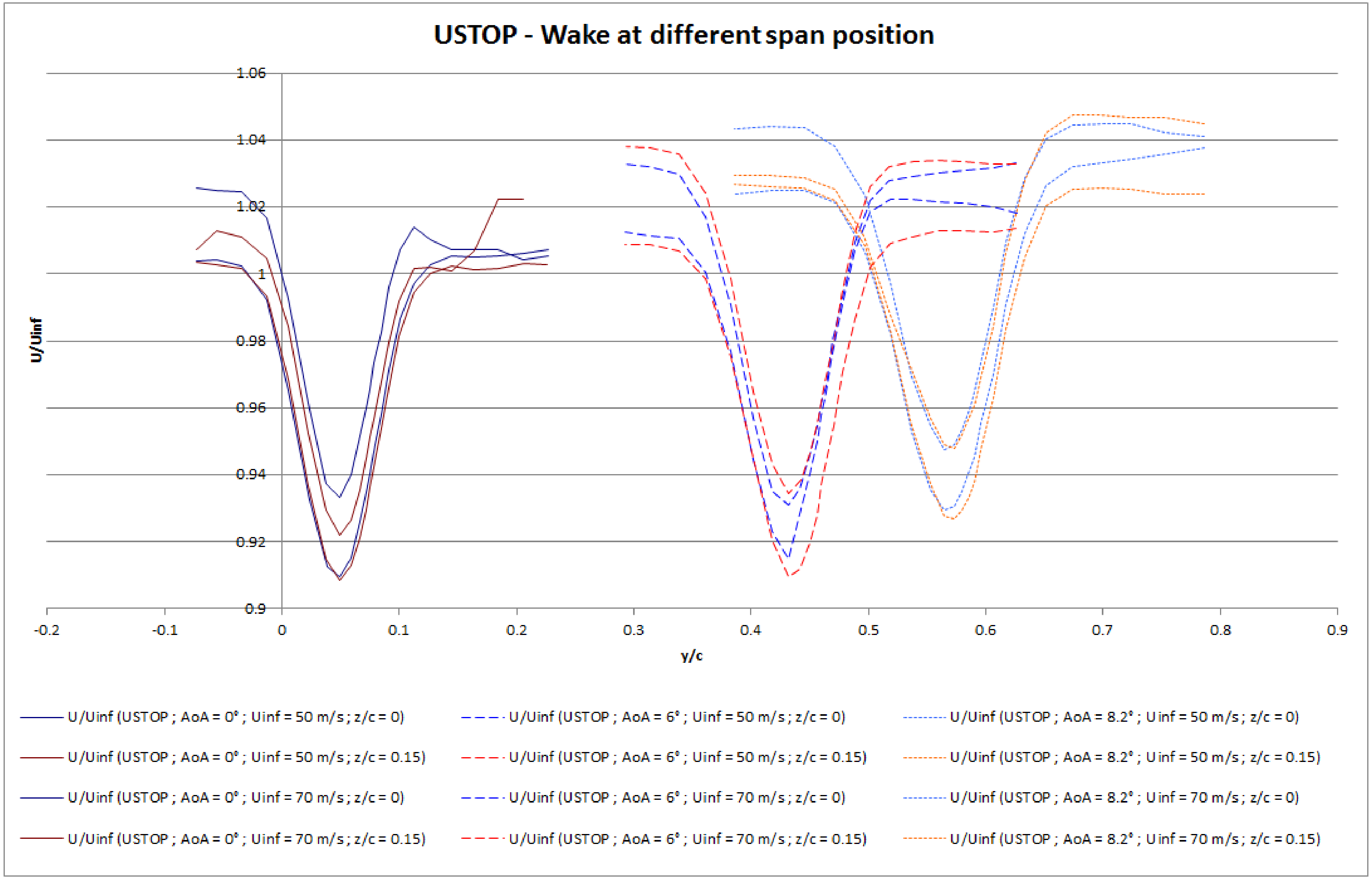

USTOP - Wake at different span position
U/Uinf
y/c
1.06
1.04
1.02
1
0.98
0.96
0.94
0.92
0.9
-0.2
-0.1
0
0.1
0.2
0.3
0.4
0.5
0.6
0.7
0.8
0.9
U/Uinf (USTOP ; AoA = 0° ; Uinf = 50 m/s ; z/c = 0)
U/Uinf (USTOP ; AoA = 0° ; Uinf = 50 m/s ; z/c = 0.15)
U/Uinf (USTOP ; AoA = 0° ; Uinf = 70 m/s ; z/c = 0)
U/Uinf (USTOP ; AoA = 0° ; Uinf = 70 m/s ; z/c = 0.15)
U/Uinf (USTOP ; AoA = 6° ; Uinf = 50 m/s ; z/c = 0)
U/Uinf (USTOP ; AoA = 6° ; Uinf = 50 m/s ; z/c = 0.15)
U/Uinf (USTOP ; AoA = 6° ; Uinf = 70 m/s ; z/c = 0)
U/Uinf (USTOP ; AoA = 6° ; Uinf = 70 m/s ; z/c = 0.15)
U/Uinf (USTOP ; AoA = 8.2° ; Uinf = 50 m/s ; z/c = 0)
U/Uinf (USTOP ; AoA = 8.2° ; Uinf = 50 m/s ; z/c = 0.15)
U/Uinf (USTOP ; AoA = 8.2° ; Uinf = 70 m/s ; z/c = 0)
U/Uinf (USTOP ; AoA = 8.2° ; Uinf = 70 m/s ; z/c = 0.15)

Figure 83 – Wake at different span positions (US-TOP)

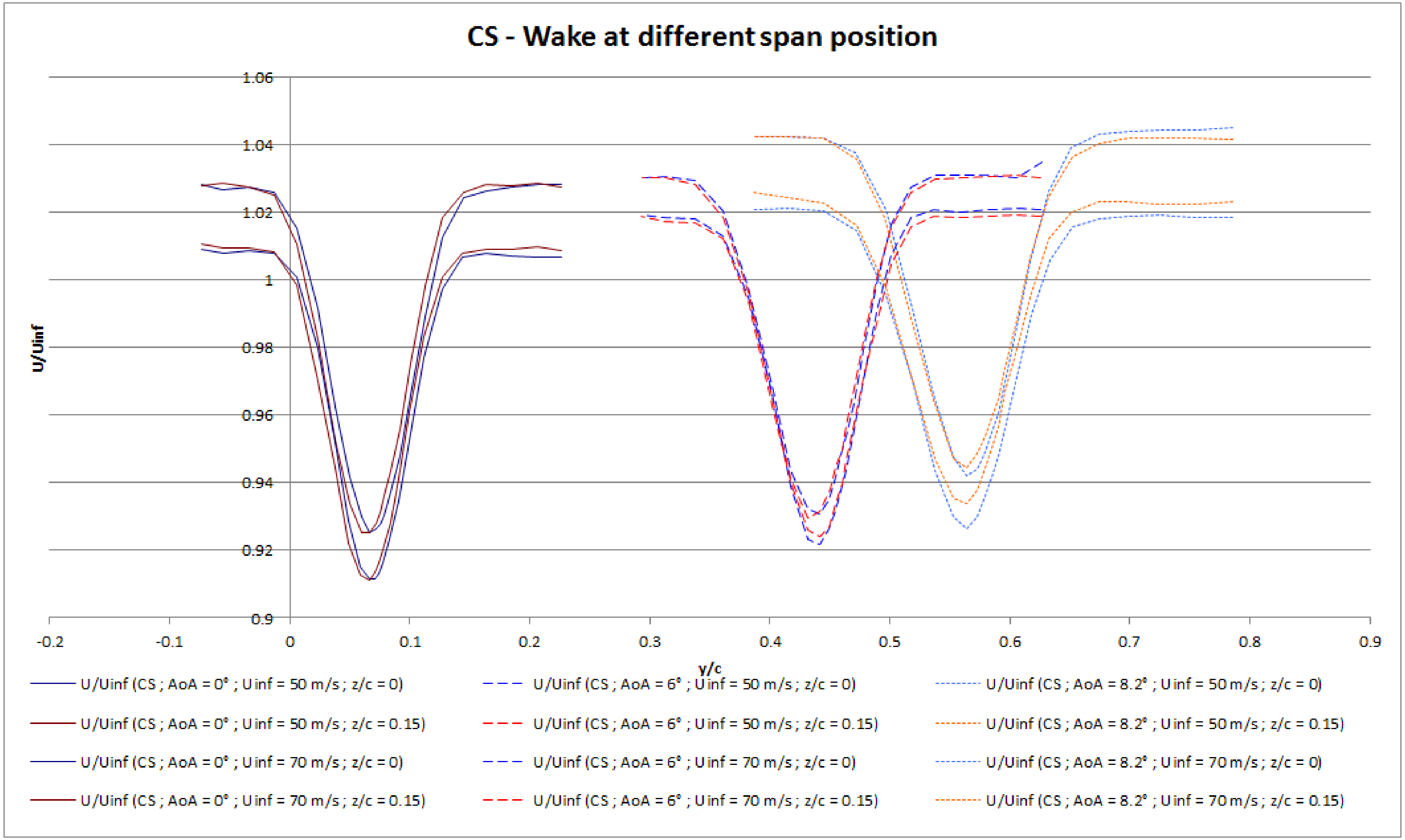

Figure 84 - Wake at different span positions (CS)

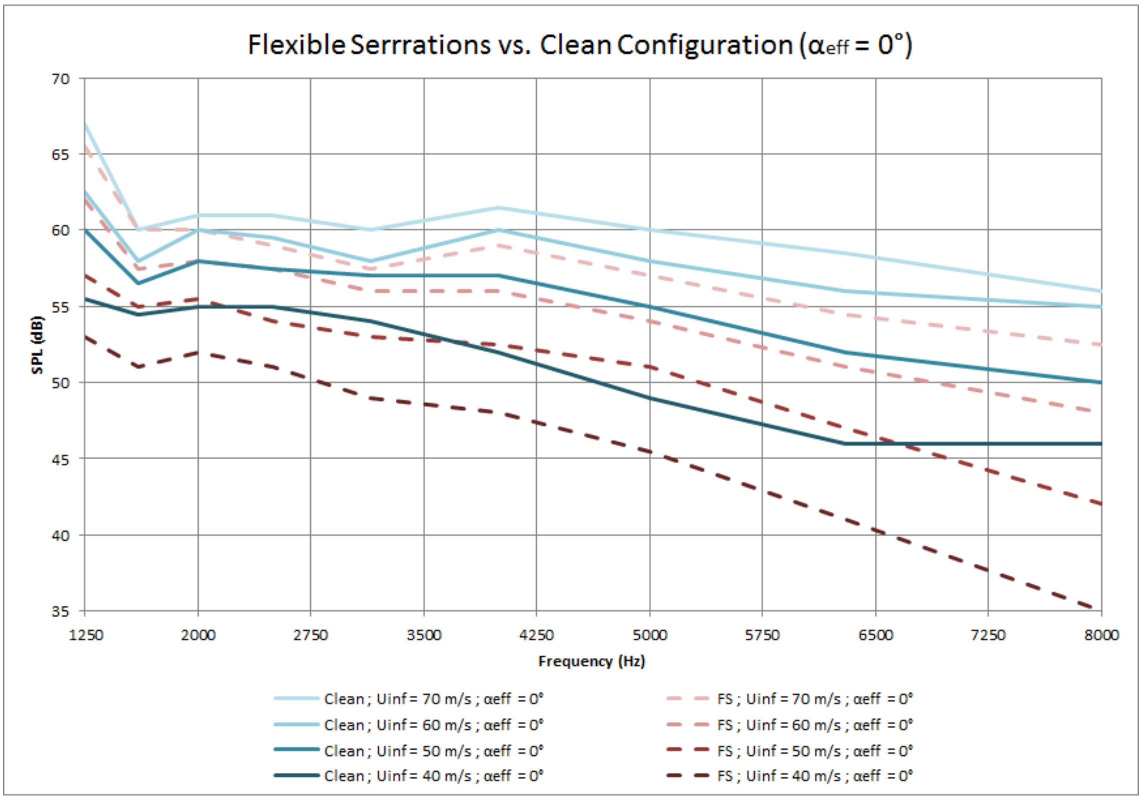

Figure 85 – Flexible Serration vs. Clean Configuration (α_{eff} = 0°)

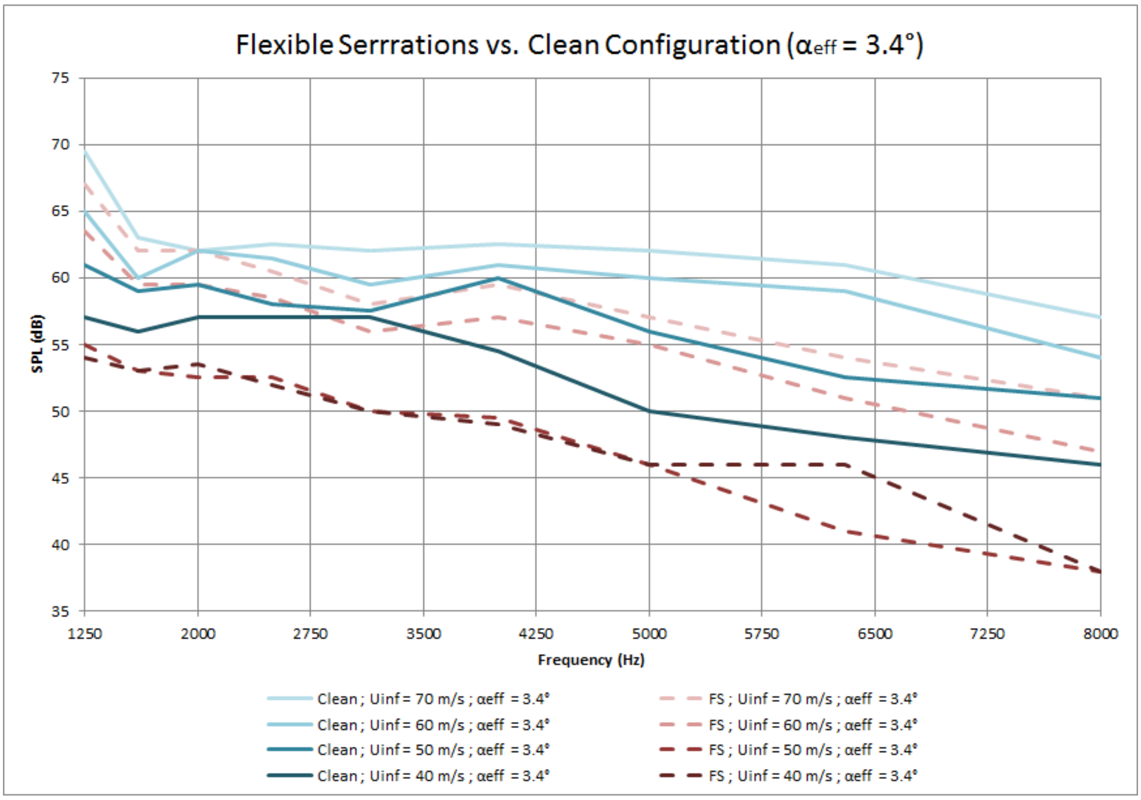

Figure 86 – Flexible Serration vs. Clean Configuration (α_{eff} = 3.4°)

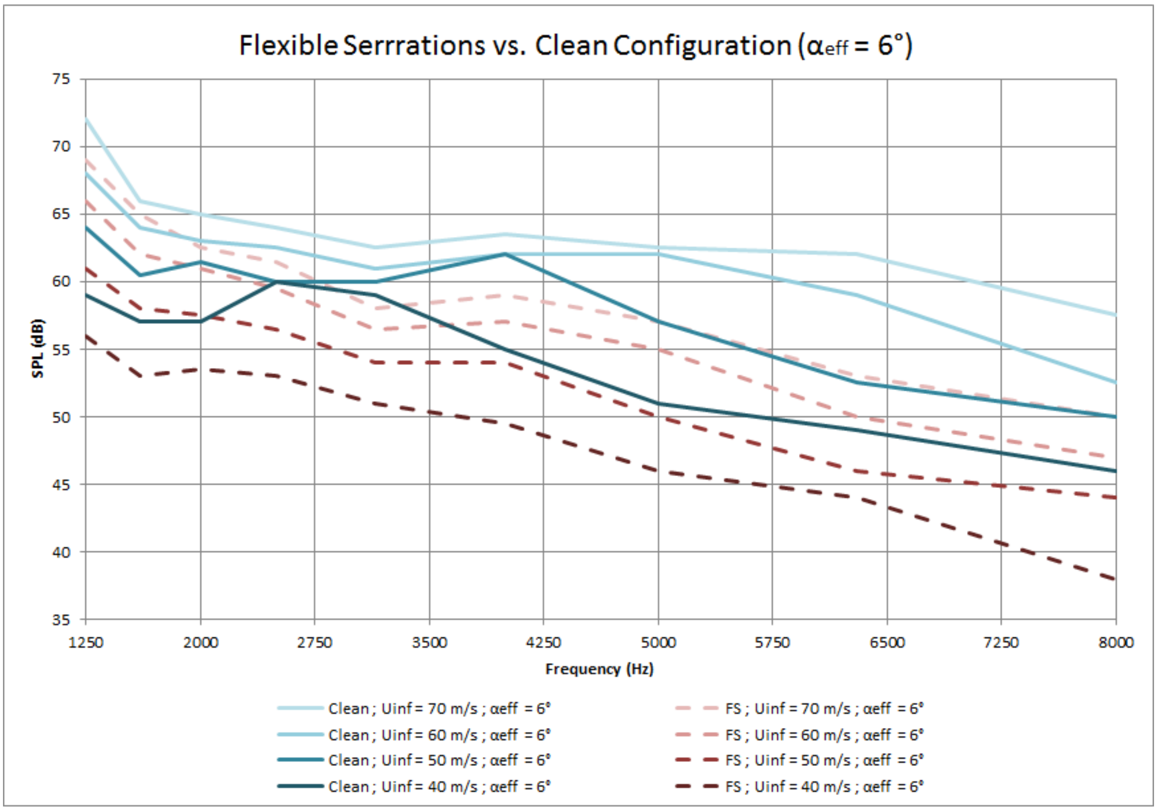

Figure 87 – Flexible Serration vs. Clean Configuration (α_{eff} = 6°)

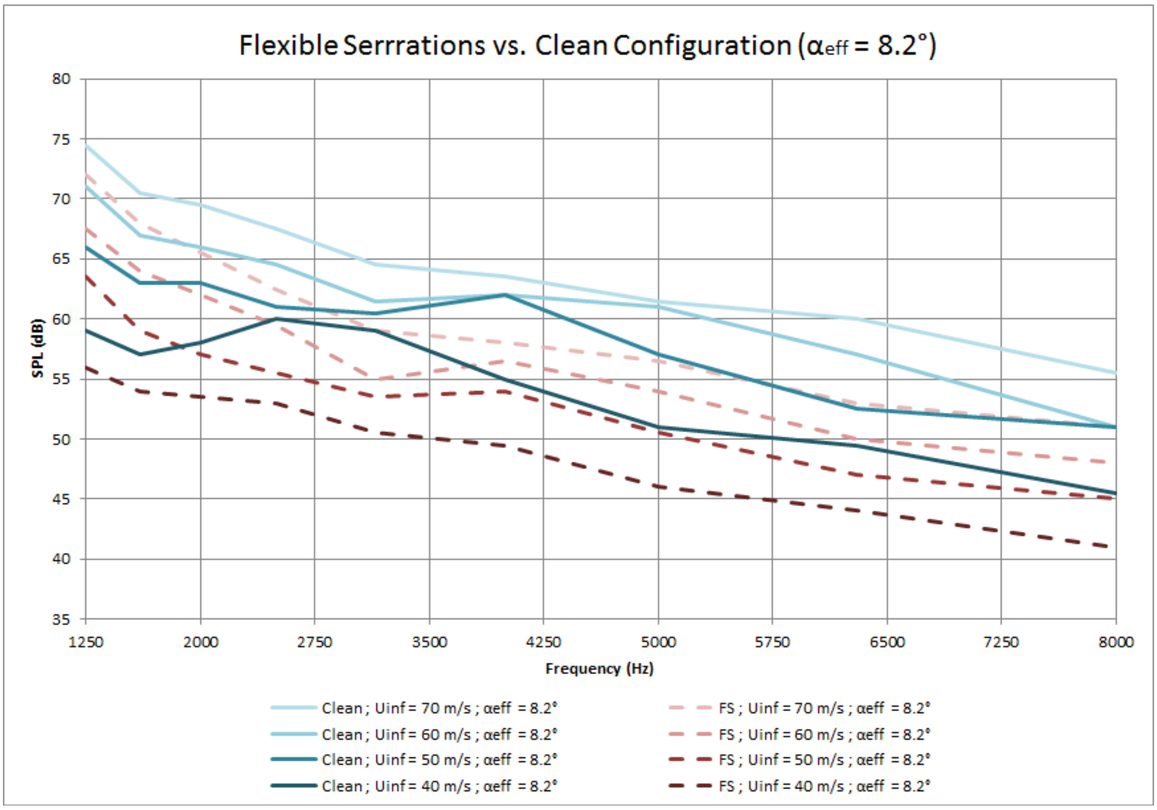

Figure 88 – Flexible Serration vs. Clean Configuration (α_{eff} = 8.2°)

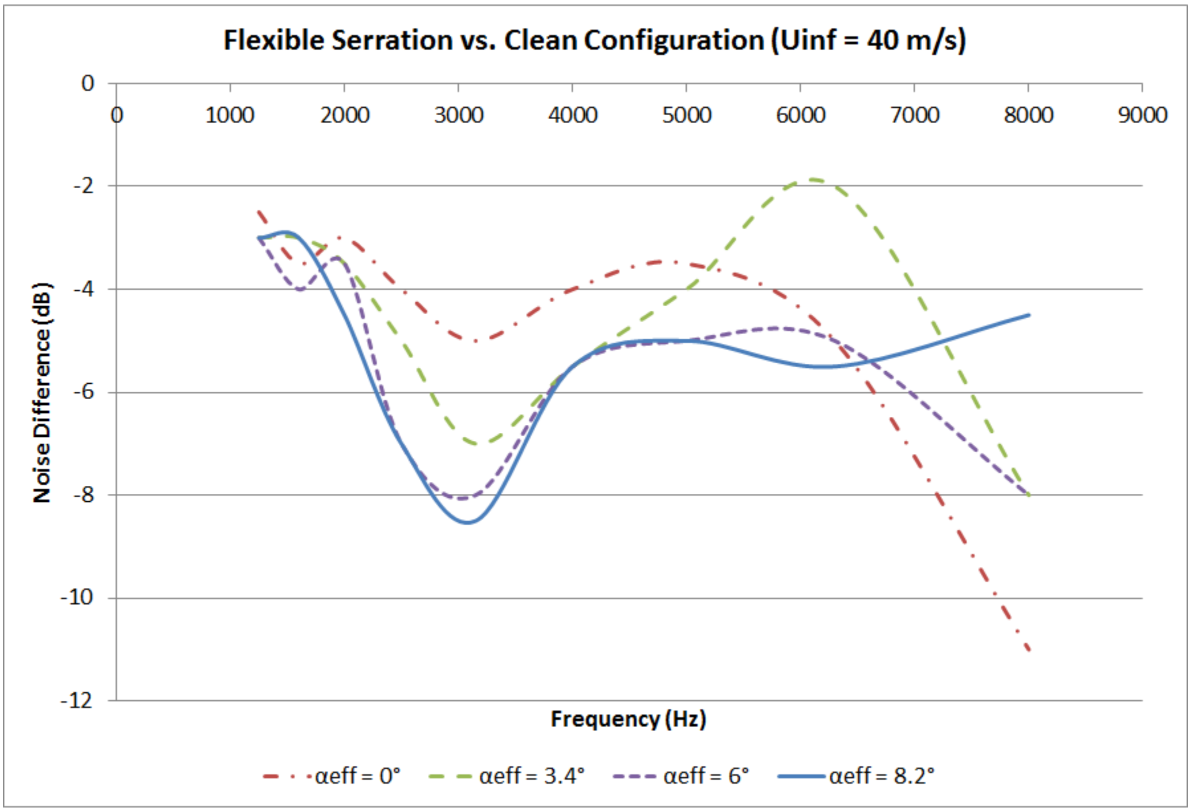

Figure 89 – Flexible Serration vs. Clean Configuration (U_∞ = 40m/s)

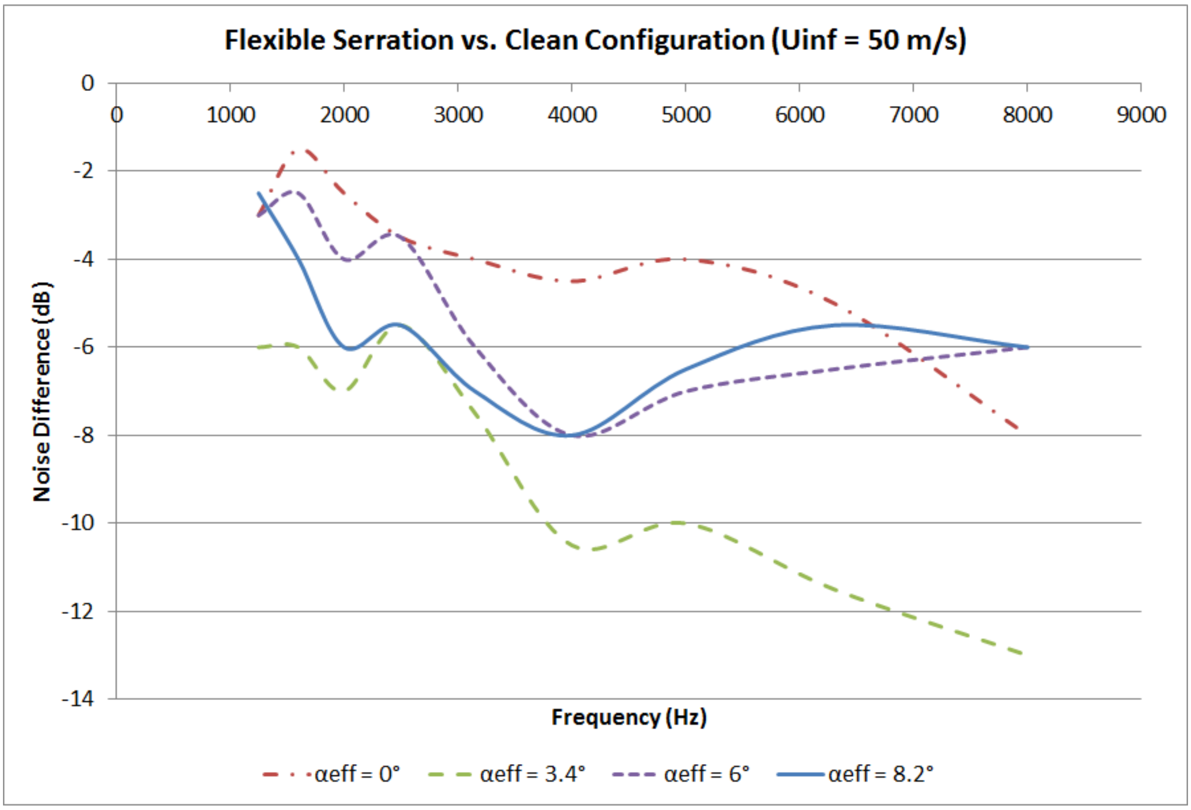

Figure 90 – Flexible Serration vs. Clean Configuration (U_∞ = 50m/s)

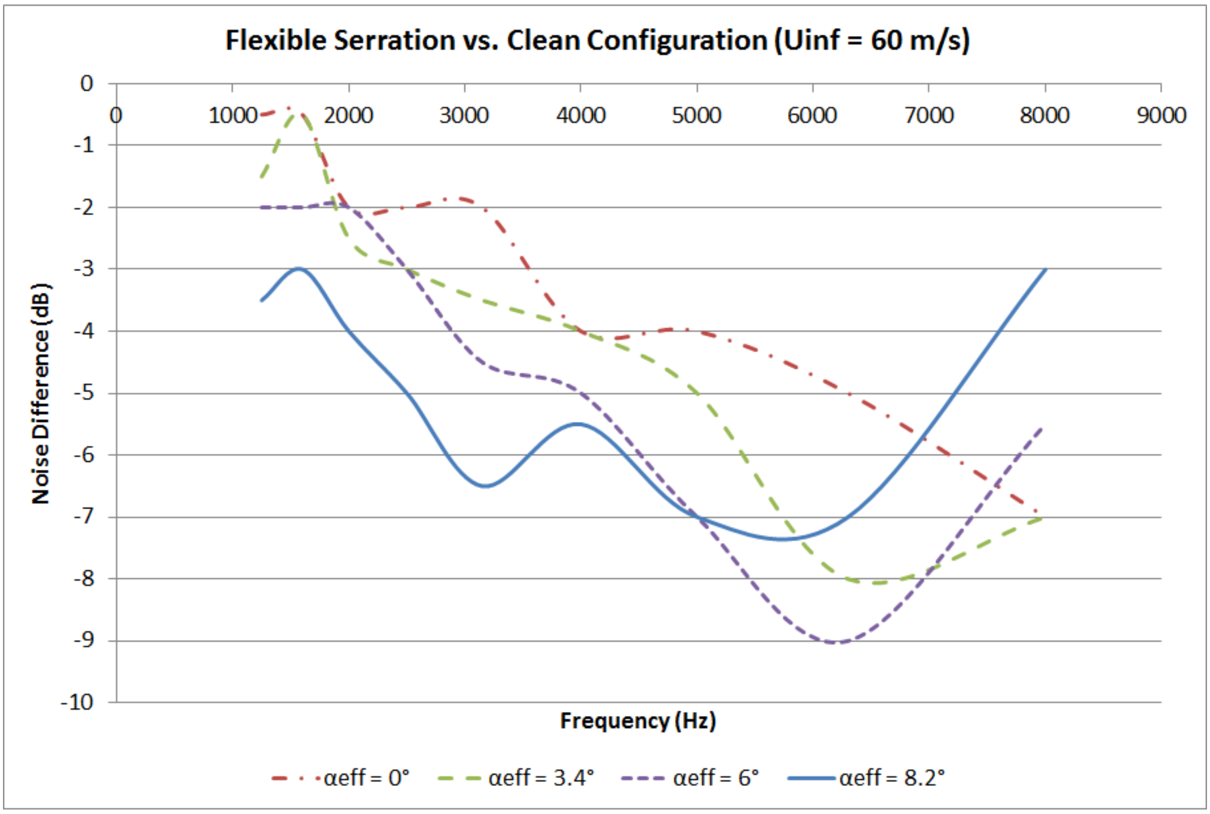

Figure 91 – Flexible Serration vs. Clean Configuration (U_∞ = 60m/s)

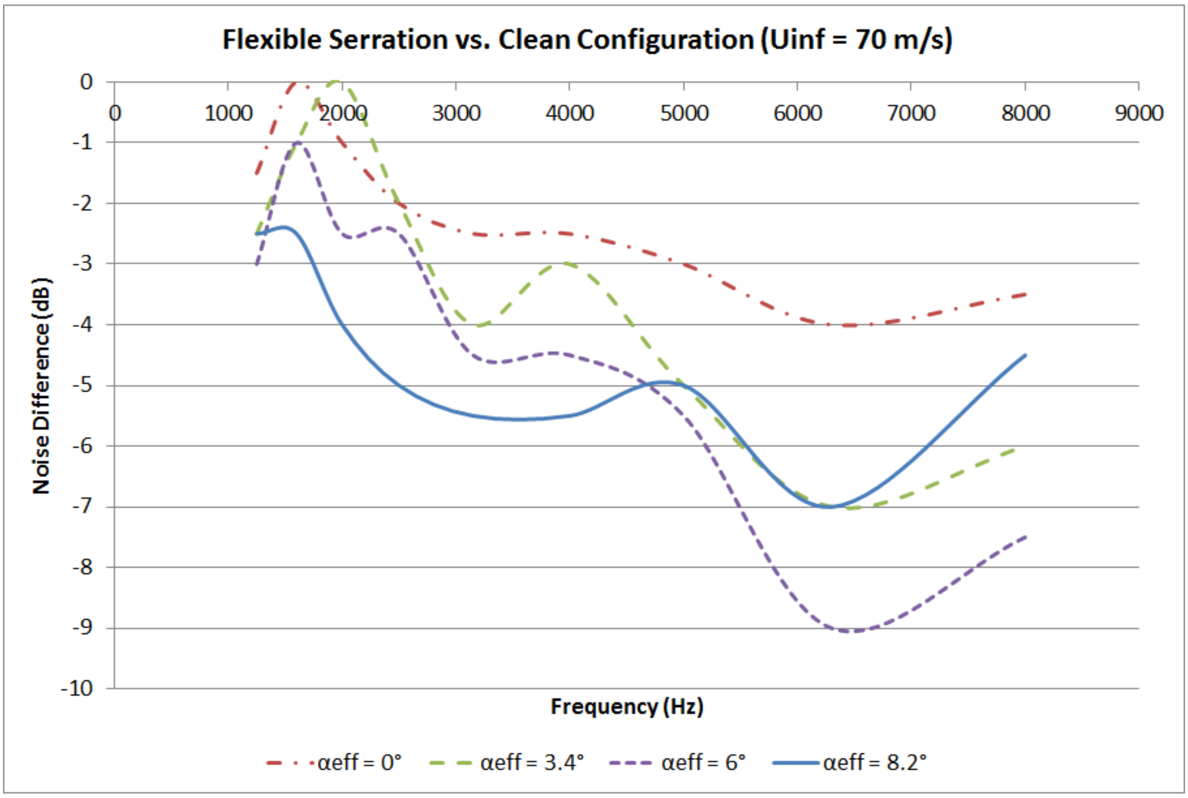

Figure 92 – Flexible Serration vs. Clean Configuration (U_∞ = 70m/s)

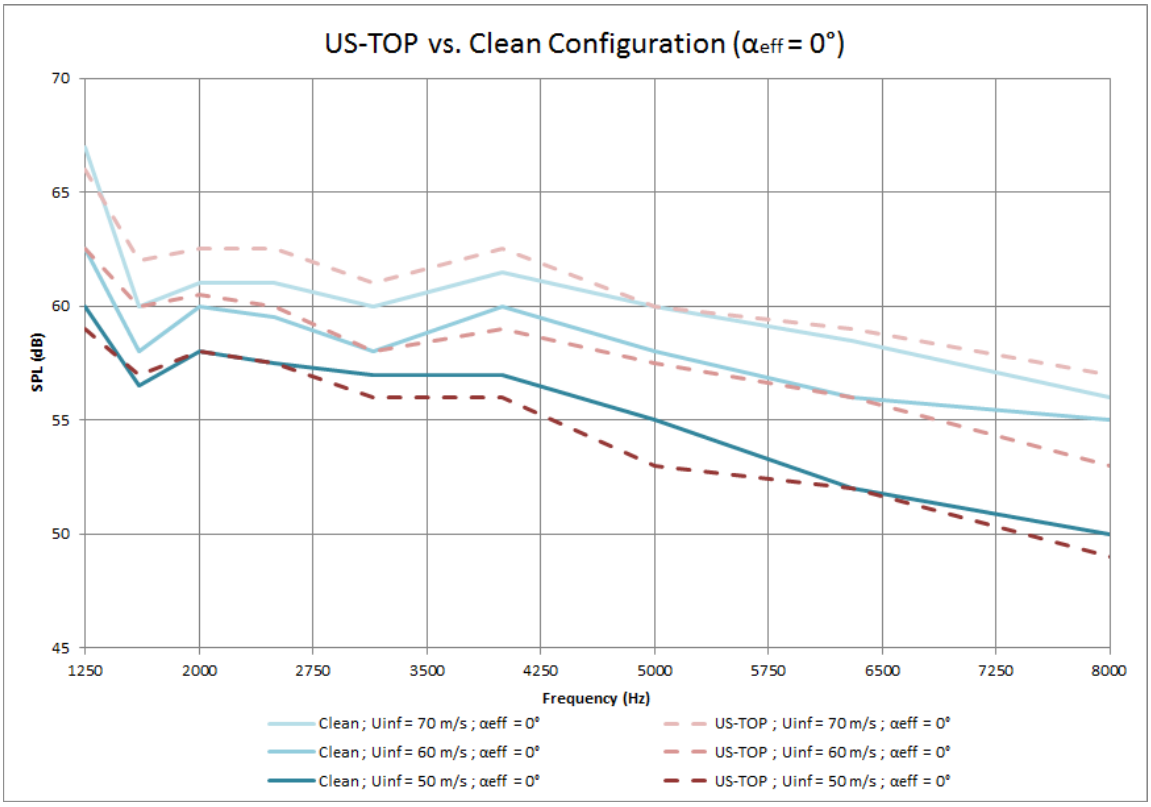

Figure 93 – US-TOP vs. Clean Configuration (α_{eff} = 0°)

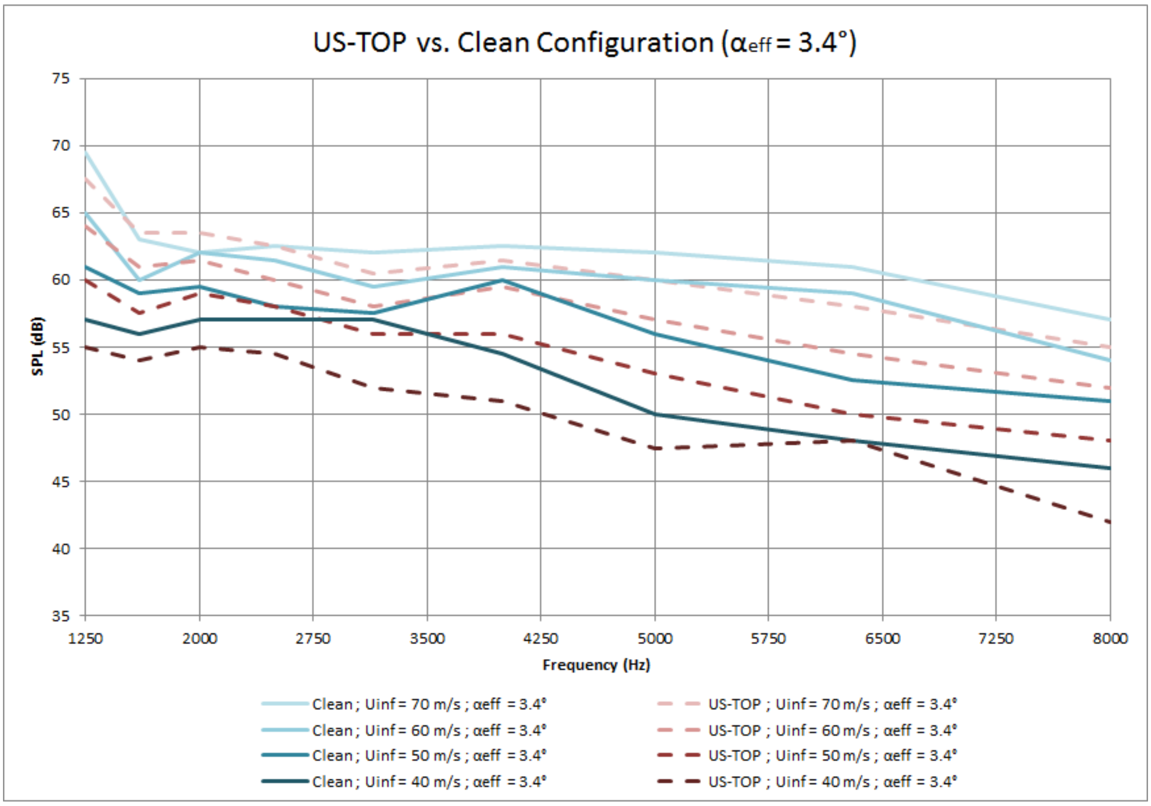

Figure 94 - US-TOP vs. Clean Configuration (α_{eff} = 3.4°)

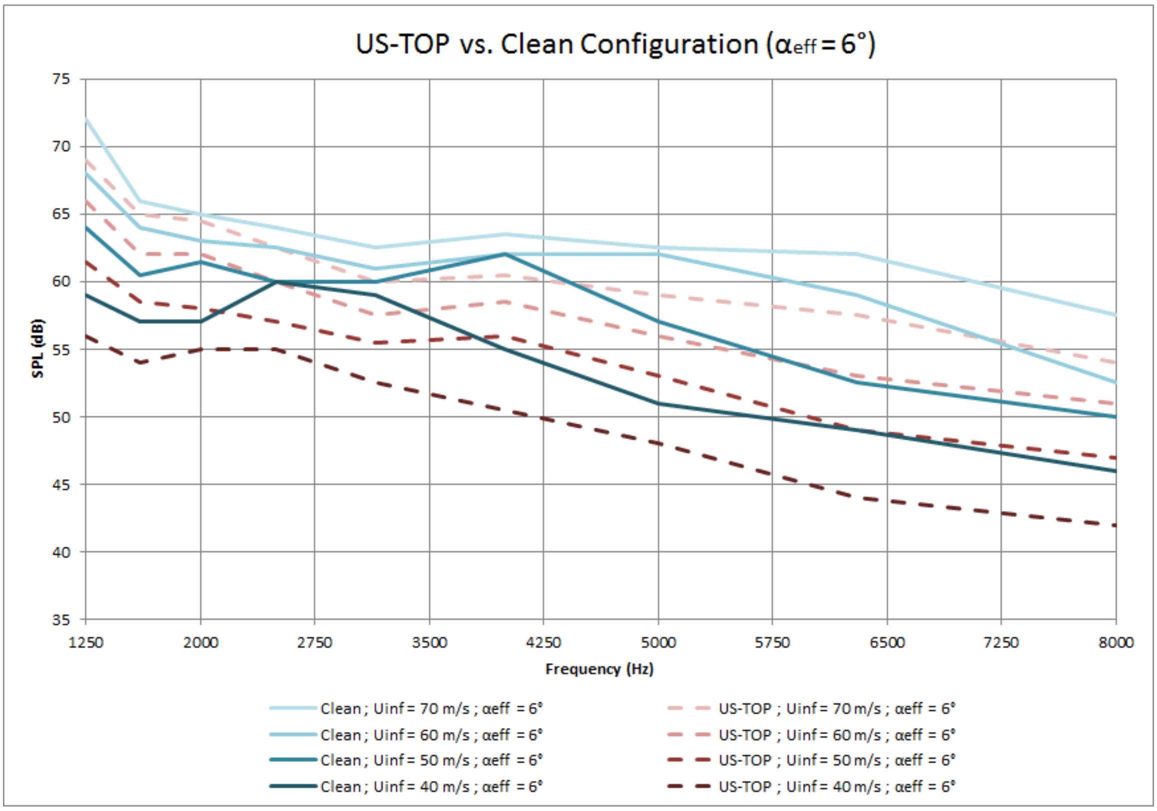

Figure 95 – US-TOP vs. Clean Configuration (α_{eff} = 6°)

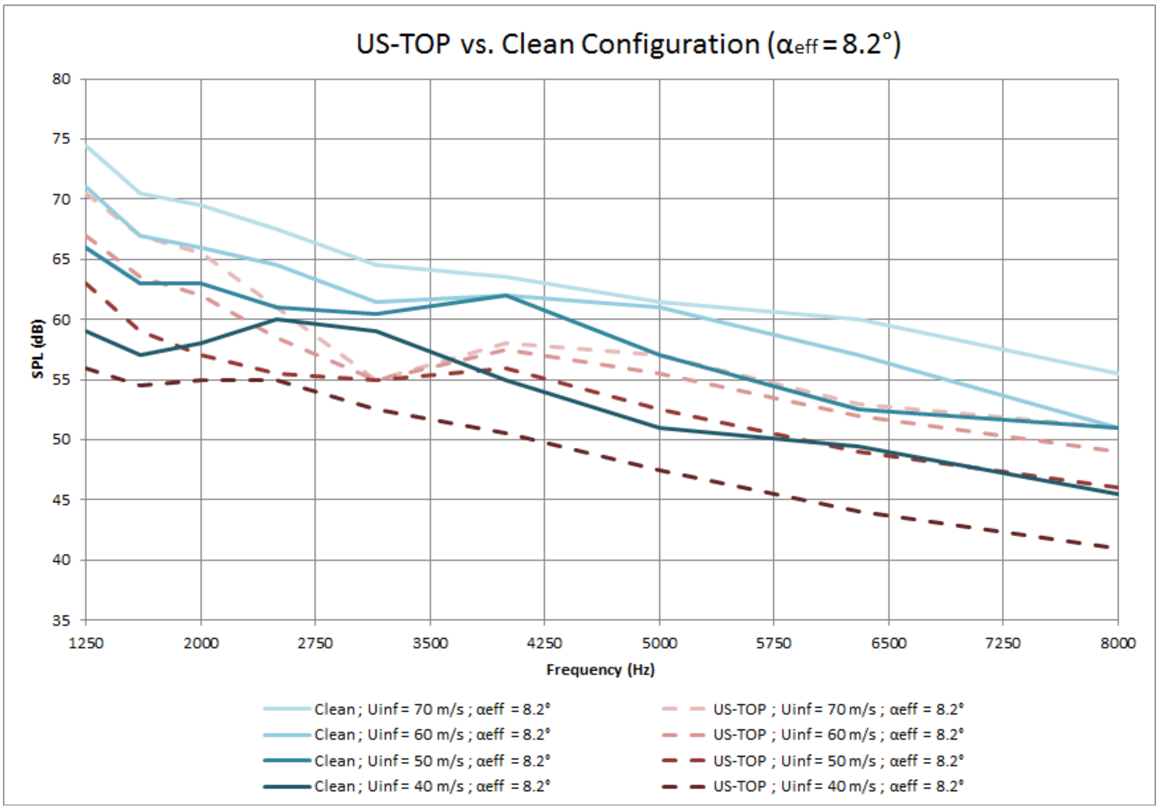

Figure 96 – US-TOP vs. Clean Configuration (α_{eff} = 8.2°)

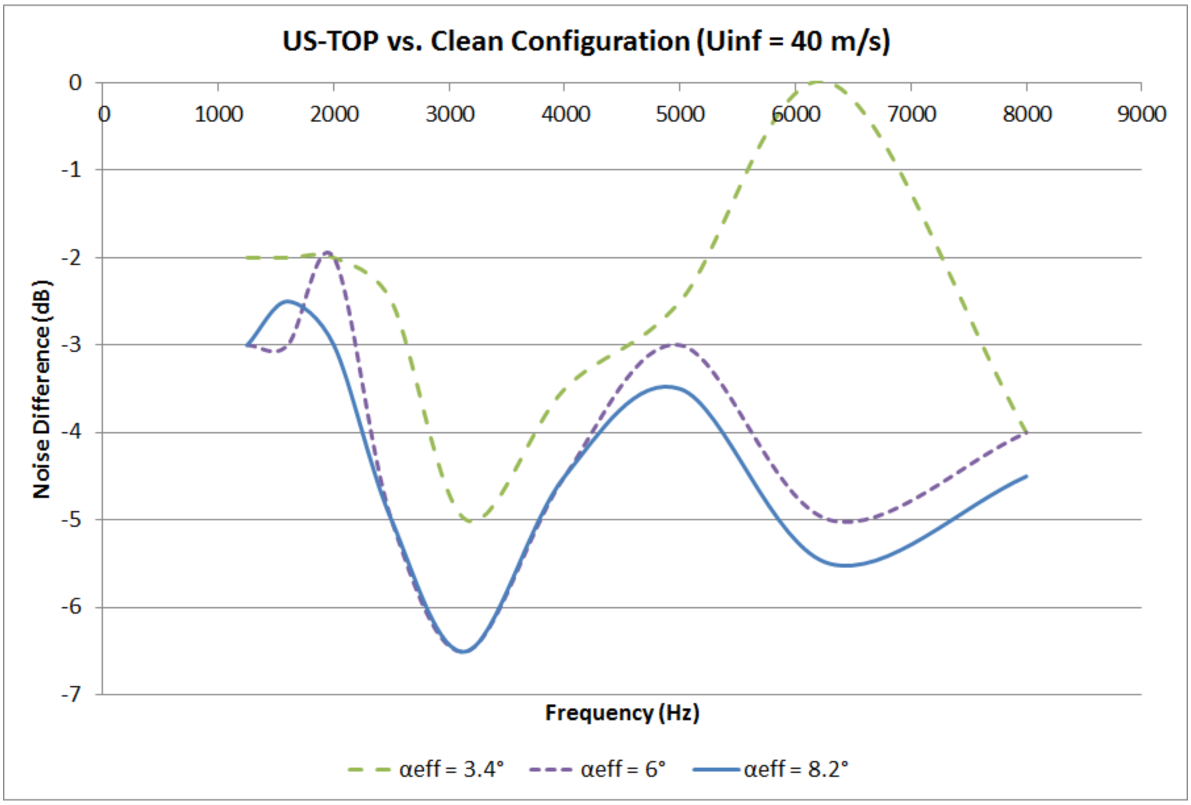

Figure 97 – US-TOP vs. Clean Configuration (U_∞ = 40m/s)

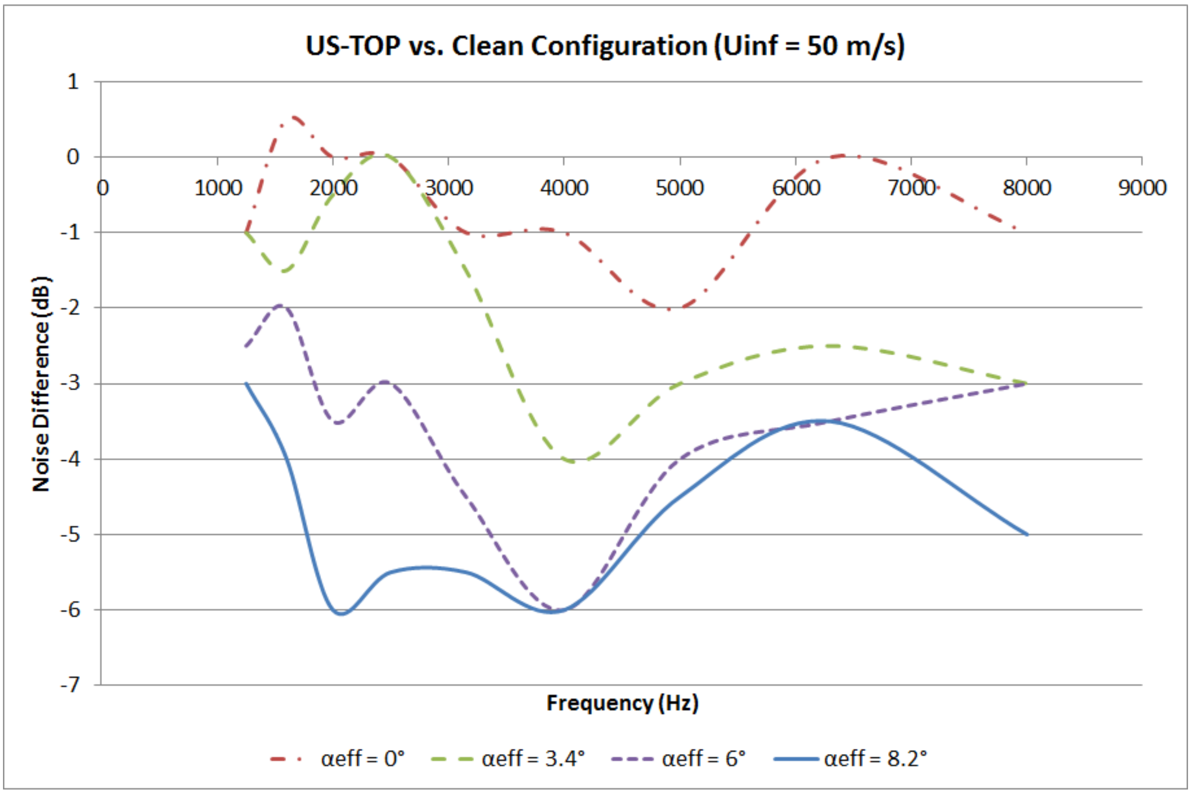

Figure 98 - US-TOP vs. Clean Configuration (U_∞ = 50m/s)

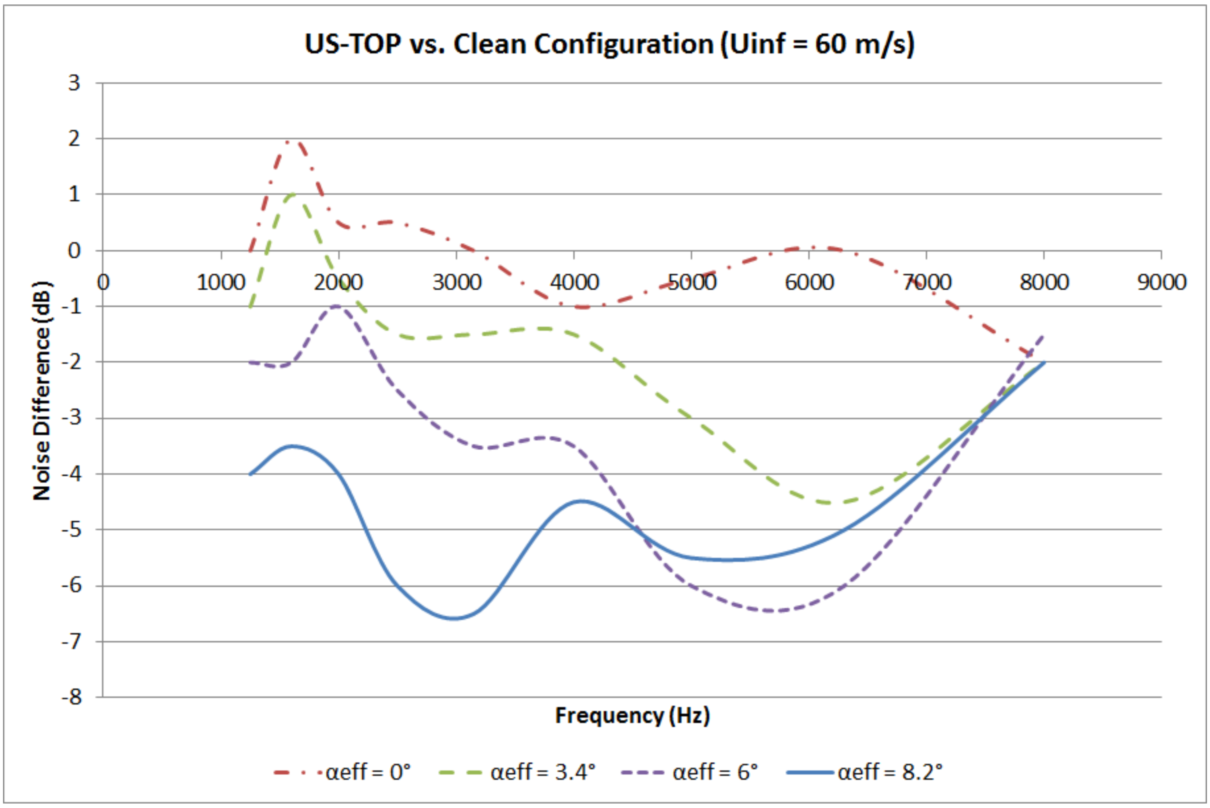

Figure 99 – US-TOP vs. Clean Configuration (U_∞ = 60m/s)

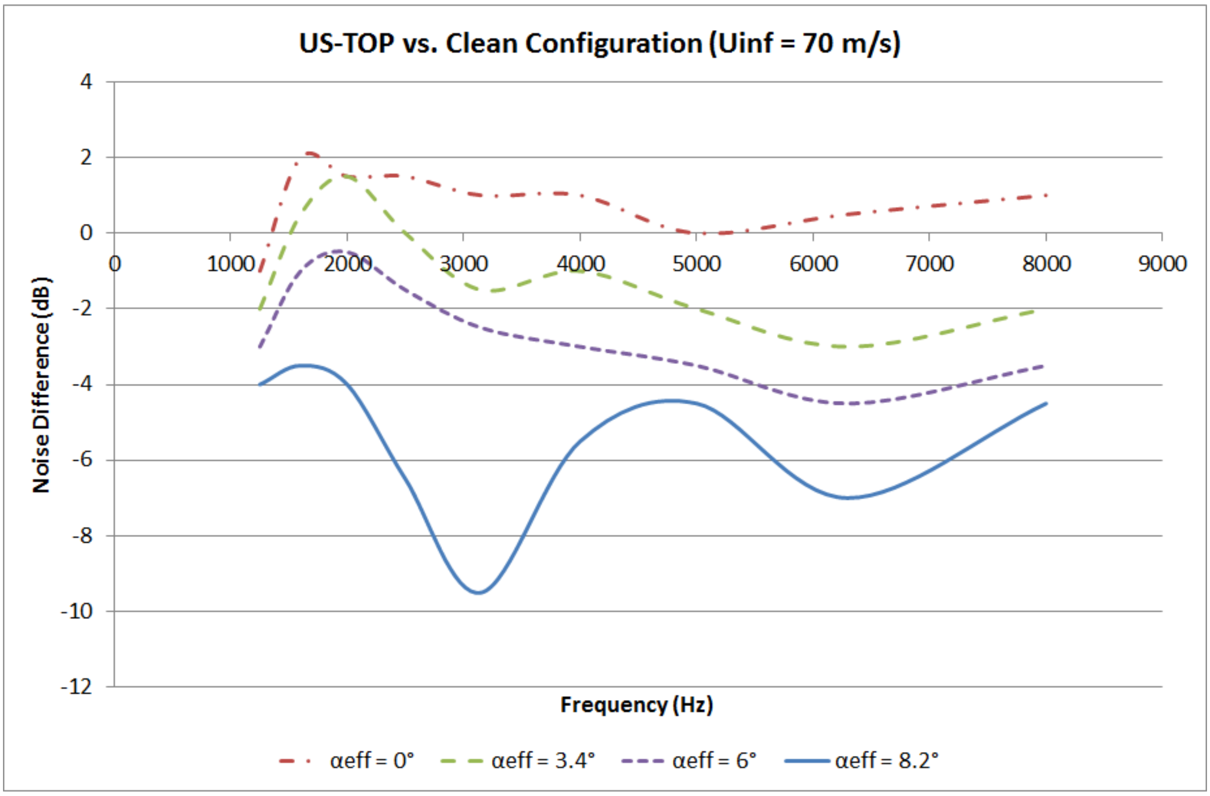

Figure 100 – US-TOP vs. Clean Configuration (U_∞ = 70m/s)

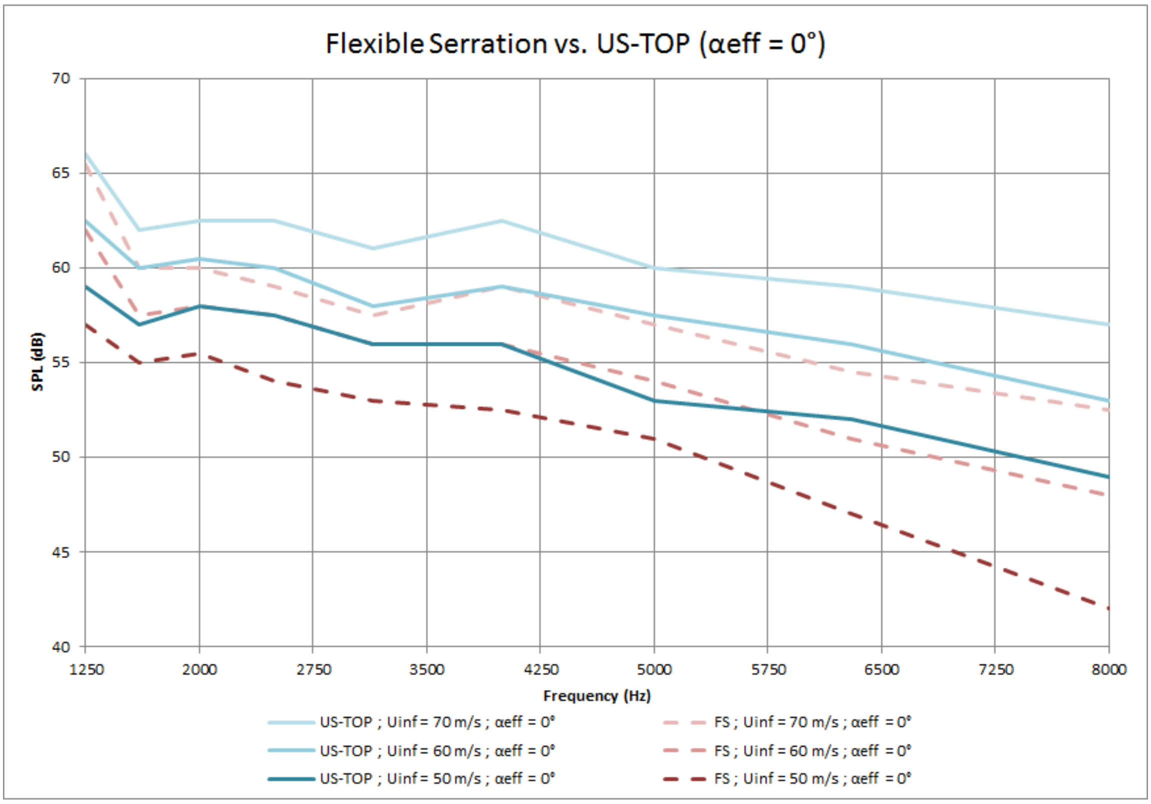

Figure 101 – Flexible Serration vs. US-TOP (α_{eff} = 0°)

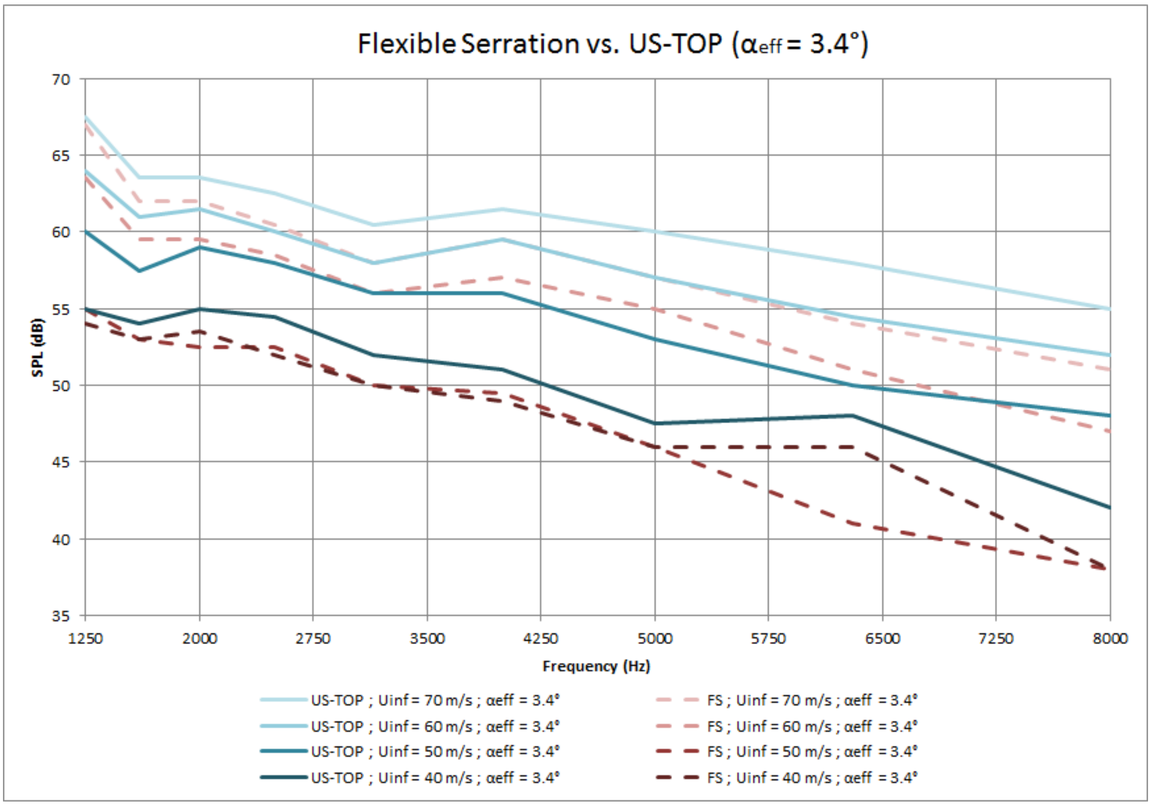

Figure 102 - Flexible Serration vs. US-TOP (α_{eff} = 3.4°)

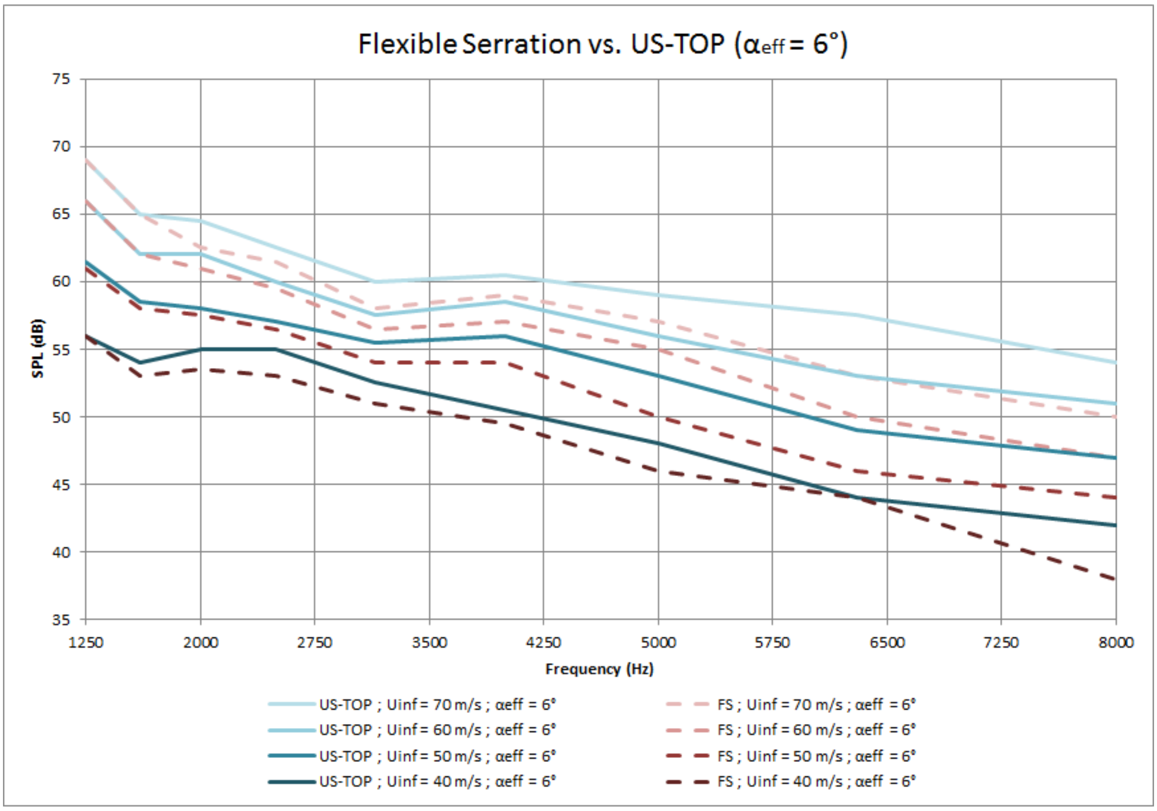

Figure 103 – Flexible Serration vs. US-TOP (α_{eff} = 6°)

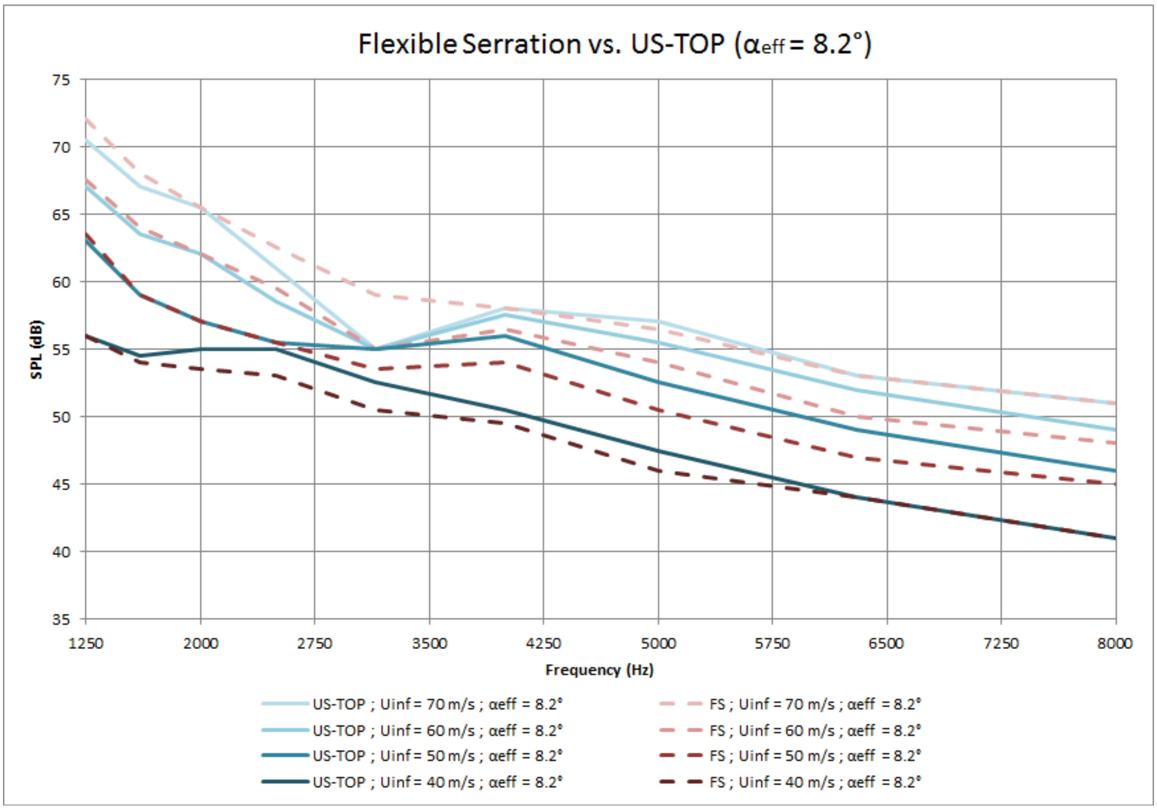

Figure 104 – Flexible Serration vs. US-TOP (α_{eff} = 8.2°)

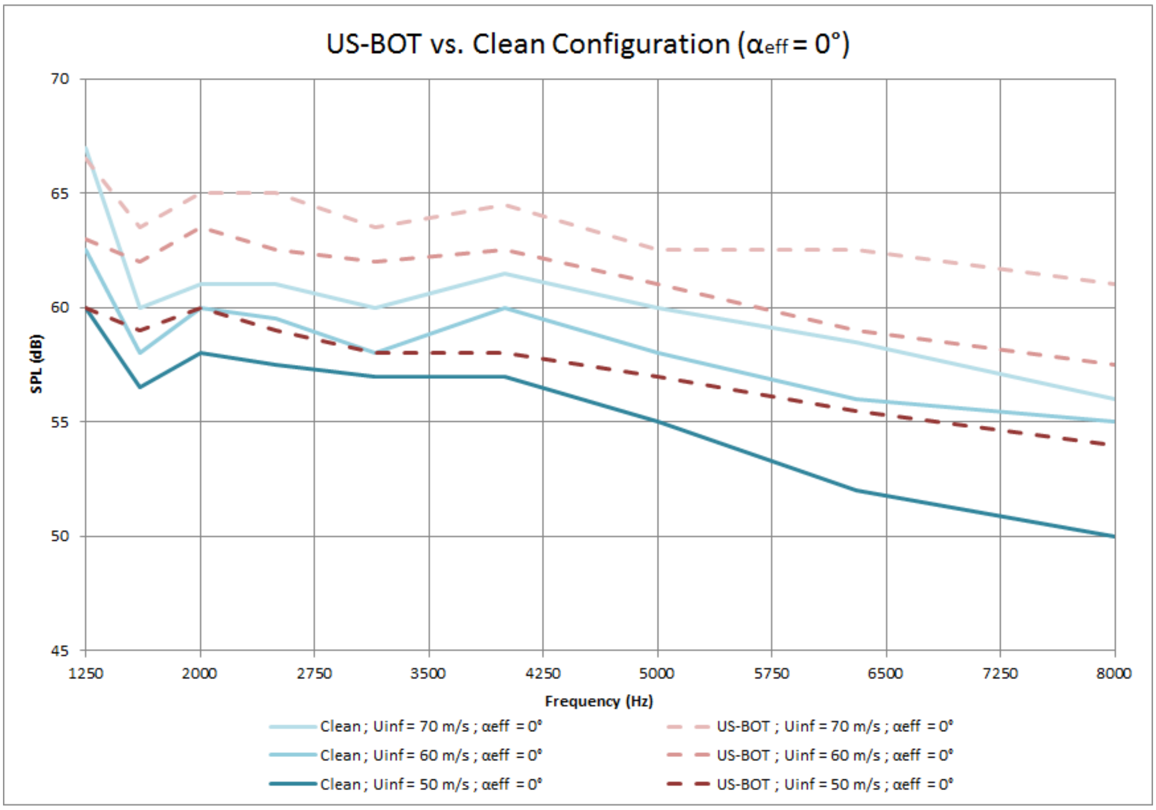

Figure 105 – US-BOT vs. Clean Configuration (α_{eff} = 0°)

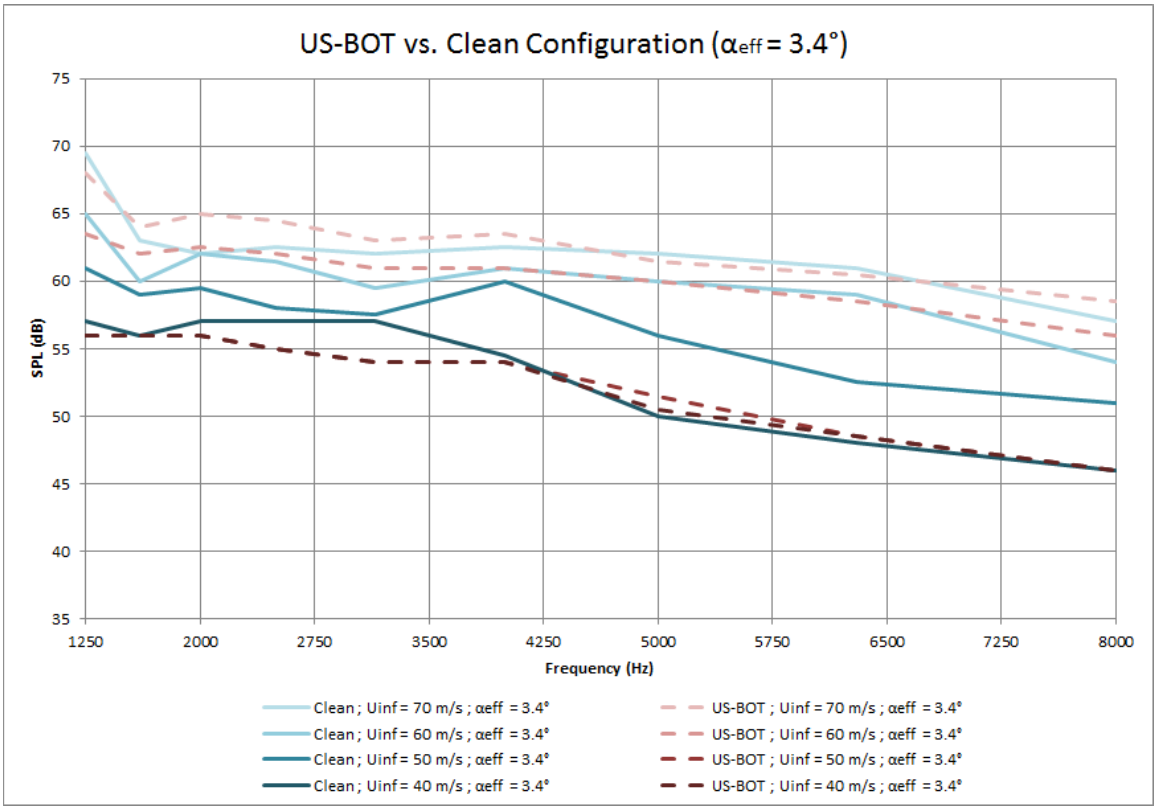

Figure 106 - US-BOT vs. Clean Configuration (α_{eff} = 3.4°)

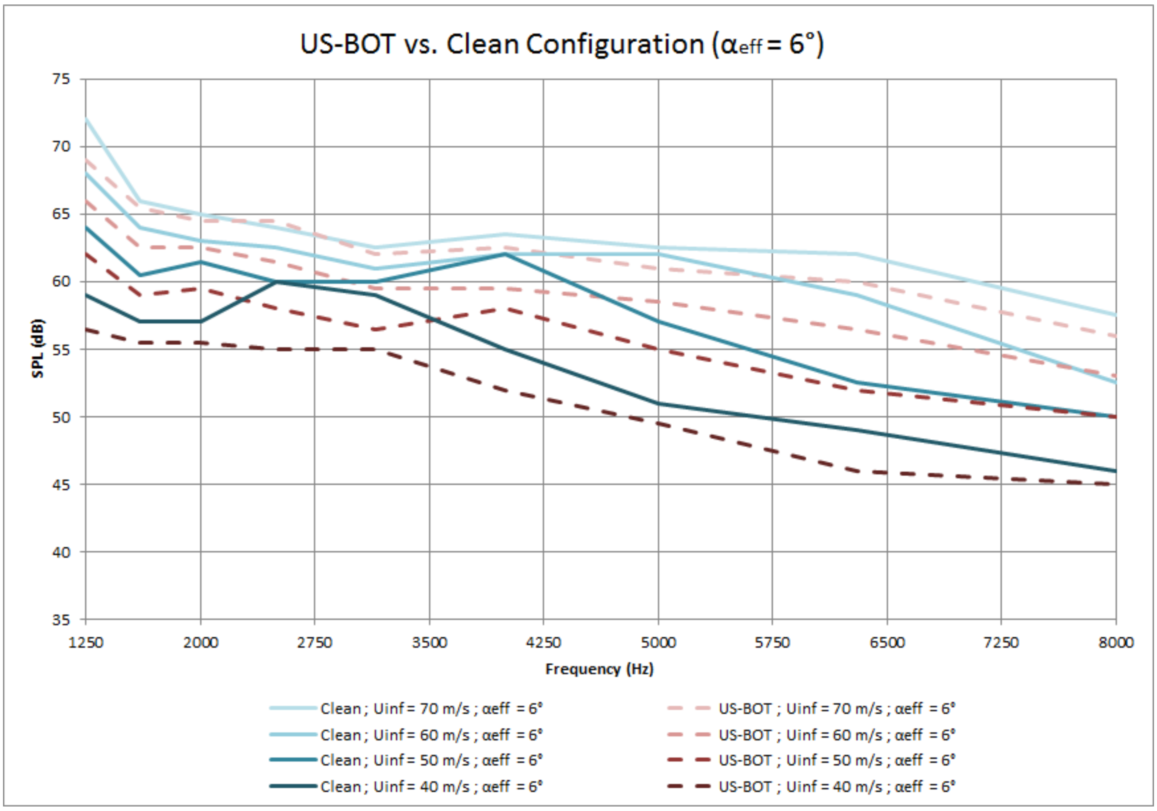

Figure 107 – US-BOT vs. Clean Configuration (α_{eff} = 6°)

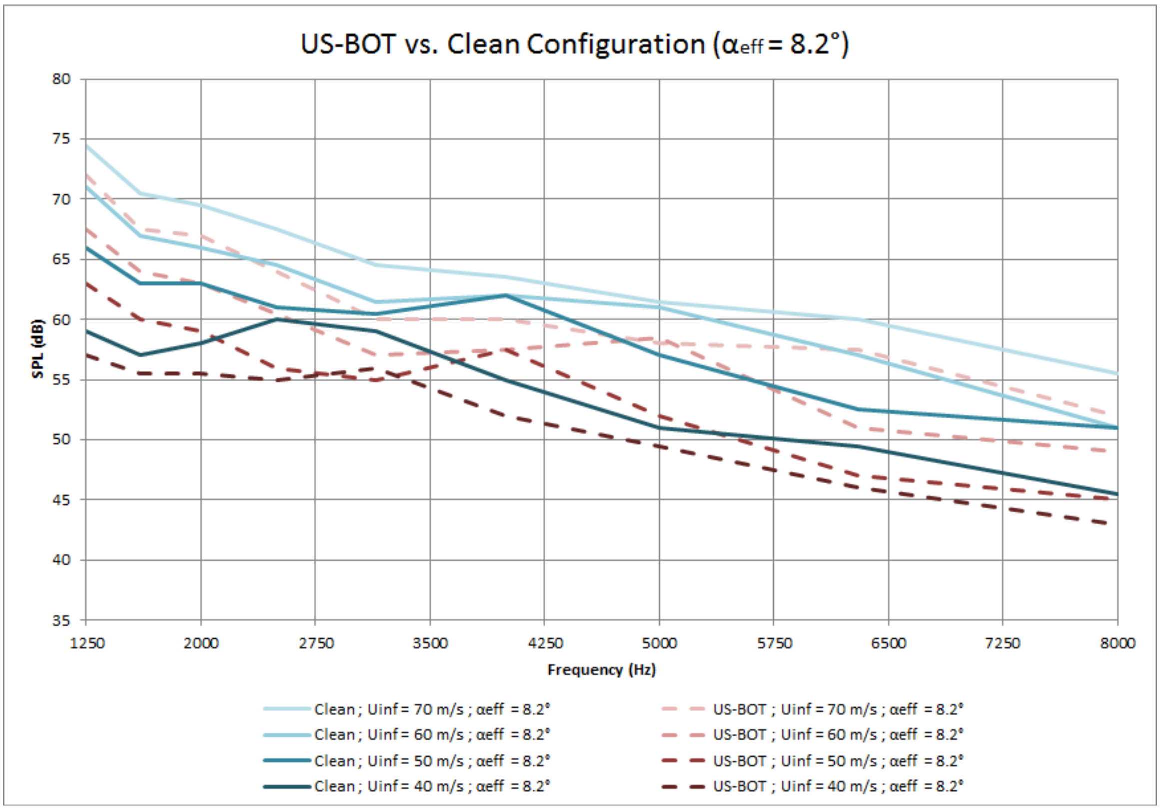

Figure 108 – US-BOT vs. Clean Configuration (α_{eff} = 8.2°)

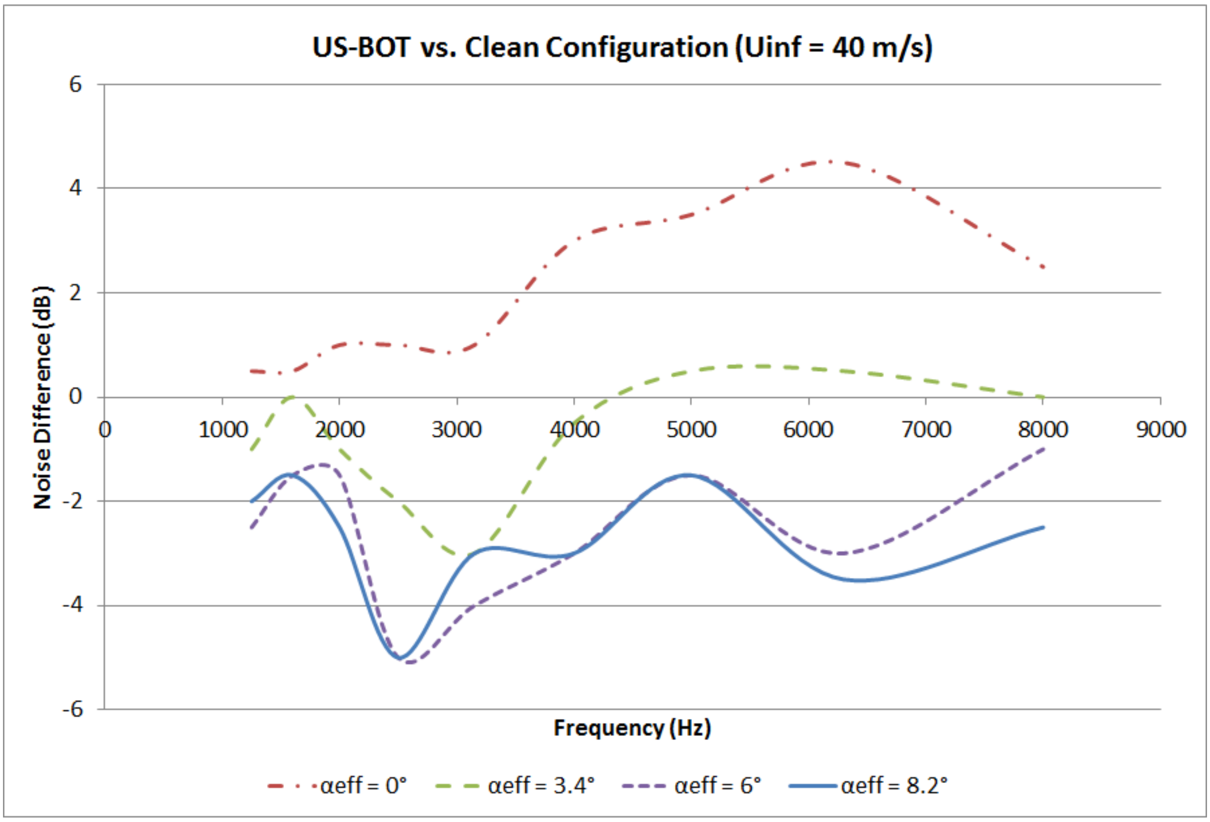

Figure 109– US-BOT vs. Clean Configuration (U_∞ = 40 m/s)

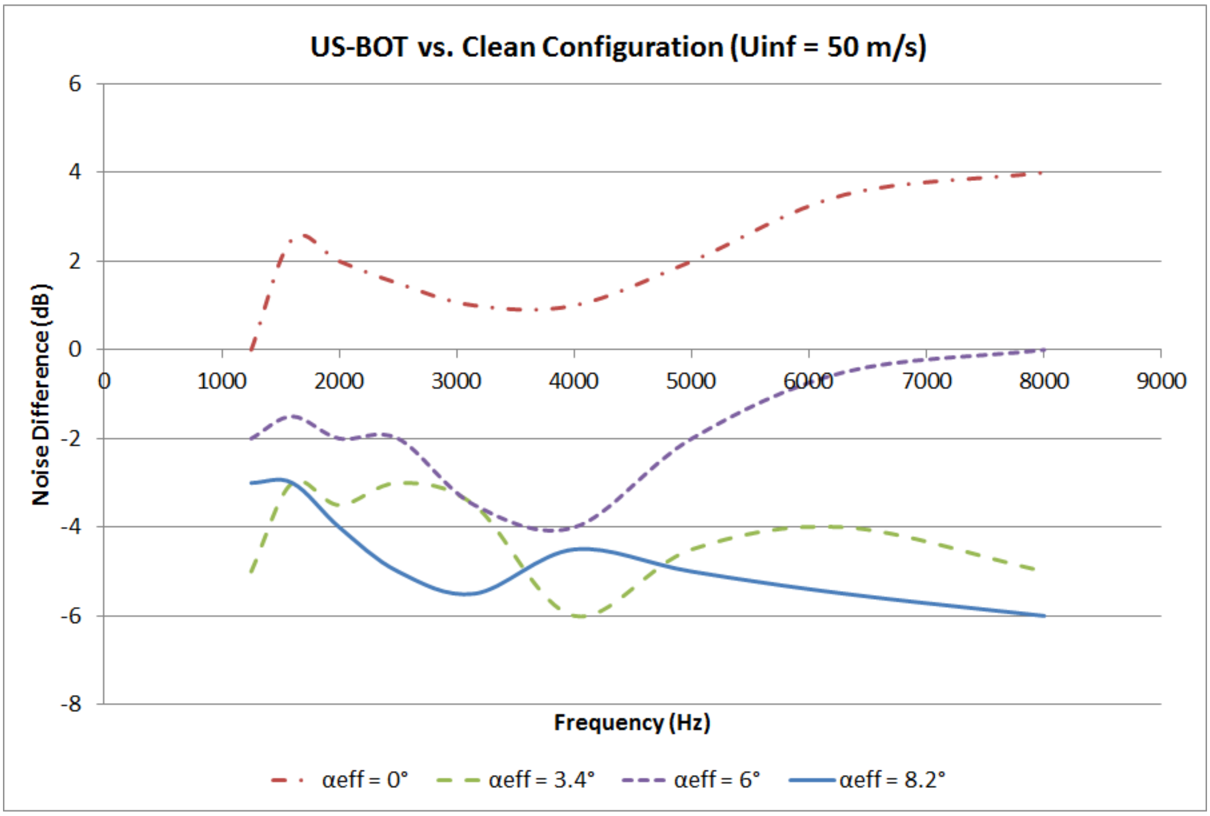

Figure 110 - US-BOT vs. Clean Configuration (U_∞ = 50 m/s)

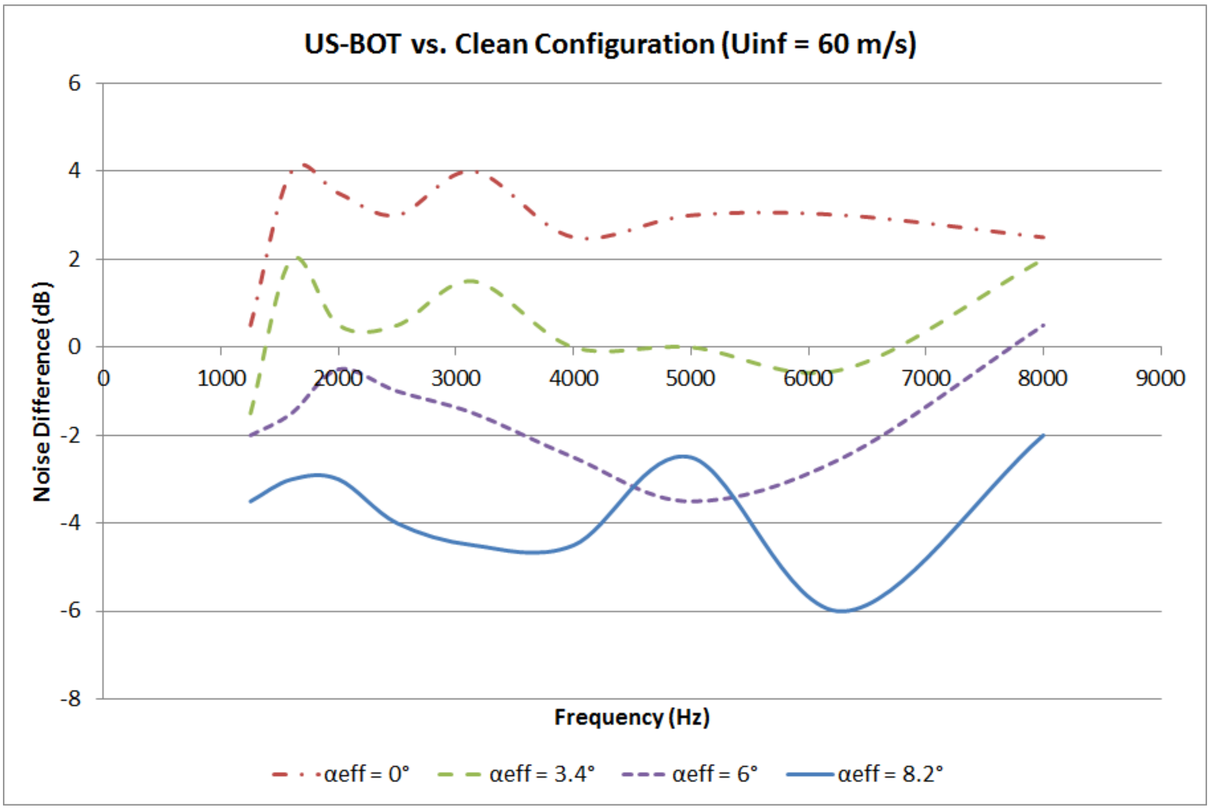

Figure 111 – US-BOT vs. Clean Configuration (U_∞ = 60 m/s)

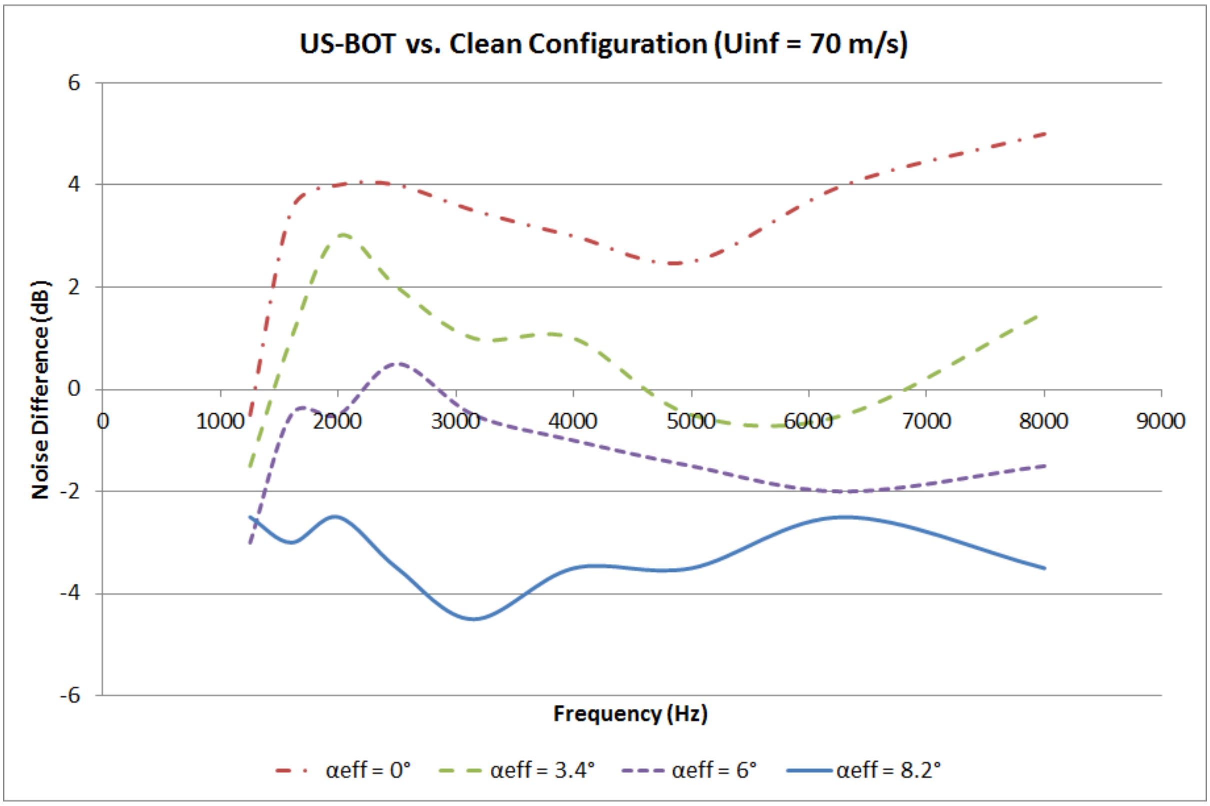

Figure 112 – US-BOT vs. Clean Configuration (U_∞ = 70 m/s)

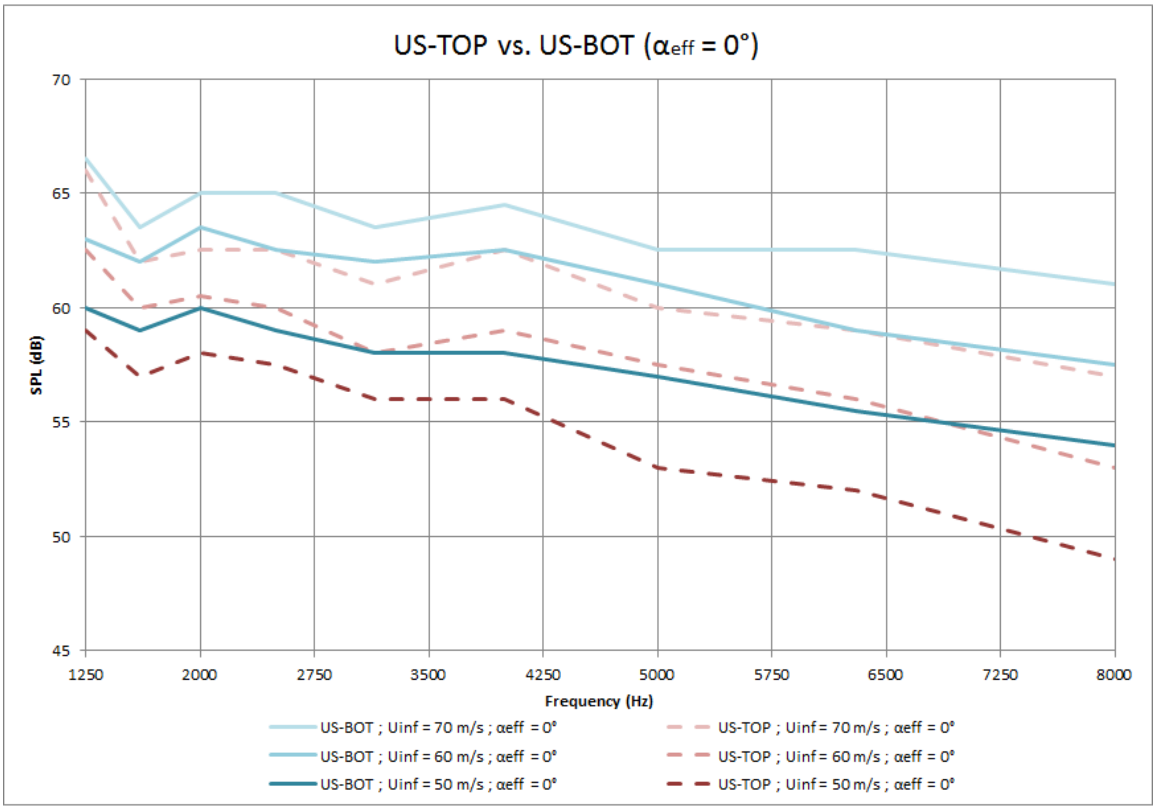

Figure 113 – US-TOP vs. US-BOT (α_{eff} = 0°)

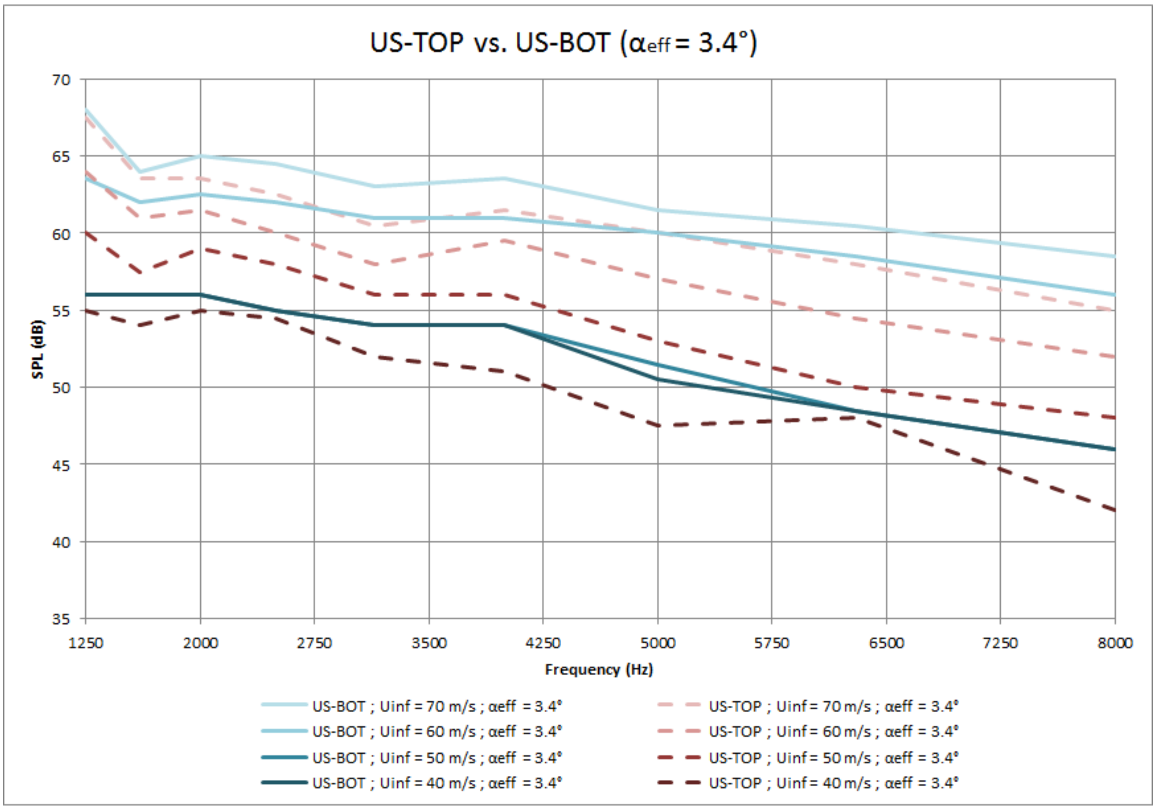

Figure 114 - US-TOP vs. US-BOT (α_{eff} = 3.4°)

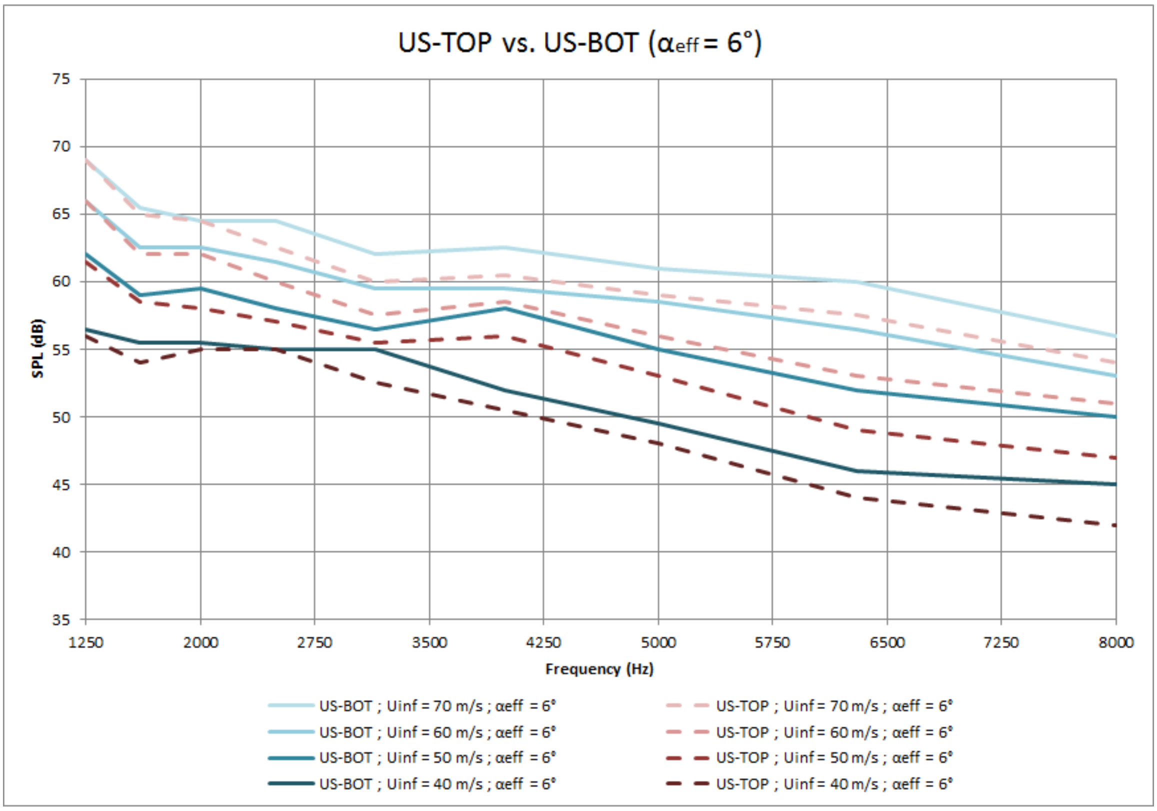

Figure 115 – US-TOP vs. US-BOT (α_{eff} = 6°)

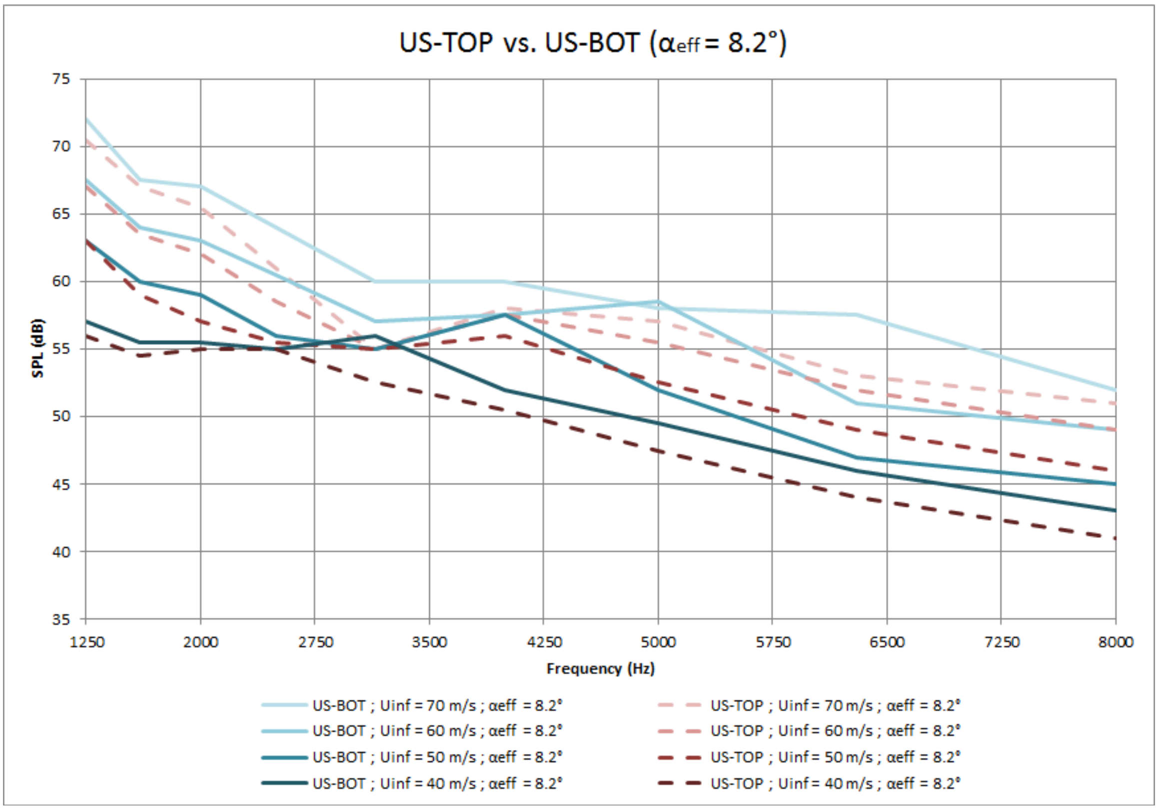

Figure 116 – US-TOP vs. US-BOT (αeff = 8.2°)

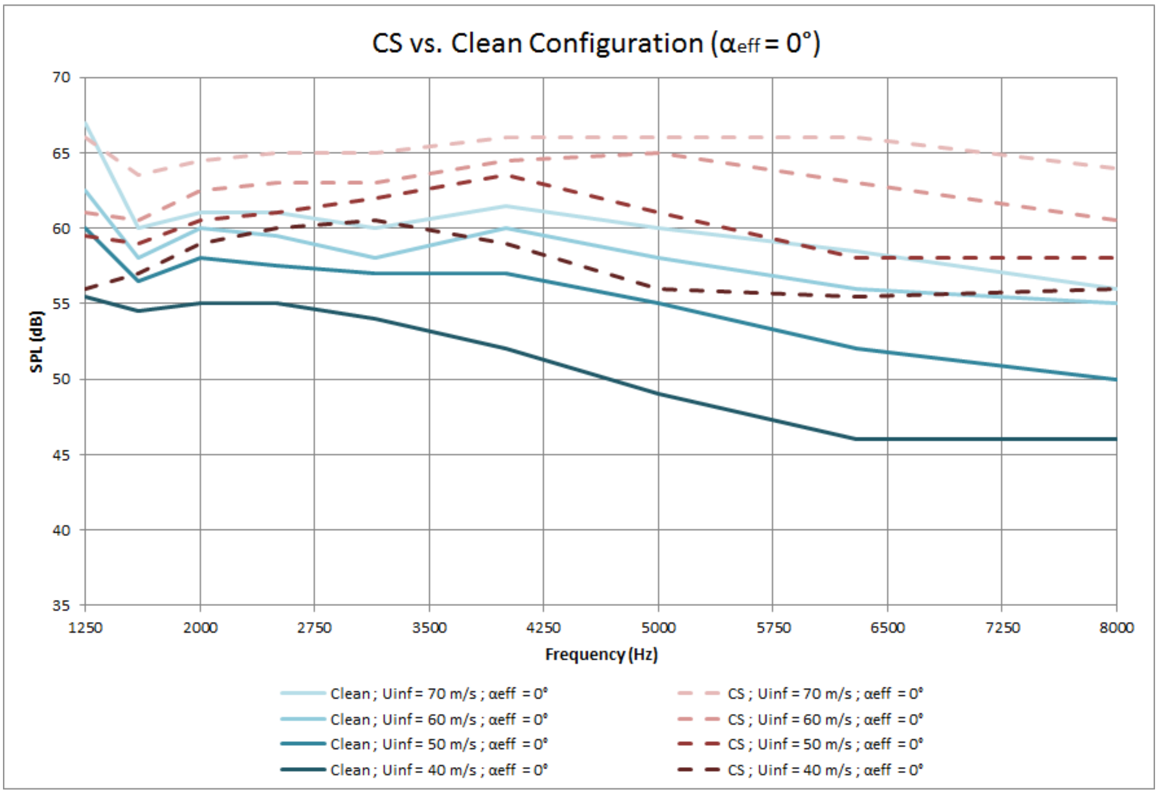

Figure 117 – CS vs. Clean Configuration (α_{eff} = 0°)

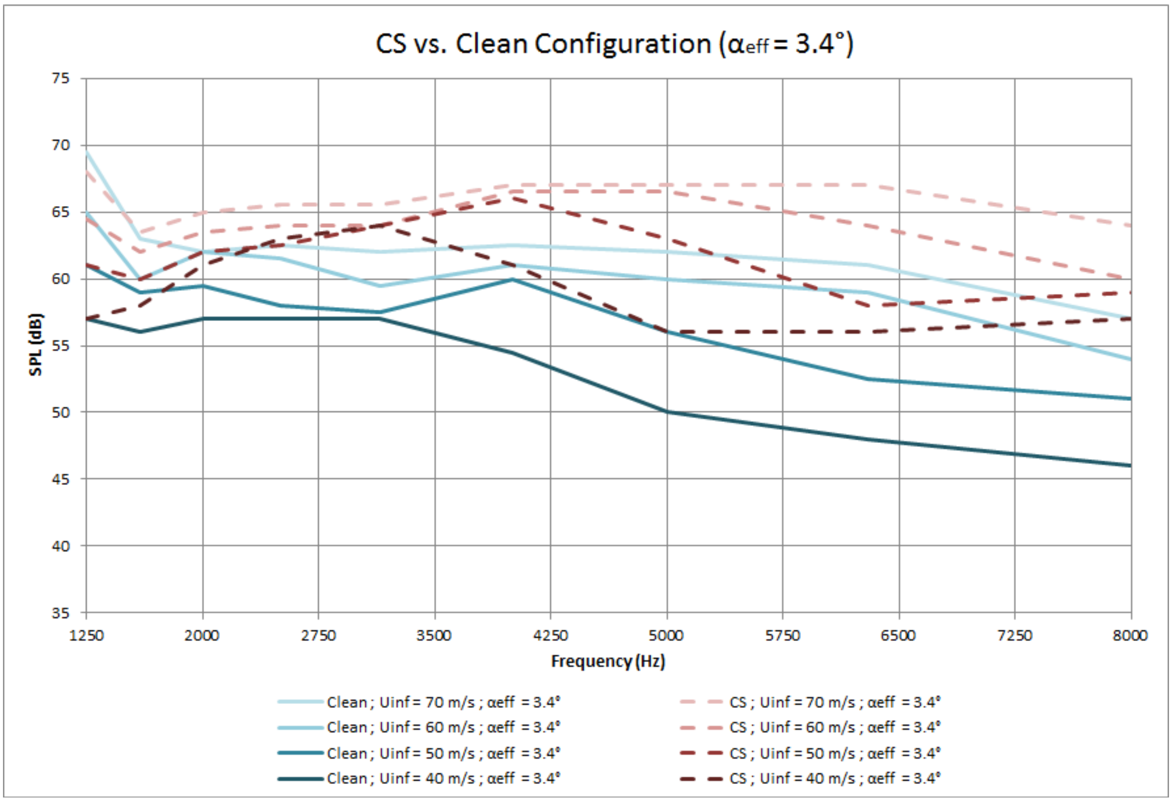

Figure 118 – CS vs. Clean Configuration (αeff = 3.4°)

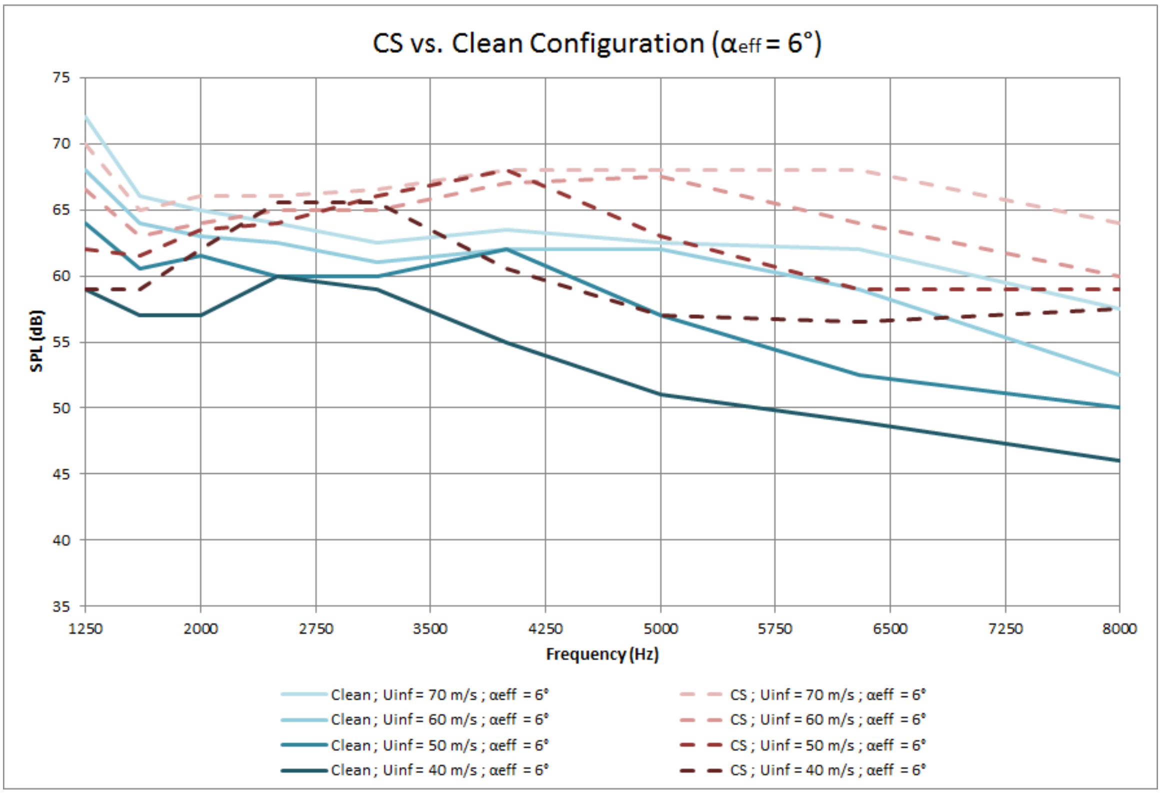

Figure 119 – CS vs. Clean Configuration (α_{eff} = 6°)

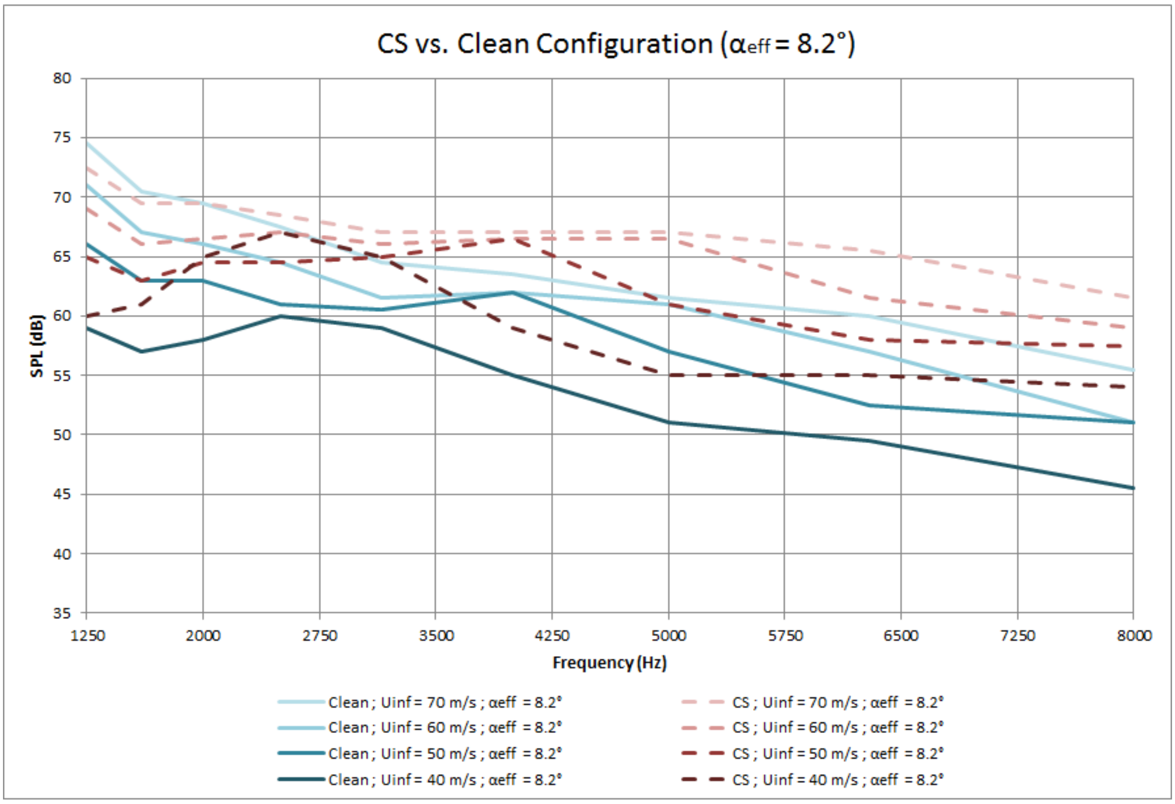

Figure 120 – CS vs. Clean Configuration (αeff = 8.2°)

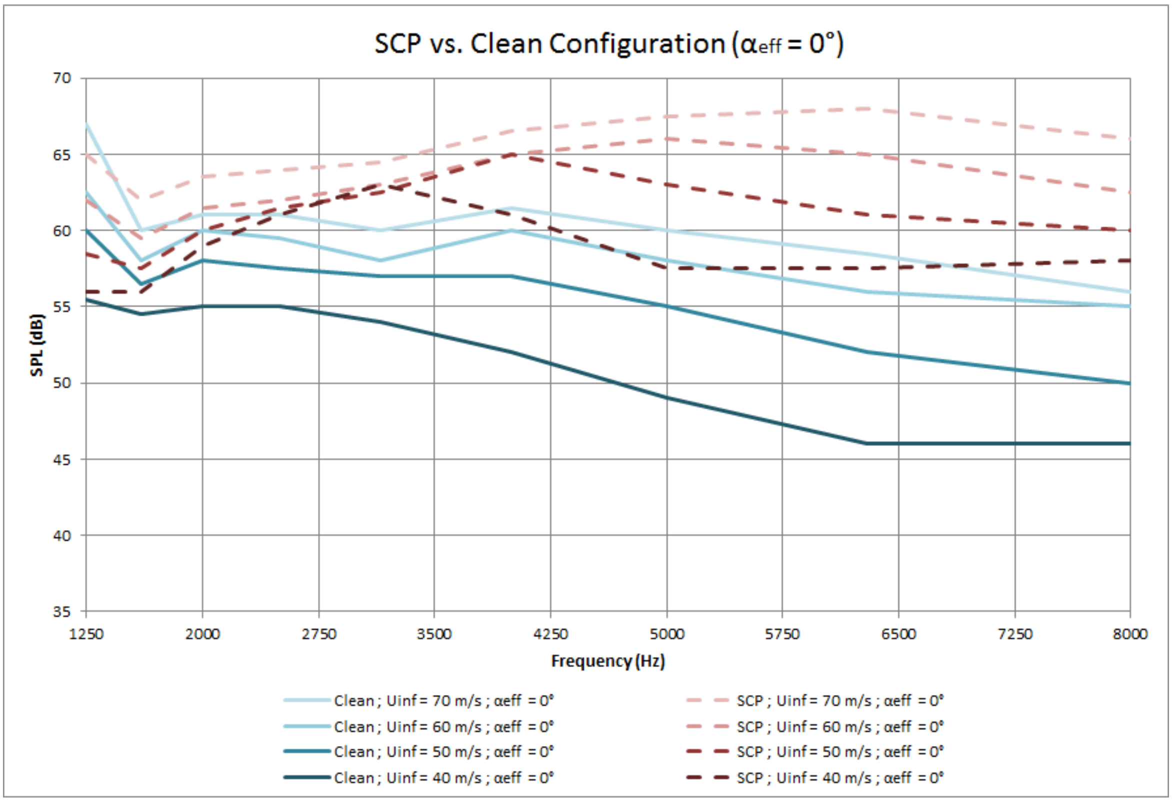

Figure 121 – SCP vs. Clean Configuration (α_{eff} = 0°)

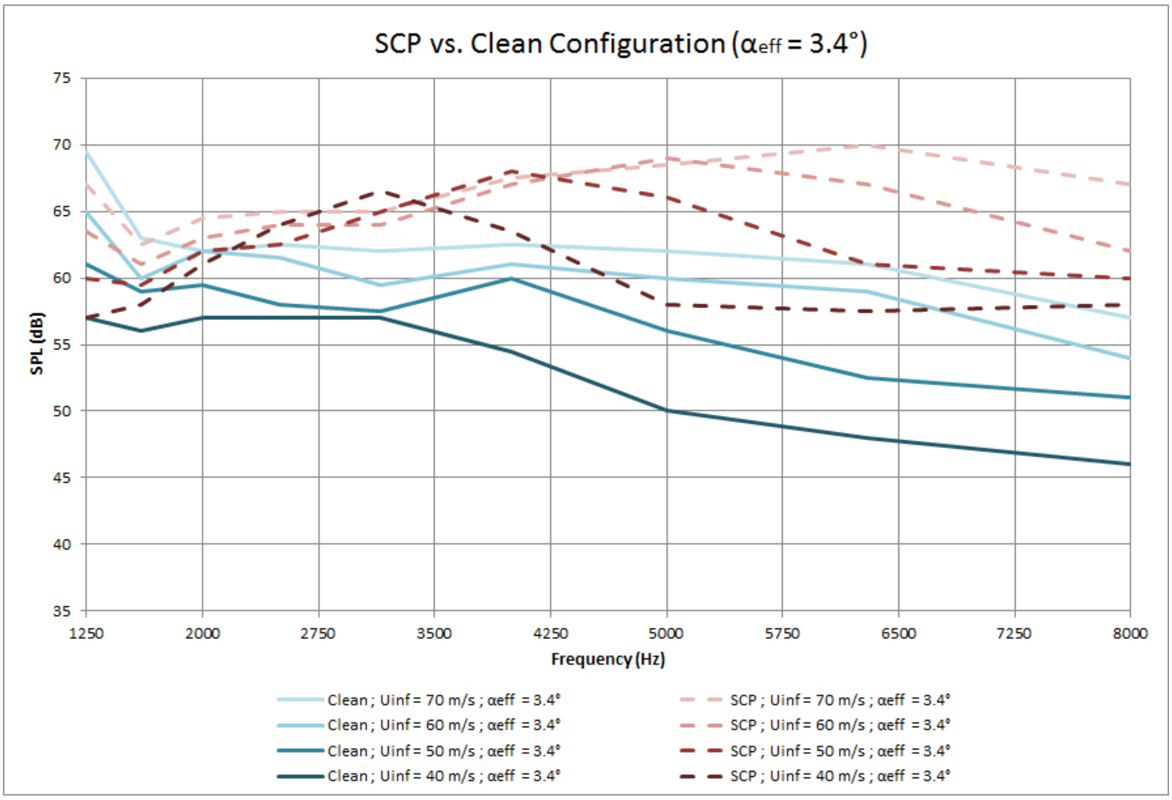

Figure 122 – SCP vs. Clean Configuration (αeff = 3.4°)

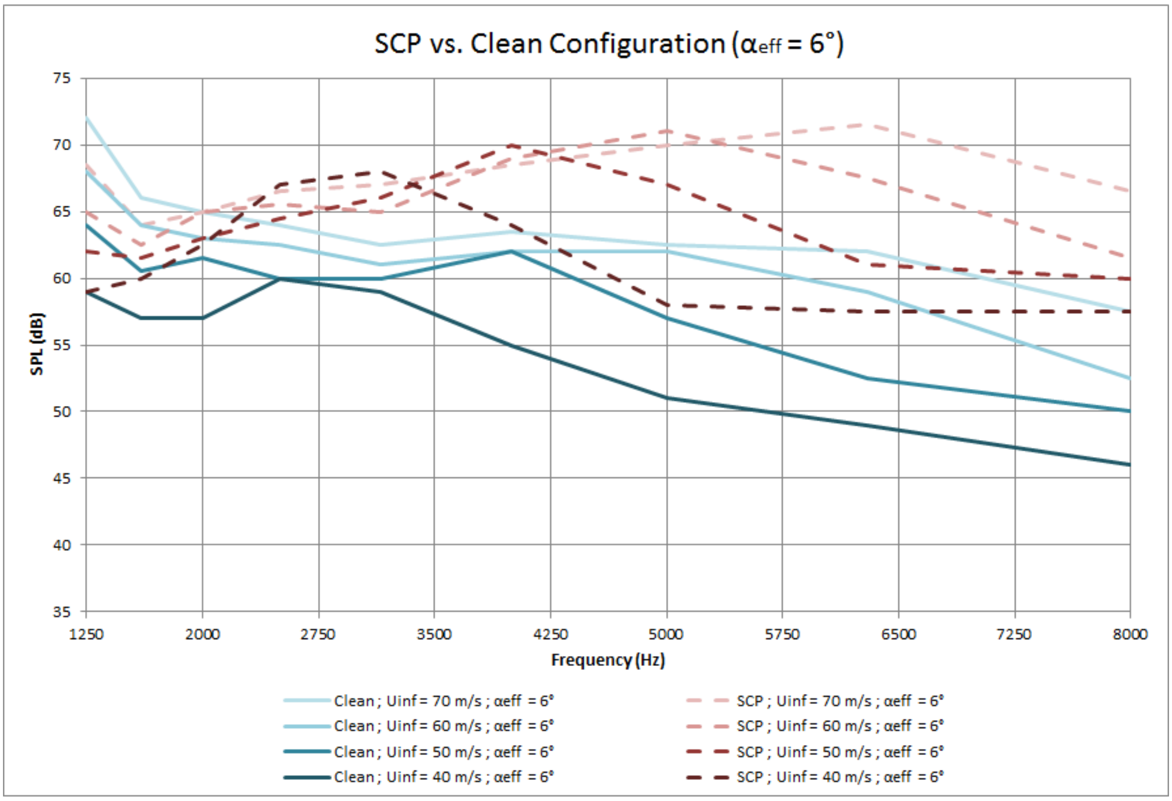

Figure 123 – SCP vs. Clean Configuration (α_{eff} = 6°)

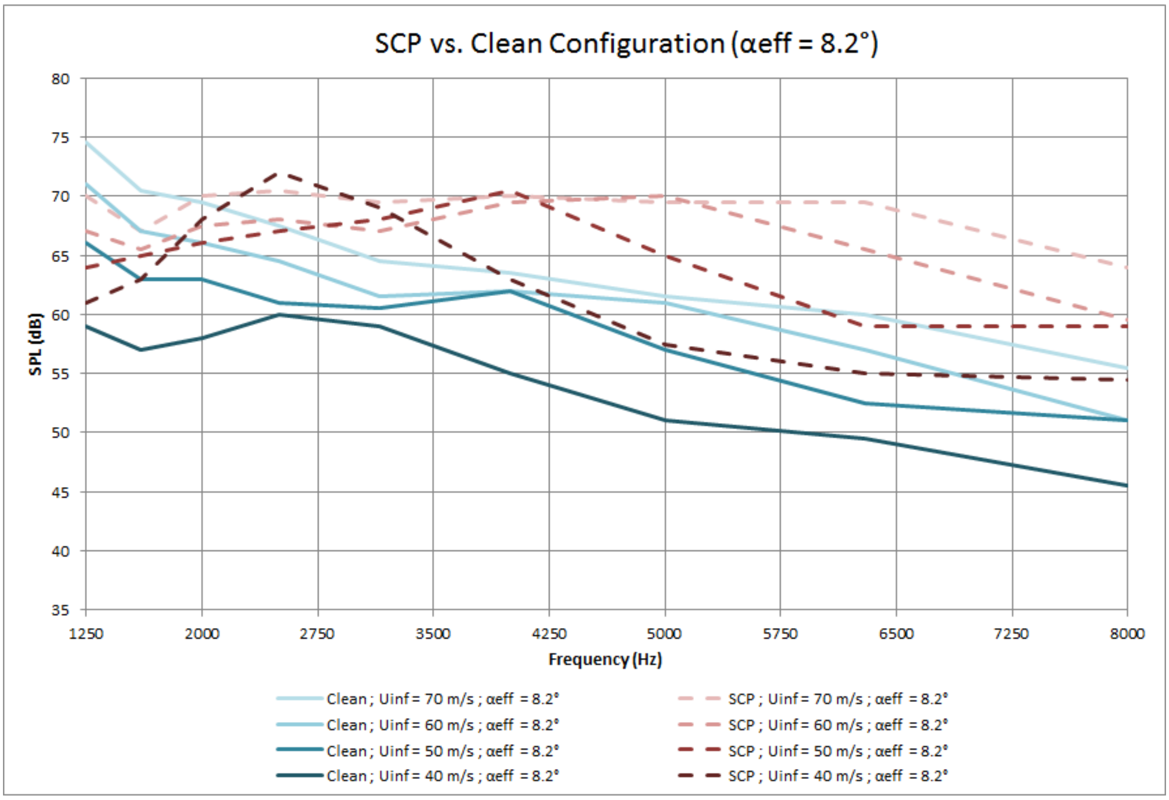

Figure 124 – SCP vs. Clean Configuration (αeff = 8.2°)

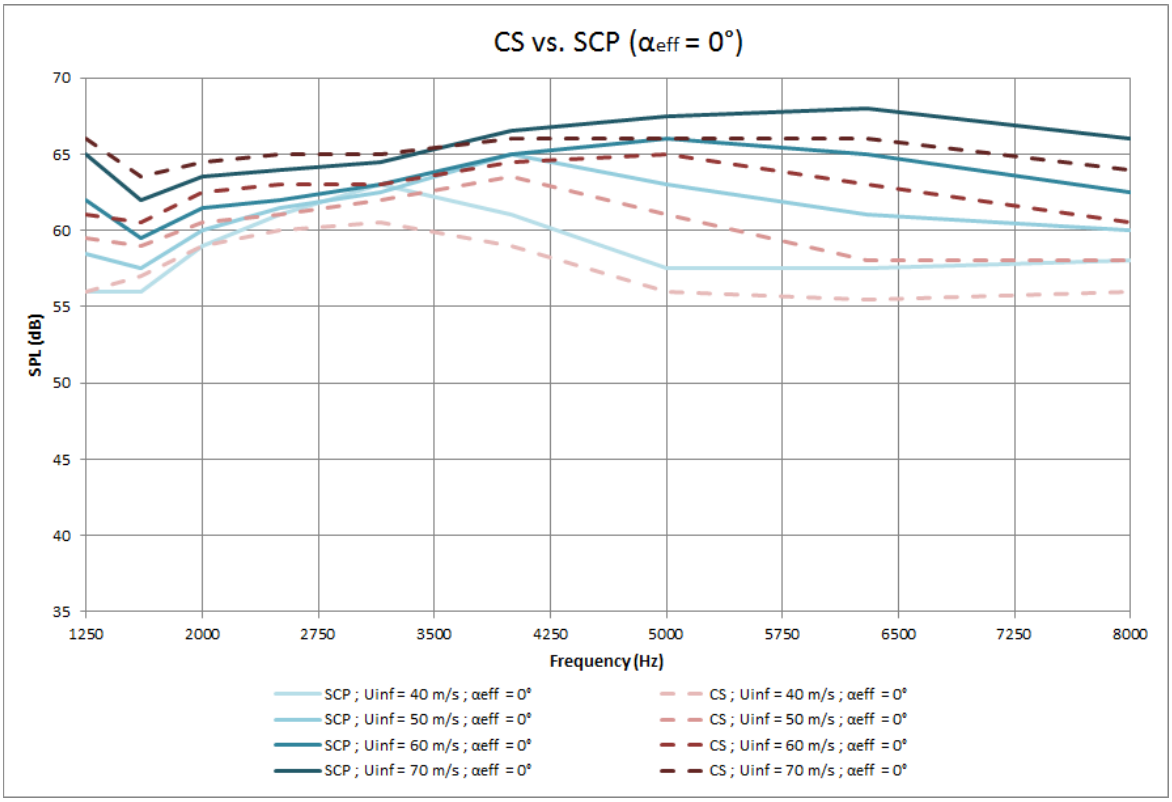

Figure 125 – CS vs. SCP (α_{eff} = 0°)

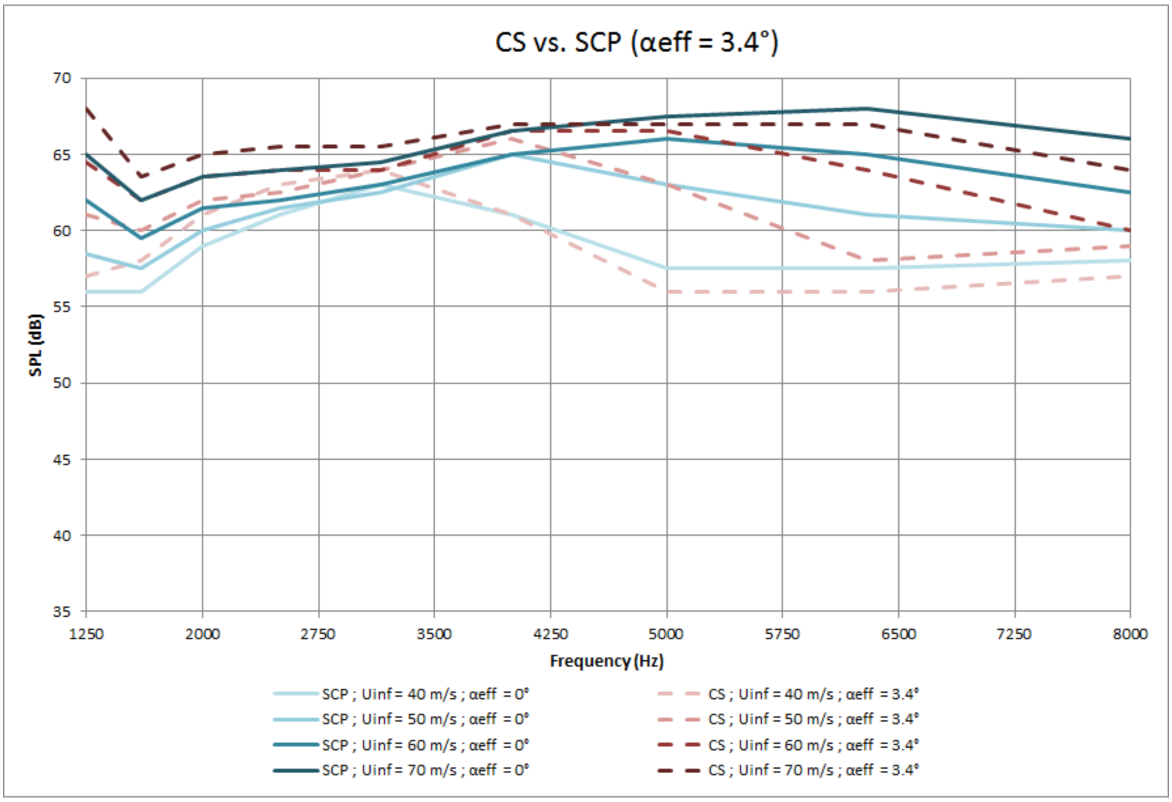

Figure 126 – US CS vs. SCP (αeff = 3.4°)

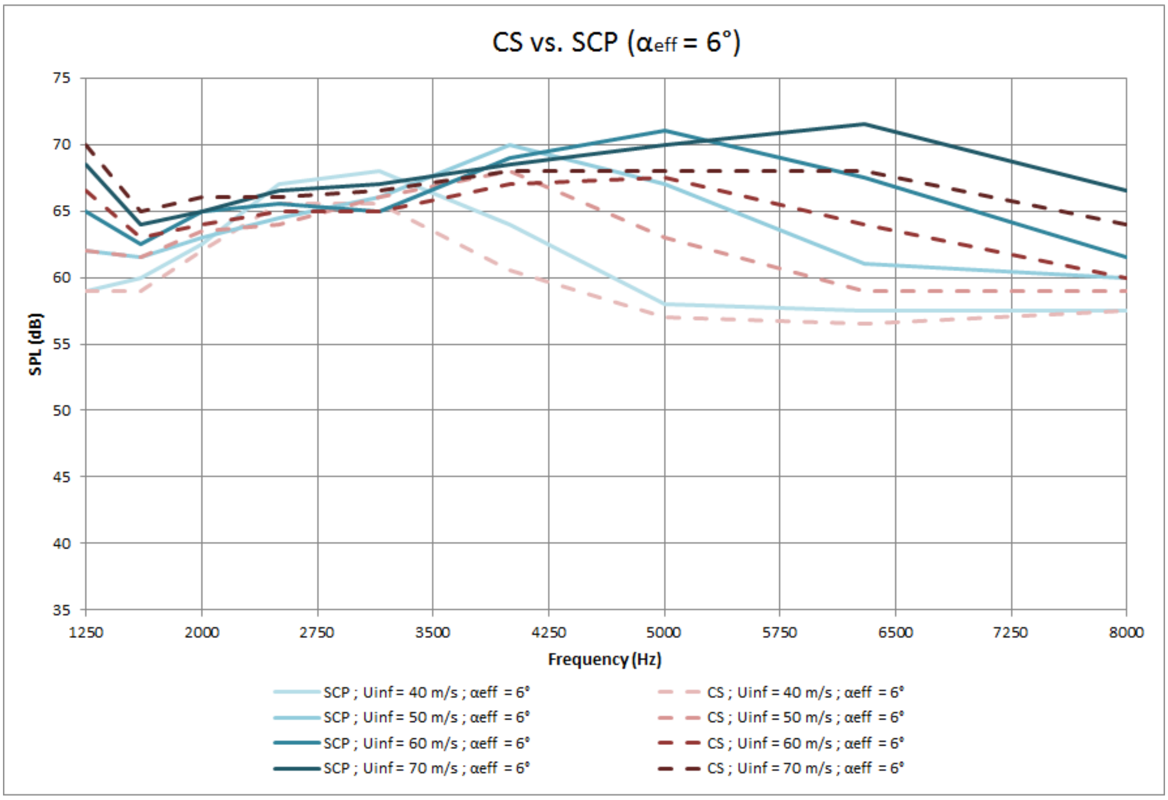

Figure 127 – CS vs. SCP (α_{eff} = 6°)

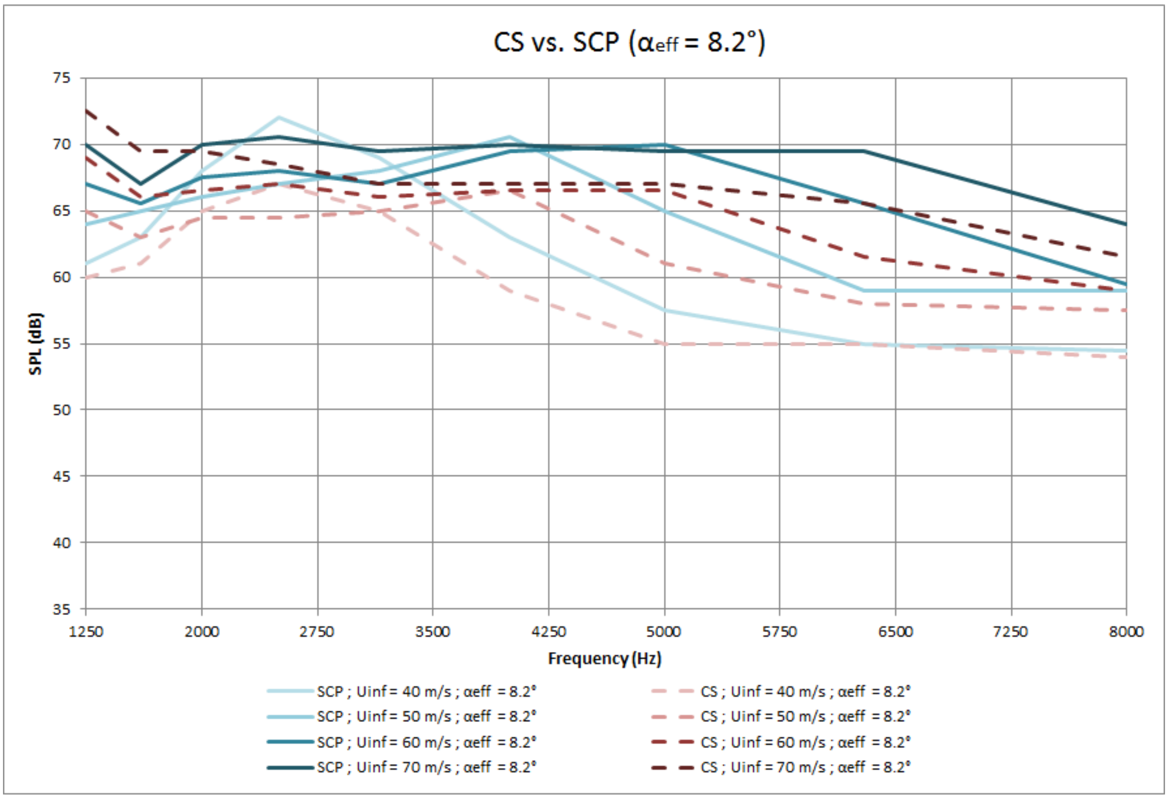

Figure 128 – CS vs. SCP (αeff = 8.2°)

References

1. **Wagner, S., Bareiss, R., and Guidati, G.** *Wind Turbine Noise.* 1996 : Springer–Verlag, New York.

2. **Oerlemans, S. et al.** *Location and quantification of noise sources on a wind turbine.* 2007. pp. 869-883.

3. **Brooks T. F., Pope D. S., Marcolini M. A.** *Airfoil Self-Noise and Prediction.* Washington, D.C. : Nasa Reference Publication, 1989.

4. **Howe, M. S.** *A Review of the Theory of Trailing Edge Noise.* Cambridge, Massachusetts : NASA, 1978.

5. —. *Aerodynamic Noise of a Serrated Trailing Edge.* 1991. pp. 33-45.

6. —. *Noise Produced by a Sawtooth Trailing Edge.* 1991. pp. 482-487.

7. **Moreau D. J., Doolan C. J.** *Noise-Reduction Mechanism of a Flat-Plate Serrated Trailing Edge.* 2003. p. DOI: 10.2514/1.J052436.

8. **Gruber, M. et al.** *On the mechanisms of serrated airfoil trailing edge noise reduction.* 2011.

9. **Braun, K.A. et al.** *Serrated Trailing Edge Noise (STENO).* s.l. : EU-Project JOR3-CT95-0073, 1998.

10. **Timmer, W.A. and van Rooij, R.P.J.O.M.** *Summary of the Delft University Wind Turbine Dedicated Airfoils.* 2003.

11. **Blake, W.** *Mechanics of Flow Induced Sound and Vibration: Complex.* New York : Academic Press, 1986.

12. **Oerlemans, S. et al.** *Reduction of Wind Turbine Noise Using Optimized.* 2009. pp. 1470-1481.

13. **Manwell J.F., MCGowan J.G., Rogers A.L.** *Wind Energy Explained.* Chichester : John Wiley & Sons Ltd., 2009.

14. **FFOWCS WILLIAMS, J. E. AND HALL, L. H.** *Aerodynamic Sound Generation by Turbulent Flow in the Vicinity of a Scattering Half Plane.* London : J. Fluid Mech., 1970. vol. 40, part 4, pp. 657-670.

15. **Schlichting, H.** *Boundary-Layer Theory.* New York : McGraw-Hill, 1979.

16. **Drela, M.** XFOIL 6.9 User Primer. [Online] November 30, 2001. [Cited: 10 15, 2014.] http://web.mit.edu/drela/Public/web/xfoil/xfoil_doc.txt.

17. **Oerlemans, S. and Gooden J.H.M.** *Acoustic and Aerodynamic Wind Tunnel Tests on a Flat Plate.* Amsterdam : National Aerospace Laboratory NLR, 2012.

18. **Young, W. C. and Budynas, R. G.** *Roark's Formulas for Stress and Strain.* s.l. : McGraw-Hill, 2002.

19. **Hah, C., Lakshminarayna, B.** *Measurement and prediction of mean velocity and.* 1982. pp. 251-282.

20. **Brooks, T.F. and Marcolini, M.A.** *Airfoil Trailing Edge Flow Measurements and Comparison with Theory Incorporating Open Wind Tunnel Corrections.* New York : American Institute of Aeronautics and Astronautics, 1984.

21. History of Wind Energy. *Office of Energy Efficiency & Renewable Energy.* [Online] 07 17, 2014. http://Energy.gov.

22. **Braslow, A. L et al.** *Use of Grit-Type Boudary-Layer-Transition Trips on Wind-Tunnel Models.* Washington, D.C. : National Aeronautics and Space Administration, 1966.

23. **Von Doenhoff, A. E. and Horton, E. A.** *A Low-Speed Experimental Investigation of the Effect of a Sandpaper Type of Roughness on Boundary-Layer Transition.* Langley Field : Langley Aeronautical Laboratory, National Advisory Committee for Aeronautics, 1956.

24. **Doolan, C. et al.** *Trailing Edge Noise Production, Prediction and Control.* 2012.

25. **Kerho M. F. and Bragg, M. B.** *Airfoil Boundary-Layer Development and Transition with Large Leading-Edge Roughness.* 1997.

Appendix A Comparison of Displacement thicknesses at Different Reynolds Numbers

Appendix A.1 Reynolds Number 0.206×10^6, meaning c = 0.15 m and U_∞ = 20 m/s

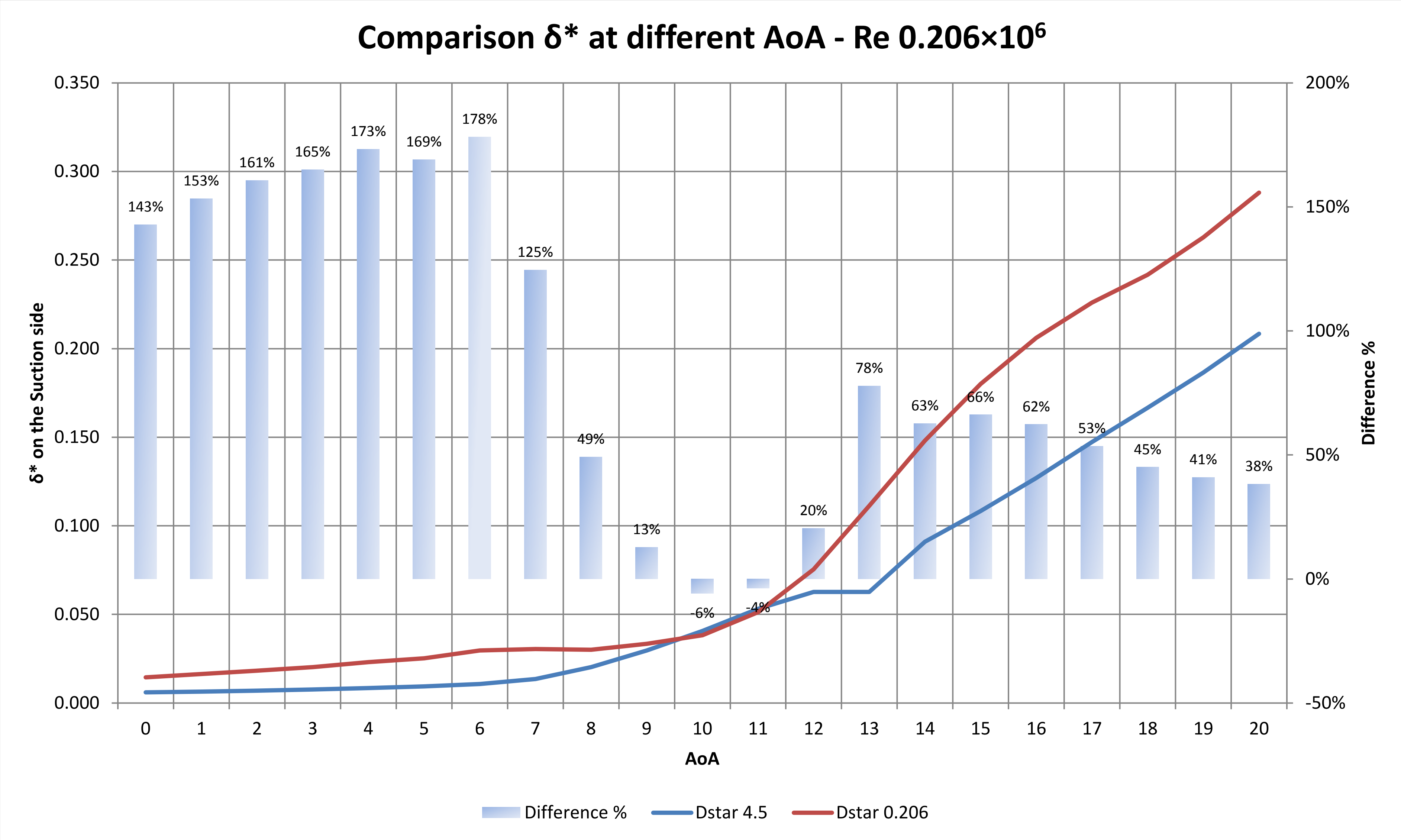

Figure 129 - Comparison δ at different AoA – Re = 0.206×10^6*

Appendix A.2 Reynolds Number 0.412×10^6, meaning c = 0.15 m and U_∞ = 40 m/s

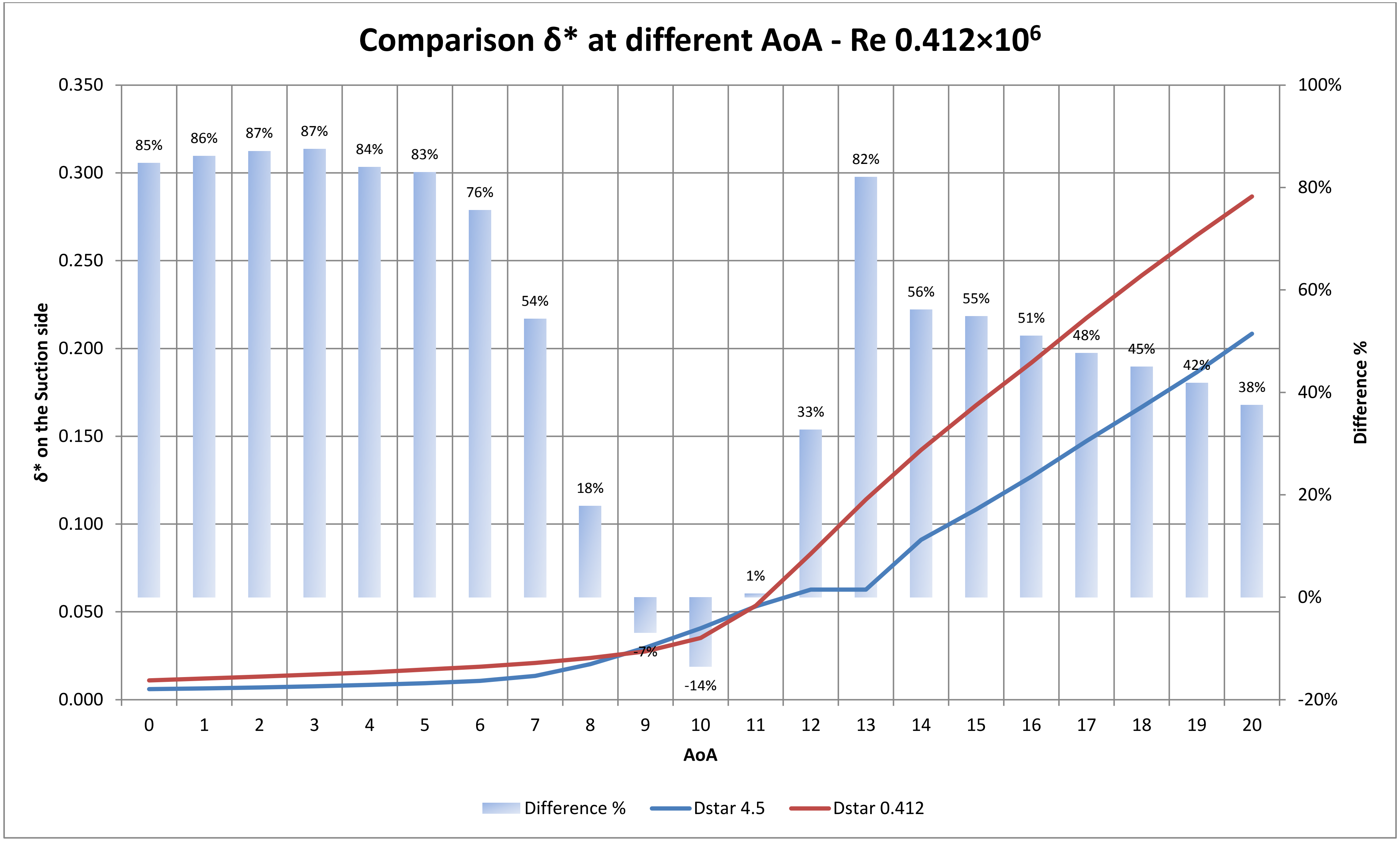

Figure 130 - Comparison δ at different AoA – Re = 0.412×10^6*

Appendix A.3 Reynolds Number 0.96×10^6, meaning c = 0.20 m and U_∞ = 70 m/s

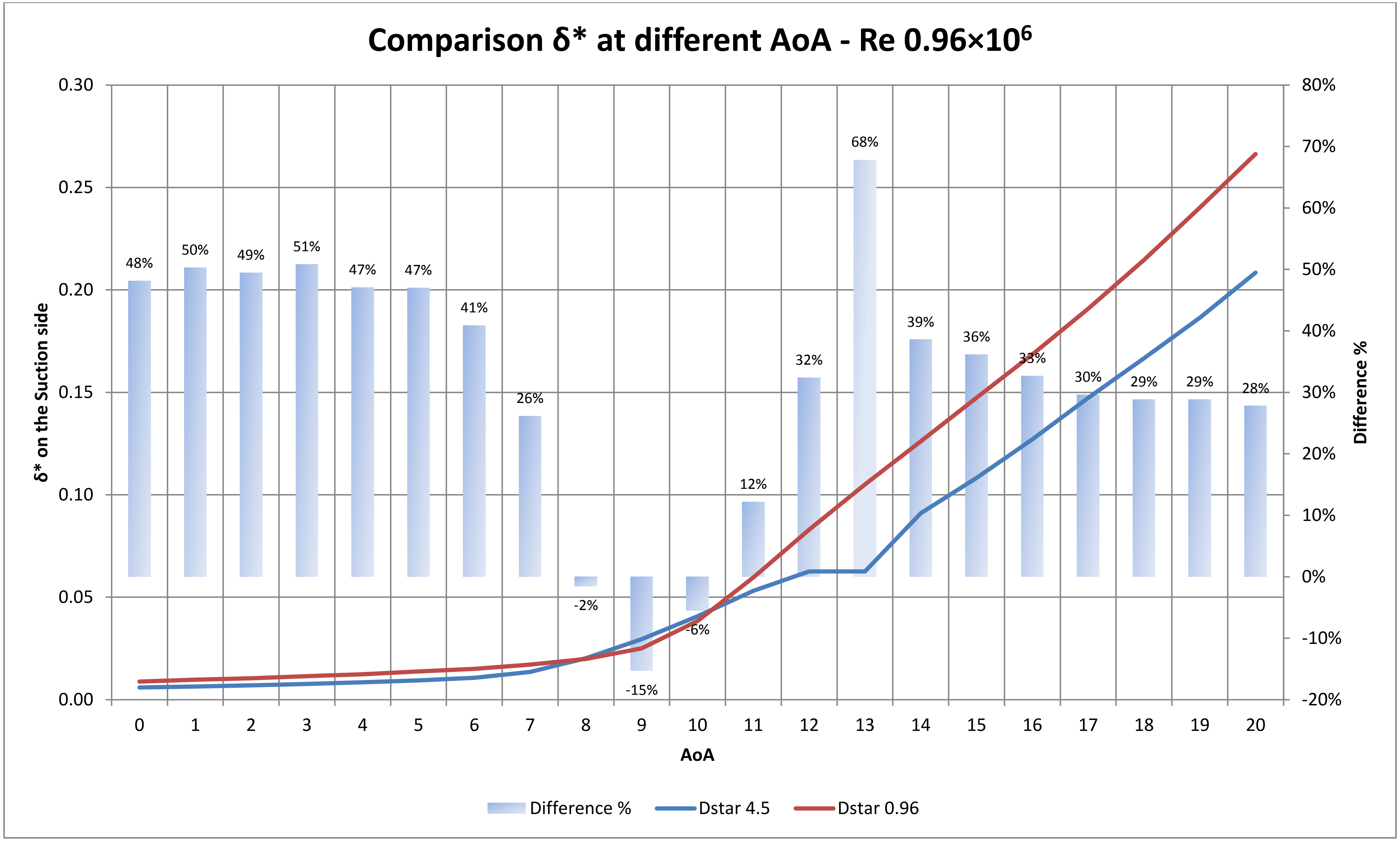

Figure 131 - Comparison δ at different AoA – Re = 0.96×10^6*

Appendix B Acoustic Source Maps

a) Clean Configuration

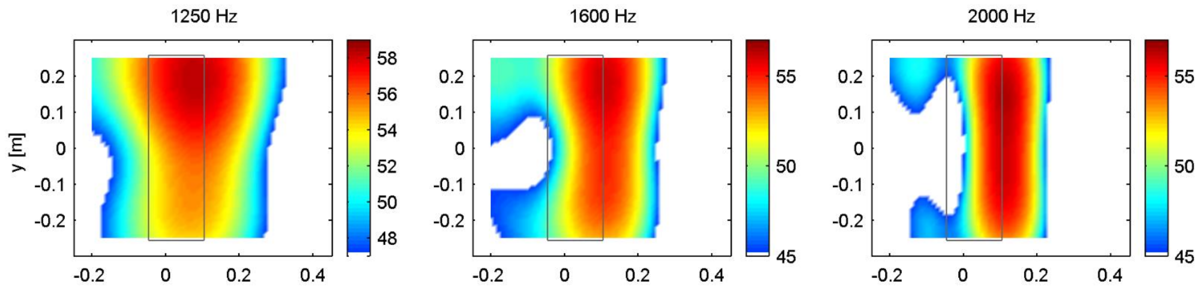

b) Serration Fixed on the Pressure Side

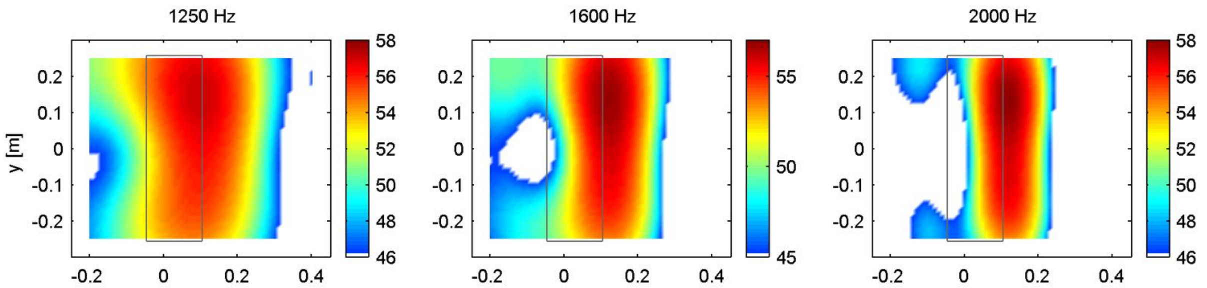

c) Flexible Serration

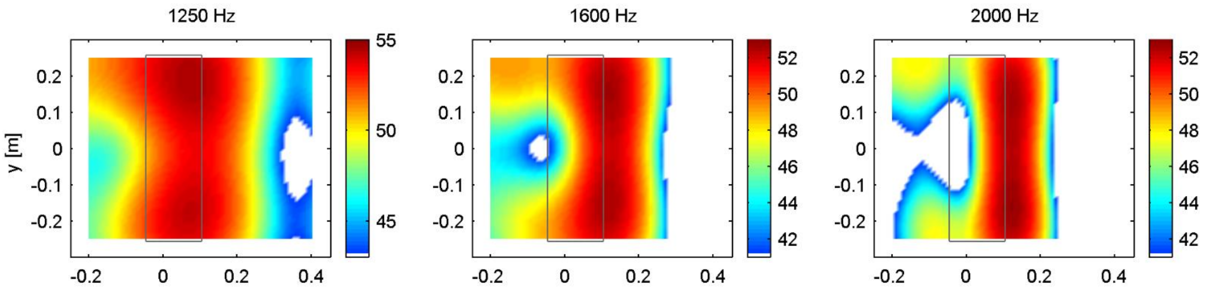

d) Cutted Serration

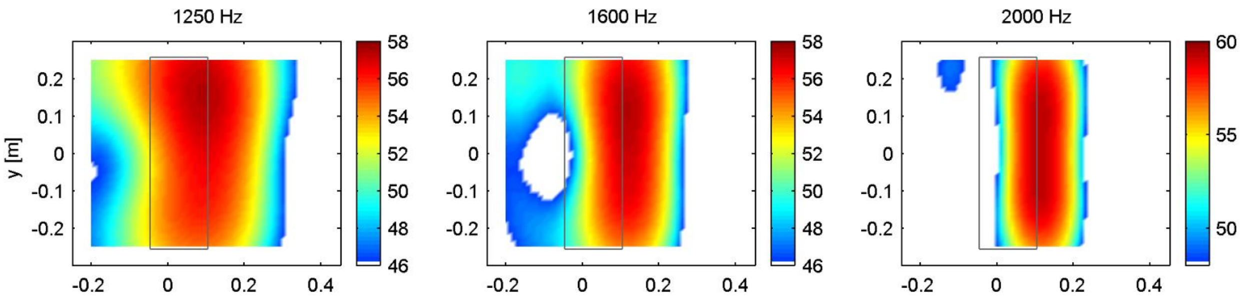

e) Serration with Cutted Plate

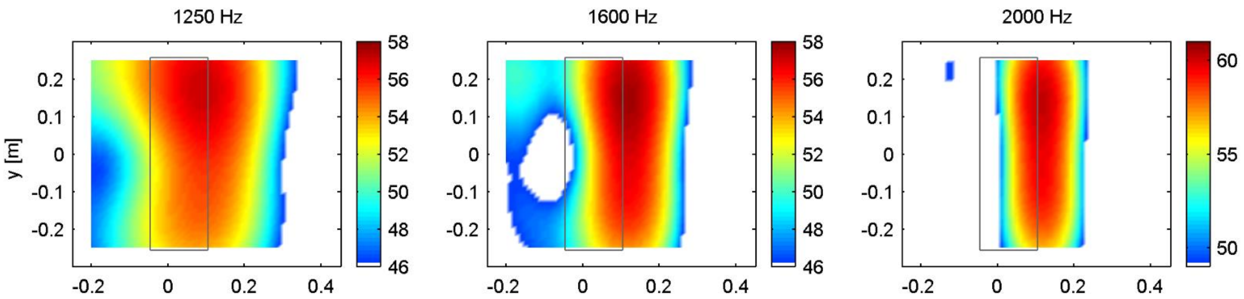

Figure 132 – **Low Frequency Acoustic Maps – Free stream velocity 40 m/s; AoA = 0° (α_{eff} = 0°)**

a) Clean Configuration

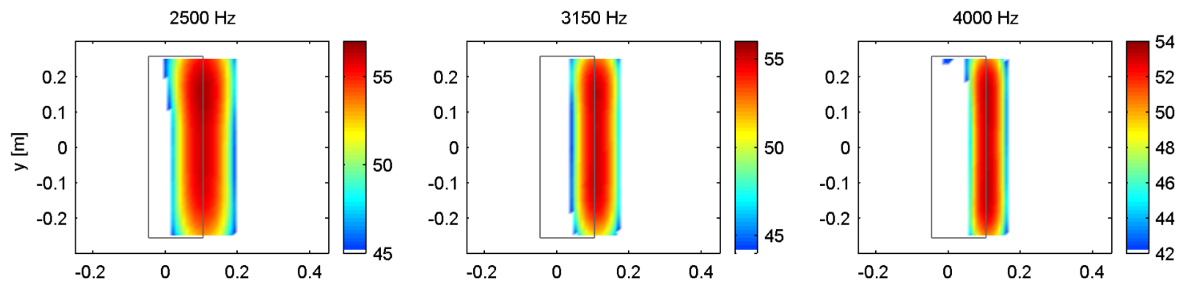

b) Serration Fixed on the Pressure Side

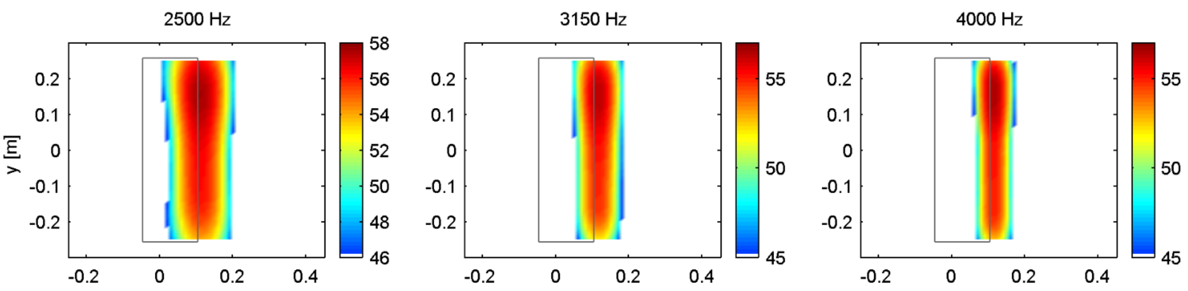

c) Flexible Serration

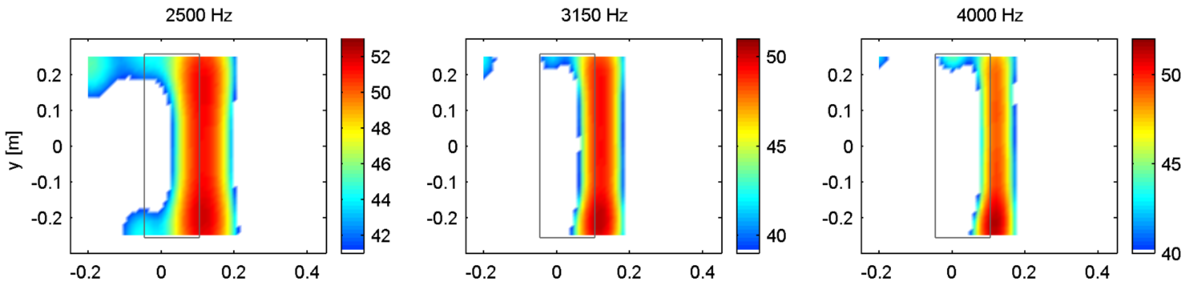

d) Cutted Serration

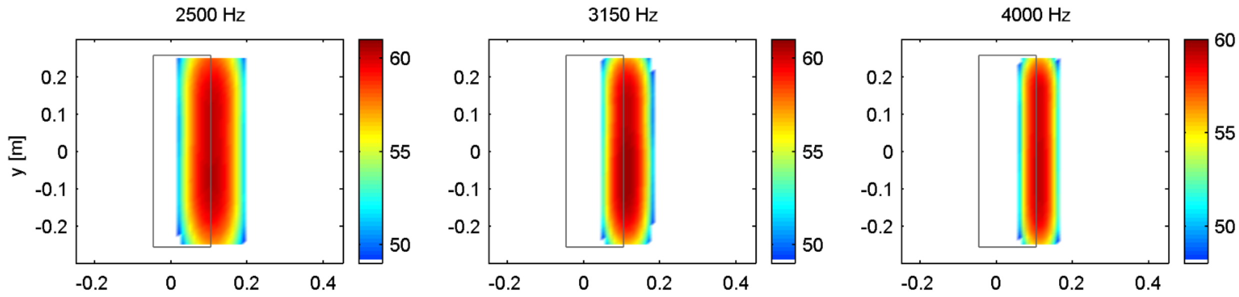

e) Serration with Cutted Plate

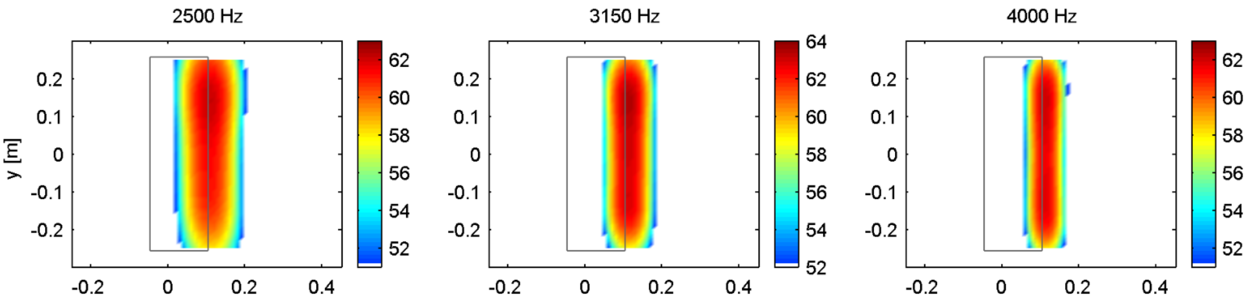

Figure 133 – **Medium Frequency Acoustic Maps – Free stream velocity 40 m/s; AoA = 0° (α_{eff} = 0°)**

a) Clean Configuration

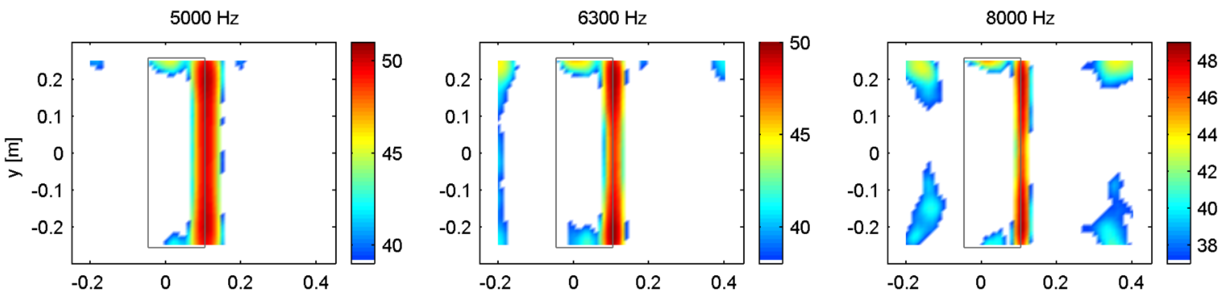

b) Serration Fixed on the Pressure Side

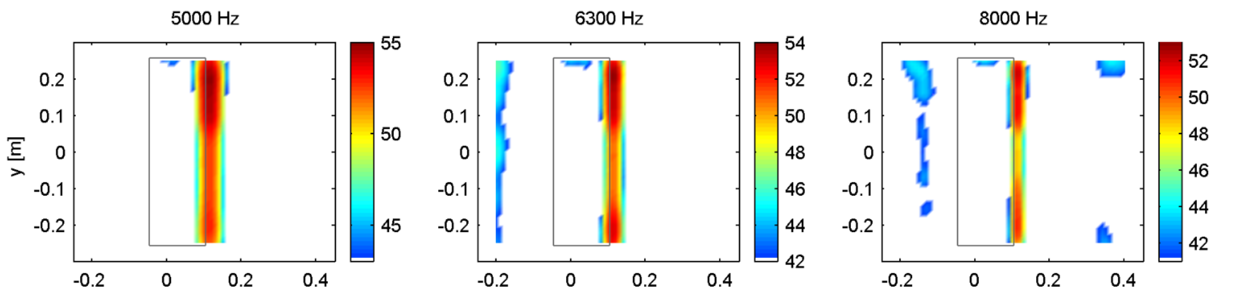

c) Flexible Serration

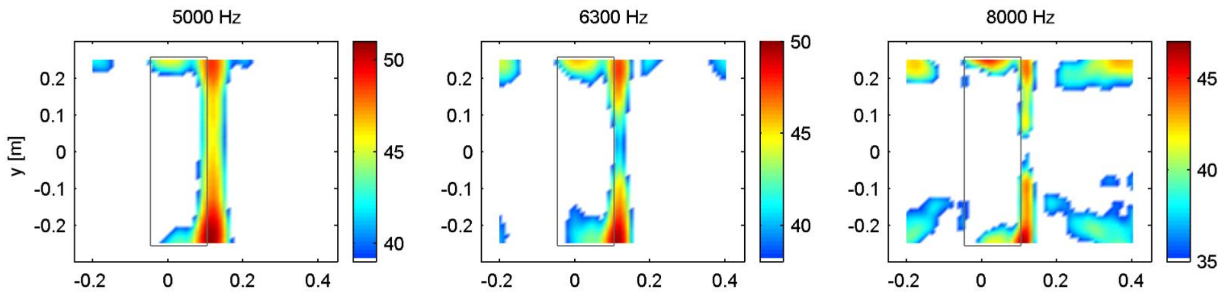

d) Cutted Serration

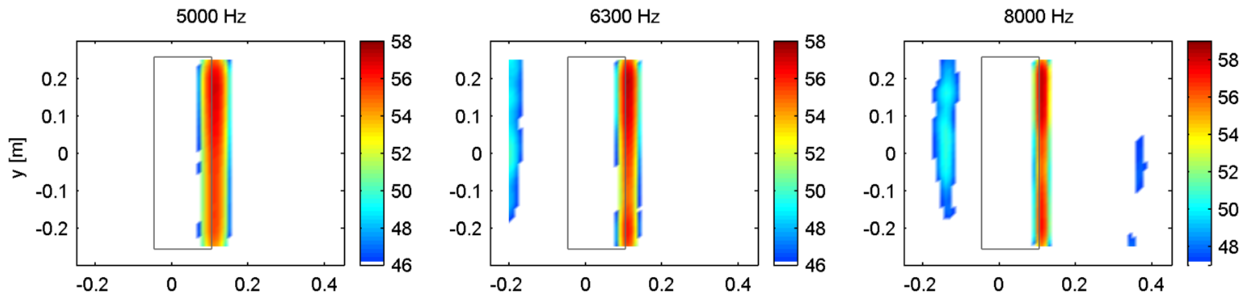

e) Serration with Cutted Plate

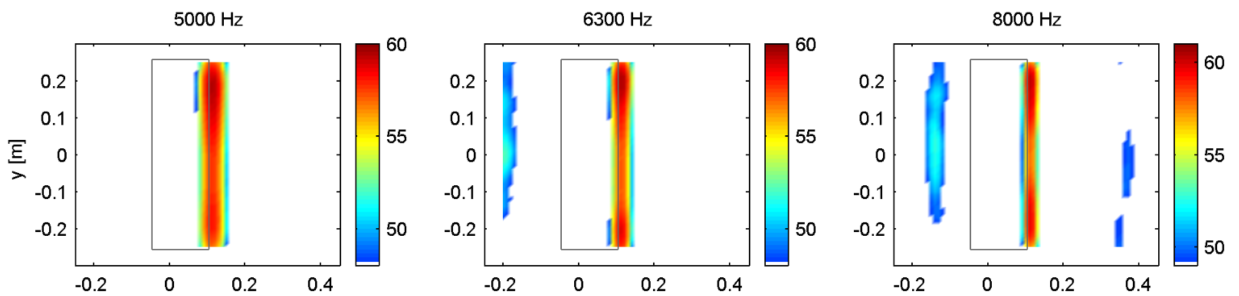

Figure 134 **– High Frequency Acoustic Maps – Free stream velocity 40 m/s; AoA = 0° (α_{eff} = 0°)**

a) Clean Configuration

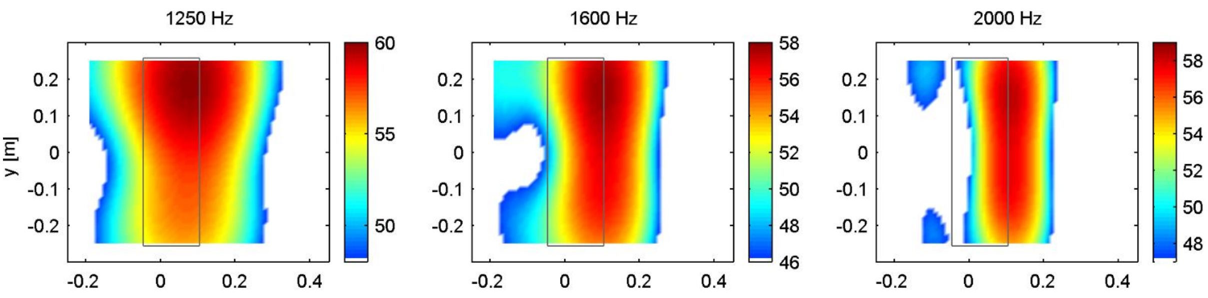

b) Serration Fixed on the Pressure Side

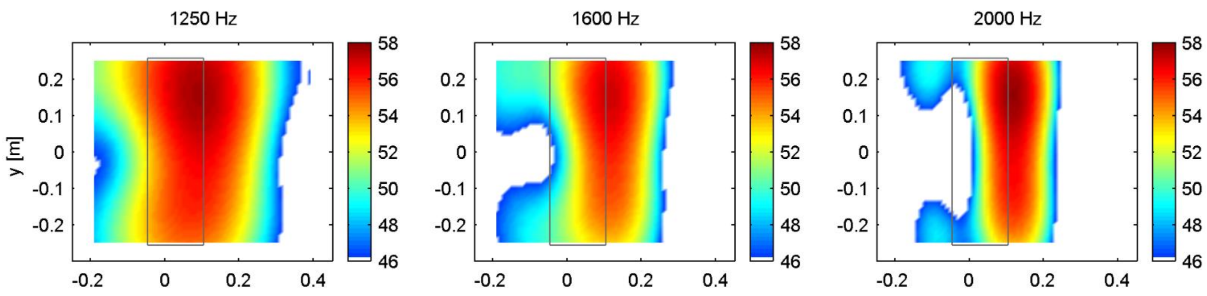

c) Serration Fixed on the Suction Side

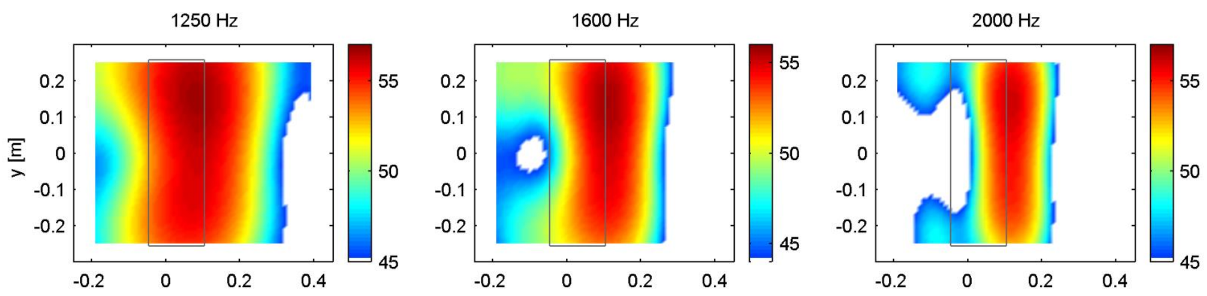

d) Flexible Serration

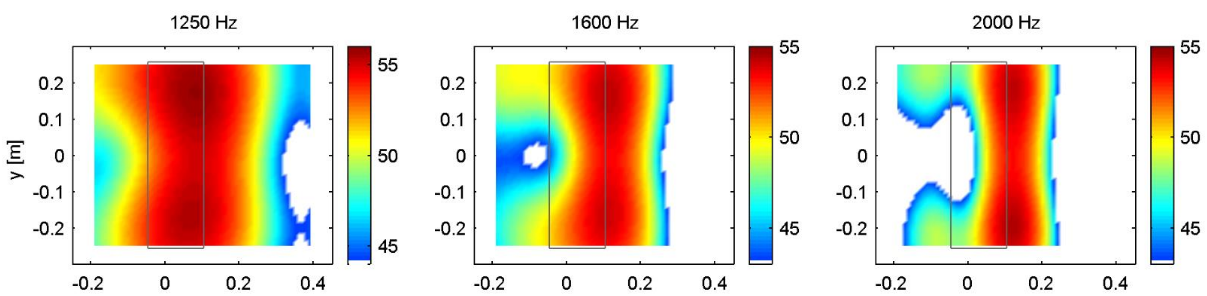

e) Cutted Serration

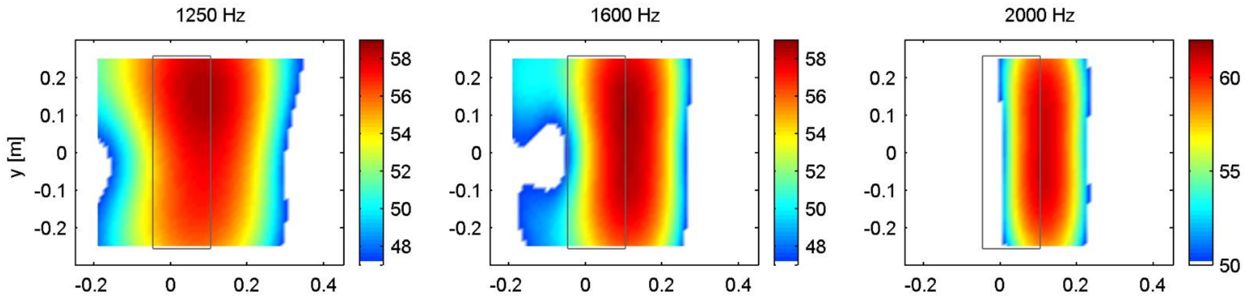

f) Serration with Cutted Plate

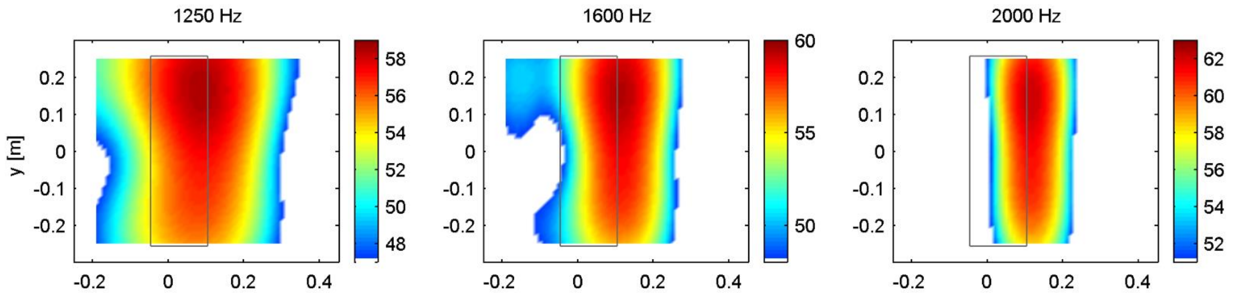

Figure 135 – **Low Frequency Acoustic Maps – Free stream velocity 40 m/s; AoA = 6° (α_{eff} = 3.4°)**

a) Clean Configuration

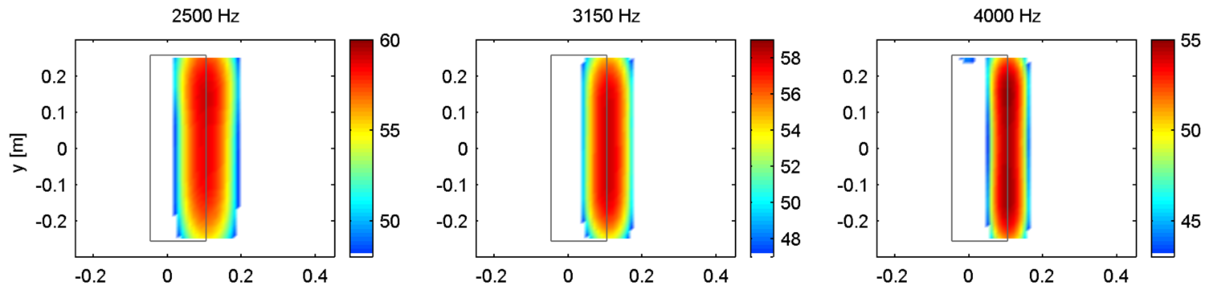

b) Serration Fixed on the Pressure Side

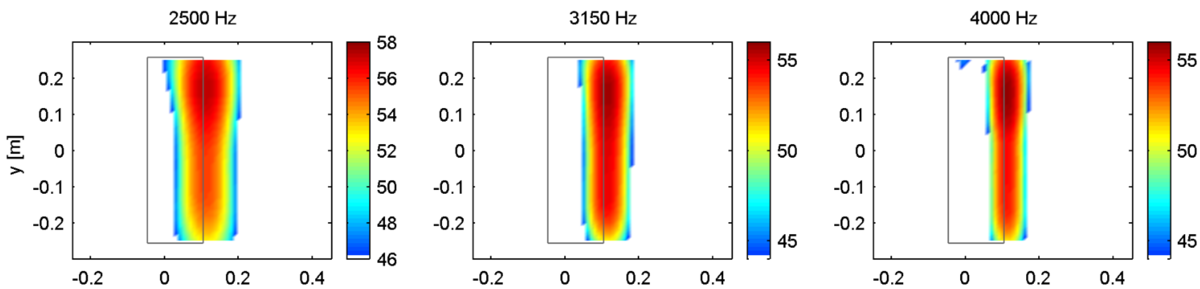

c) Serration Fixed on the Suction Side

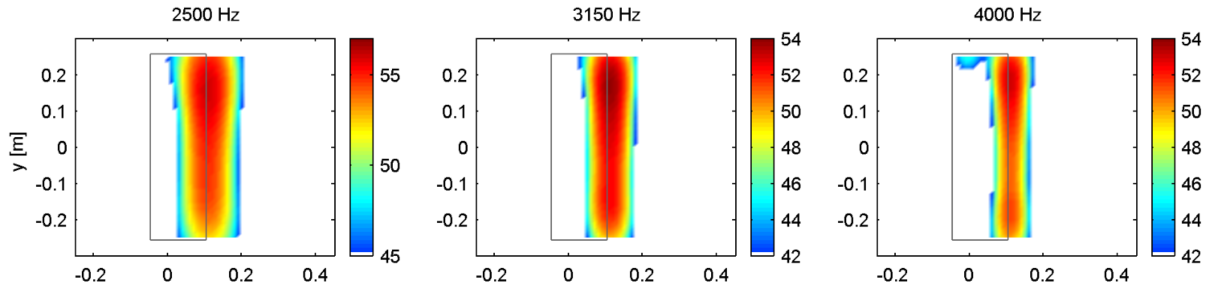

d) Flexible Serration

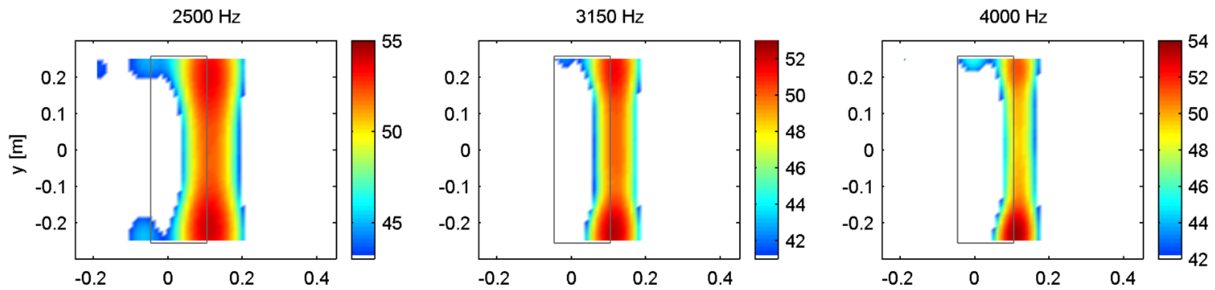

e) Cutted Serration

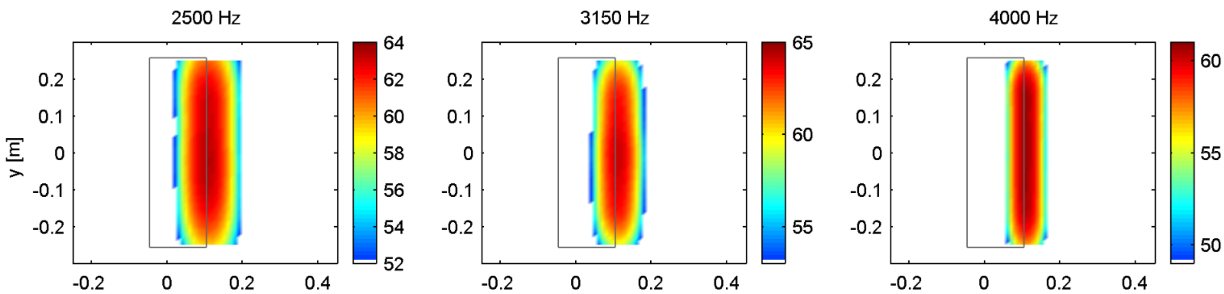

f) Serration with Cutted Plate

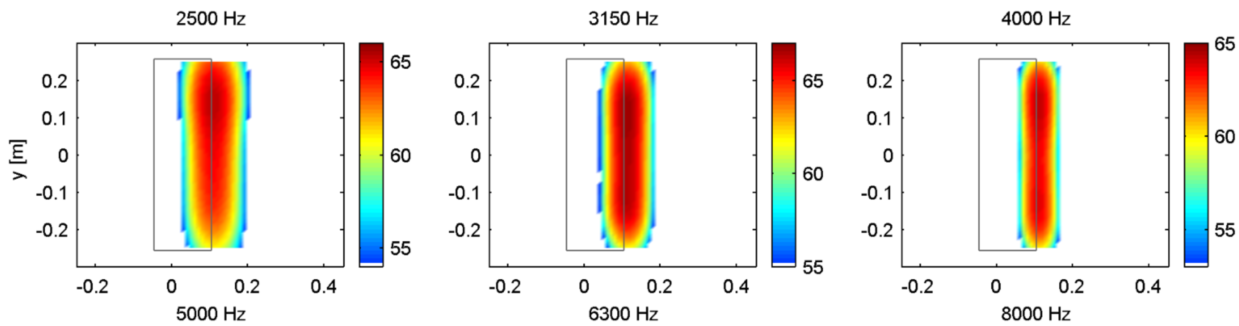

Figure 136 – **Medium Frequency Acoustic Maps – Free stream velocity 40 m/s; AoA = 6° (α_{eff} = 3.4°)**

a) Clean Configuration

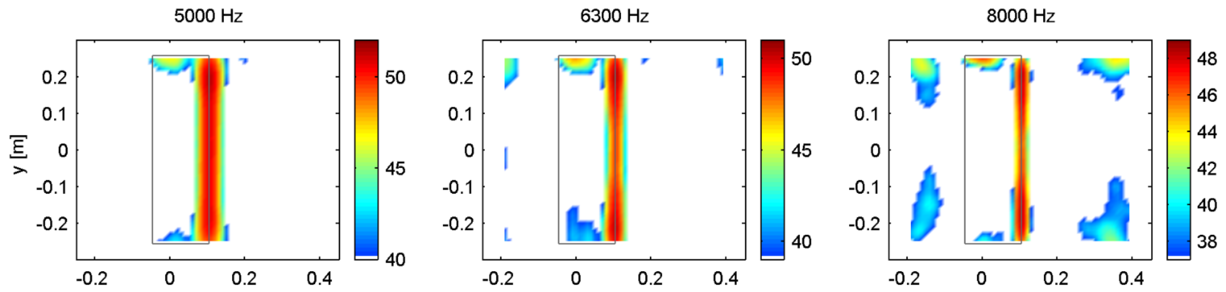

b) Serration Fixed on the Pressure Side

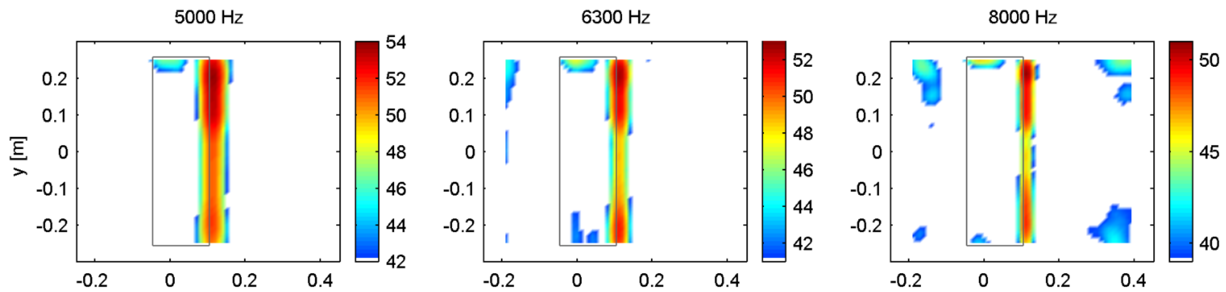

c) Serration Fixed on the Suction Side

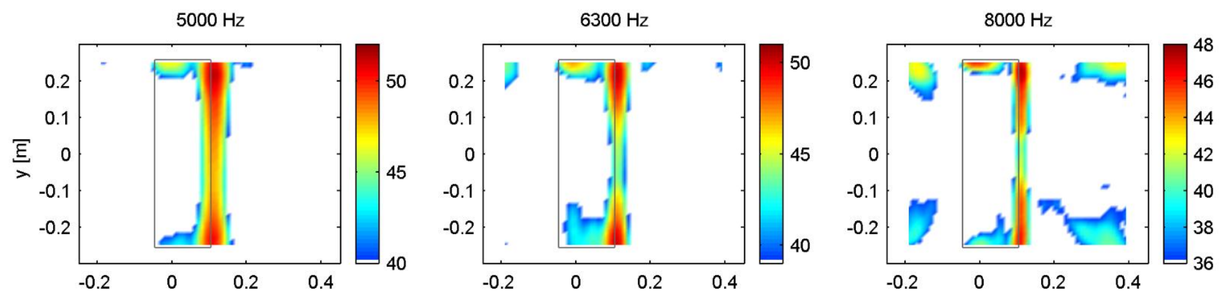

d) Flexible Serration

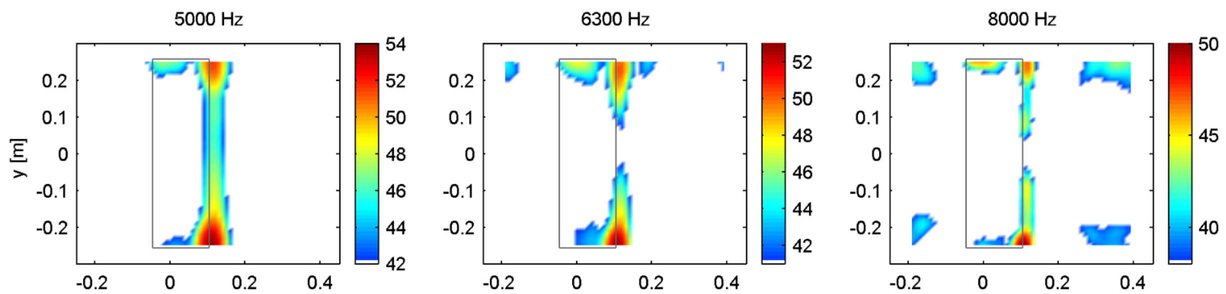

e) Cutted Serration

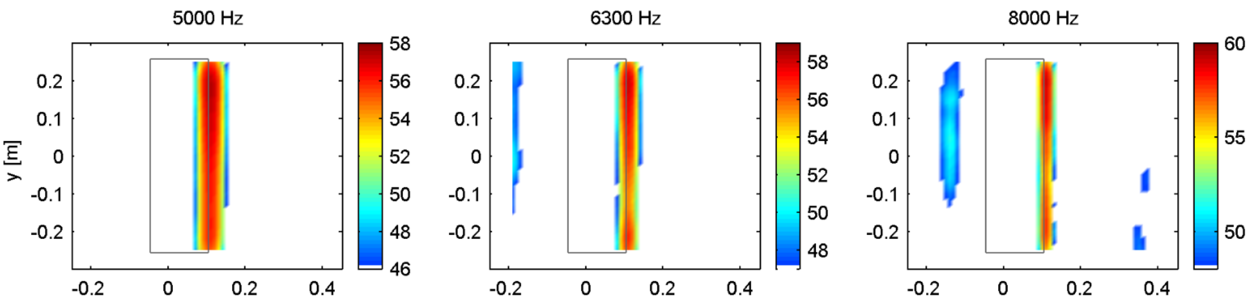

f) Serration with Cutted Plate

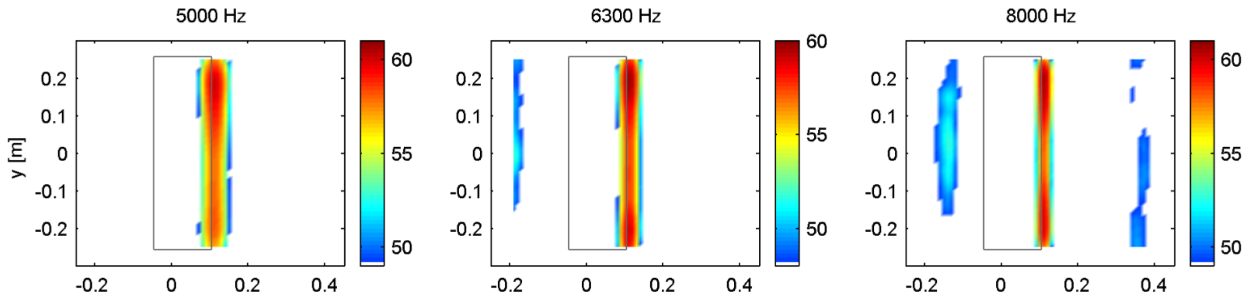

Figure 137 – **High Frequency Acoustic Maps – Free stream velocity 40 m/s; AoA = 6° (α_{eff} = 3.4°)**

a) Clean Configuration

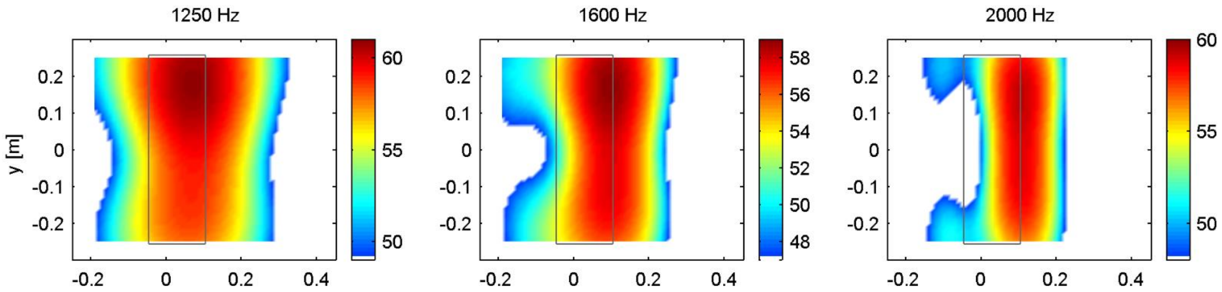

b) Serration Fixed on the Pressure Side

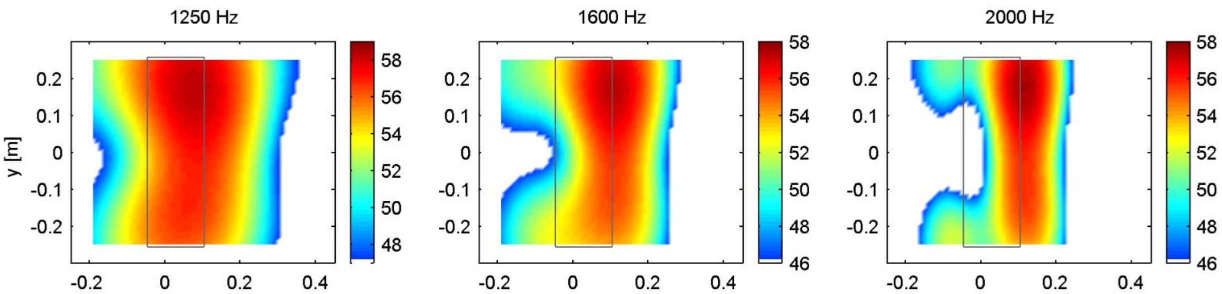

c) Serration Fixed on the Suction Side

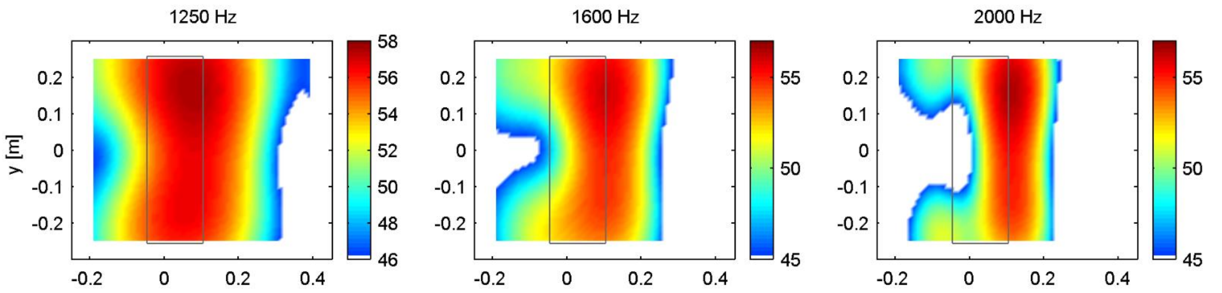

d) Flexible Serration

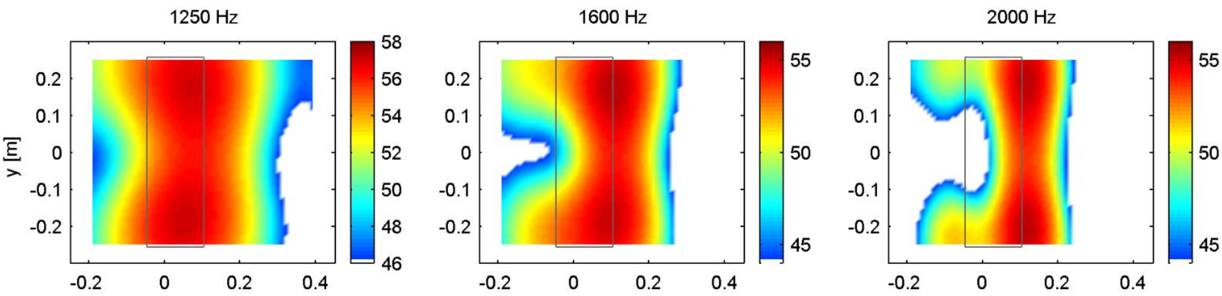

e) Cutted Serration

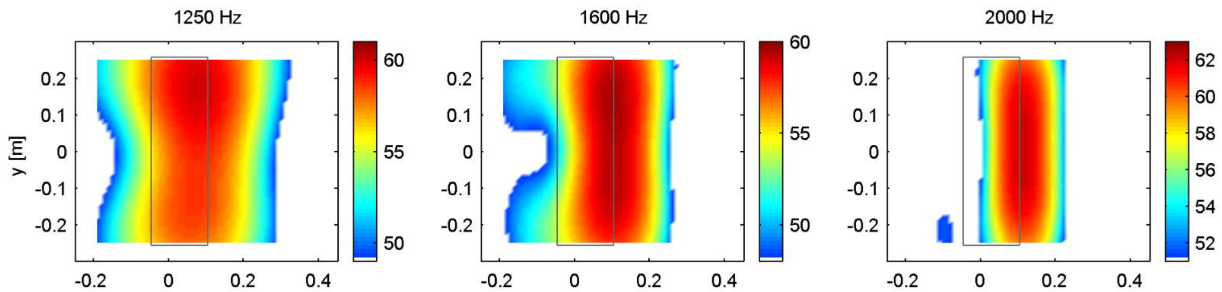

f) Serration with Cutted Plate

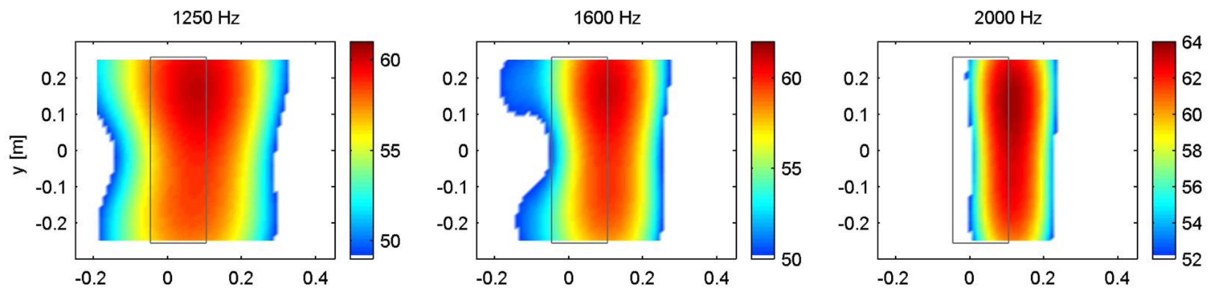

Figure 138 **– Low Frequency Acoustic Maps – Free stream velocity 40 m/s; AoA = 10.51° (α_{eff} = 6°)**

a) Clean Configuration

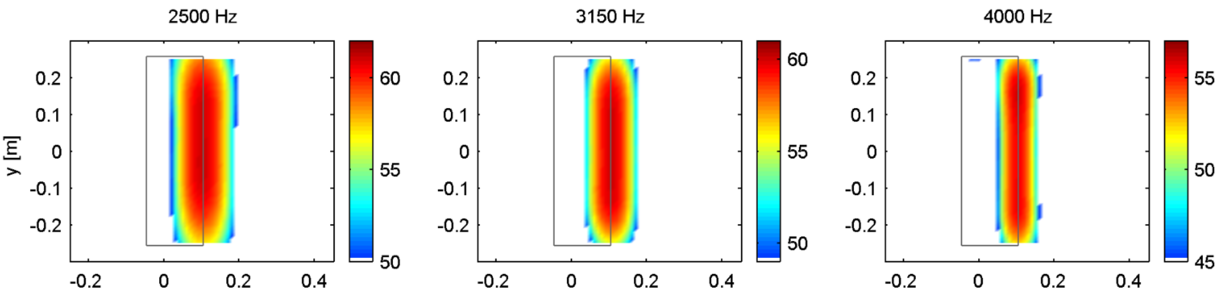

b) Serration Fixed on the Pressure Side

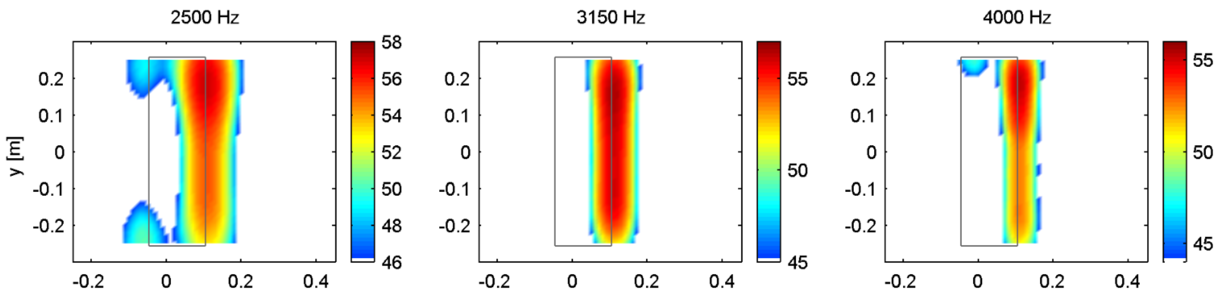

c) Serration Fixed on the Suction Side

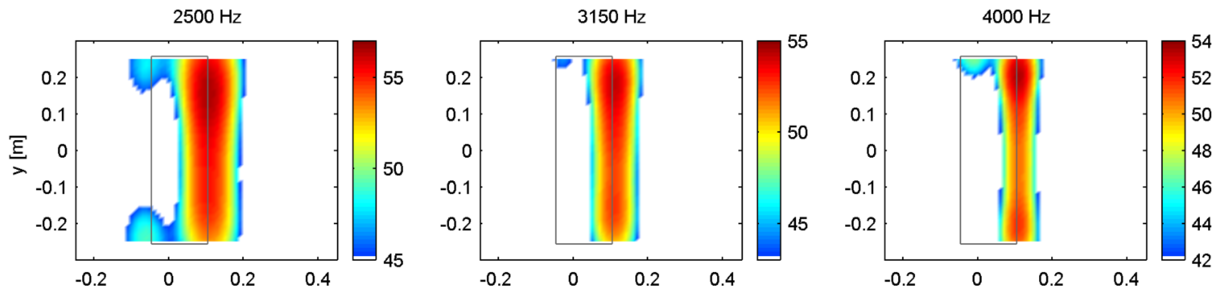

d) Flexible Serration

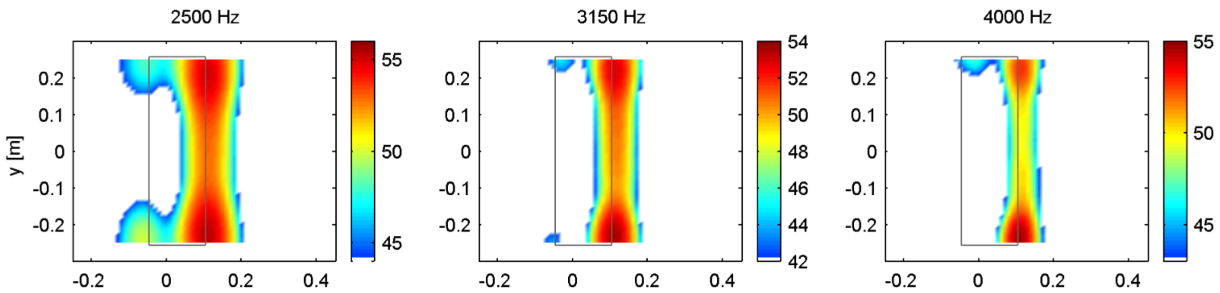

e) Cutted Serration

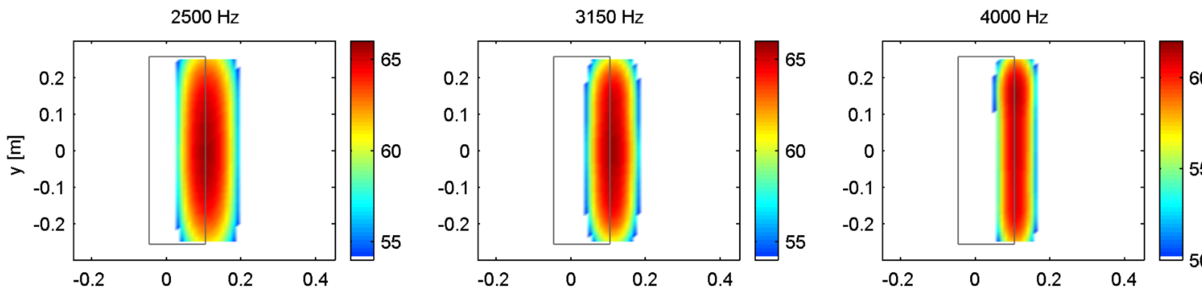

f) Serration with Cutted Plate

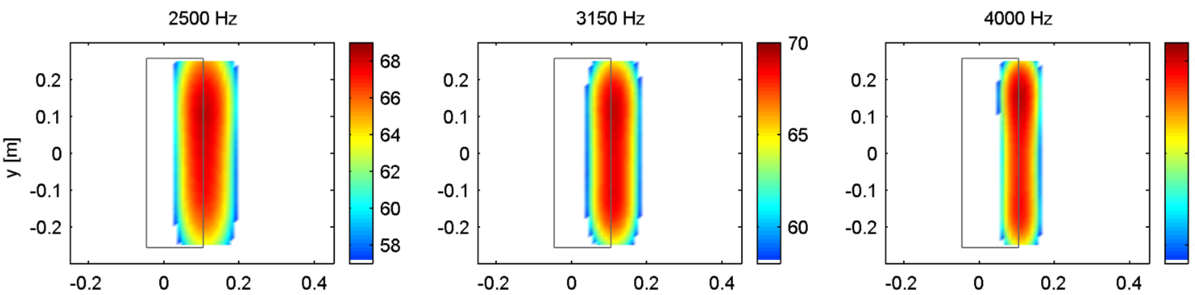

Figure 139 – **Medium Frequency Acoustic Maps – Free stream velocity 40 m/s; AoA = 10.51° (α_{eff} = 6°)**

a) Clean Configuration

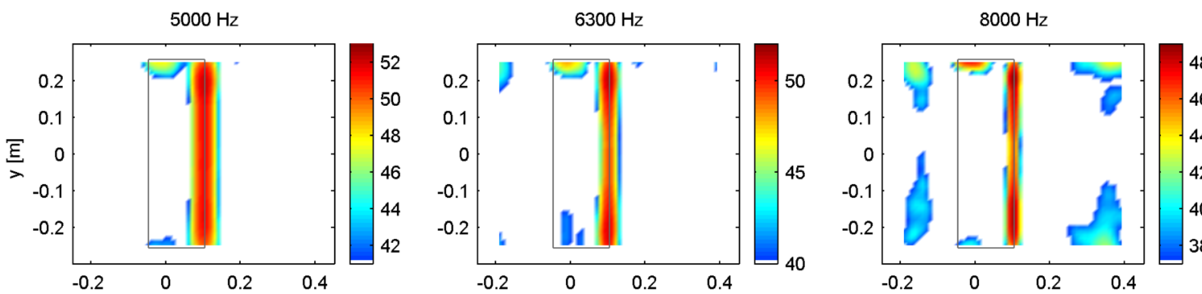

b) Serration Fixed on the Pressure Side

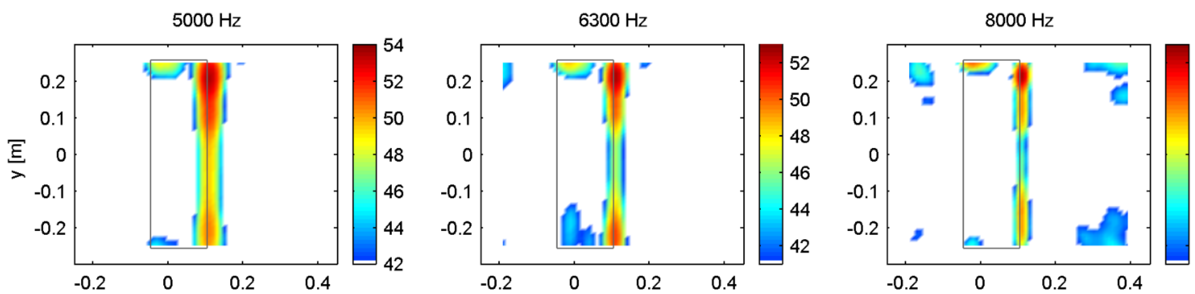

c) Serration Fixed on the Suction Side

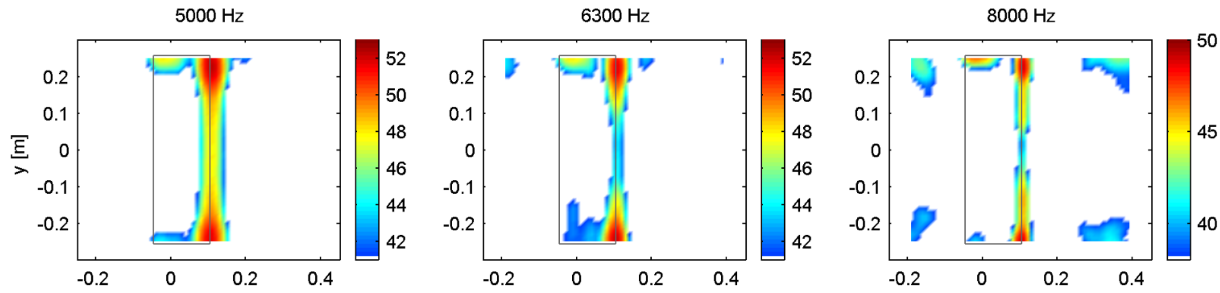

d) Flexible Serration

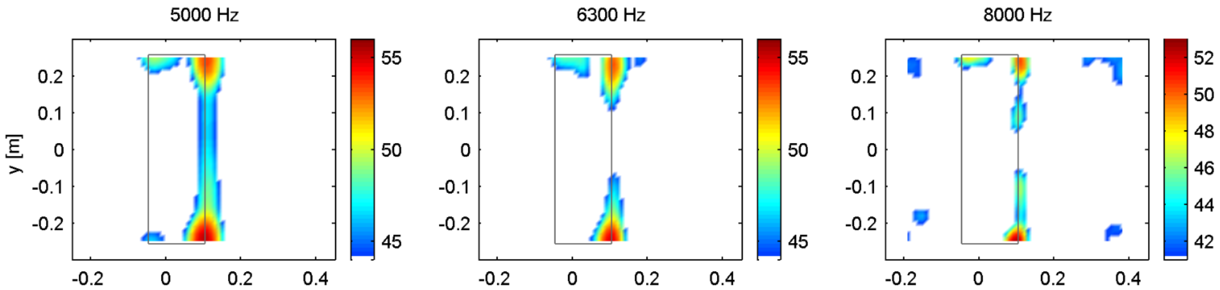

e) Cutted Serration

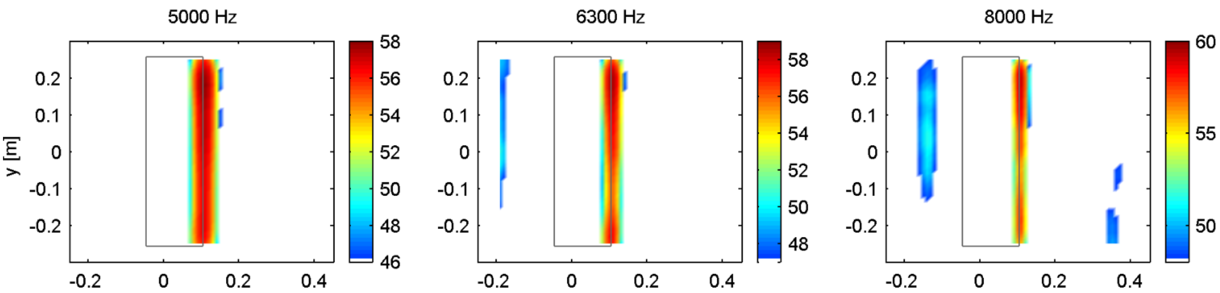

f) Serration with Cutted Plate

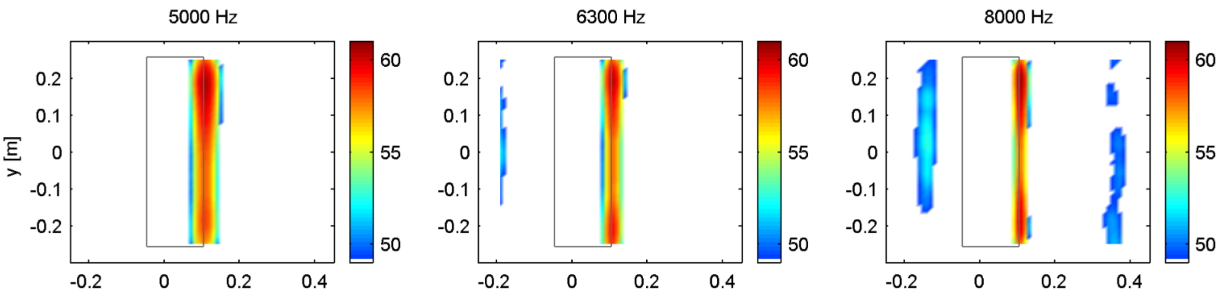

Figure 140 – **High Frequency Acoustic Maps – Free stream velocity 40 m/s; AoA = 10.51° (α_{eff} = 6°)**

a) Clean Configuration

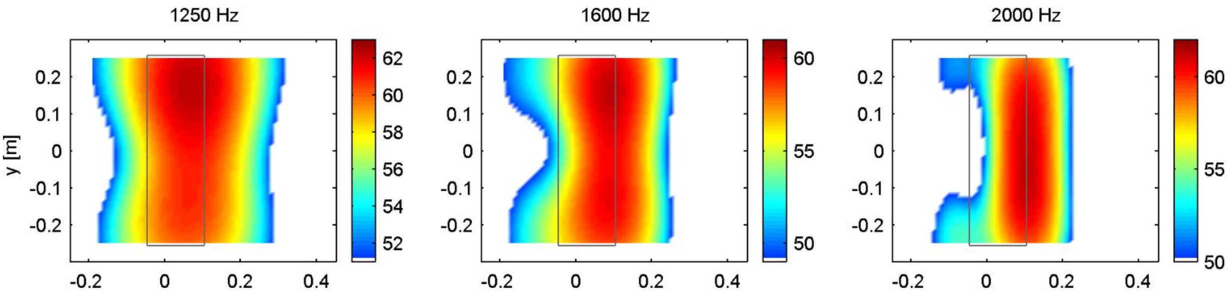

b) Serration Fixed on the Pressure Side

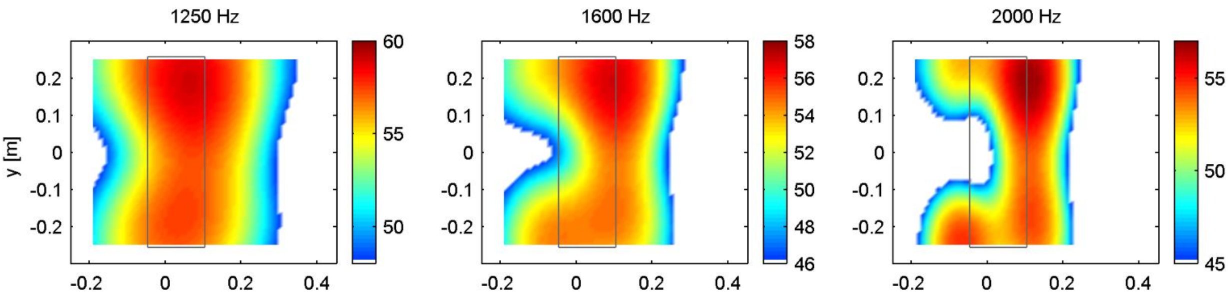

c) Serration Fixed on the Suction Side

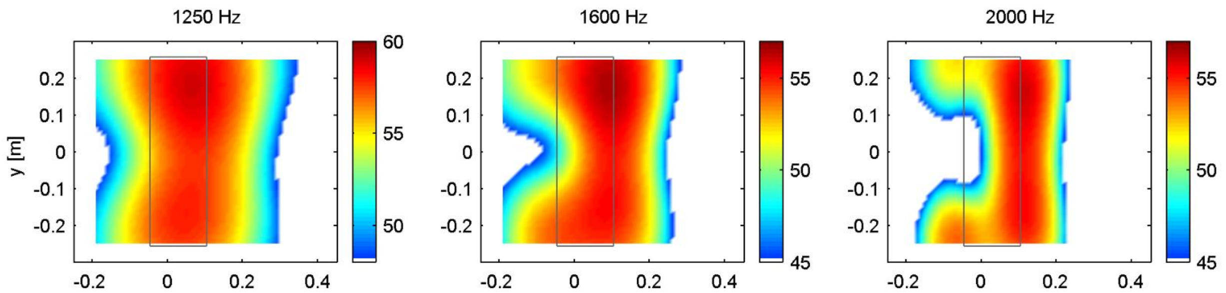

d) Flexible Serration

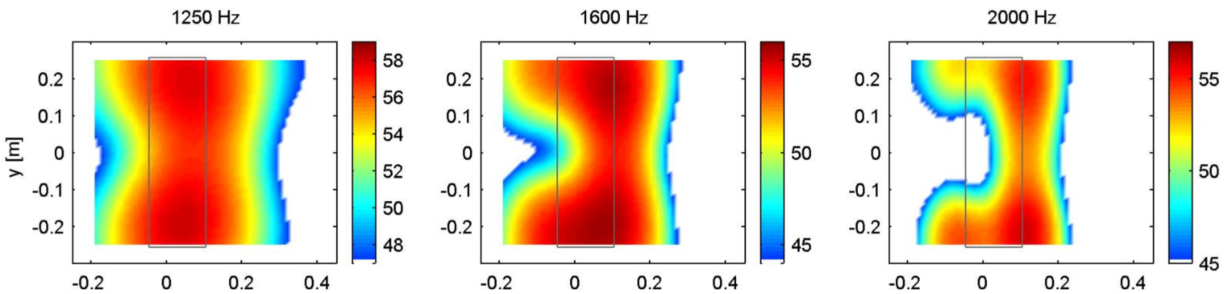

e) Cutted Serration

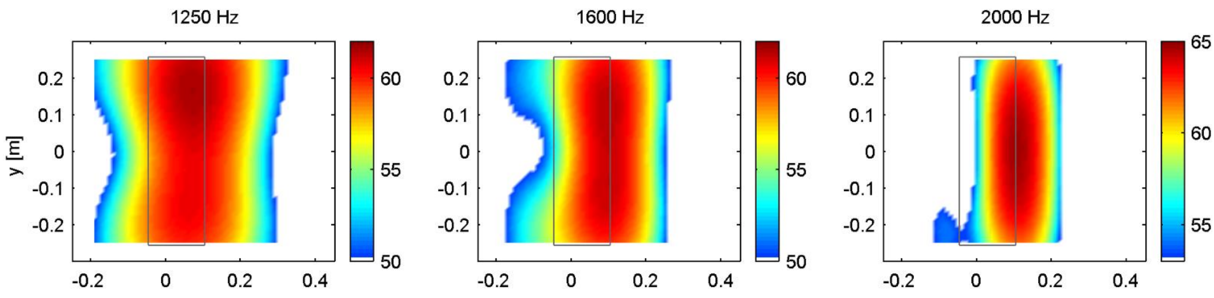

f) Serration with Cutted Plate

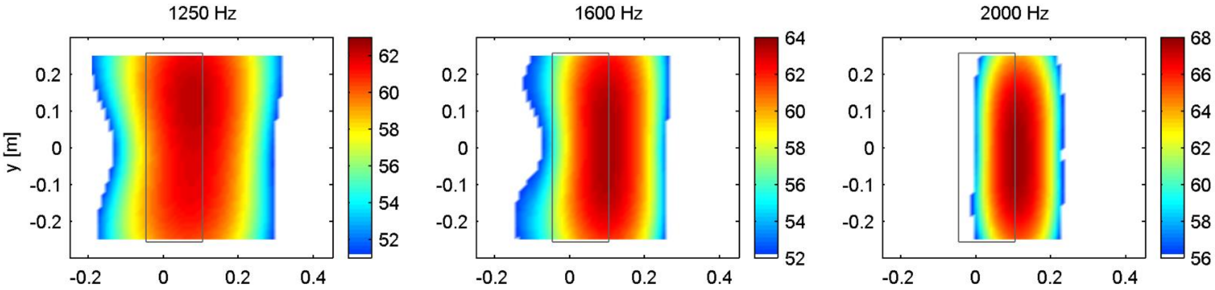

Figure 141 **– Low Frequency Acoustic Maps – Free stream velocity 40 m/s; AoA = 14.37° (α_{eff} = 8.2°)**

a) Clean Configuration

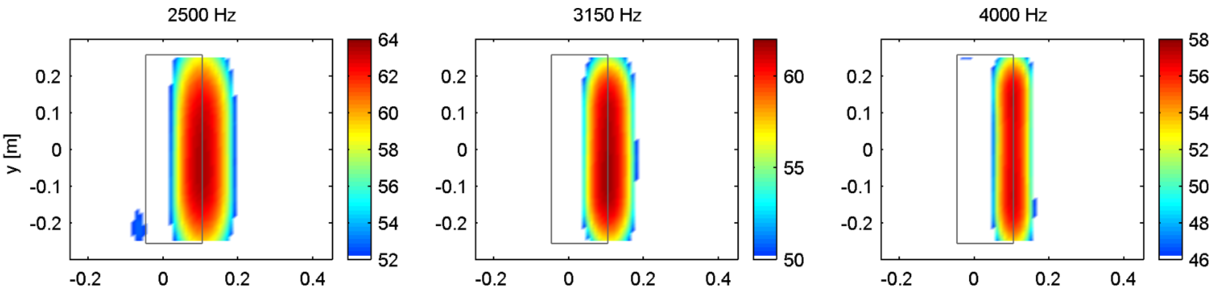

b) Serration Fixed on the Pressure Side

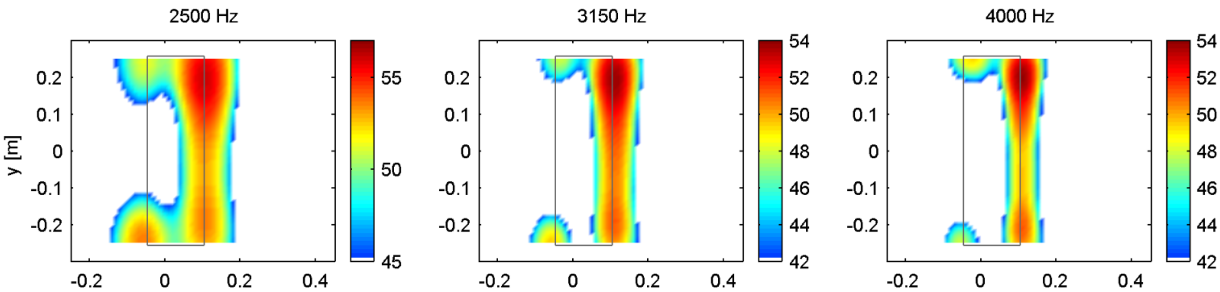

c) Serration Fixed on the Suction Side

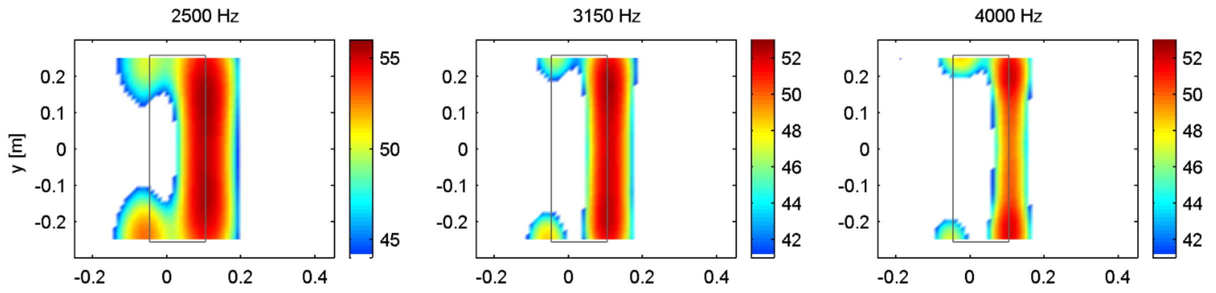

d) Flexible Serration

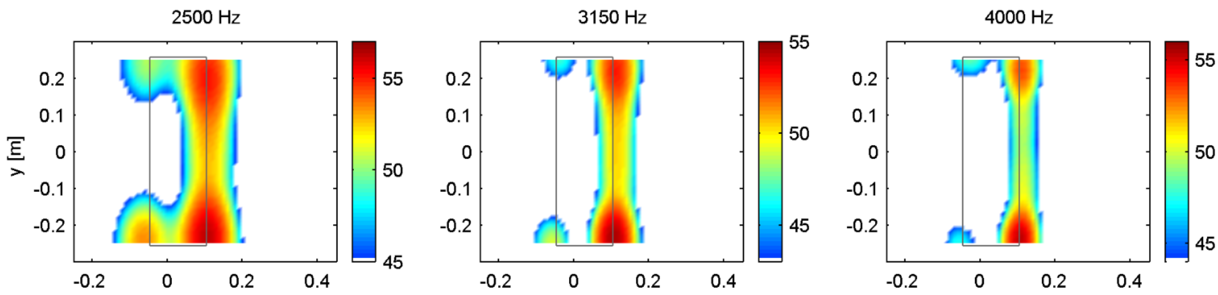

e) Cutted Serration

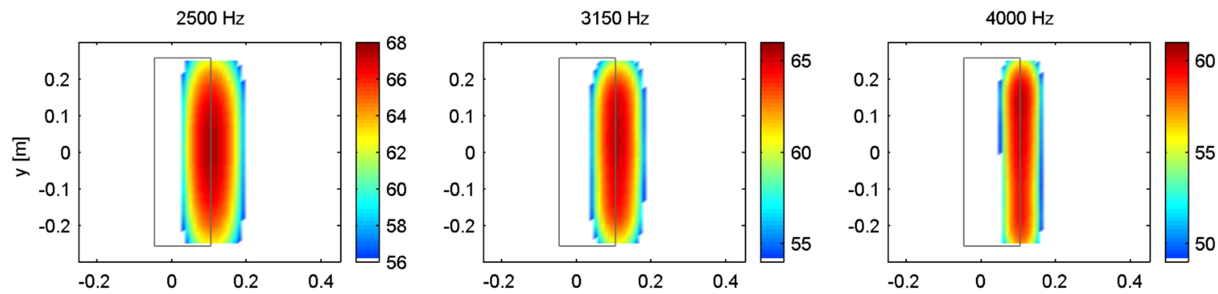

f) Serration with Cutted Plate

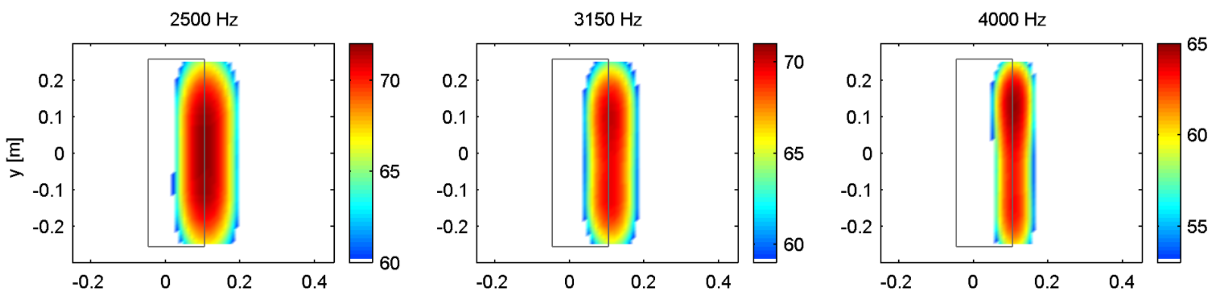

Figure 142 – **Medium Frequency Acoustic Maps – Free stream velocity 40 m/s; AoA = 14.37° (α_{eff} = 8.2°)**

a) Clean Configuration

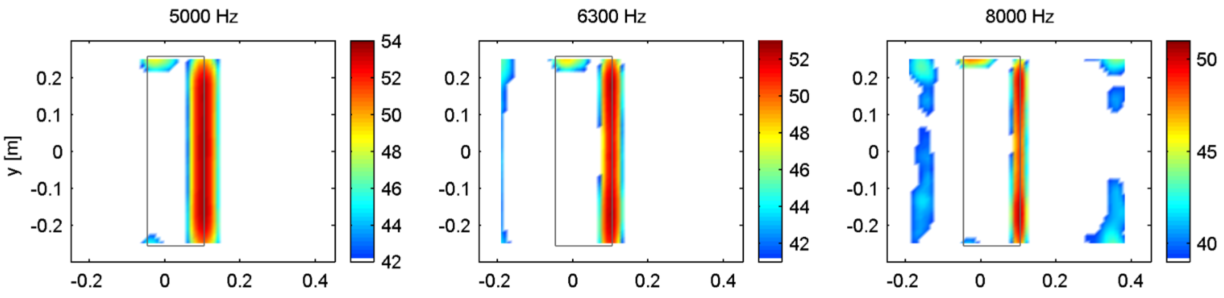

b) Serration Fixed on the Pressure Side

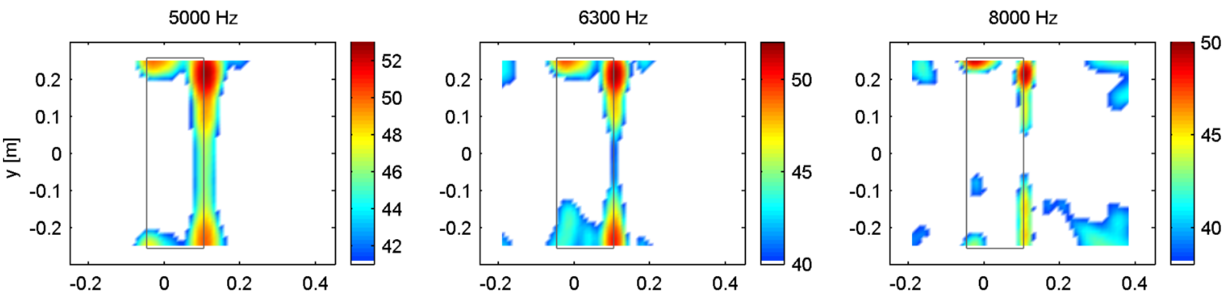

c) Serration Fixed on the Suction Side

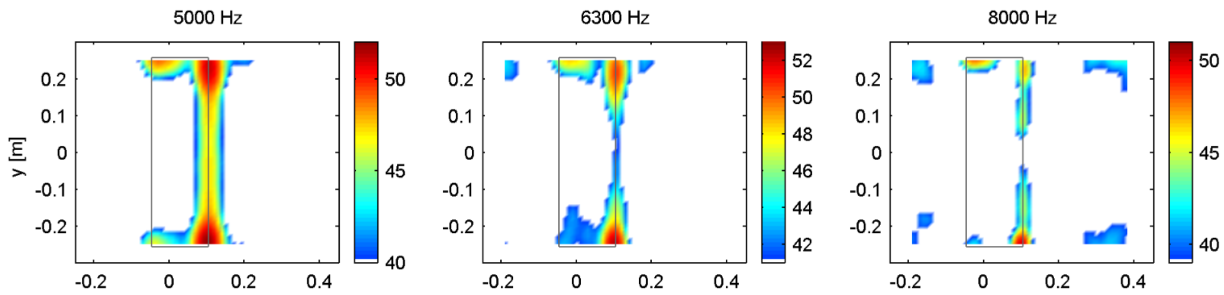

d) Flexible Serration

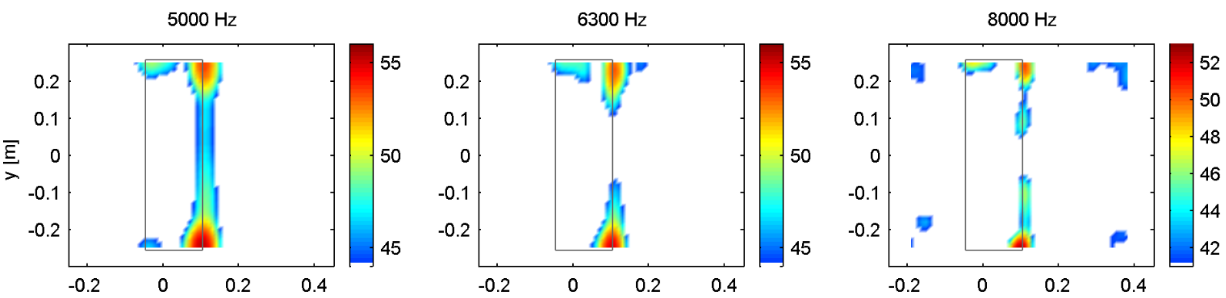

e) Cutted Serration

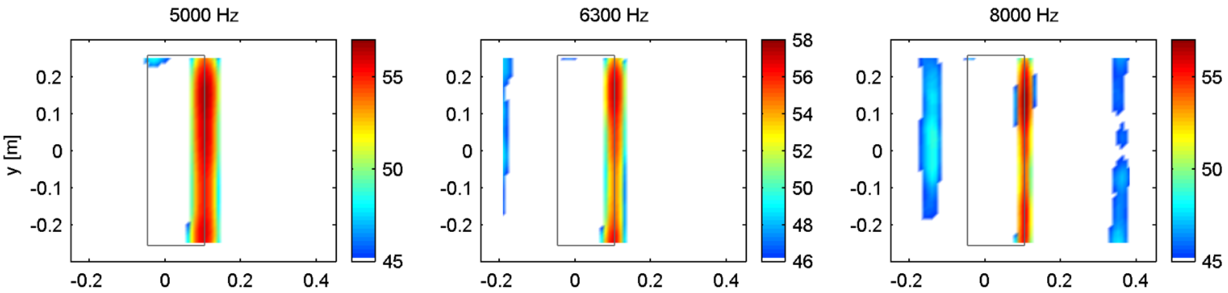

f) Serration with Cutted Plate

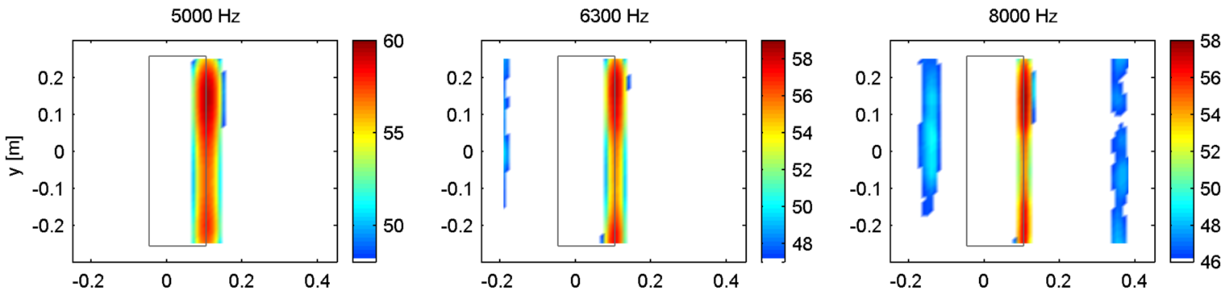

Figure 143 - **High Frequency Acoustic Maps – Free stream velocity 40 m/s; AoA = 14.37° (α_{eff} = 8.2°)**

a) Clean Configuration

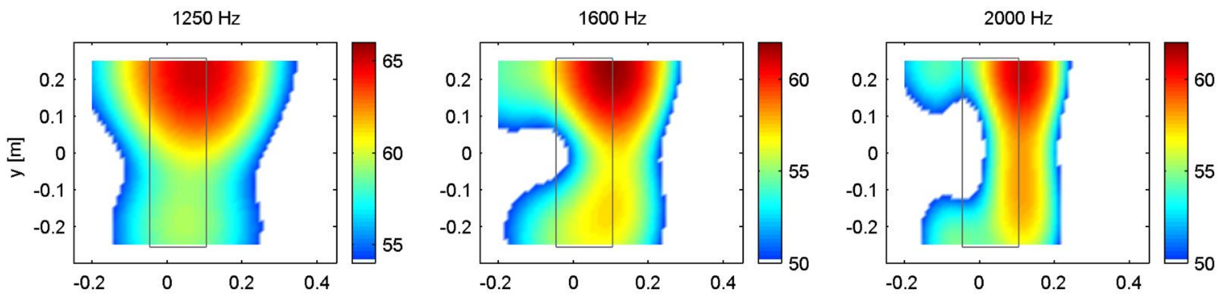

b) Serration Fixed on the Pressure Side

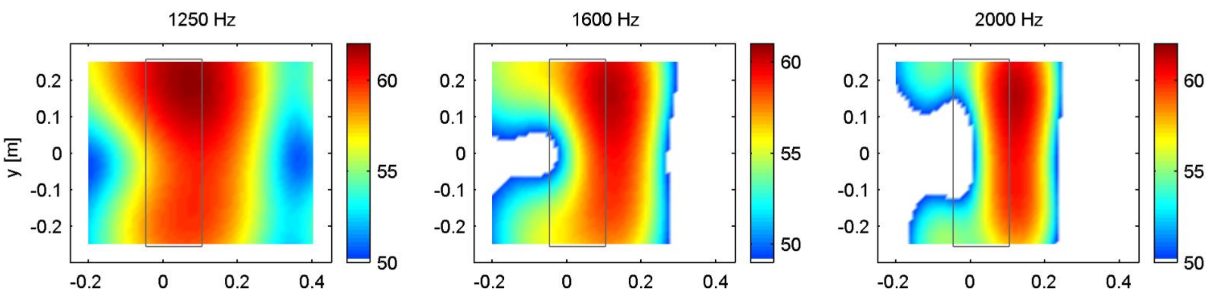

c) Serration Fixed on the Suction Side

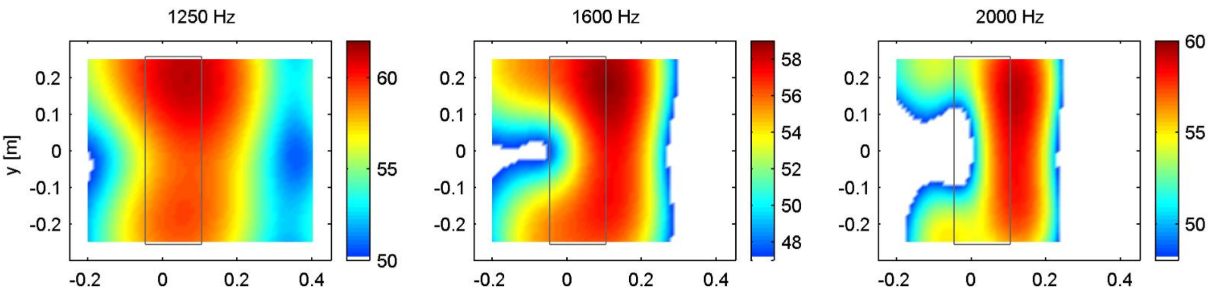

d) Flexible Serration

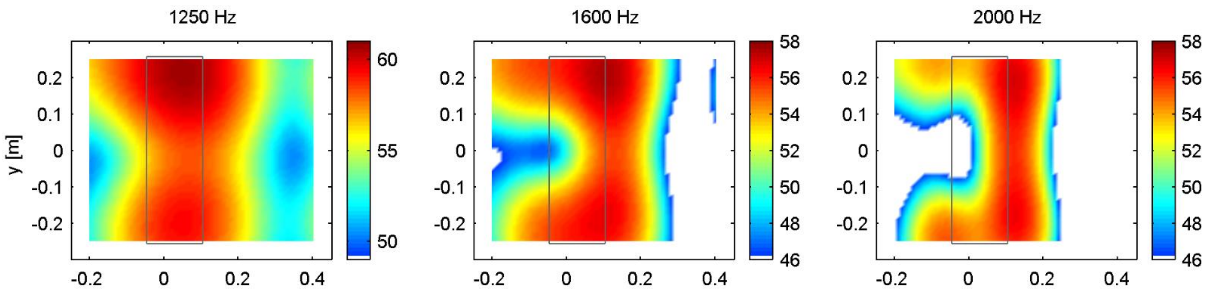

e) Cutted Serration

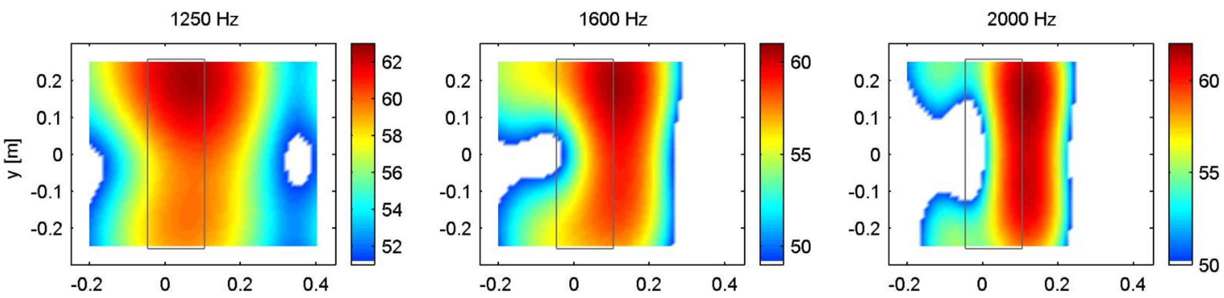

f) Serration with Cutted Plate

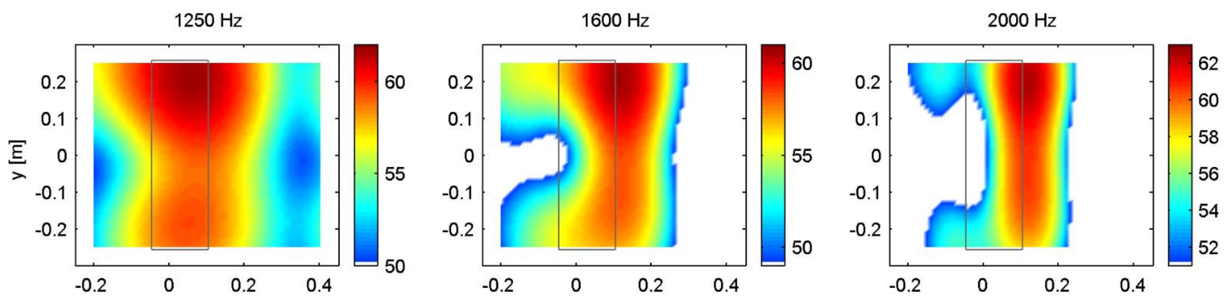

Figure 144 – **Low Frequency Acoustic Maps – Free stream velocity 50 m/s; AoA = 0° (α_{eff} = 0°)**

a) Clean Configuration

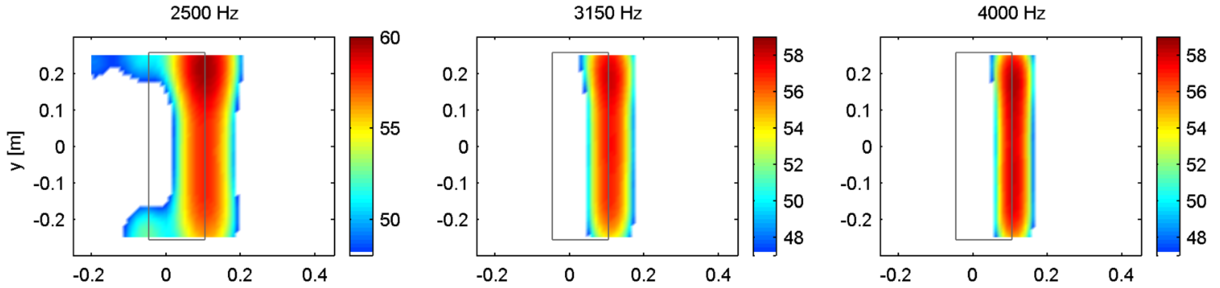

b) Serration Fixed on the Pressure Side

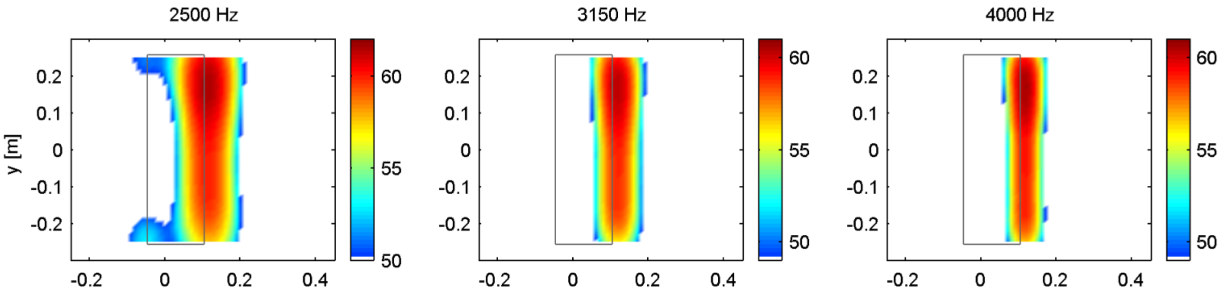

c) Serration Fixed on the Suction Side

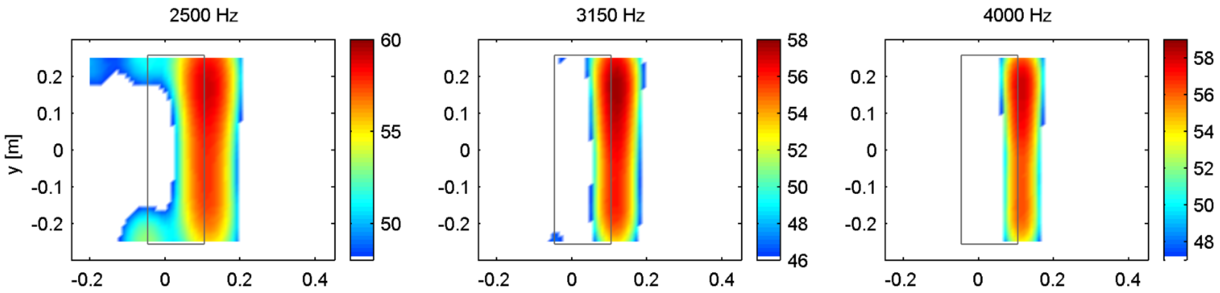

d) Flexible Serration

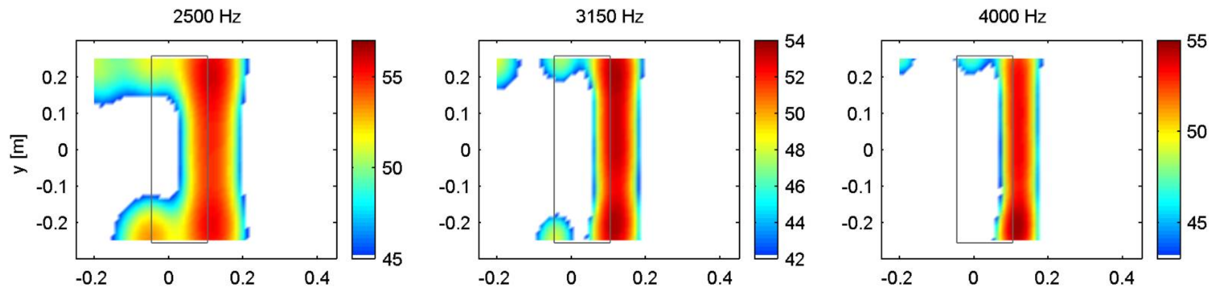

e) Cutted Serration

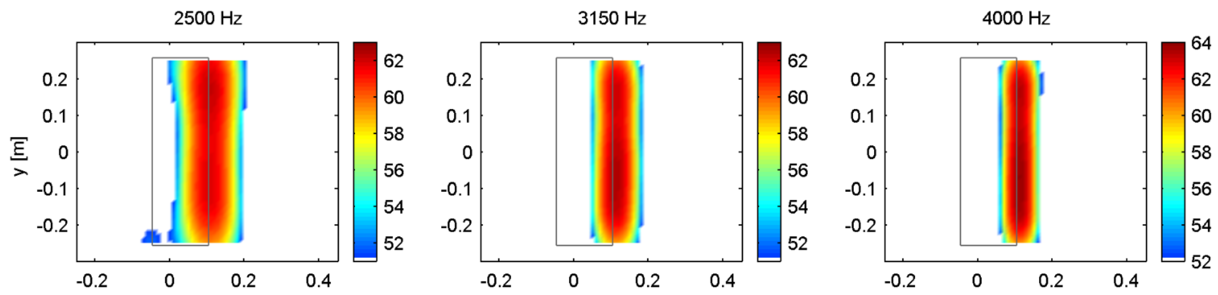

f) Serration with Cutted Plate

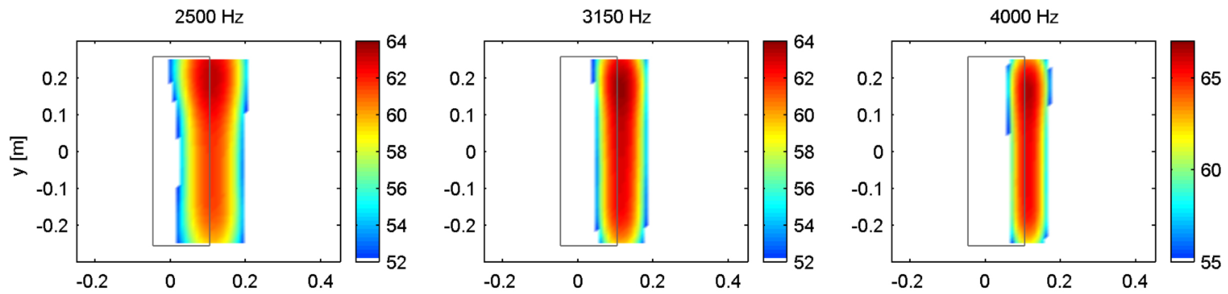

Figure 145 – **Medium Frequency Acoustic Maps – Free stream velocity 50 m/s; AoA = 0° (α_{eff} = 0°)**

a) Clean Configuration

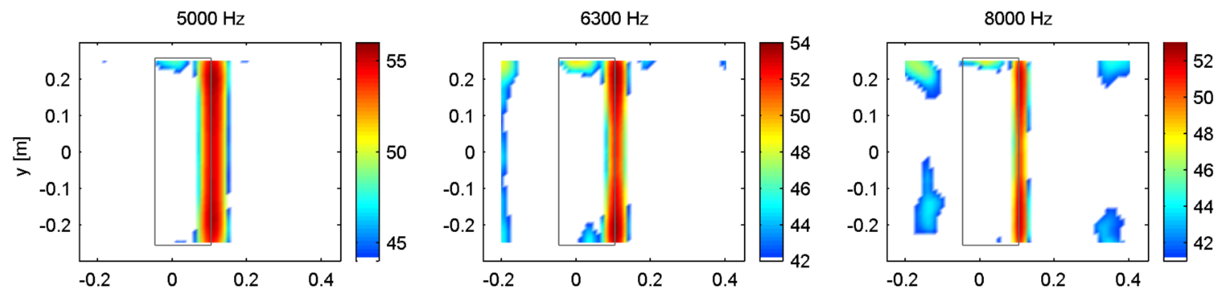

b) Serration Fixed on the Pressure Side

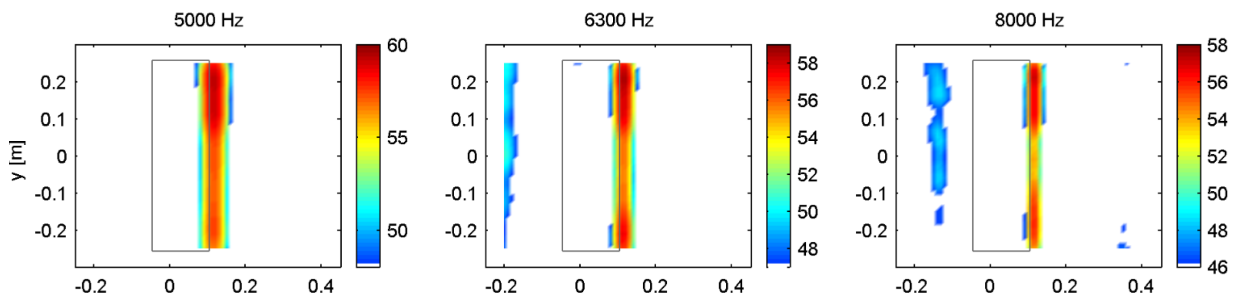

c) Serration Fixed on the Suction Side

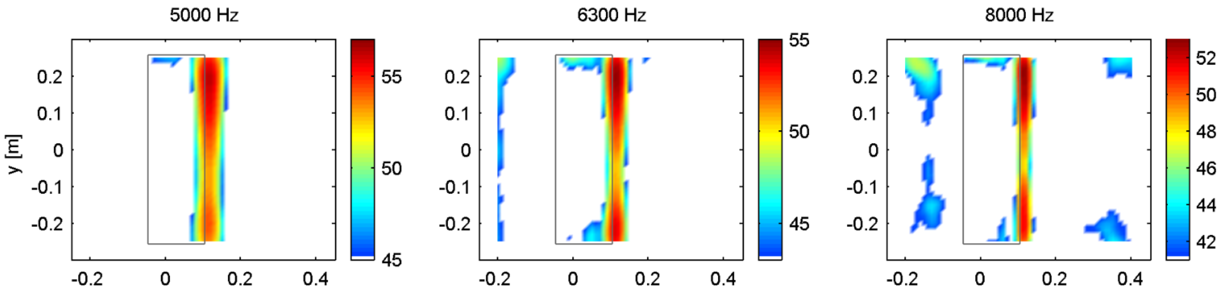

d) Flexible Serration

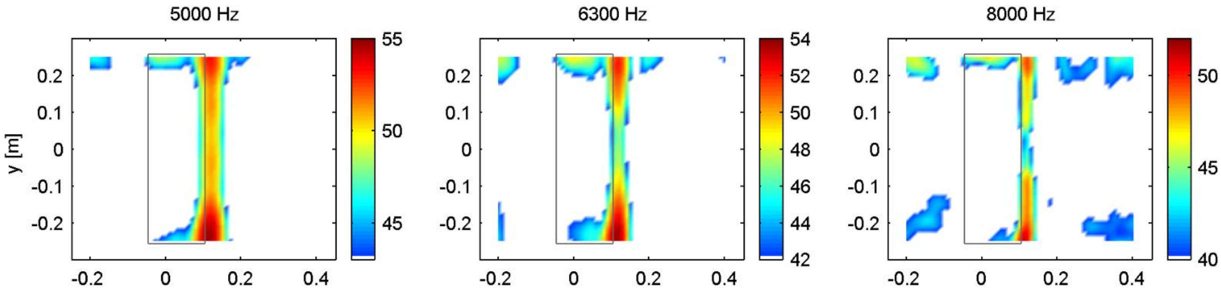

e) Cutted Serration

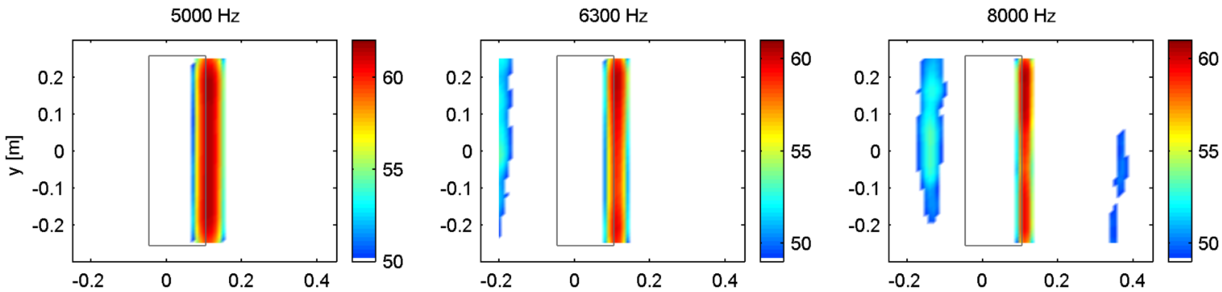

f) Serration with Cutted Plate

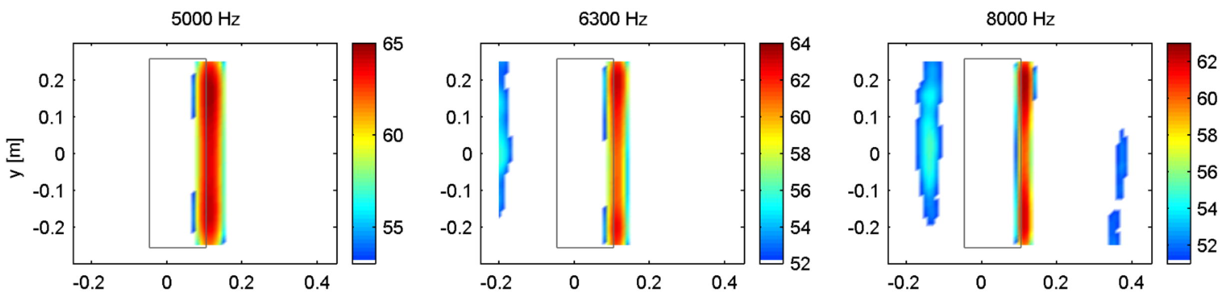

Figure 146 – **High Frequency Acoustic Maps – Free stream velocity 50 m/s; AoA = 0° (α_{eff} = 0°)**

a) Clean Configuration

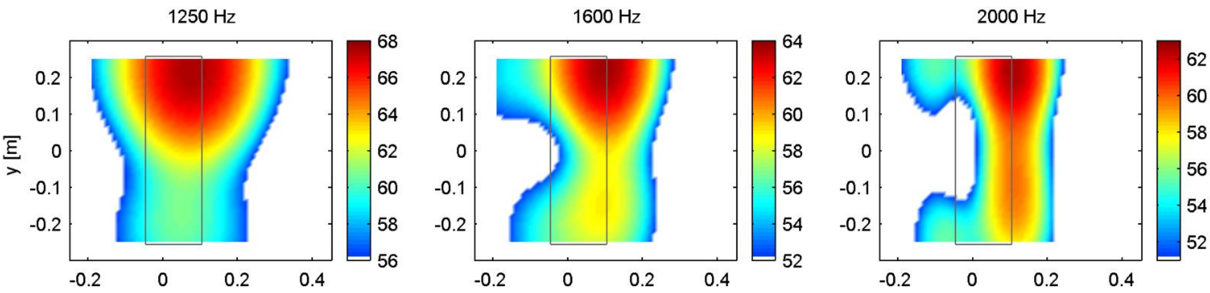

b) Serration Fixed on the Pressure Side

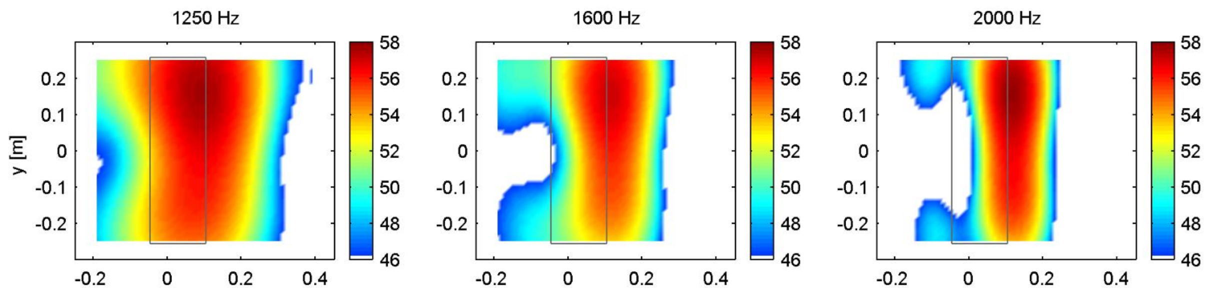

c) Serration Fixed on the Suction Side

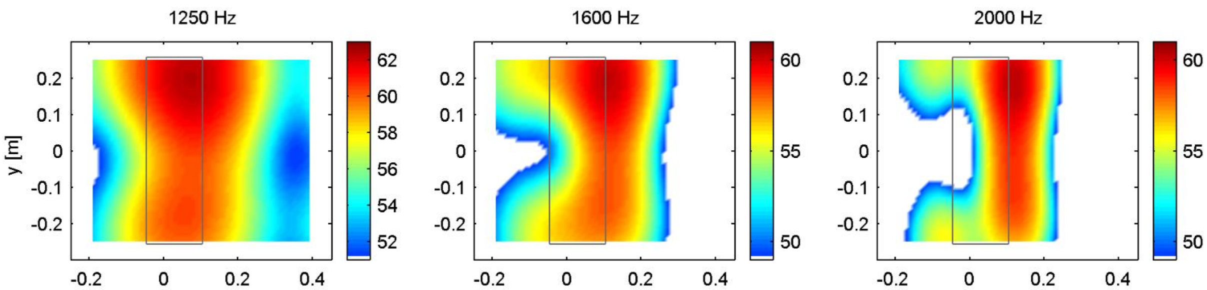

d) Flexible Serration

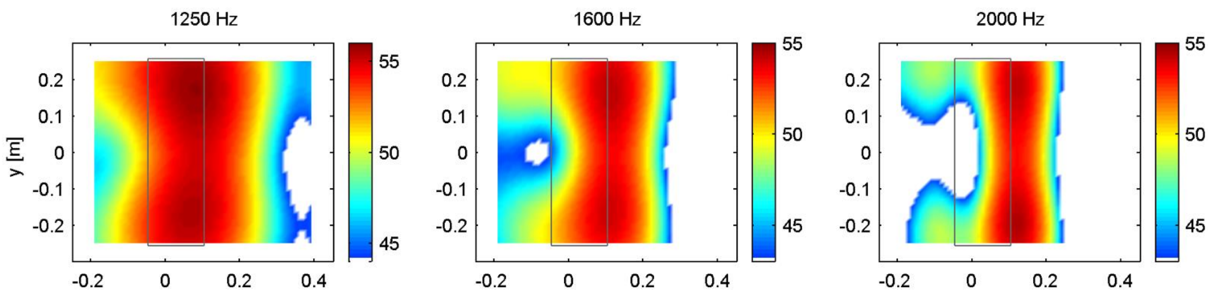

e) Cutted Serration

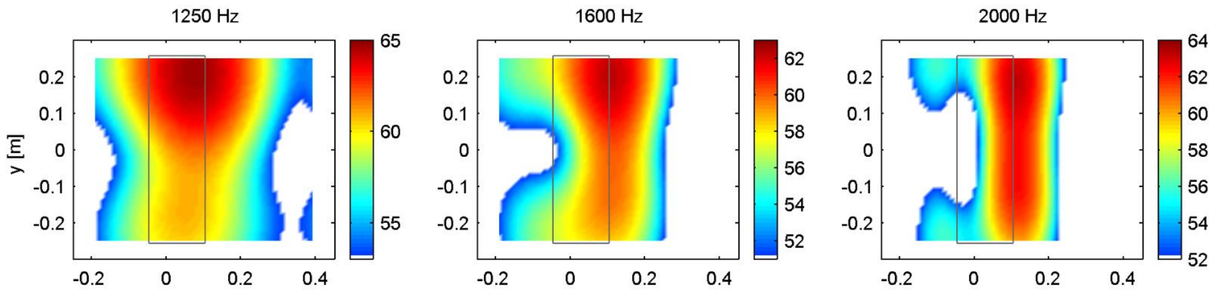

f) Serration with Cutted Plate

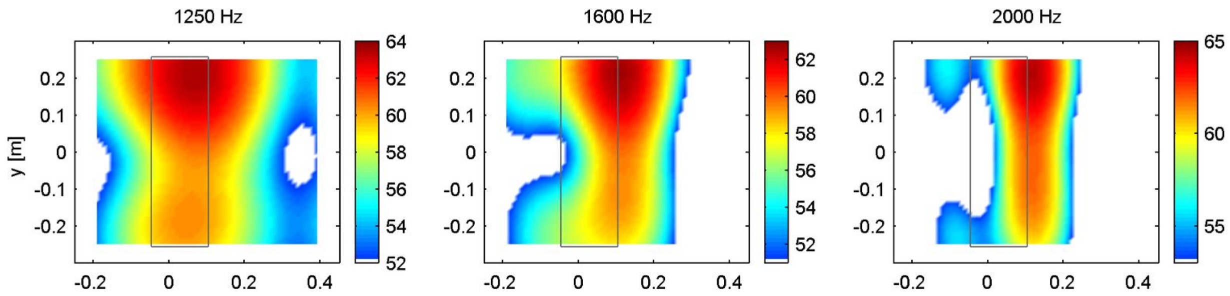

Figure 147 – **Low Frequency Acoustic Maps – Free stream velocity 50 m/s; AoA = 6° (α_{eff} = 3.4°)**

a) Clean Configuration

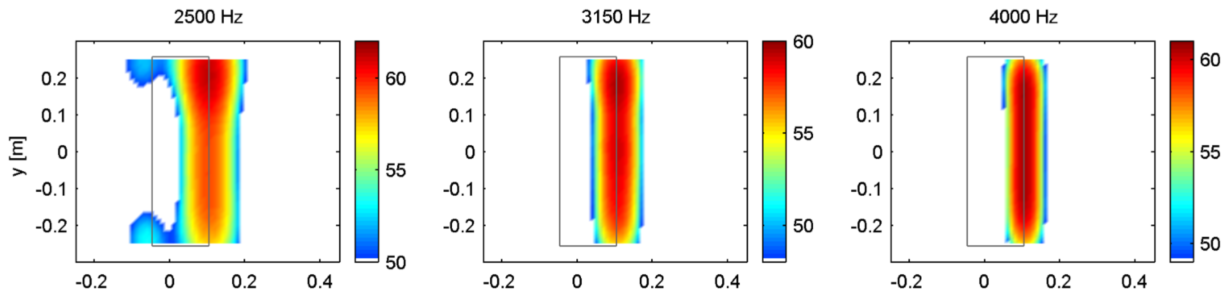

b) Serration Fixed on the Pressure Side

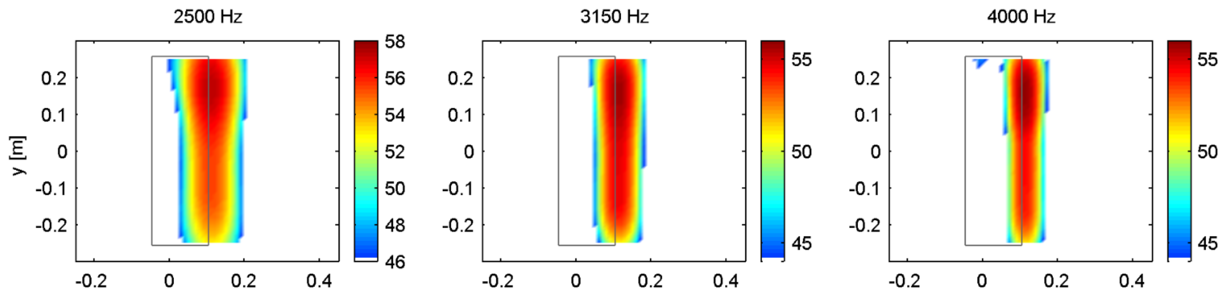

c) Serration Fixed on the Suction Side

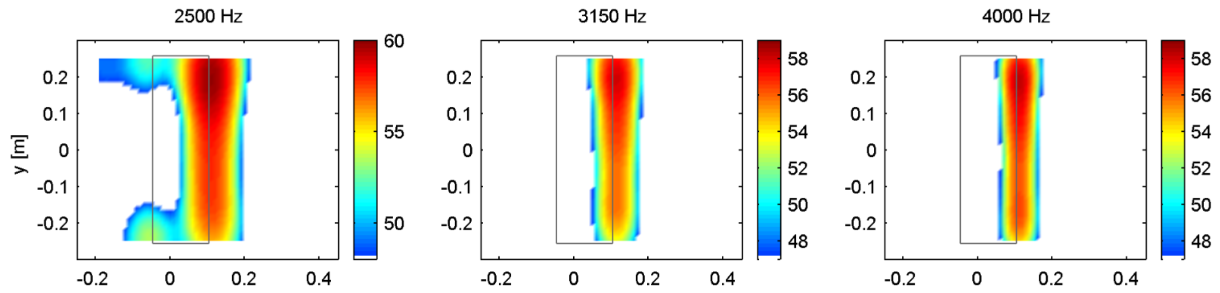

d) Flexible Serration

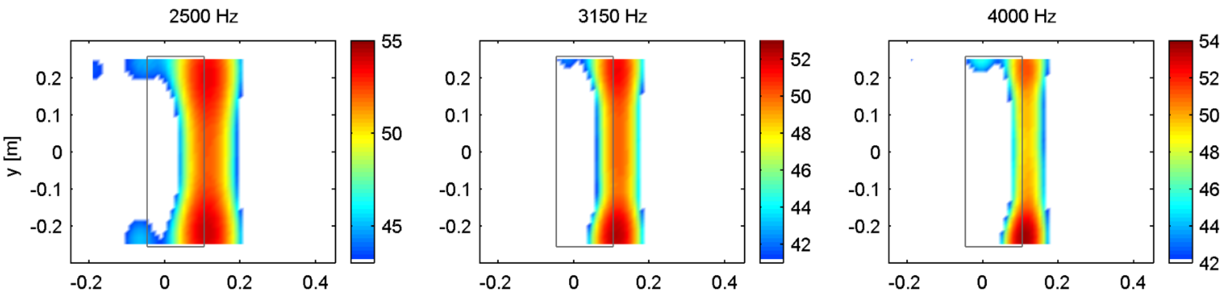

e) Cutted Serration

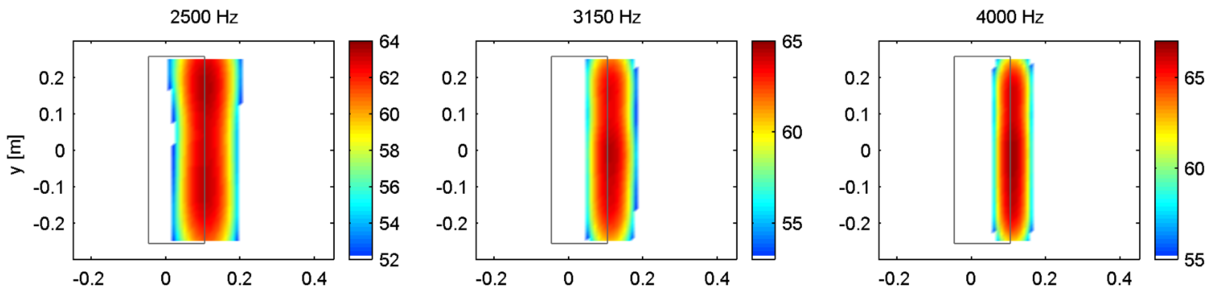

f) Serration with Cutted Plate

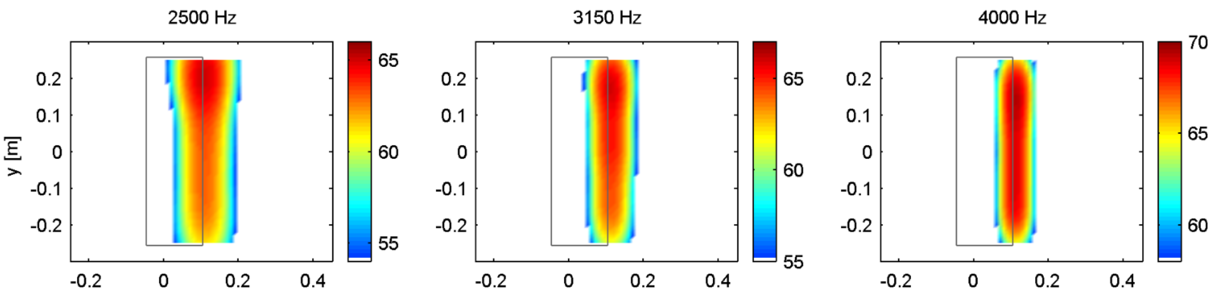

Figure 148 – **Medium Frequency Acoustic Maps – Free stream velocity 50 m/s; AoA = 6° (α_{eff} = 3.4°)**

a) Clean Configuration

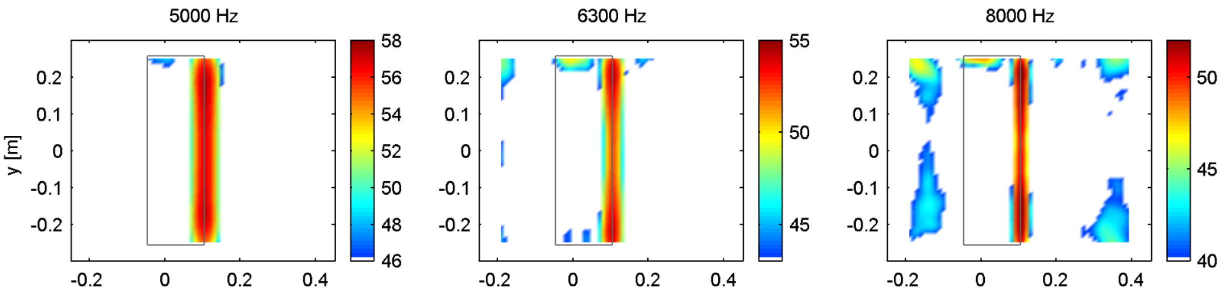

b) Serration Fixed on the Pressure Side

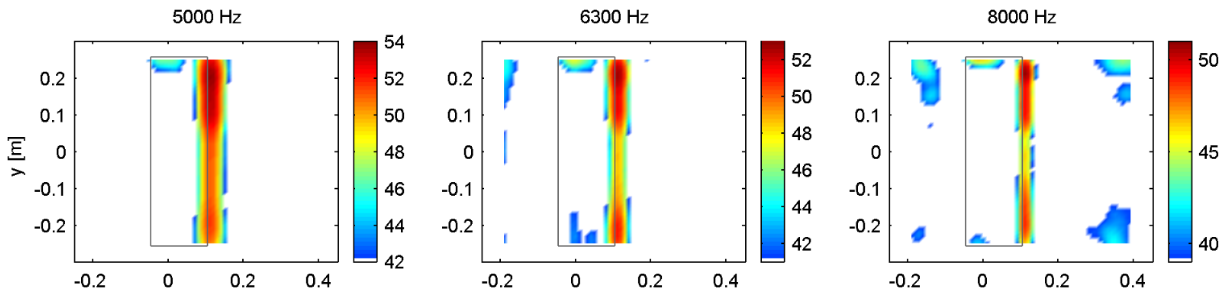

c) Serration Fixed on the Suction Side

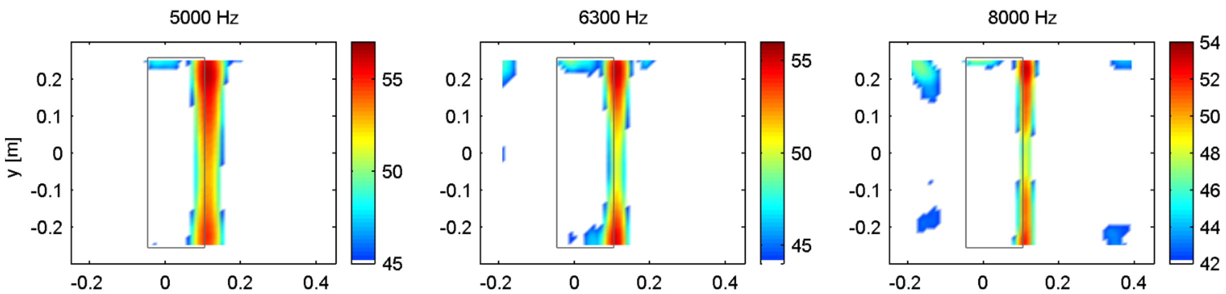

d) Flexible Serration

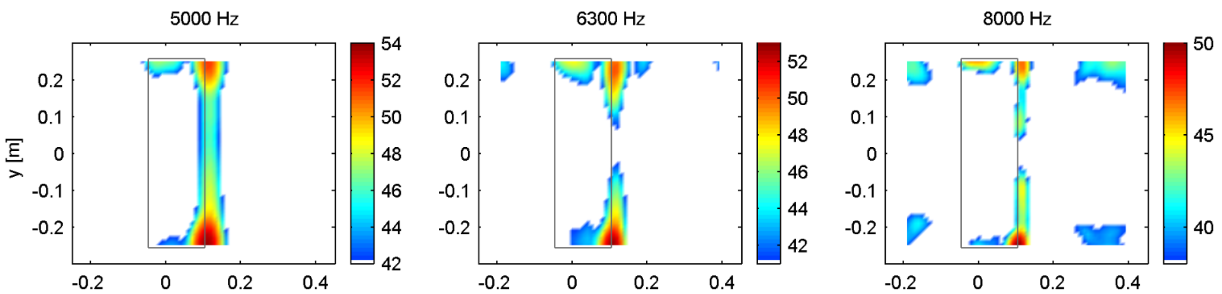

e) Cutted Serration

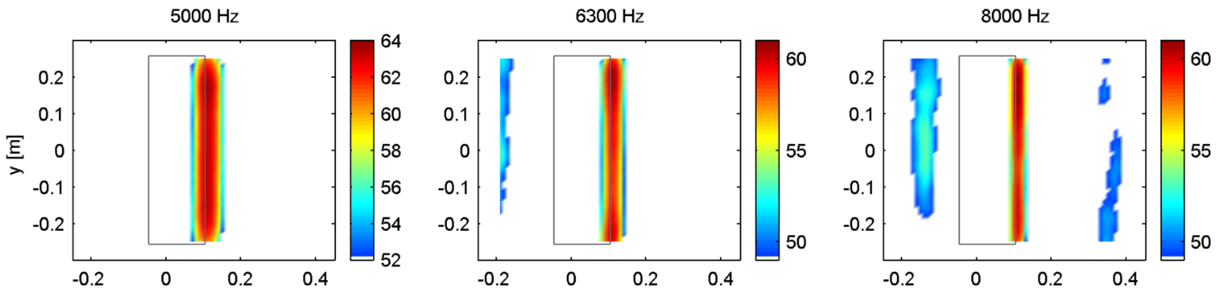

f) Serration with Cutted Plate

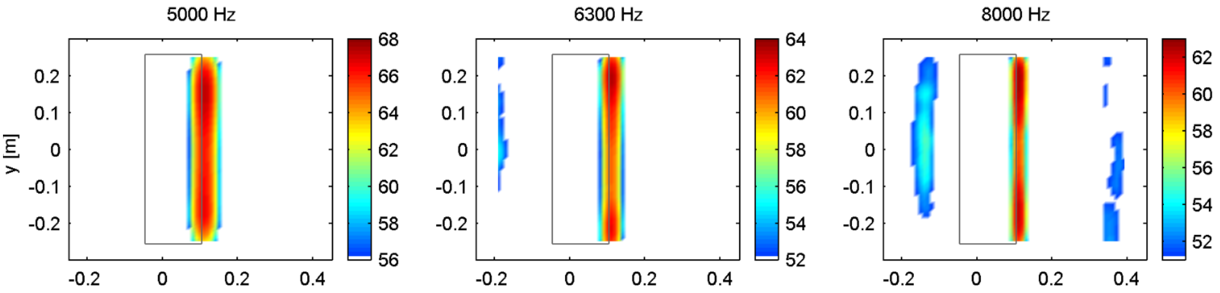

Figure 149 **– High Frequency Acoustic Maps – Free stream velocity 50 m/s; AoA = 6° (α_{eff} = 3.4°)**

a) Clean Configuration

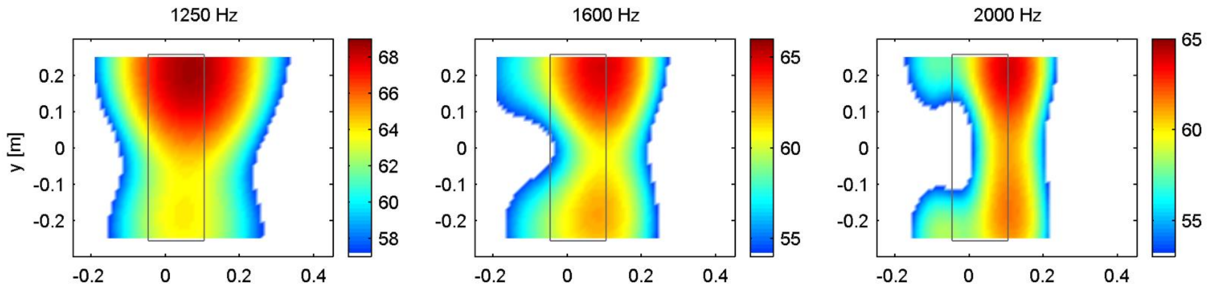

b) Serration Fixed on the Pressure Side

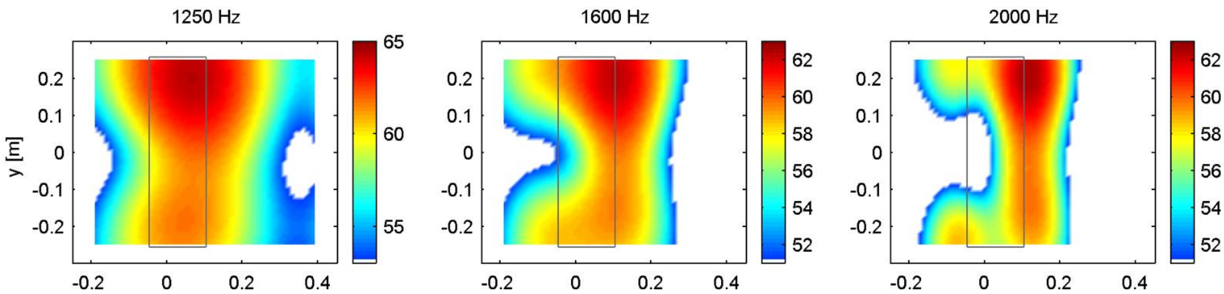

c) Serration Fixed on the Suction Side

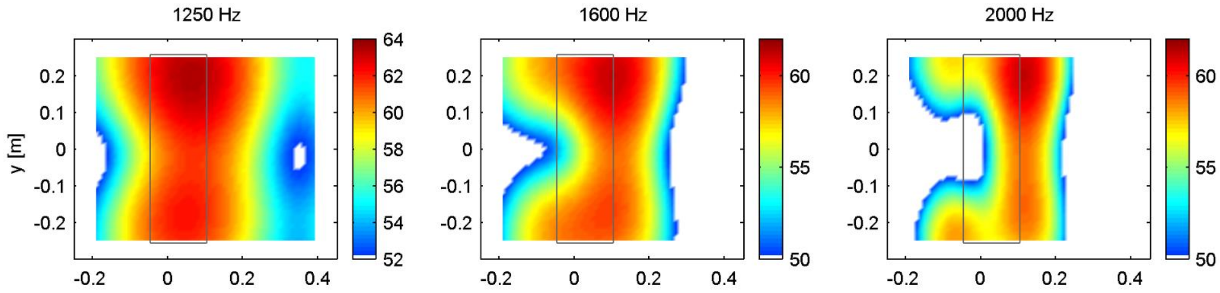

d) Flexible Serration

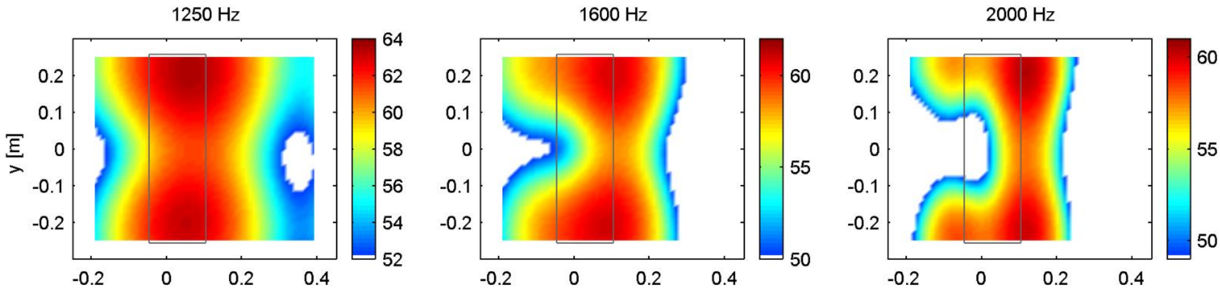

e) Cutted Serration

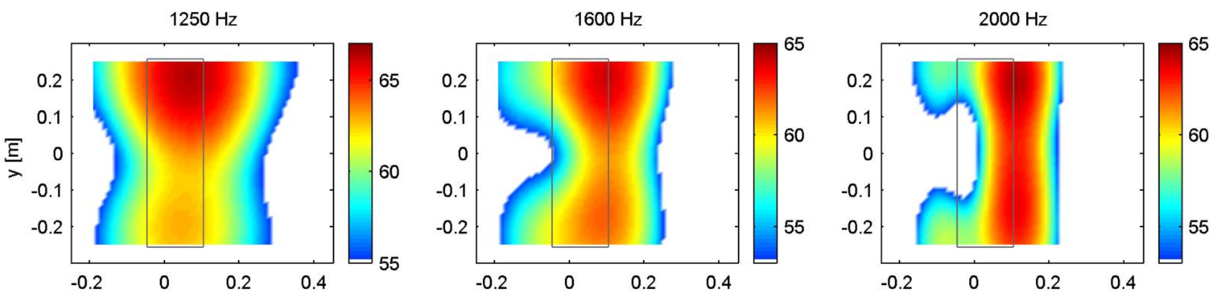

f) Serration with Cutted Plate

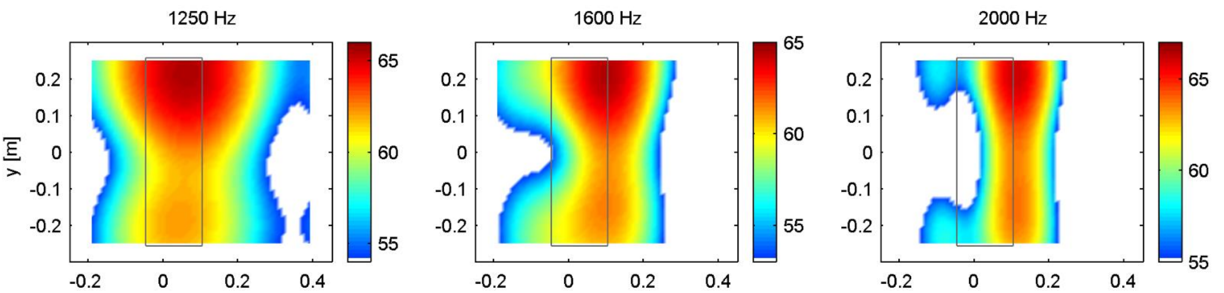

Figure 150– **Low Frequency Acoustic Maps – Free stream velocity 50 m/s; AoA = 10.51° (α_{eff} = 6°)**

a) Clean Configuration

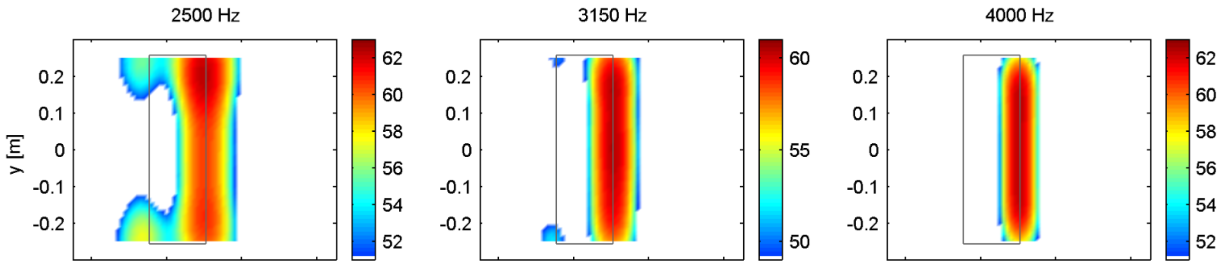

b) Serration Fixed on the Pressure Side

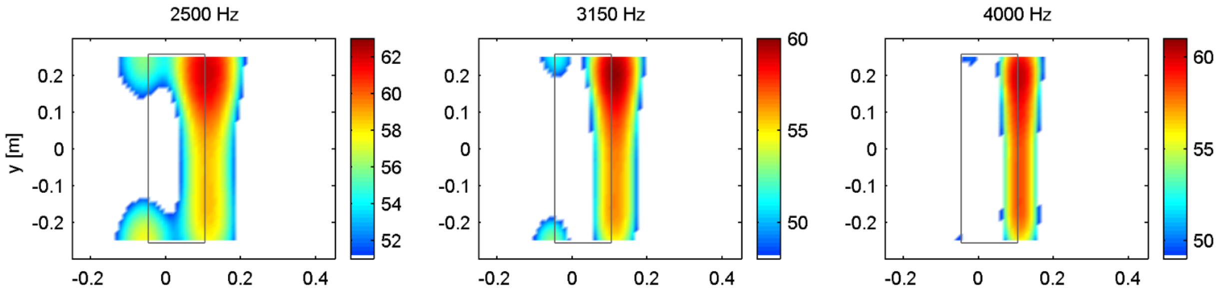

c) Serration Fixed on the Suction Side

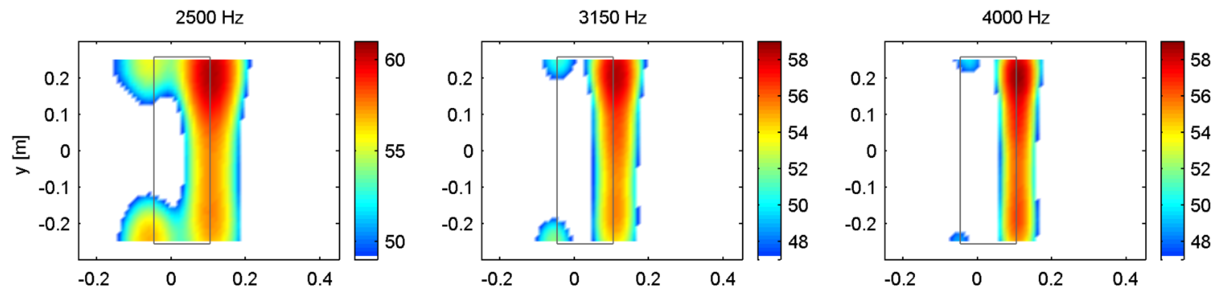

d) Flexible Serration

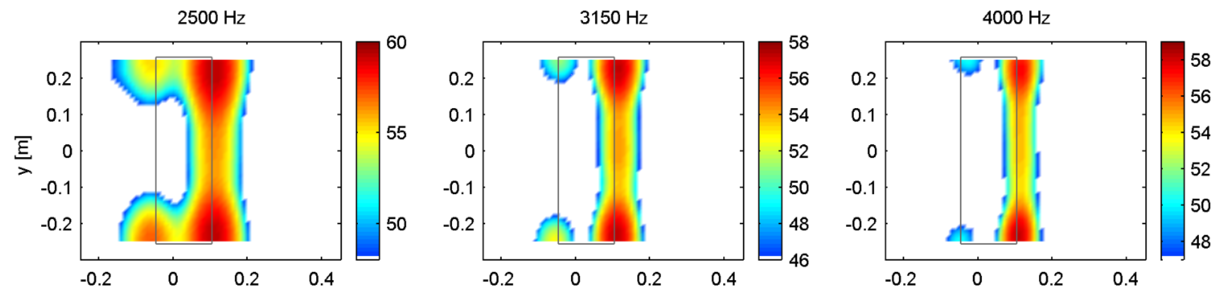

e) Cutted Serration

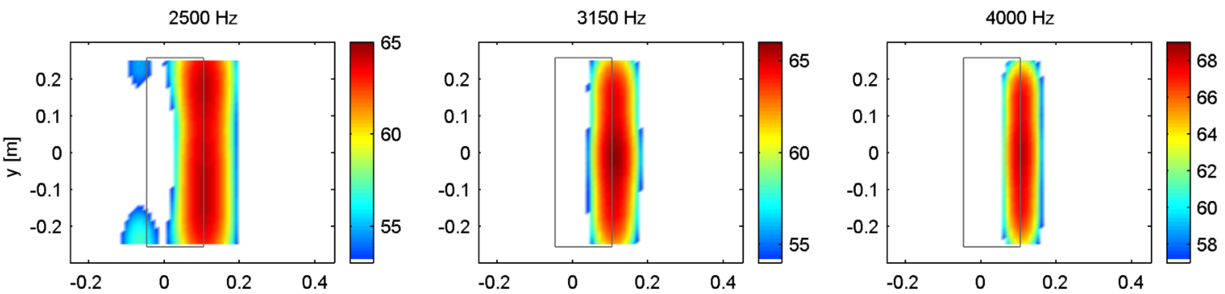

f) Serration with Cutted Plate

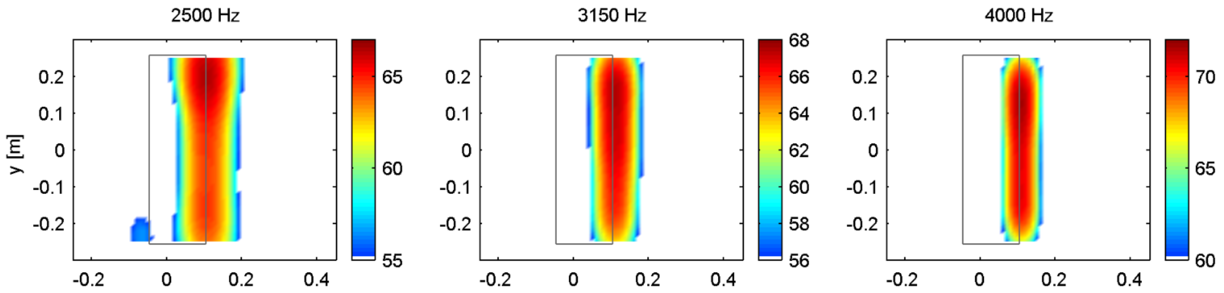

Figure 151 – **Medium Frequency Acoustic Maps – Free stream velocity 50 m/s; AoA = 10.51° (α_{eff} = 6°)**

a) Clean Configuration

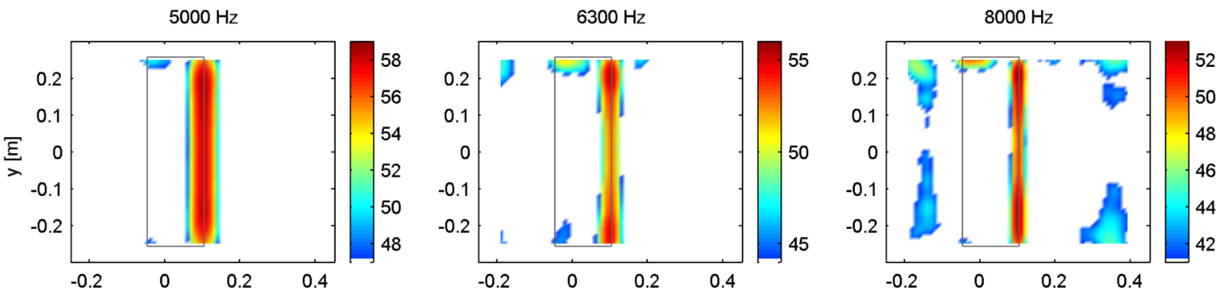

b) Serration Fixed on the Pressure Side

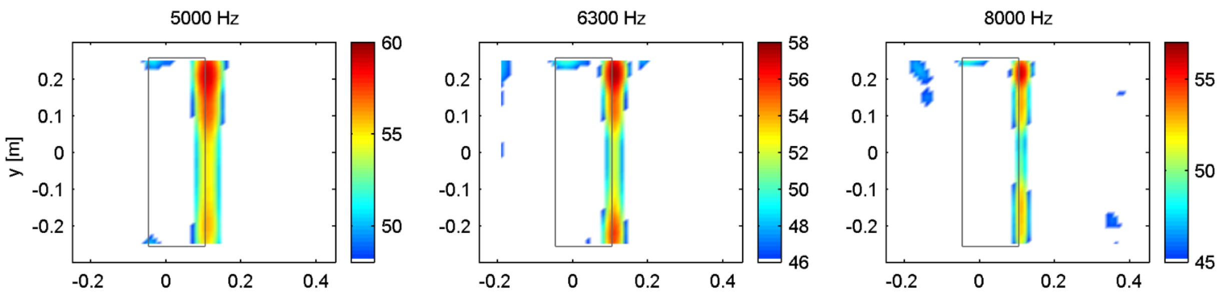

c) Serration Fixed on the Suction Side

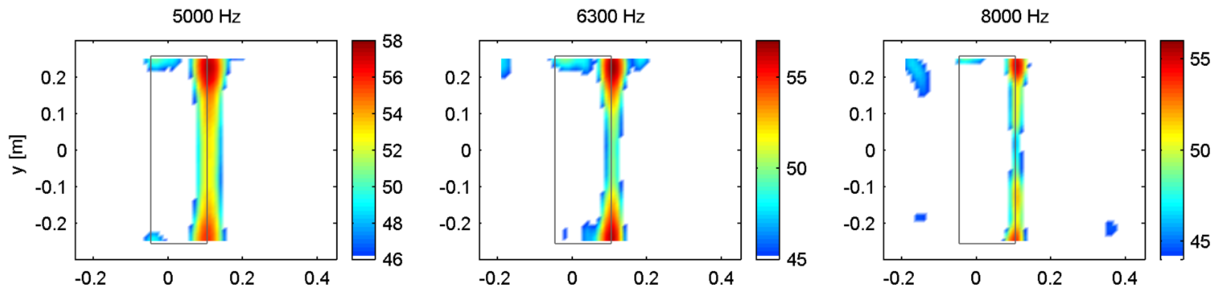

d) Flexible Serration

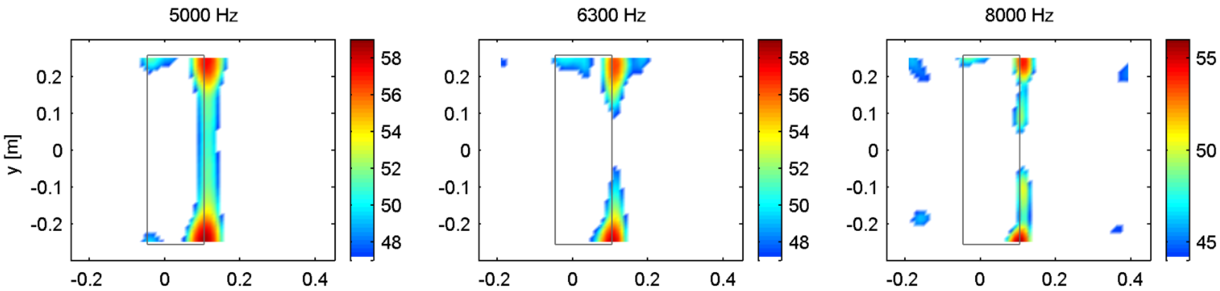

e) Cutted Serration

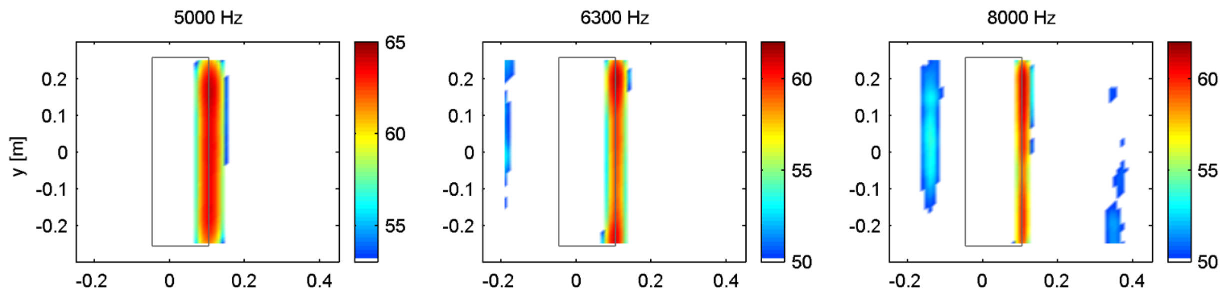

f) Serration with Cutted Plate

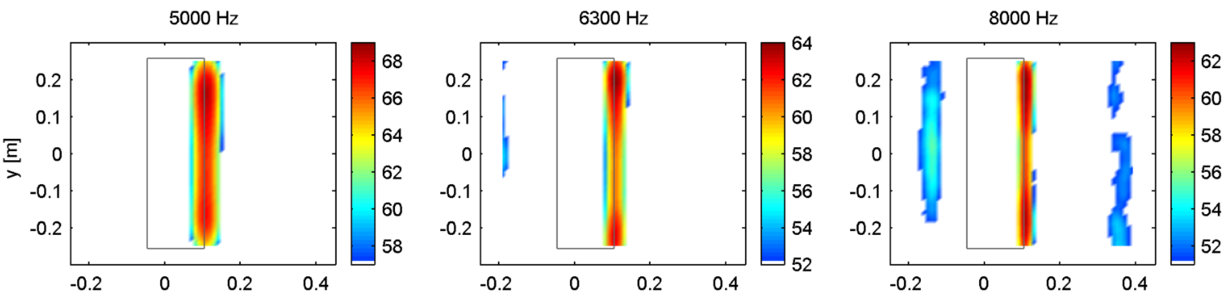

Figure 152 – **High Frequency Acoustic Maps – Free stream velocity 50 m/s; AoA = 10.51° (α_{eff} = 6°)**

a) Clean Configuration

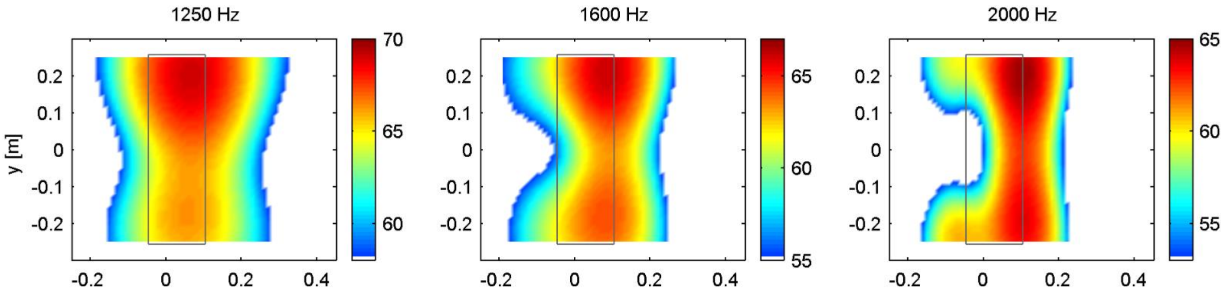

b) Serration Fixed on the Pressure Side

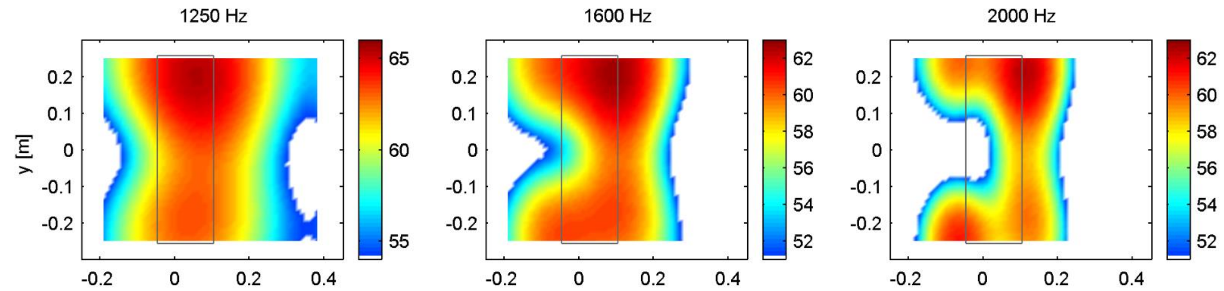

c) Serration Fixed on the Suction Side

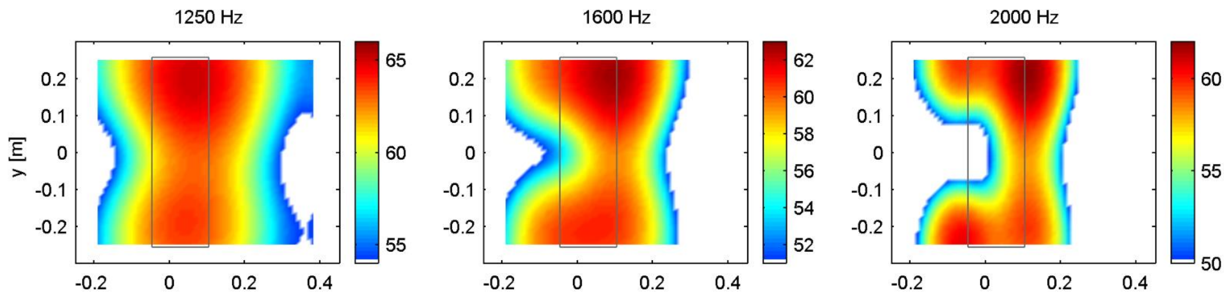

d) Flexible Serration

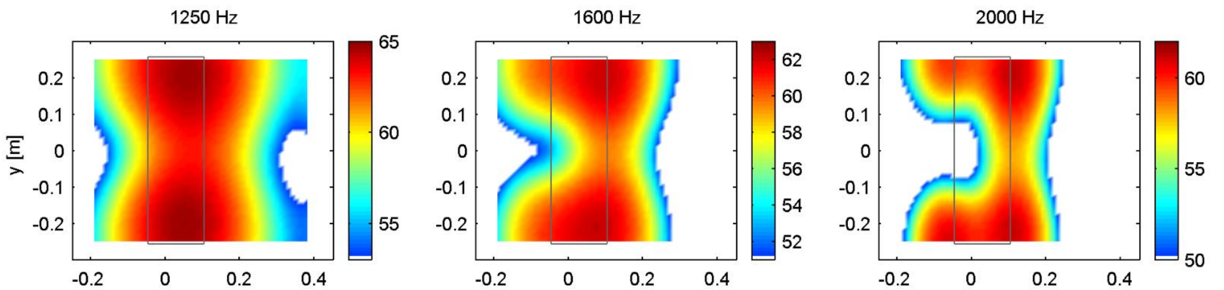

e) Cutted Serration

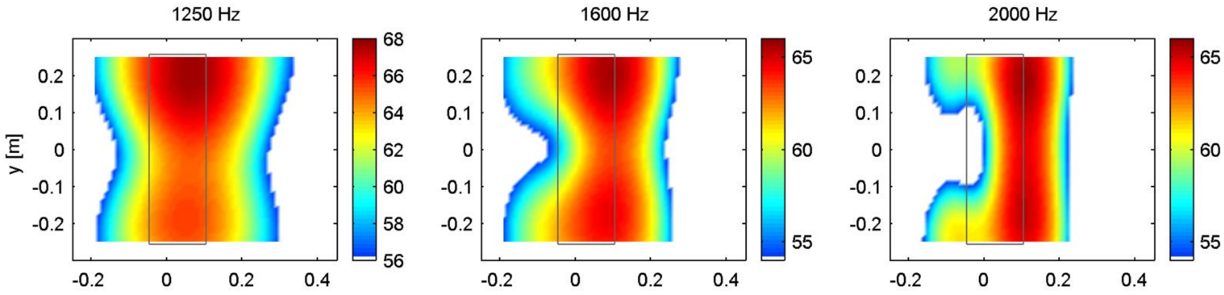

f) Serration with Cutted Plate

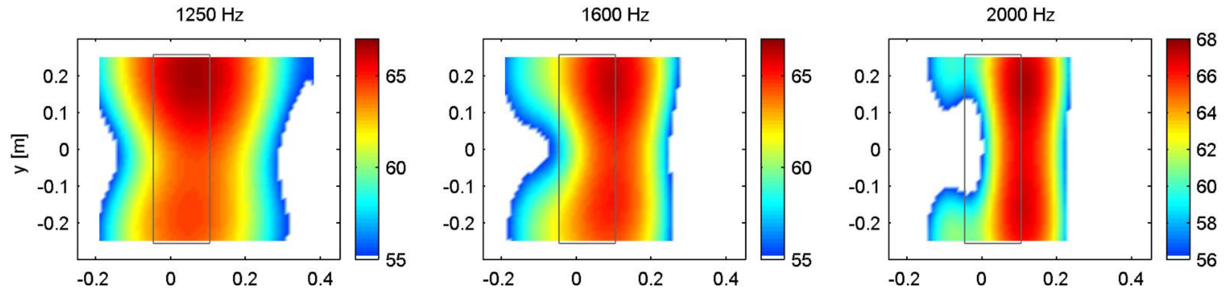

Figure 153 – **Low Frequency Acoustic Maps – Free stream velocity 50 m/s; AoA = 14.37° (α_{eff} = 8.2°)**

a) Clean Configuration

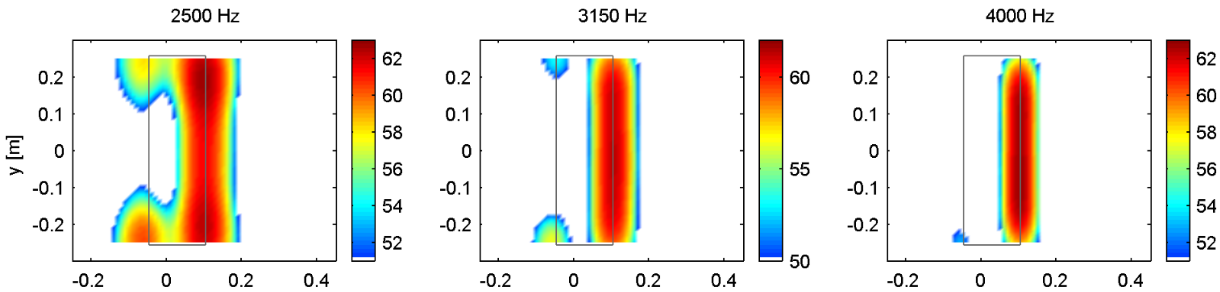

b) Serration Fixed on the Pressure Side

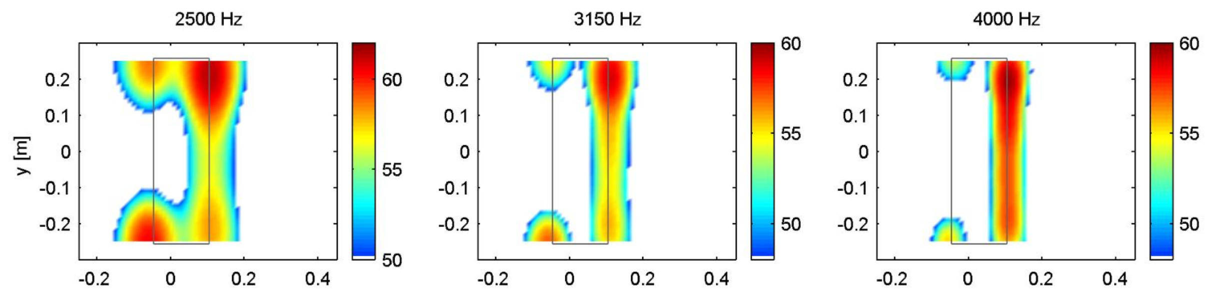

c) Serration Fixed on the Suction Side

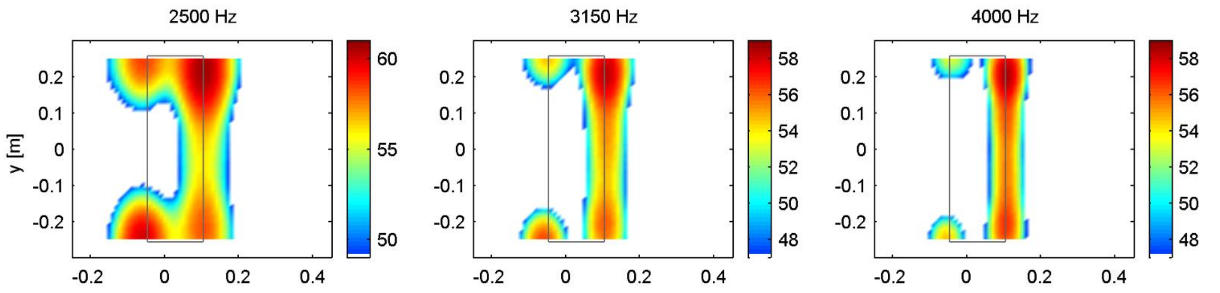

d) Flexible Serration

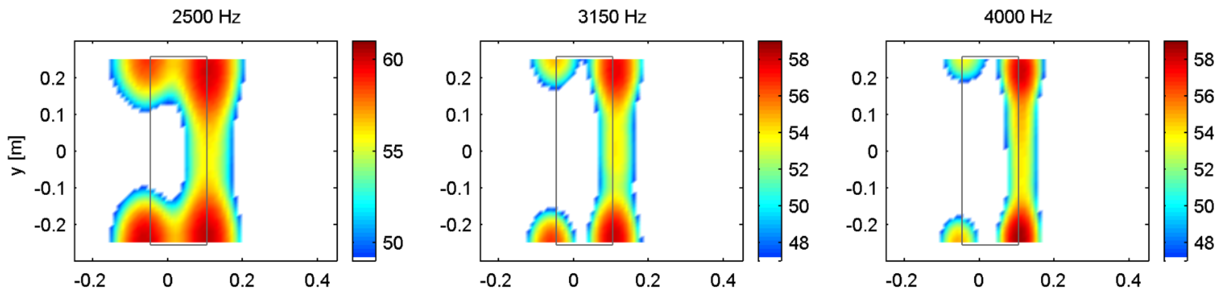

e) Cutted Serration

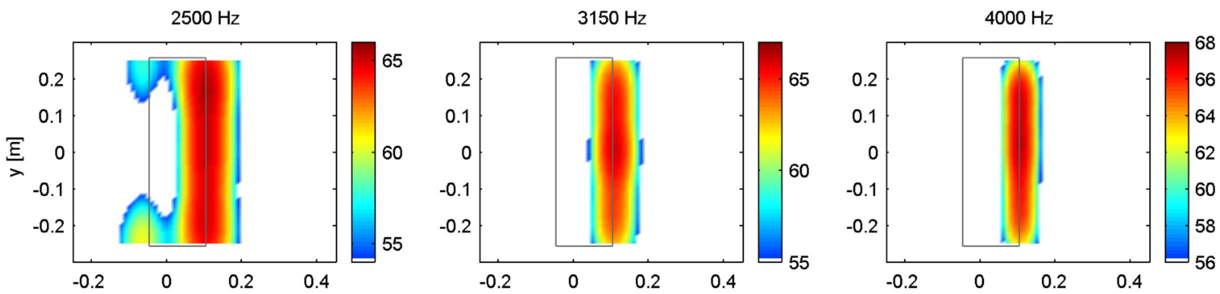

f) Serration with Cutted Plate

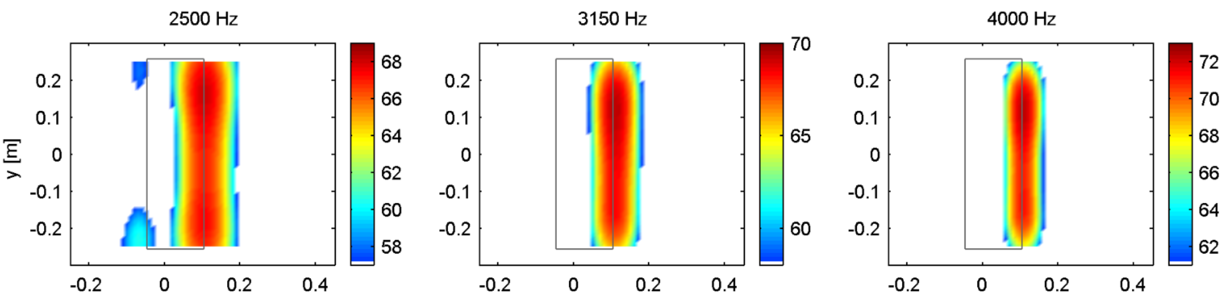

Figure 154 – **Medium Frequency Acoustic Maps – Free stream velocity 50 m/s; AoA = 14.37° (α_{eff} = 8.2°)**

a) Clean Configuration

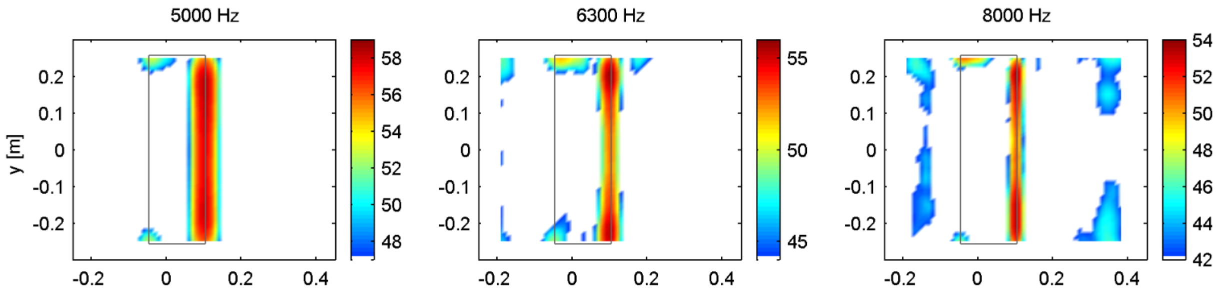

b) Serration Fixed on the Pressure Side

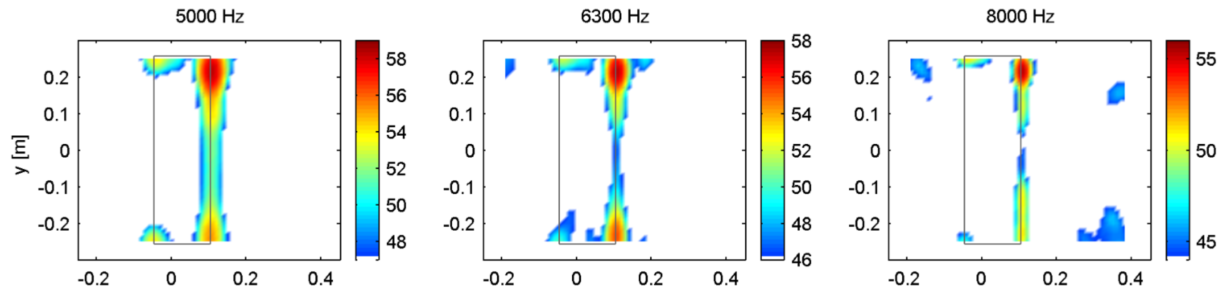

c) Serration Fixed on the Suction Side

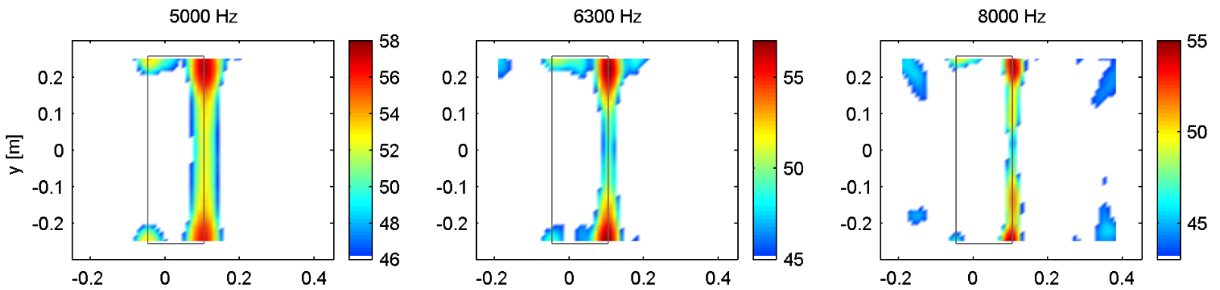

d) Flexible Serration

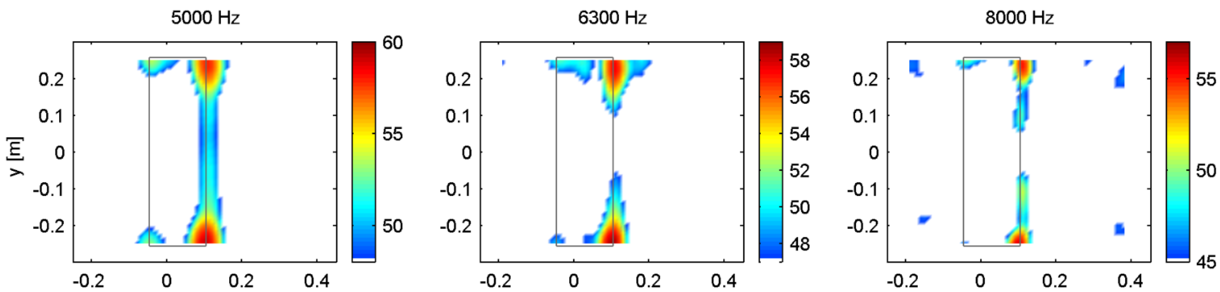

e) Cutted Serration

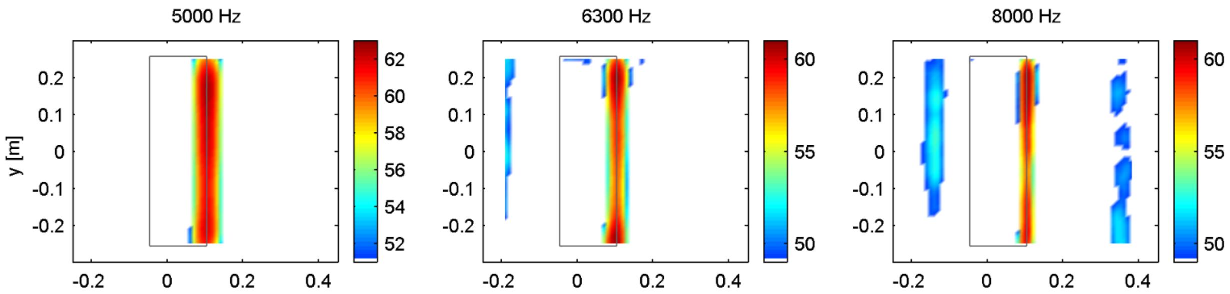

f) Serration with Cutted Plate

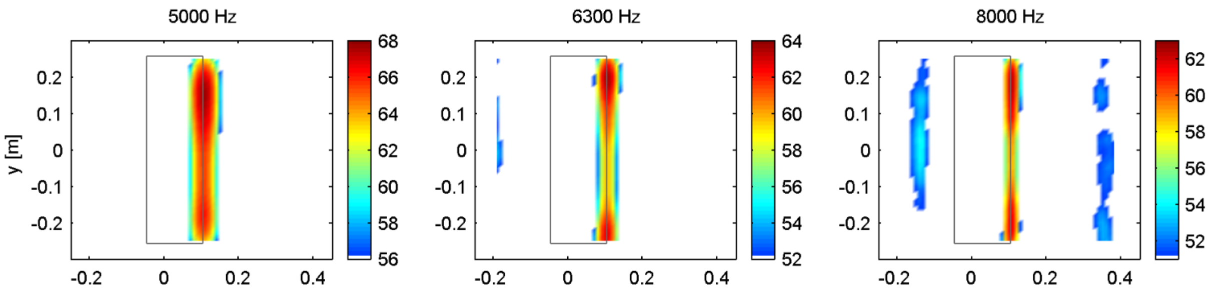

Figure 155 – **High Frequency Acoustic Maps – Free stream velocity 50 m/s; AoA = 14.37° (α_{eff} = 8.2°)**

a) Clean Configuration

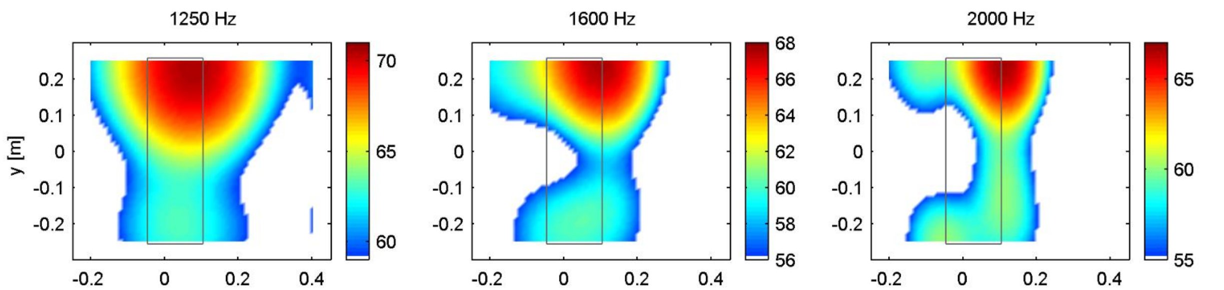

b) Serration Fixed on the Pressure Side

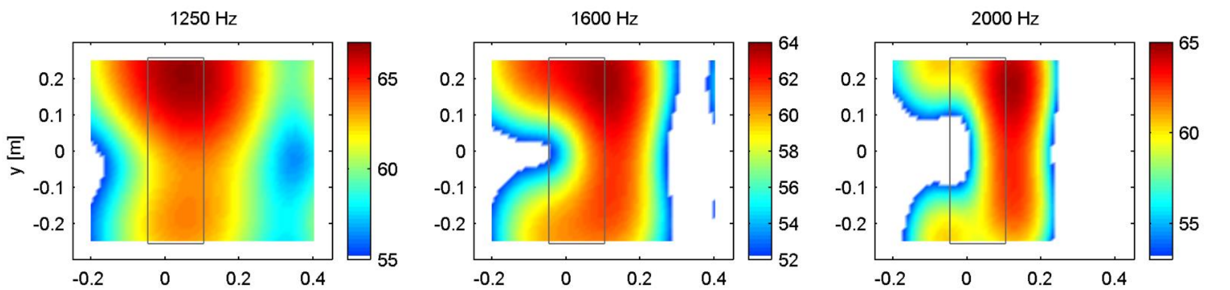

c) Serration Fixed on the Suction Side

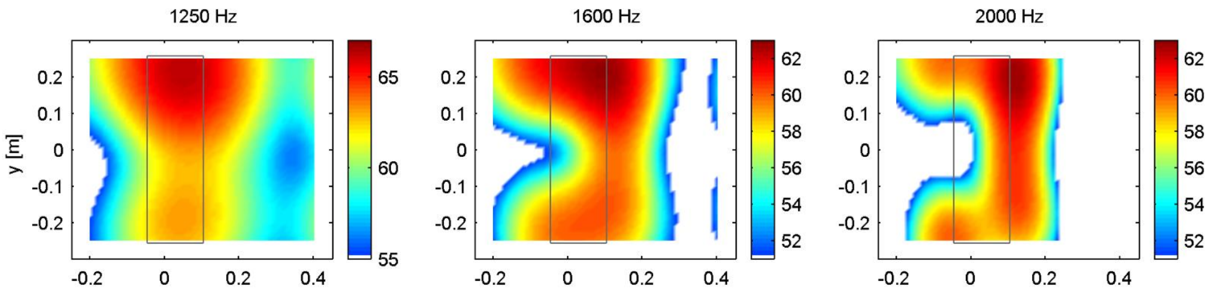

d) Flexible Serration

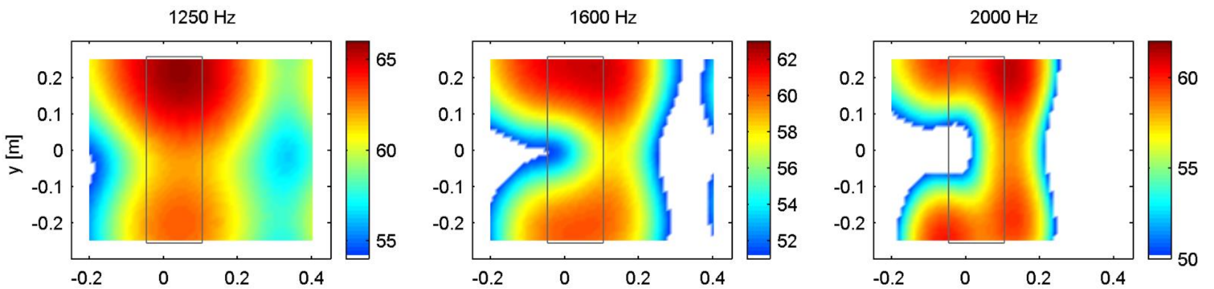

e) Cutted Serration

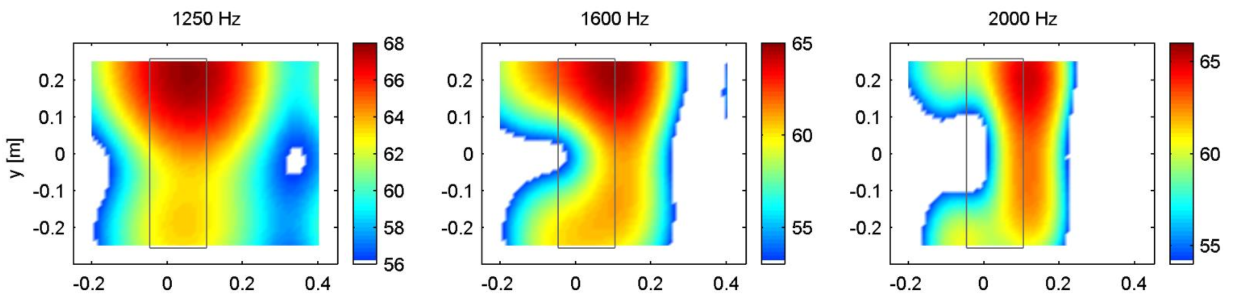

f) Serration with Cutted Plate

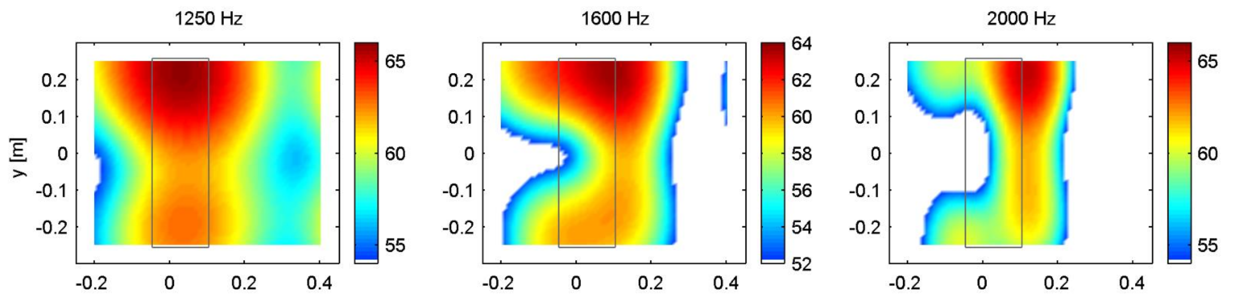

Figure 156 **– Low Frequency Acoustic Maps – Free stream velocity 60 m/s; AoA = 0° (α_{eff} = 0°)**

a) Clean Configuration

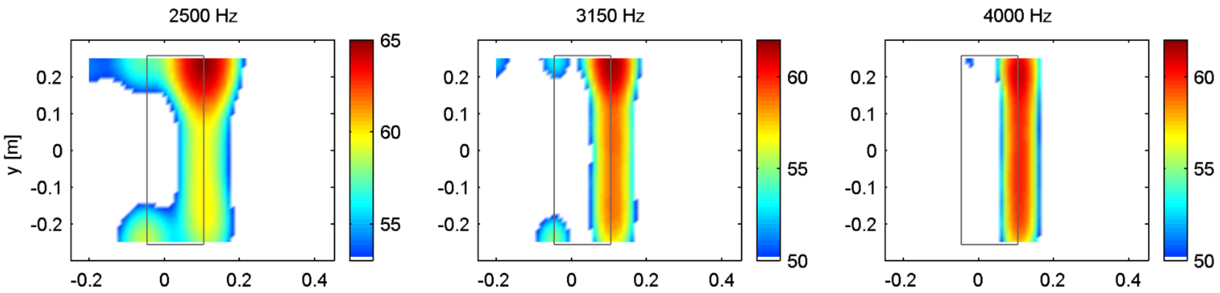

b) Serration Fixed on the Pressure Side

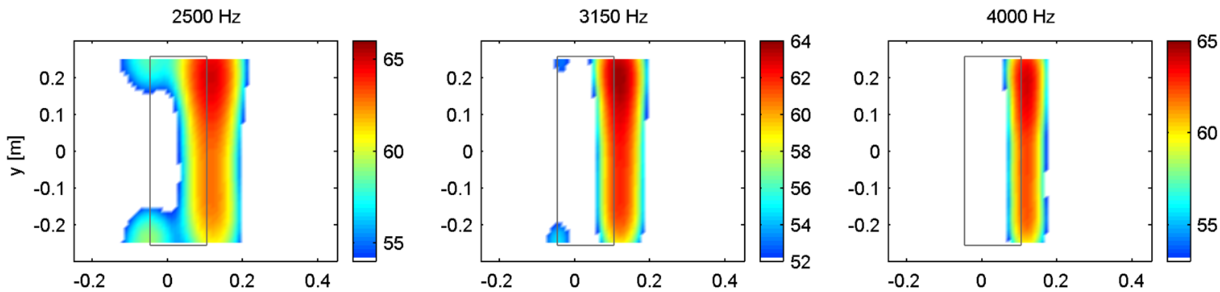

c) Serration Fixed on the Suction Side

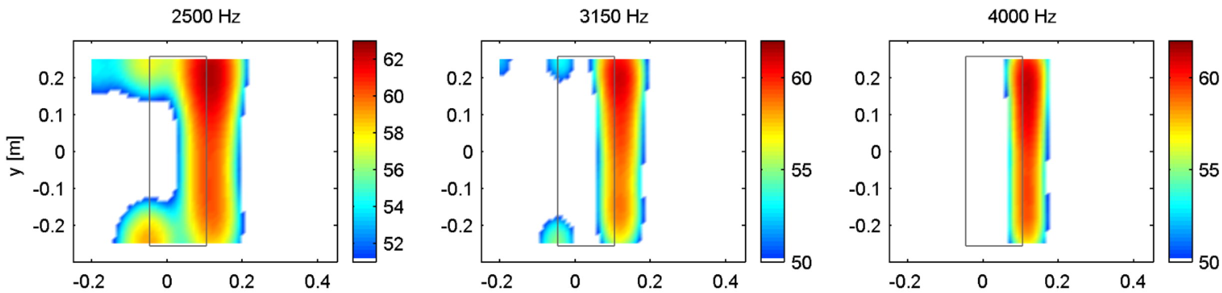

d) Flexible Serration

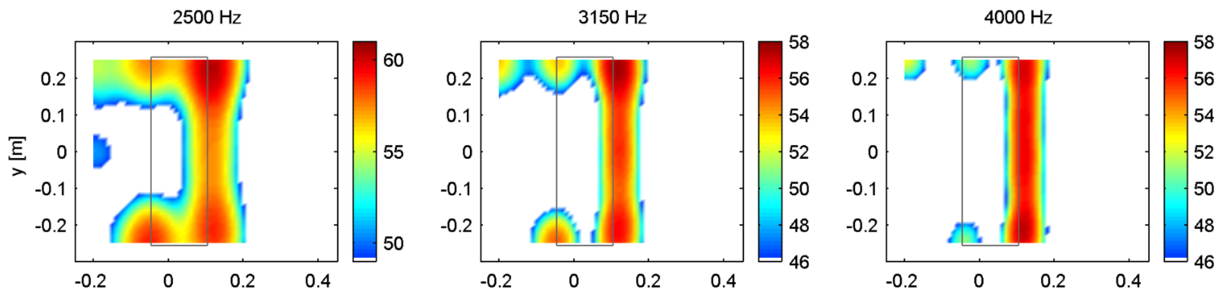

e) Cutted Serration

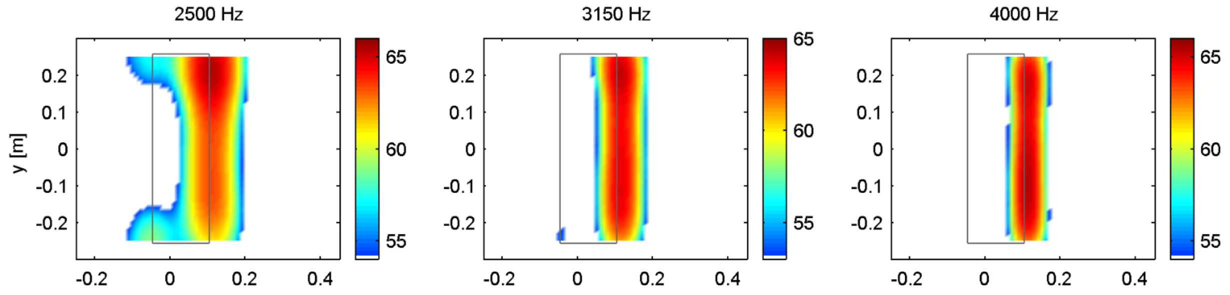

f) Serration with Cutted Plate

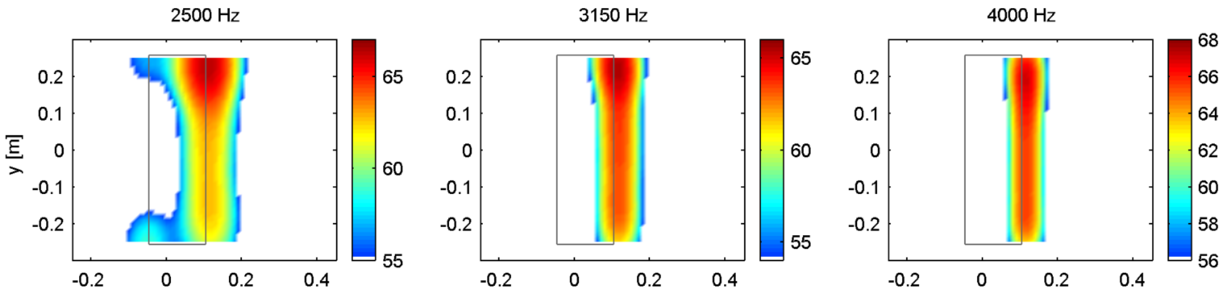

Figure 157 – **Medium Frequency Acoustic Maps – Free stream velocity 60 m/s; AoA = 0° (α_{eff} = 0°)**

a) Clean Configuration

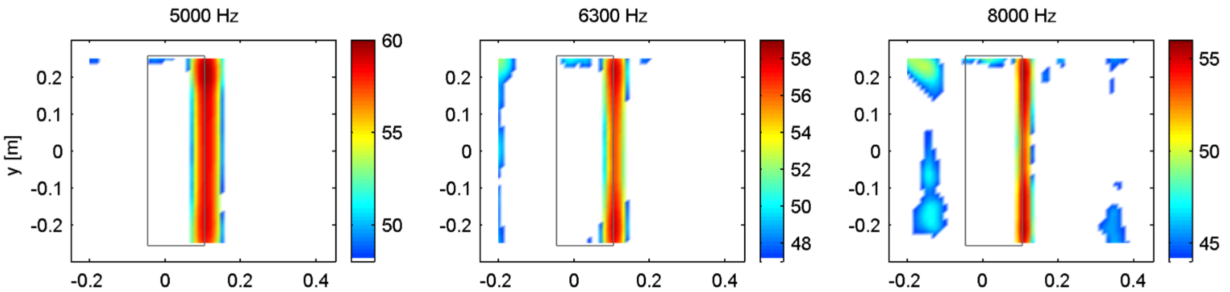

b) Serration Fixed on the Pressure Side

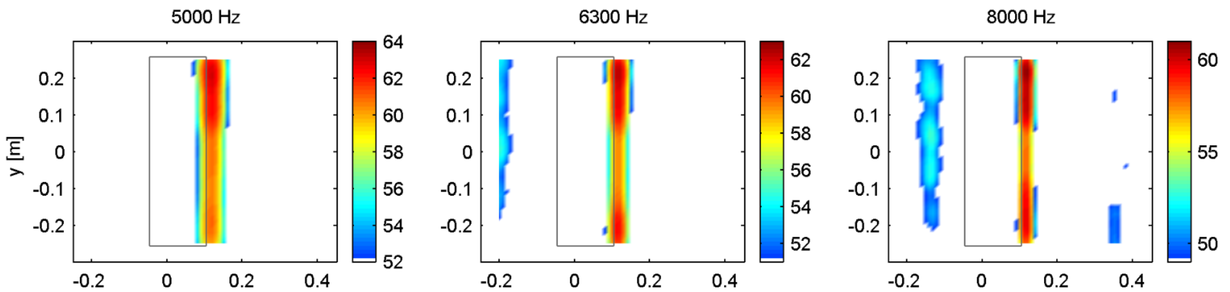

c) Serration Fixed on the Suction Side

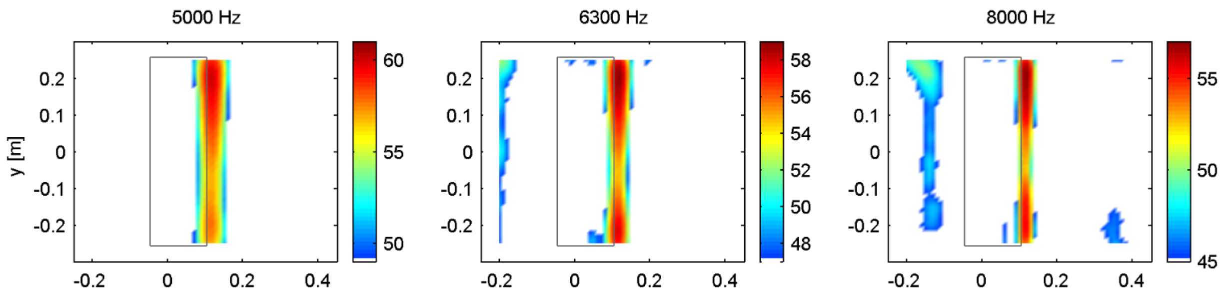

d) Flexible Serration

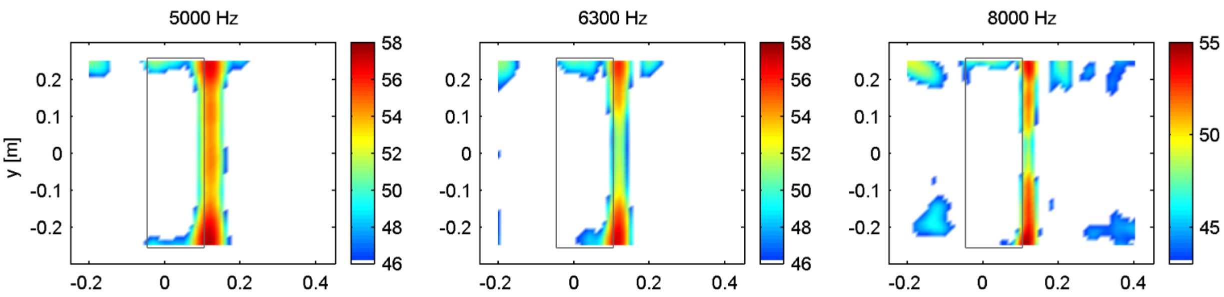

e) Cutted Serration

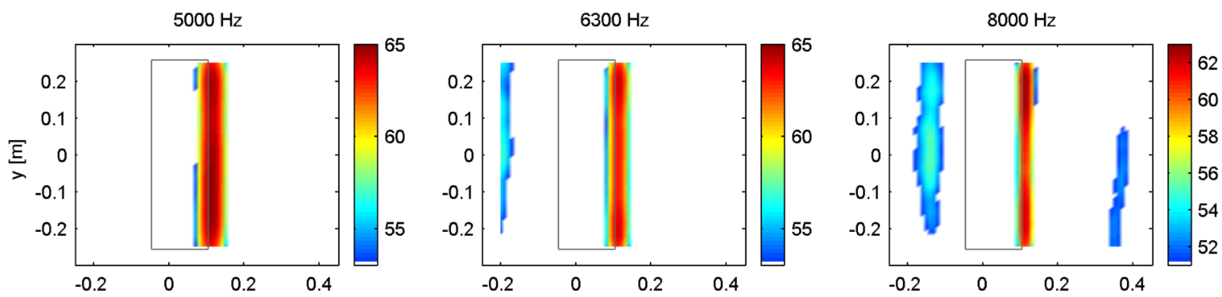

f) Serration with Cutted Plate

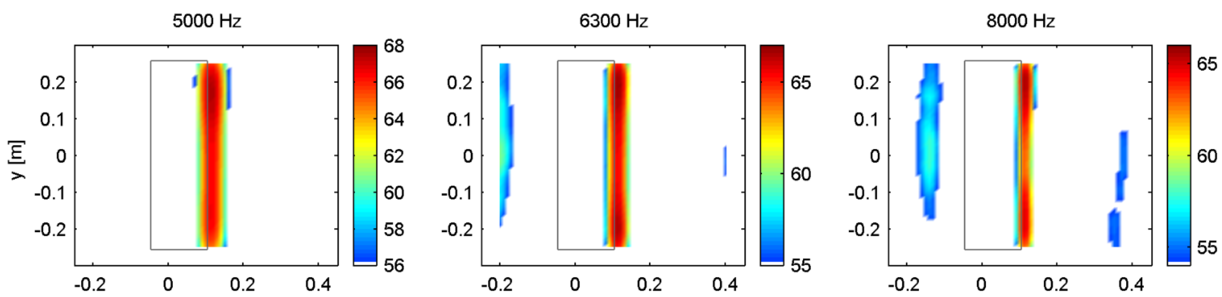

Figure 158 – **High Frequency Acoustic Maps – Free stream velocity 60 m/s; AoA = 0° (α_{eff} = 0°)**

a) Clean Configuration

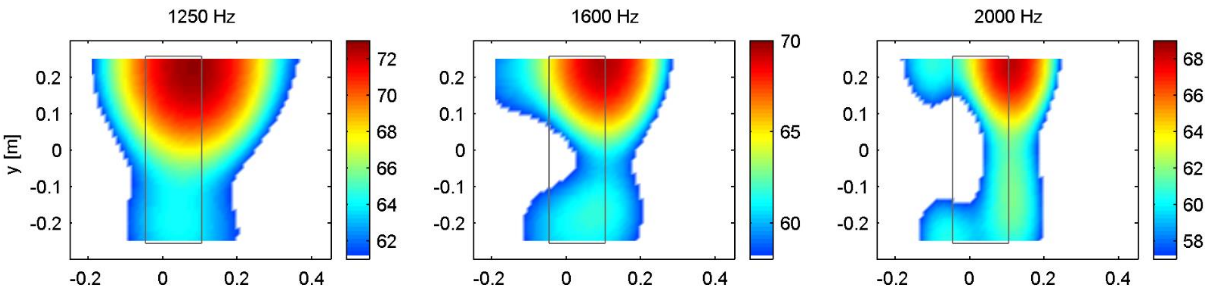

b) Serration Fixed on the Pressure Side

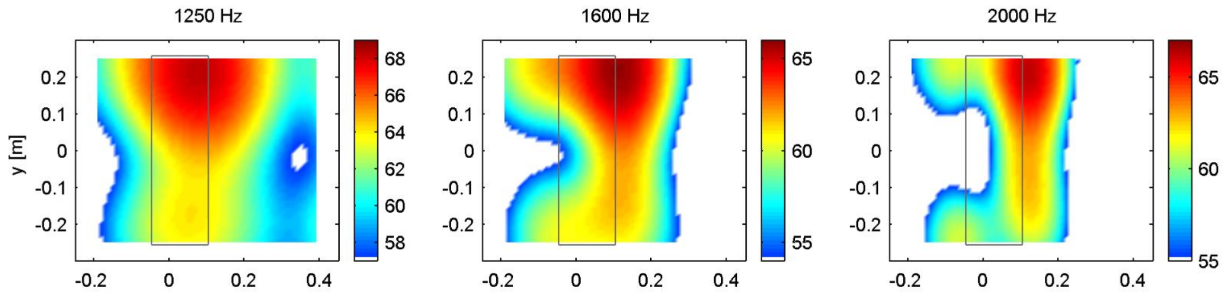

c) Serration Fixed on the Suction Side

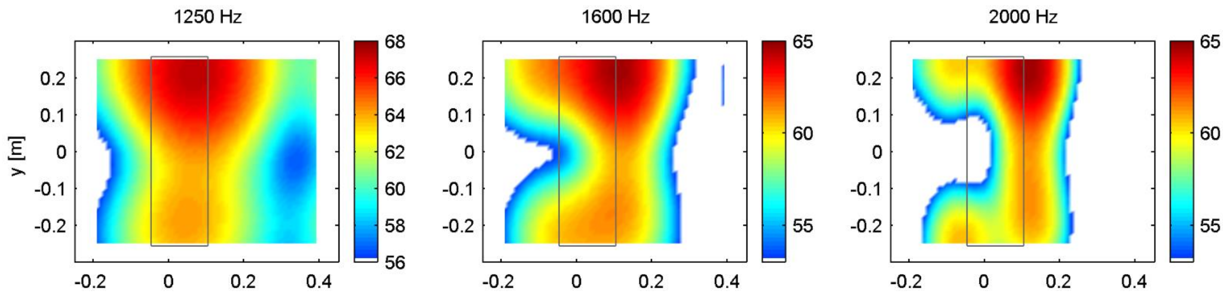

d) Flexible Serration

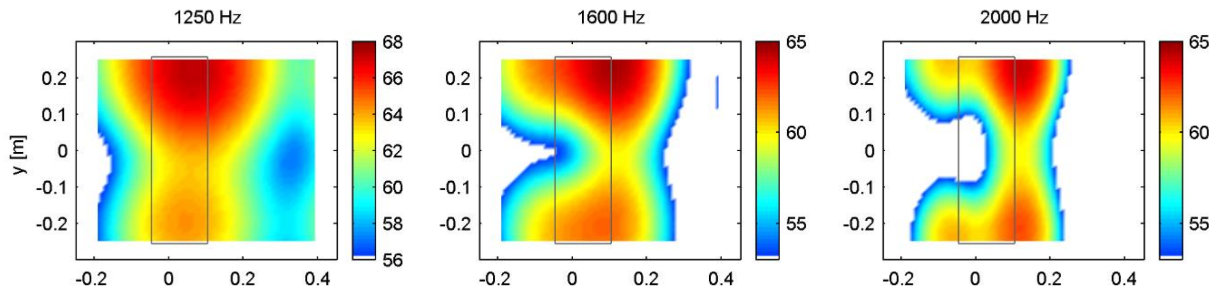

e) Cutted Serration

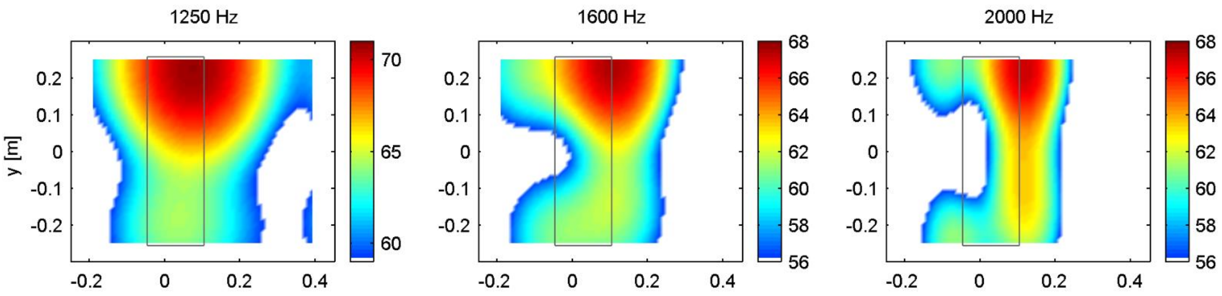

f) Serration with Cutted Plate

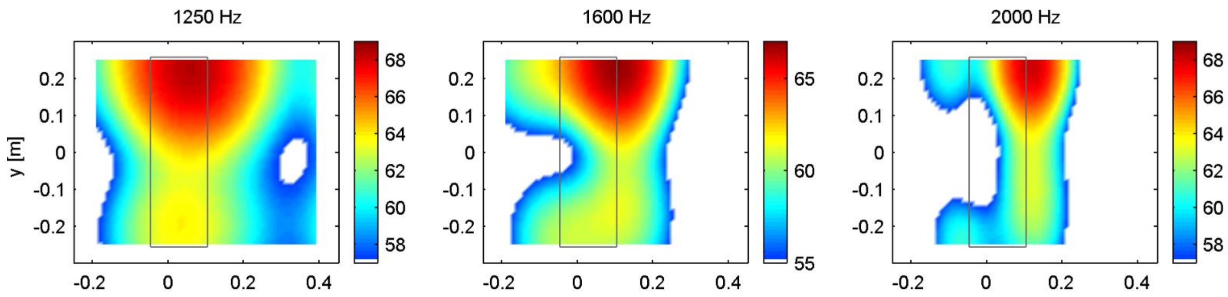

Figure 159 **– Low Frequency Acoustic Maps – Free stream velocity 60 m/s; AoA = 6° (α_{eff} = 3.4°)**

a) Clean Configuration

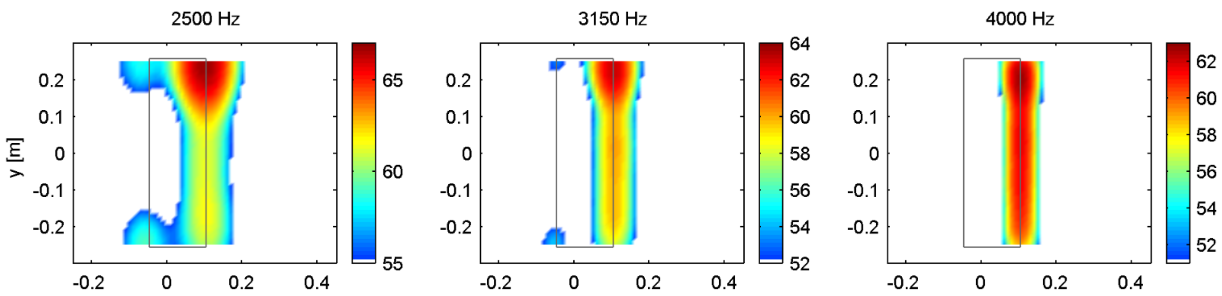

b) Serration Fixed on the Pressure Side

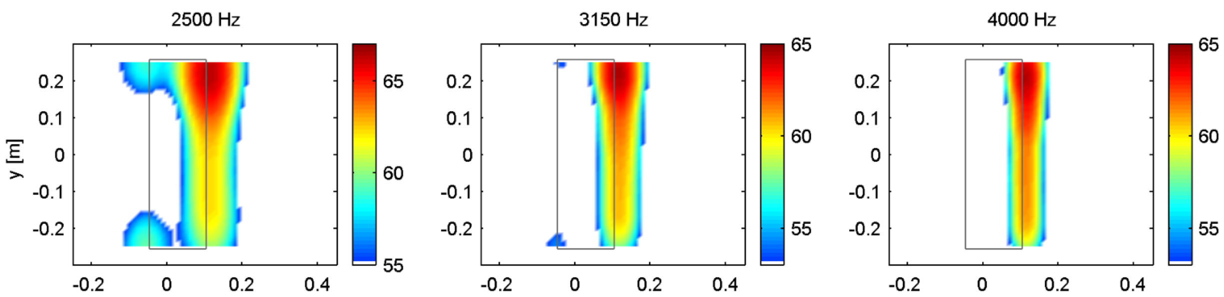

c) Serration Fixed on the Suction Side

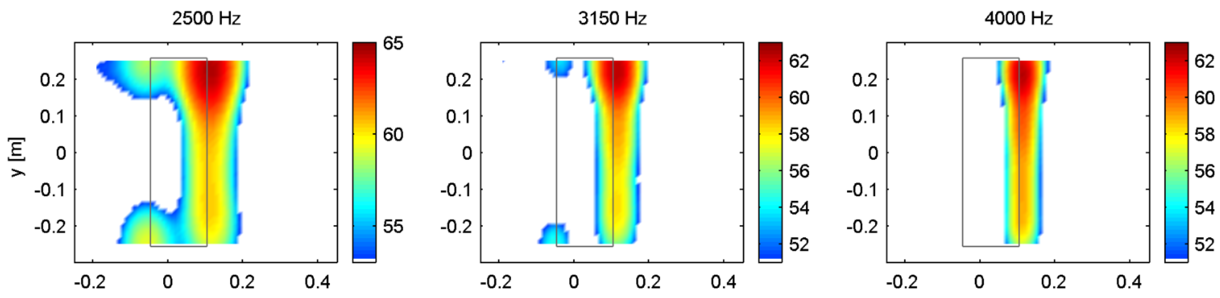

d) Flexible Serration

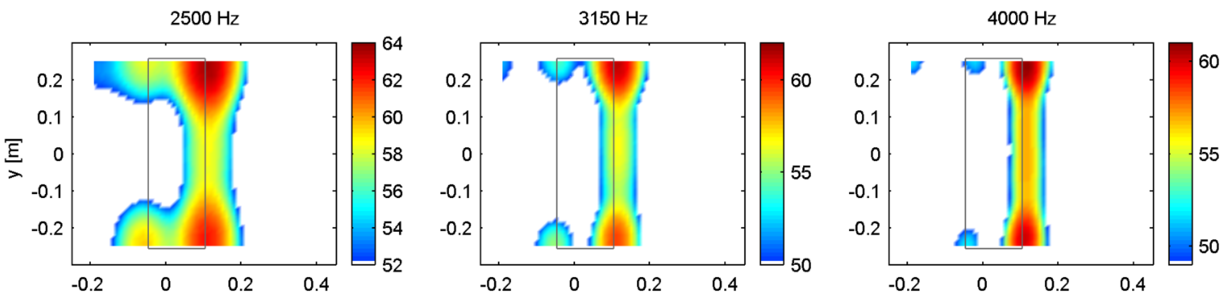

e) Cutted Serration

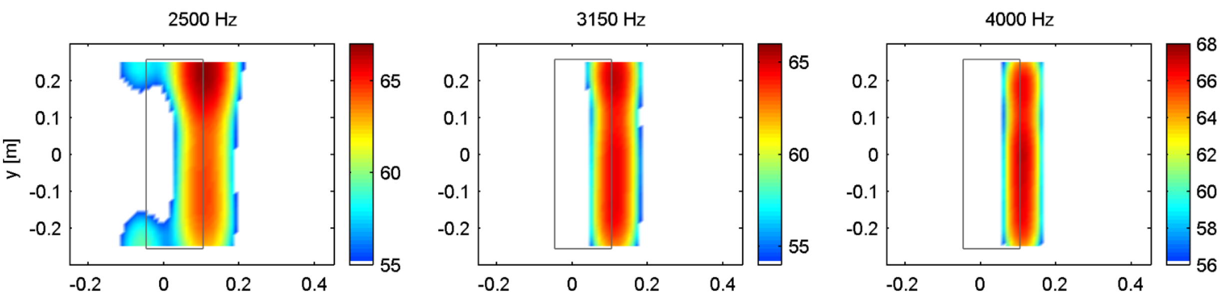

f) Serration with Cutted Plate

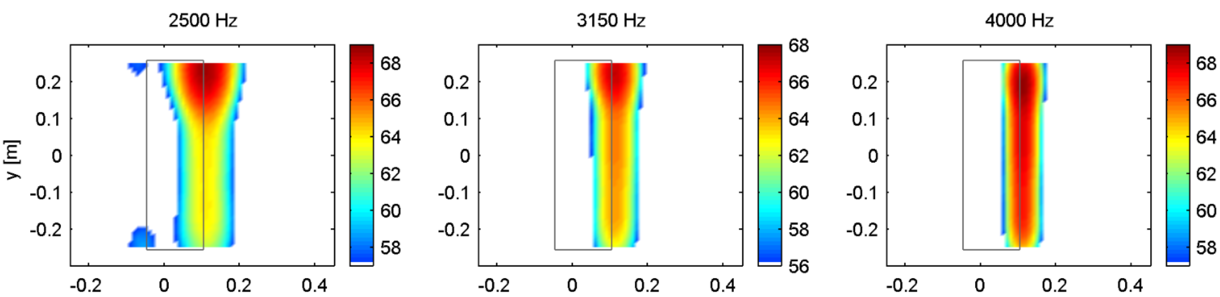

Figure 160 – **Medium Frequency Acoustic Maps – Free stream velocity 60 m/s; AoA = 6° (α_{eff} = 3.4°)**

a) Clean Configuration

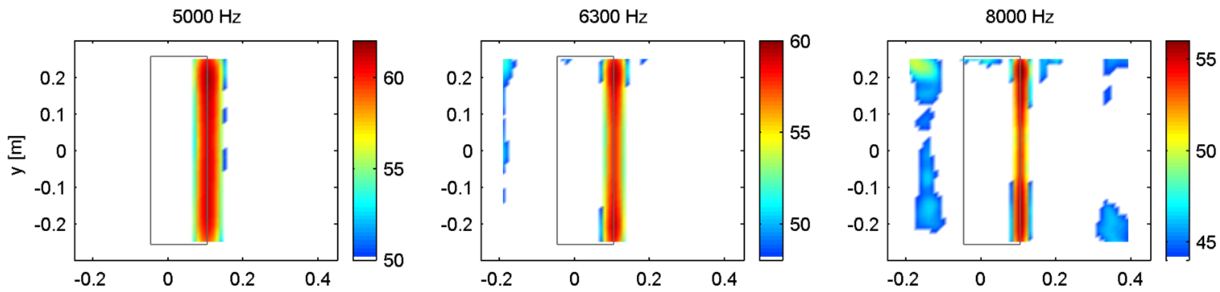

b) Serration Fixed on the Pressure Side

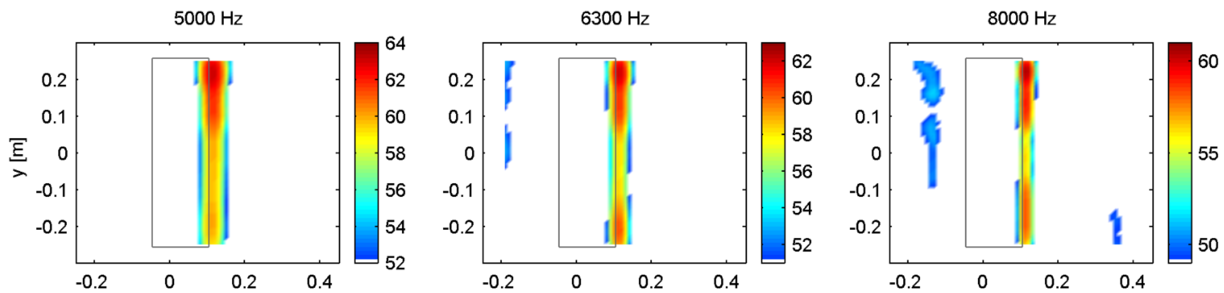

c) Serration Fixed on the Suction Side

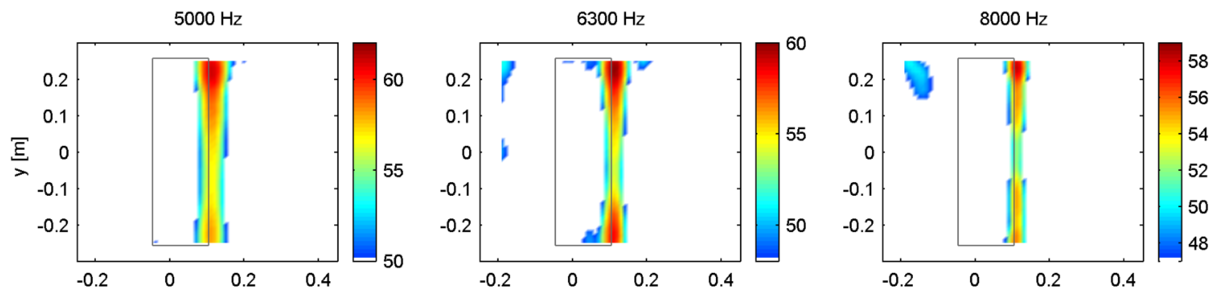

d) Flexible Serration

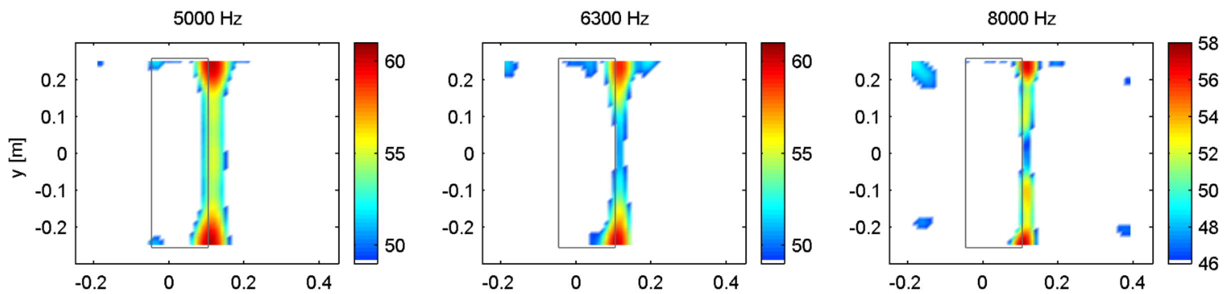

e) Cutted Serration

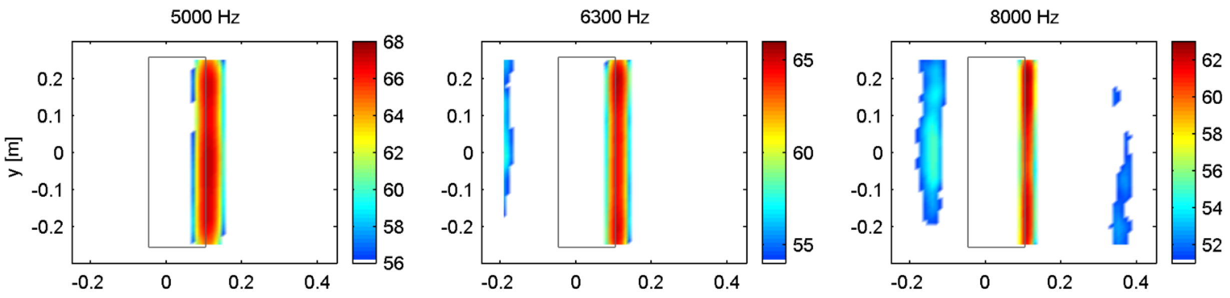

f) Serration with Cutted Plate

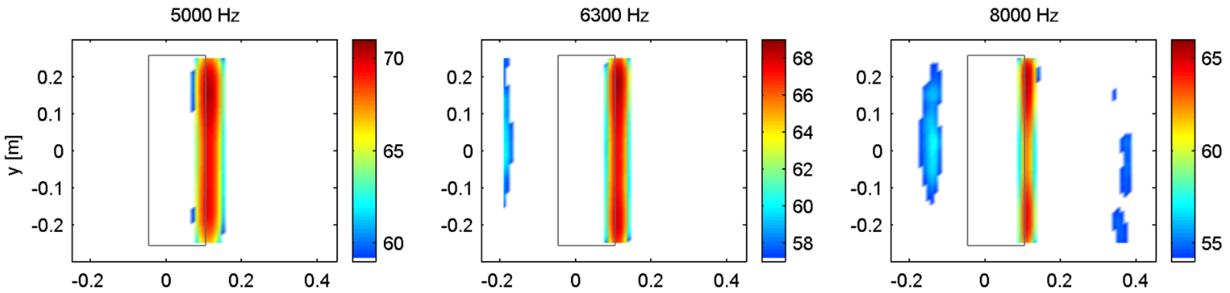

Figure 161 – **High Frequency Acoustic Maps – Free stream velocity 60 m/s; AoA = 6° (α_{eff} = 3.4°)**

a) Clean Configuration

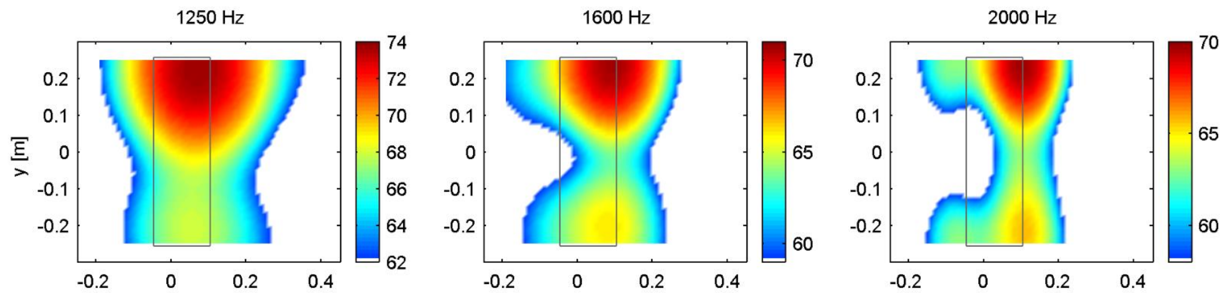

b) Serration Fixed on the Pressure Side

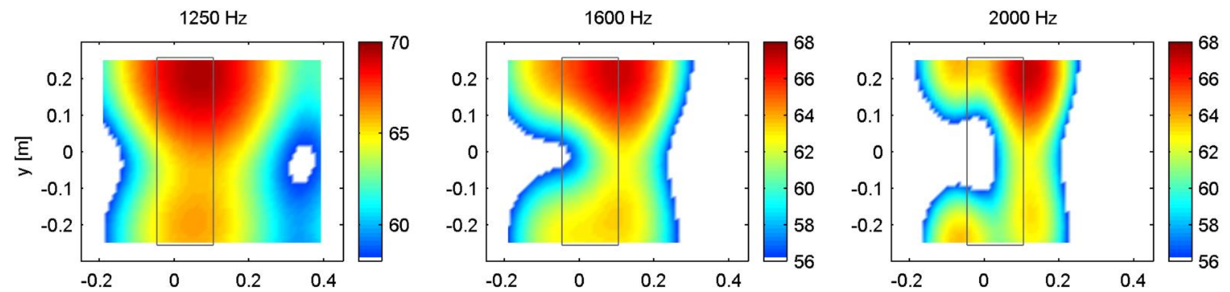

c) Serration Fixed on the Suction Side

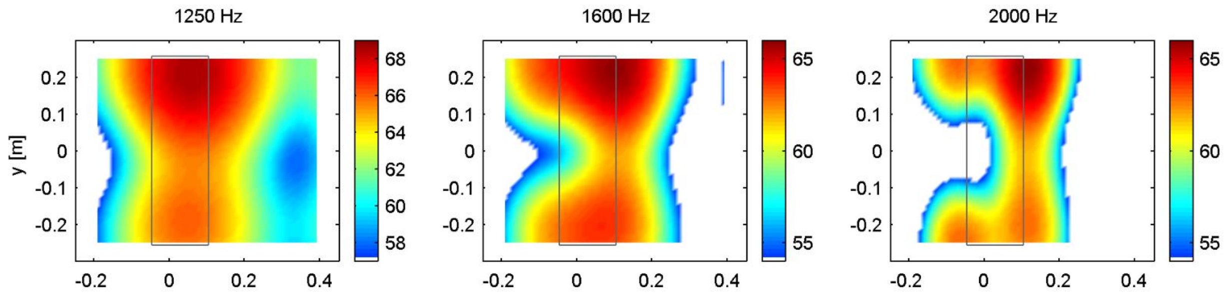

d) Flexible Serration

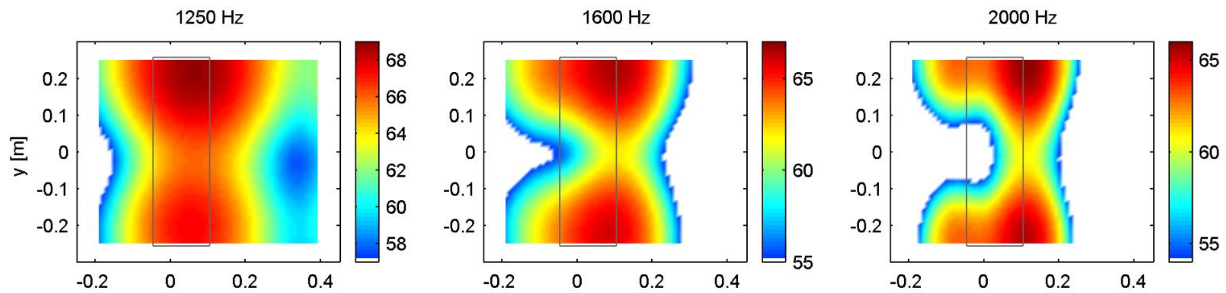

e) Cutted Serration

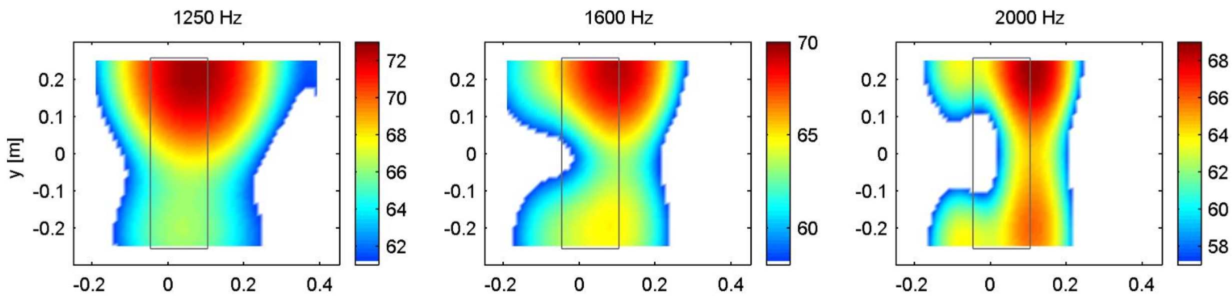

f) Serration with Cutted Plate

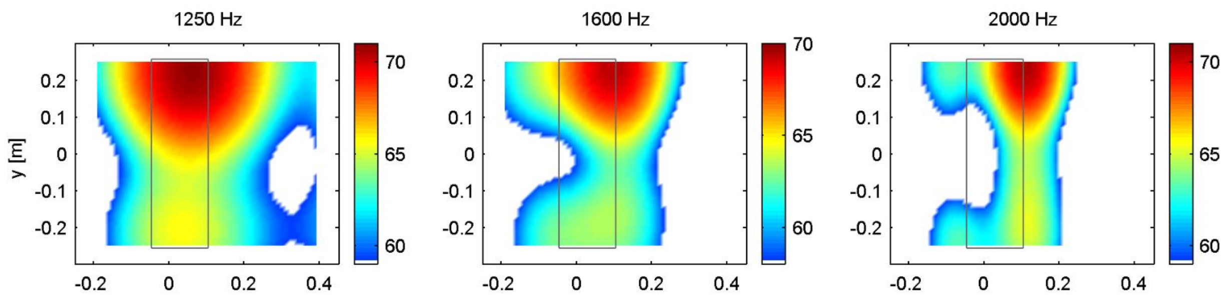

Figure 162 – **Low Frequency Acoustic Maps – Free stream velocity 60 m/s; AoA = 10.51° (α_{eff} = 6°)**

a) Clean Configuration

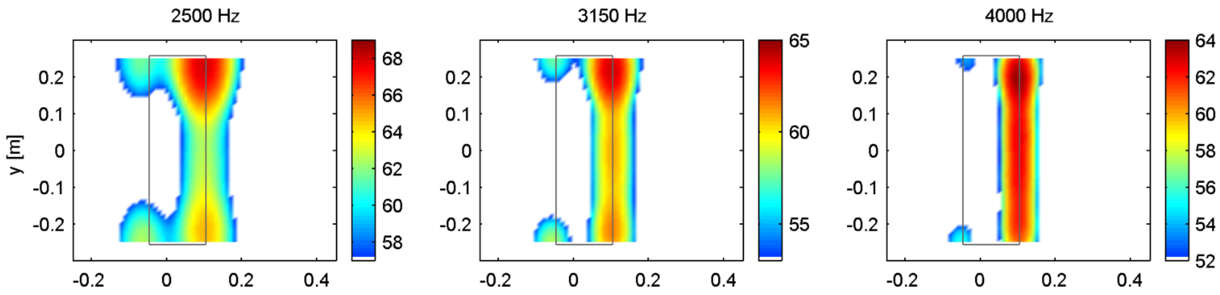

b) Serration Fixed on the Pressure Side

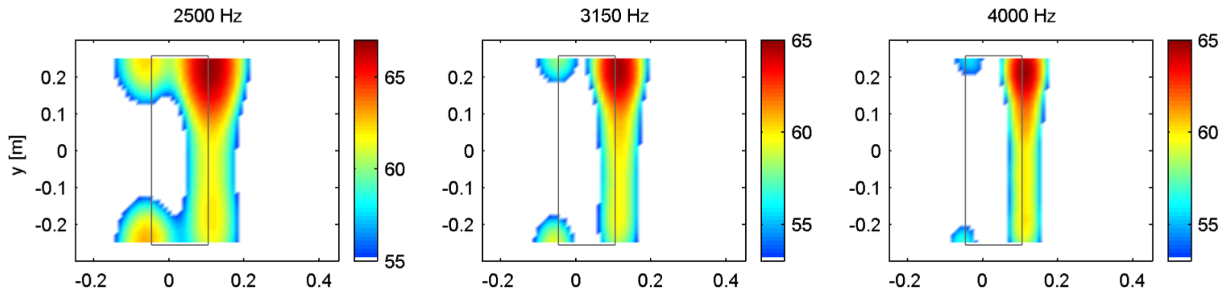

c) Serration Fixed on the Suction Side

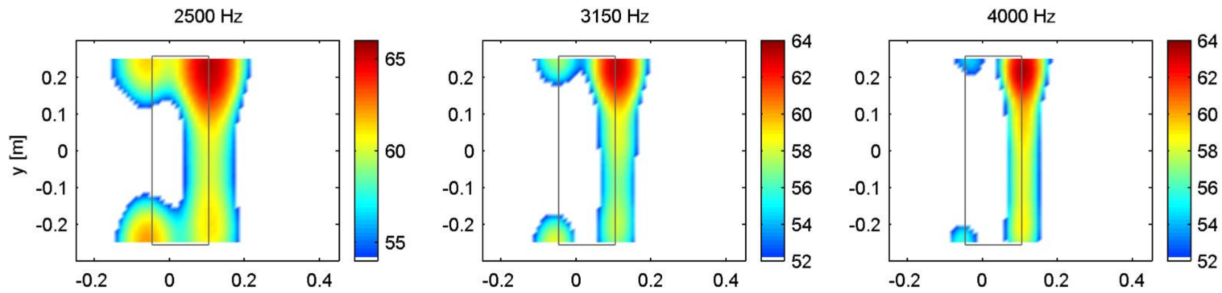

d) Flexible Serration

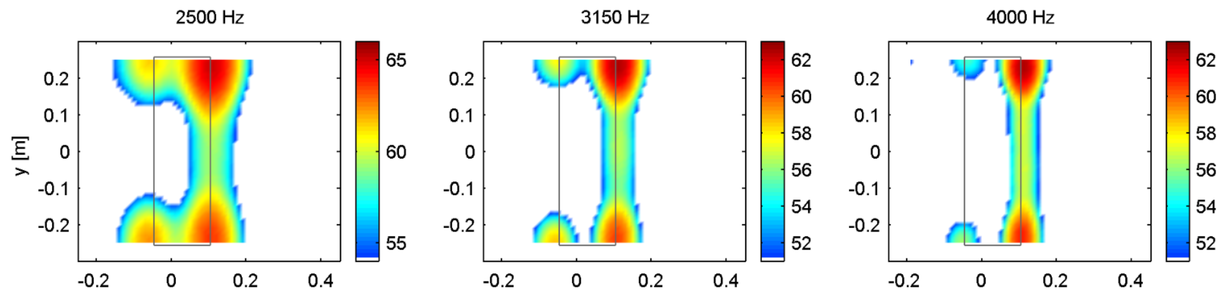

e) Cutted Serration

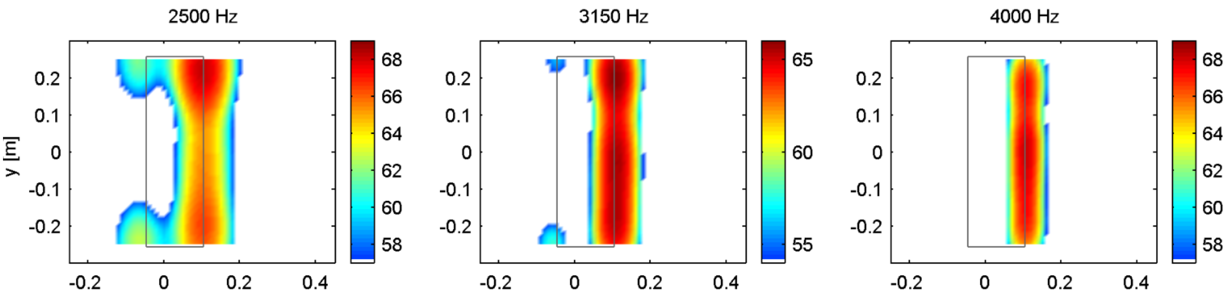

f) Serration with Cutted Plate

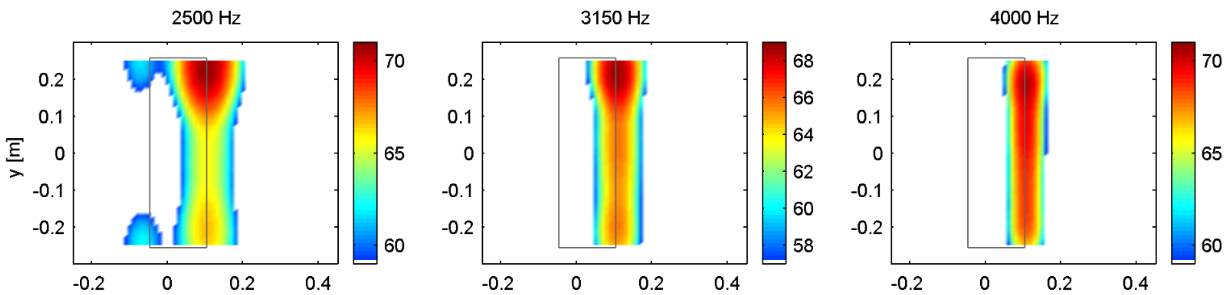

Figure 163 – **Medium Frequency Acoustic Maps – Free stream velocity 60 m/s; AoA = 10.51° (α_{eff} = 6°)**

a) Clean Configuration

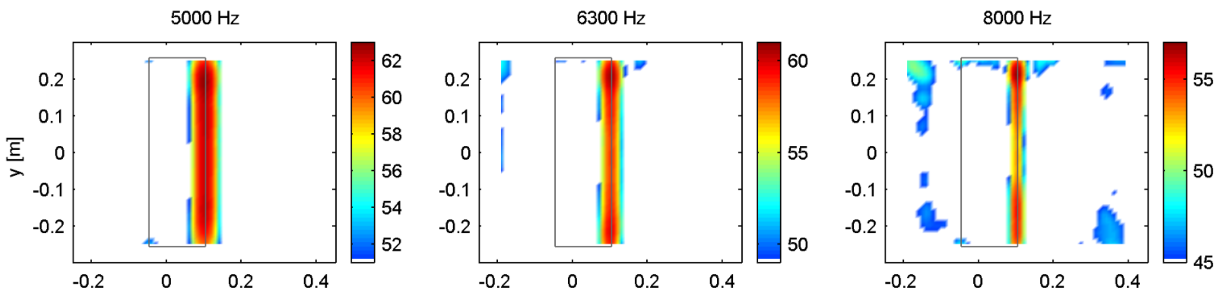

b) Serration Fixed on the Pressure Side

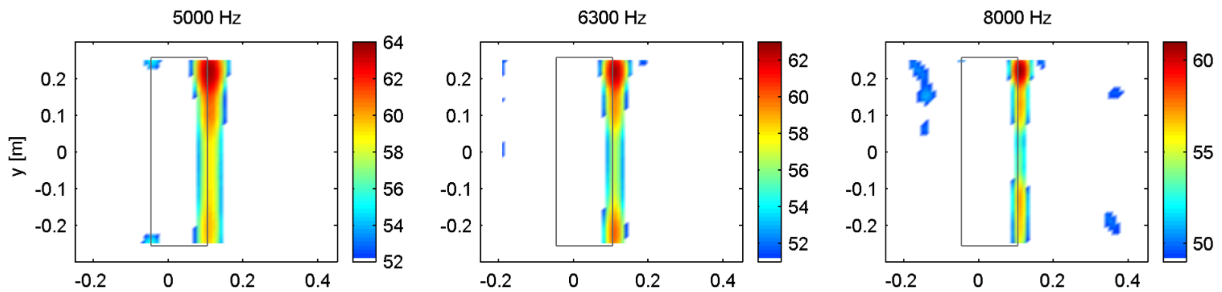

c) Serration Fixed on the Suction Side

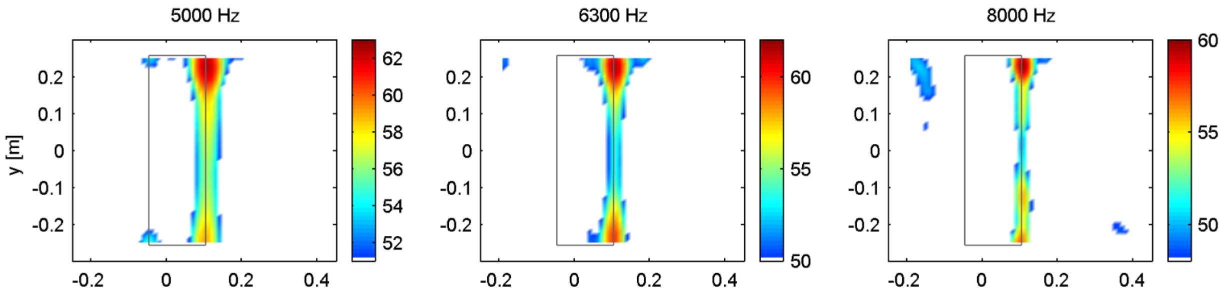

d) Flexible Serration

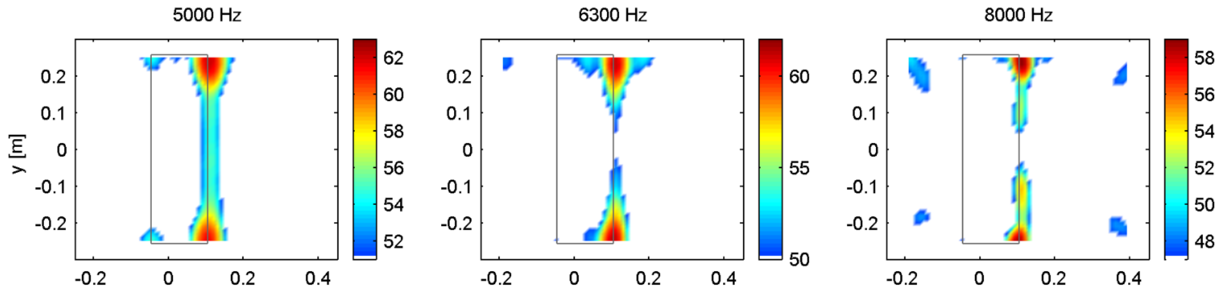

e) Cutted Serration

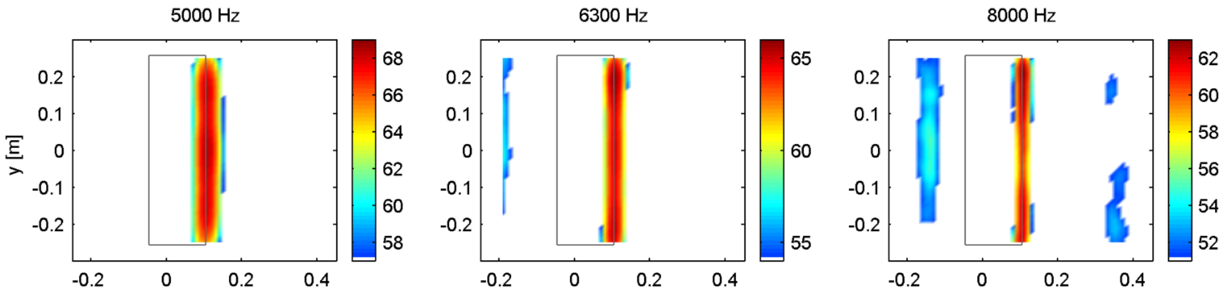

f) Serration with Cutted Plate

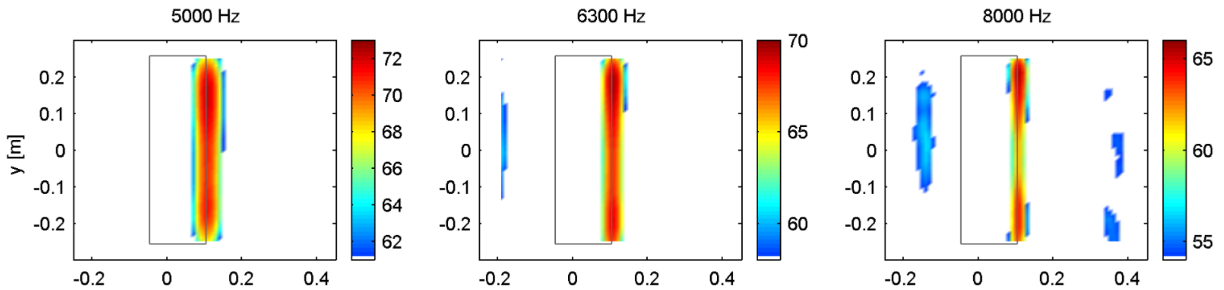

Figure 164 – **High Frequency Acoustic Maps – Free stream velocity 60 m/s; AoA = 10.51° (α_{eff} = 6°)**

a) Clean Configuration

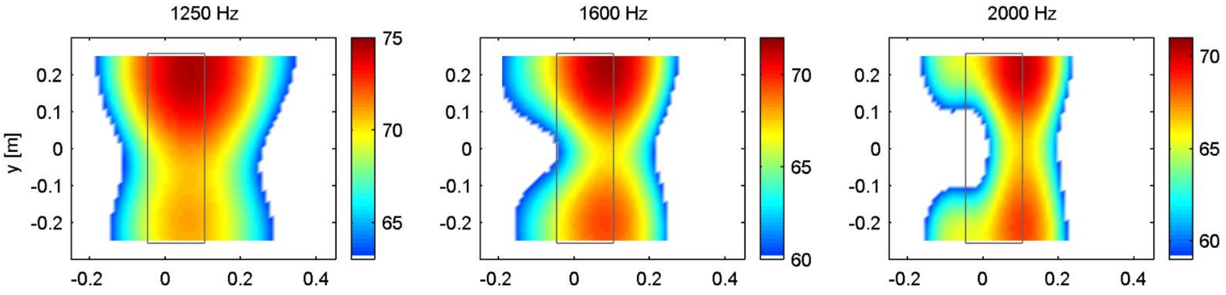

b) Serration Fixed on the Pressure Side

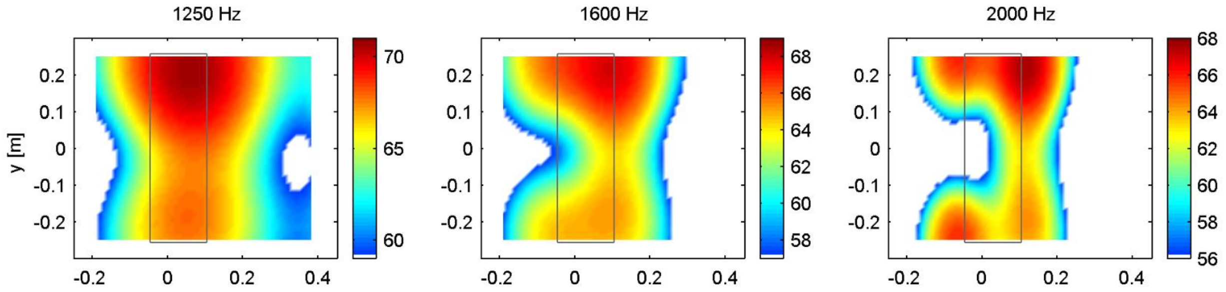

c) Serration Fixed on the Suction Side

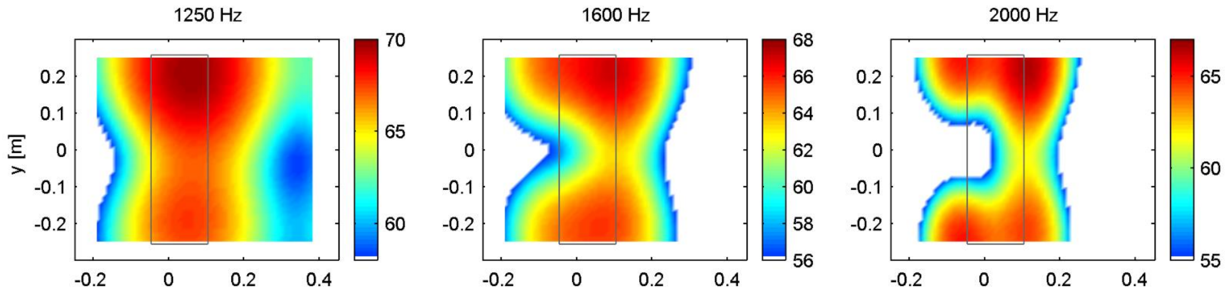

d) Flexible Serration

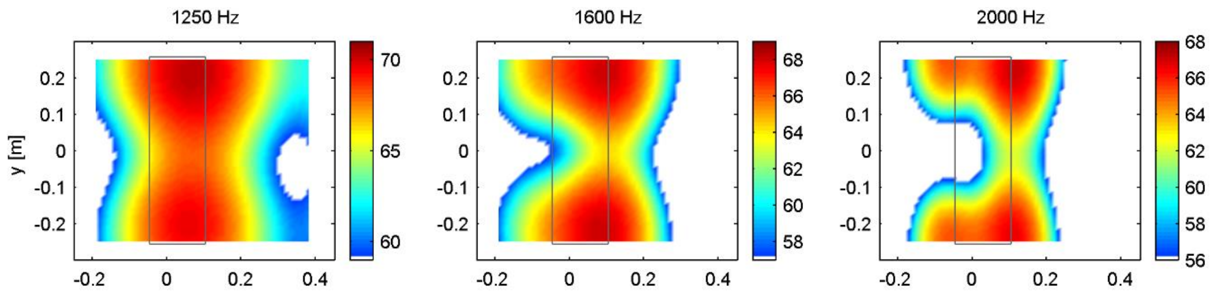

e) Cutted Serration

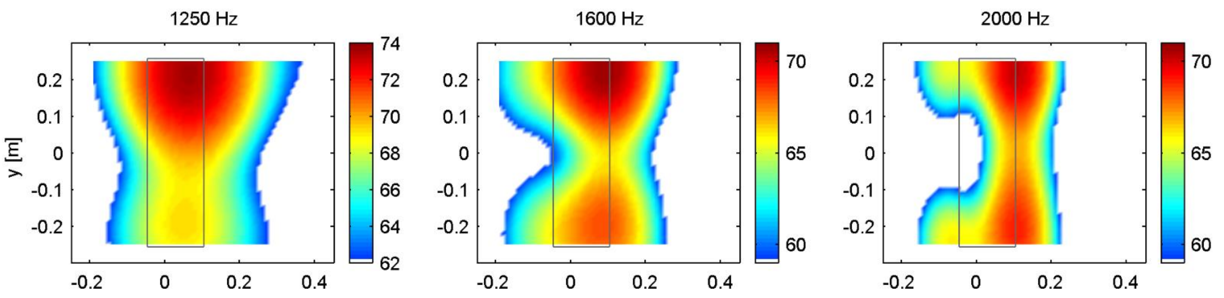

f) Serration with Cutted Plate

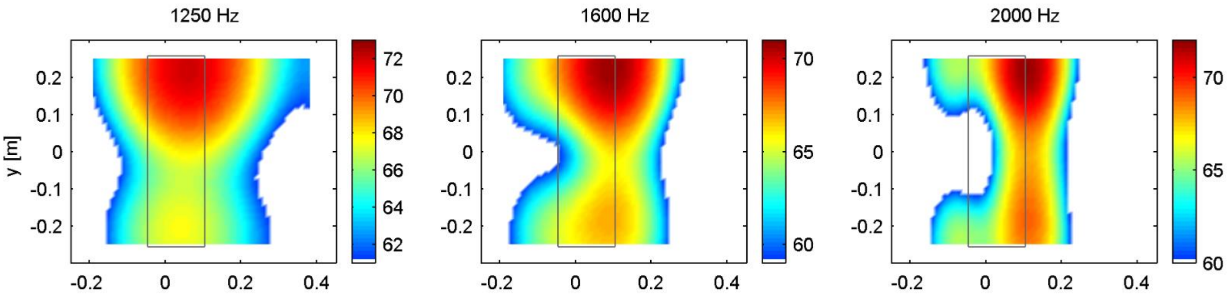

Figure 165 – **Low Frequency Acoustic Maps – Free stream velocity 60 m/s; AoA = 14.37° (α_{eff} = 8.2°)**

a) Clean Configuration

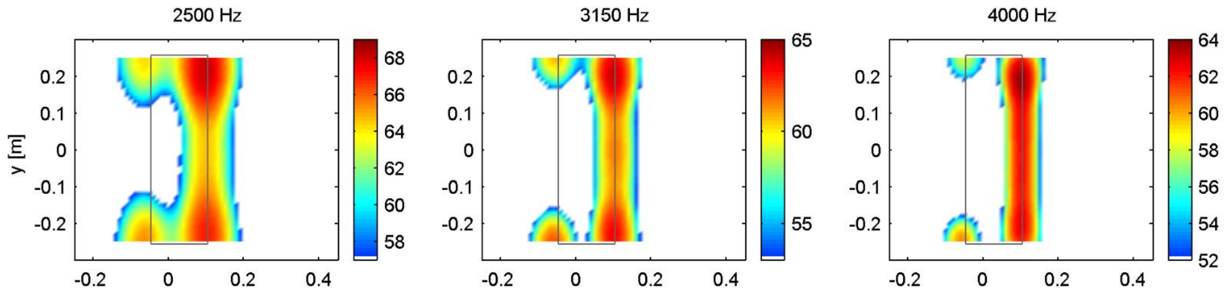

b) Serration Fixed on the Pressure Side

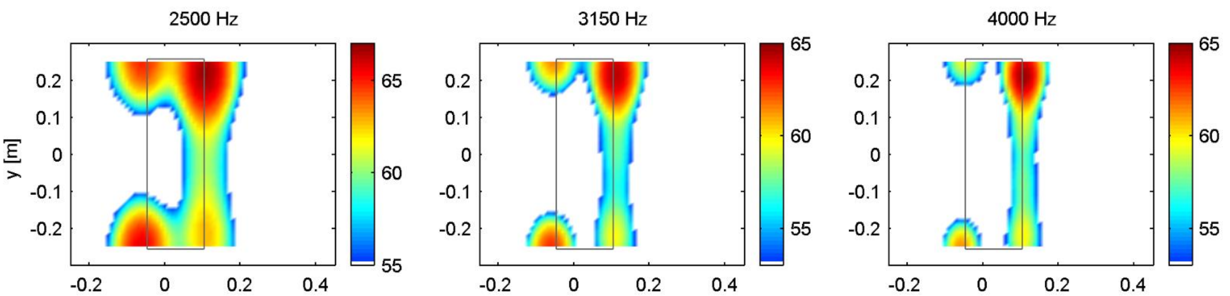

c) Serration Fixed on the Suction Side

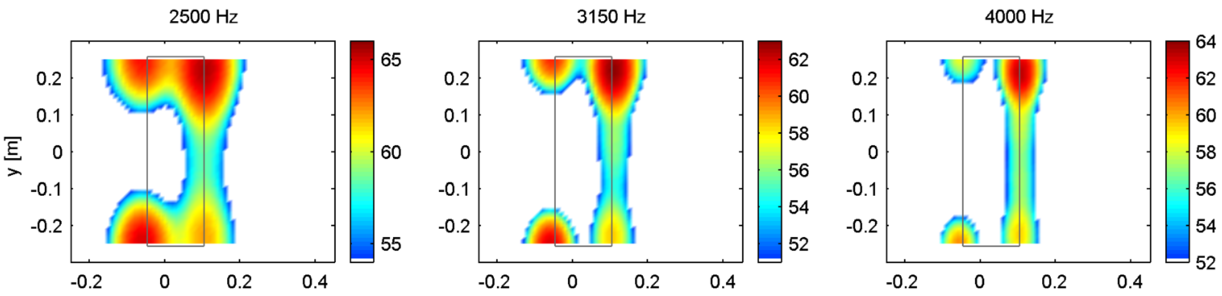

d) Flexible Serration

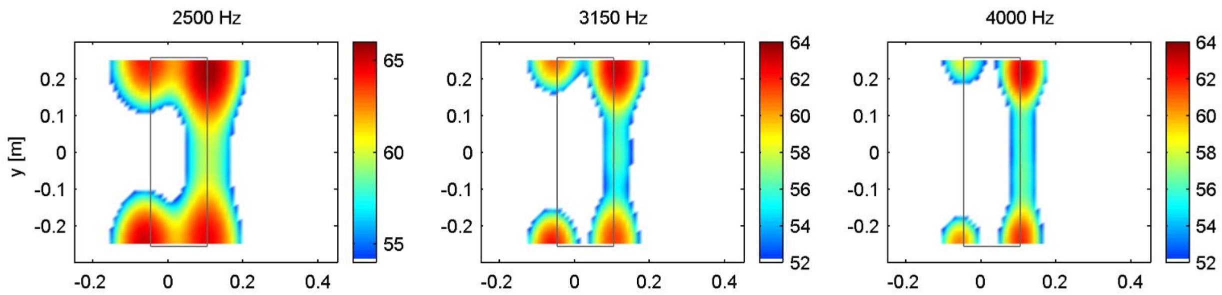

e) Cutted Serration

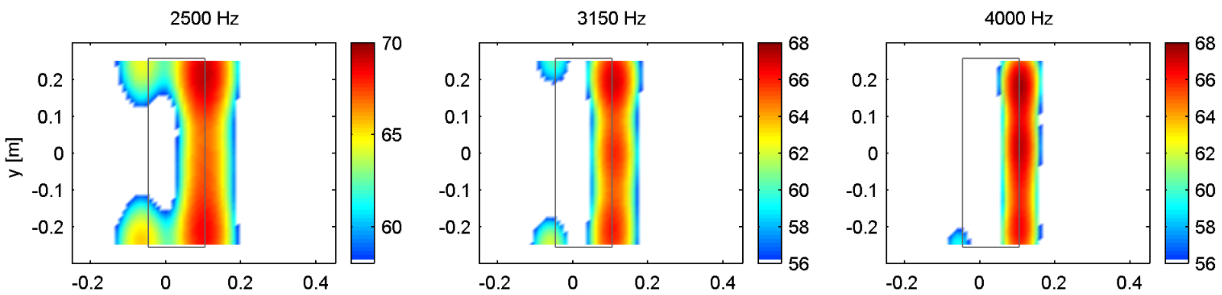

f) Serration with Cutted Plate

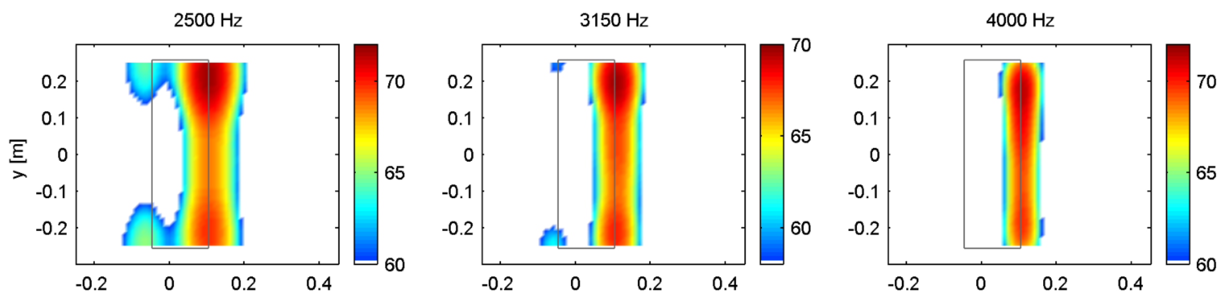

Figure 166 **– Medium Frequency Acoustic Maps – Free stream velocity 60 m/s; AoA = 14.37° (α_{eff} = 8.2°)**

a) Clean Configuration

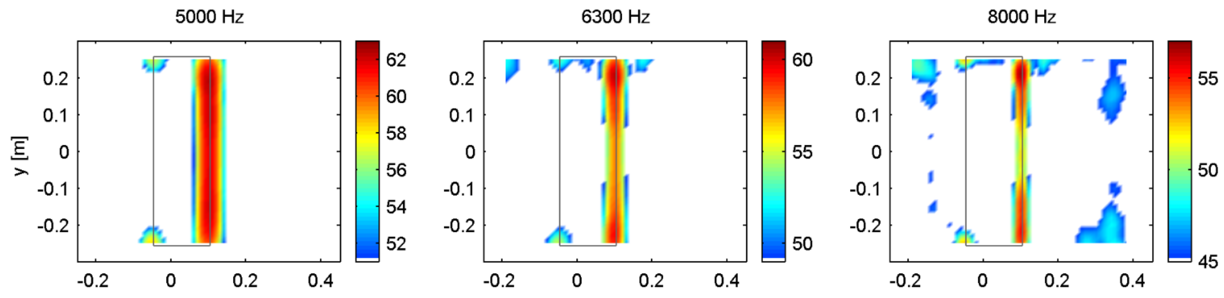

b) Serration Fixed on the Pressure Side

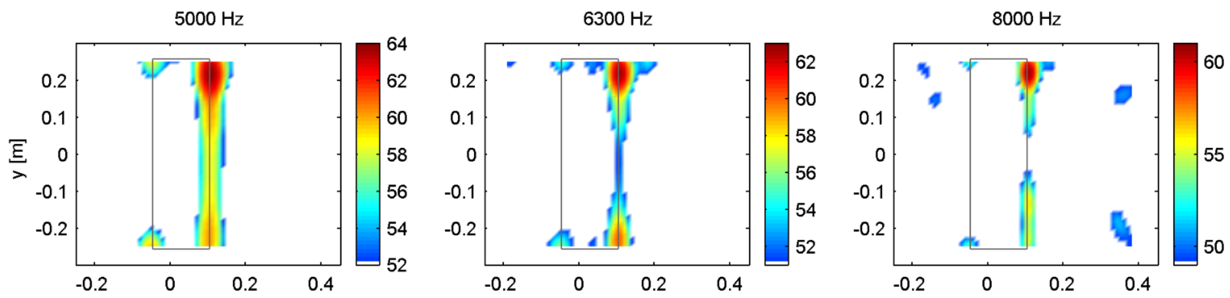

c) Serration Fixed on the Suction Side

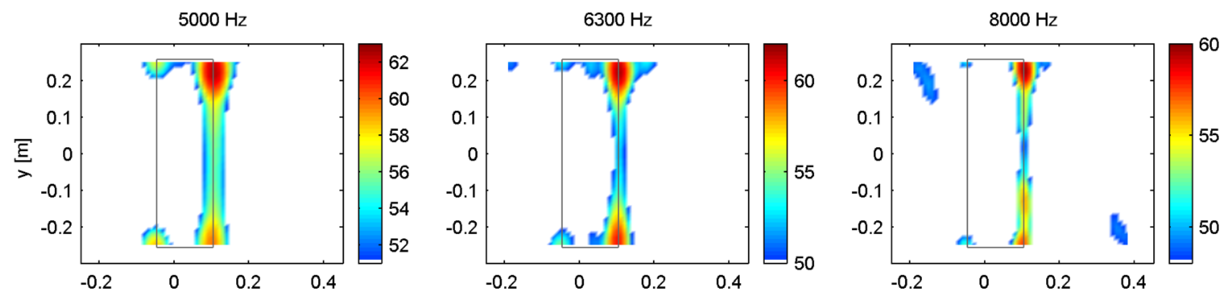

d) Flexible Serration

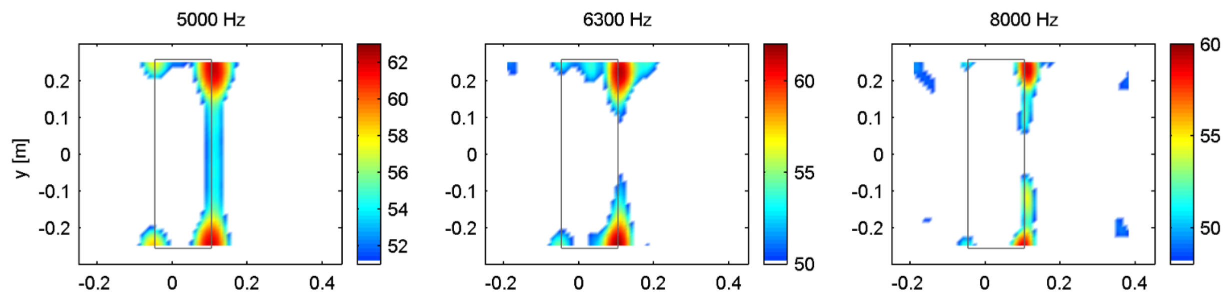

e) Cutted Serration

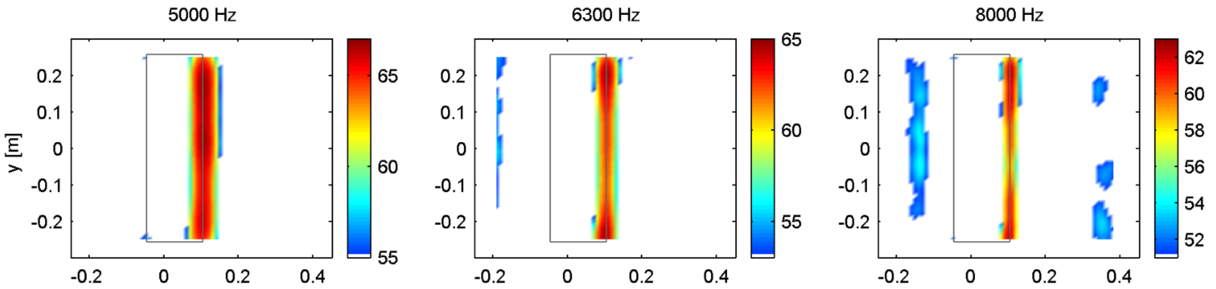

f) Serration with Cutted Plate

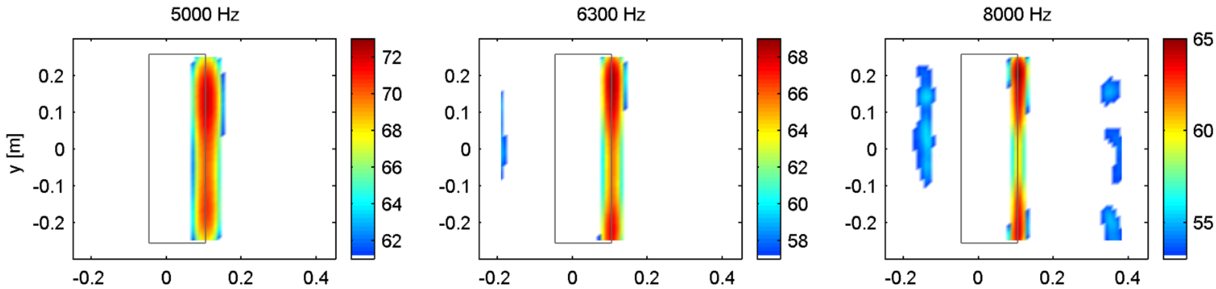

Figure 167 – **High Frequency Acoustic Maps – Free stream velocity 60 m/s; AoA = 14.37° (α_{eff} = 8.2°)**

a) Clean Configuration

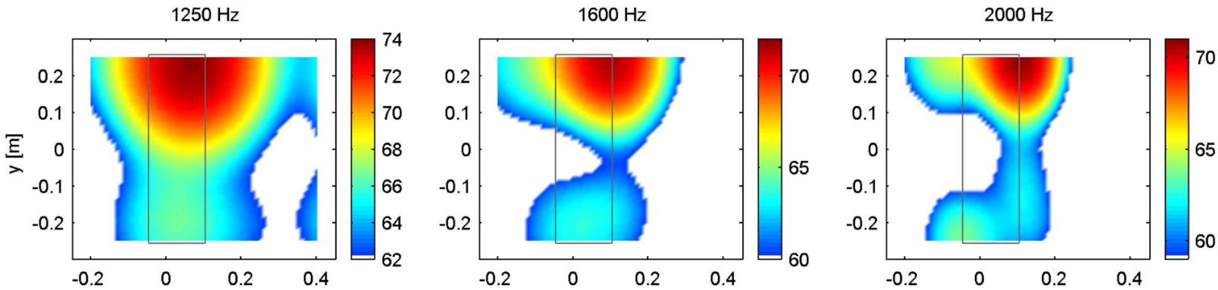

b) Serration Fixed on the Pressure Side

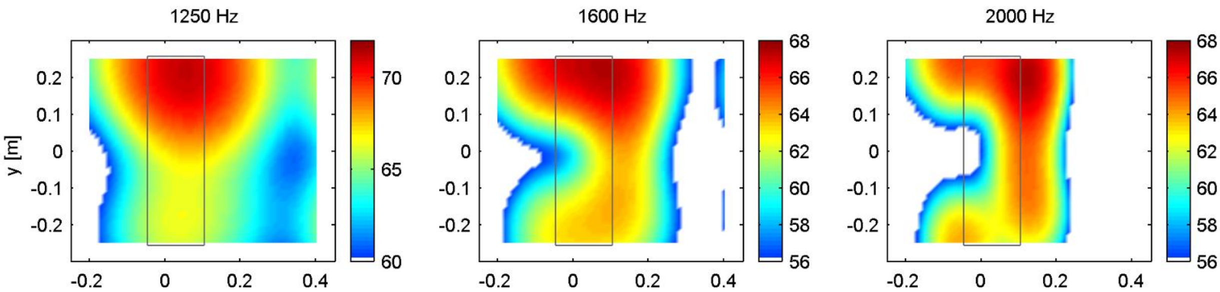

c) Serration Fixed on the Suction Side

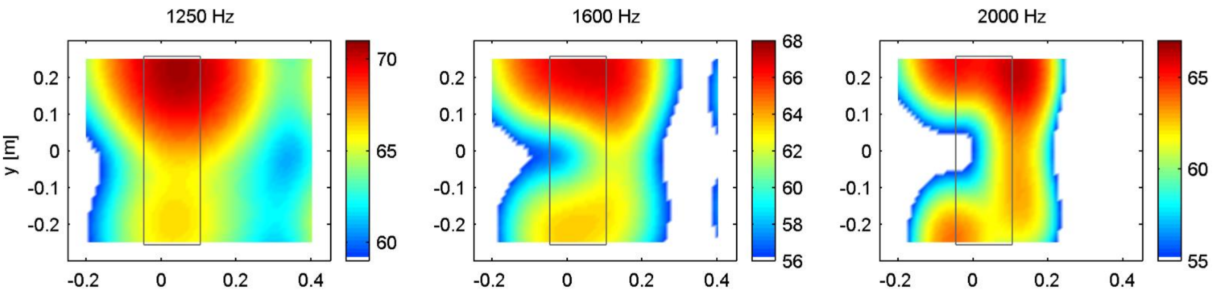

d) Flexible Serration

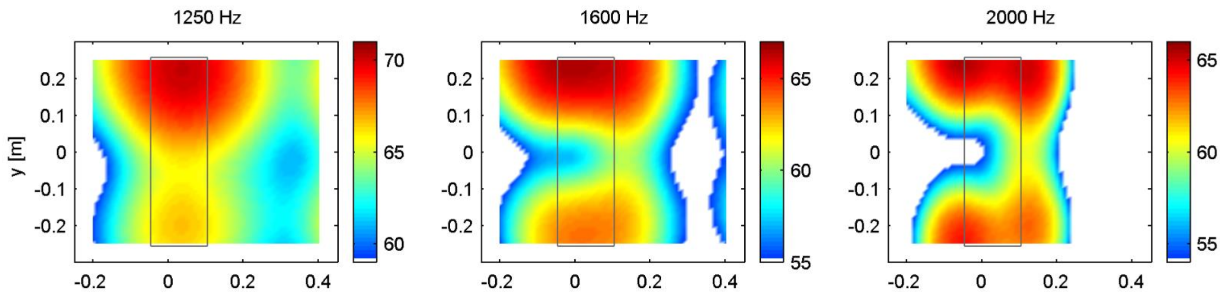

e) Cutted Serration

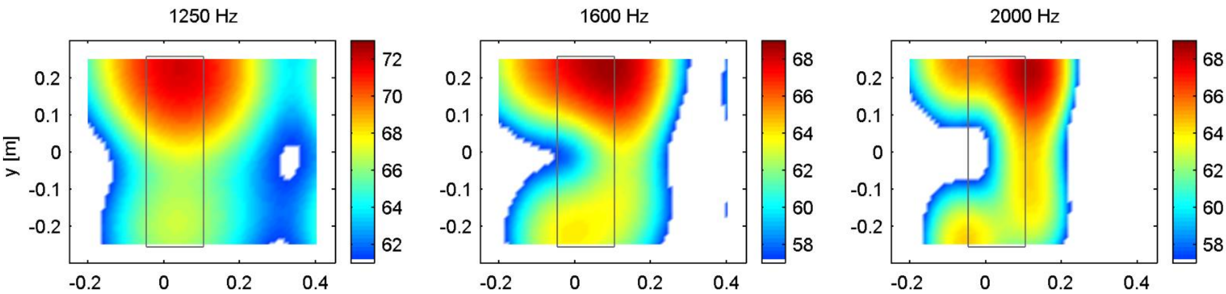

f) Serration with Cutted Plate

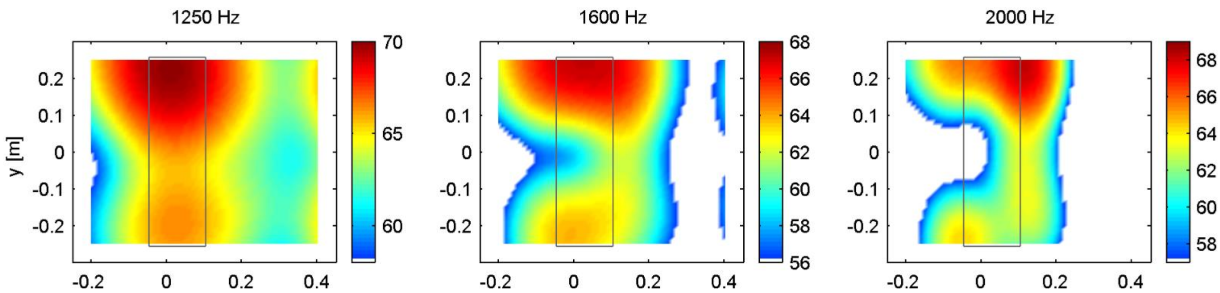

Figure 168 **– Low Frequency Acoustic Maps – Free stream velocity 70 m/s; AoA = 0° (α_{eff} = 0°)**

a) Clean Configuration

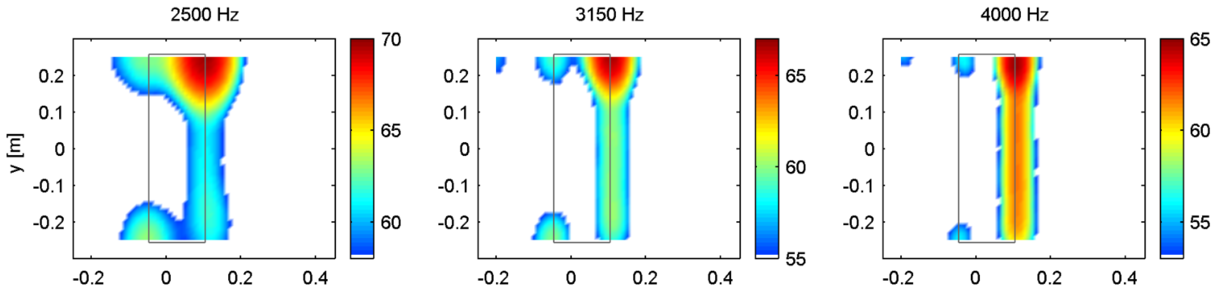

b) Serration Fixed on the Pressure Side

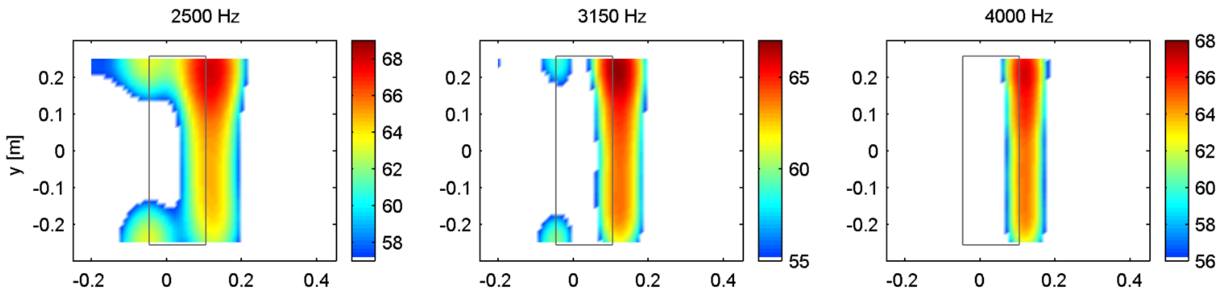

c) Serration Fixed on the Suction Side

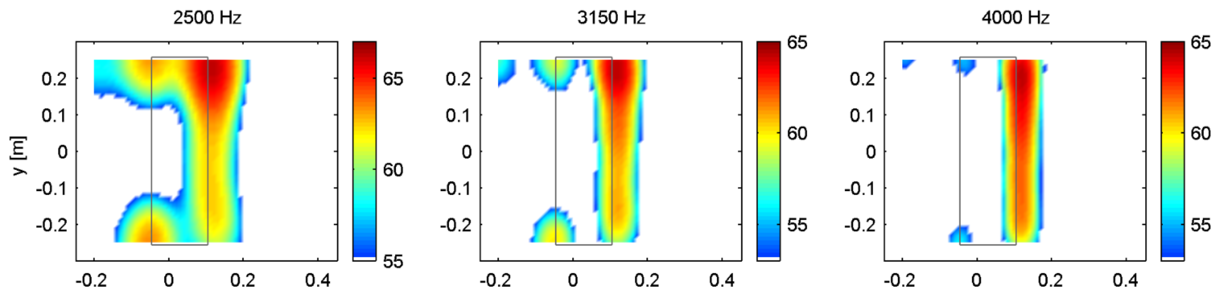

d) Flexible Serration

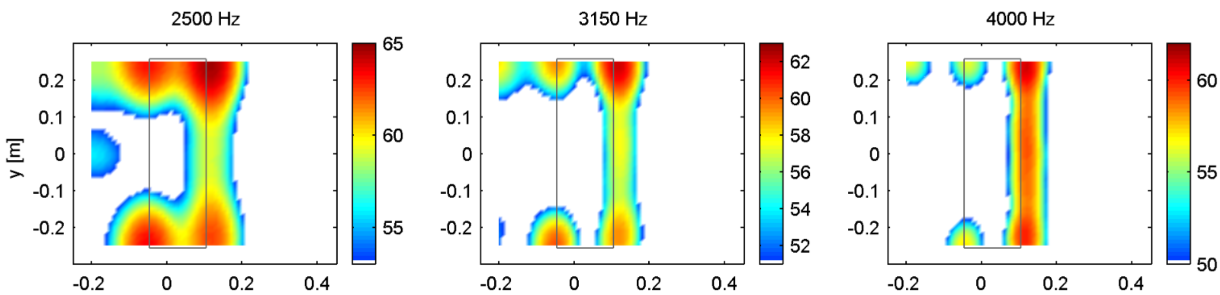

e) Cutted Serration

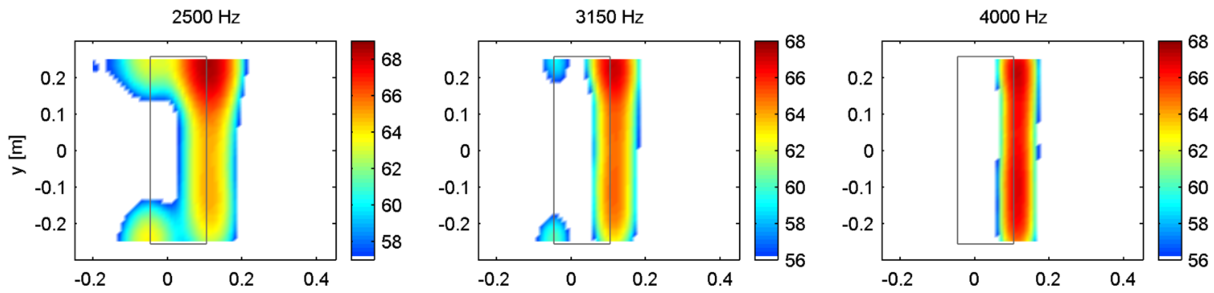

f) Serration with Cutted Plate

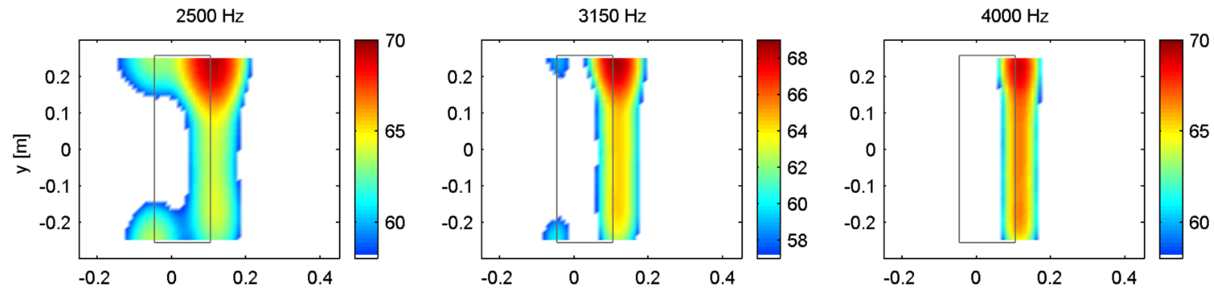

Figure 169 – **Medium Frequency Acoustic Maps – Free stream velocity 70 m/s; AoA = 0° (α_{eff} = 0°)**

a) Clean Configuration

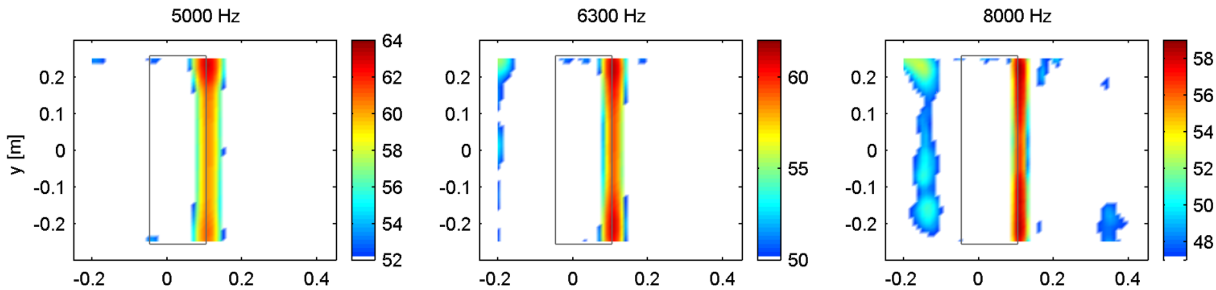

b) Serration Fixed on the Pressure Side

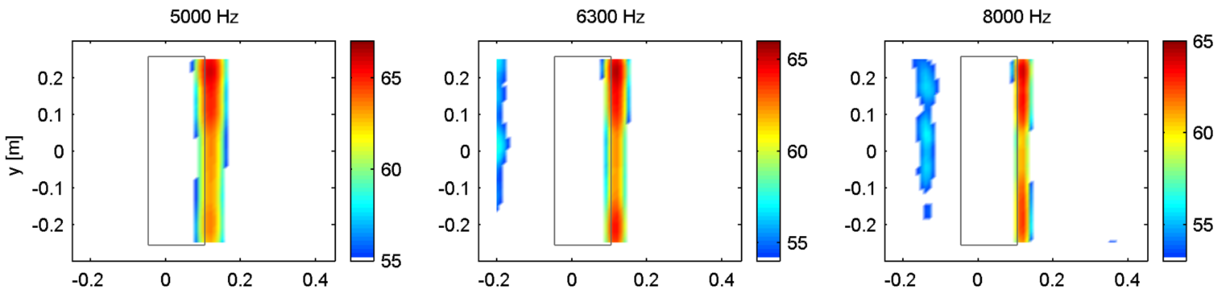

c) Serration Fixed on the Suction Side

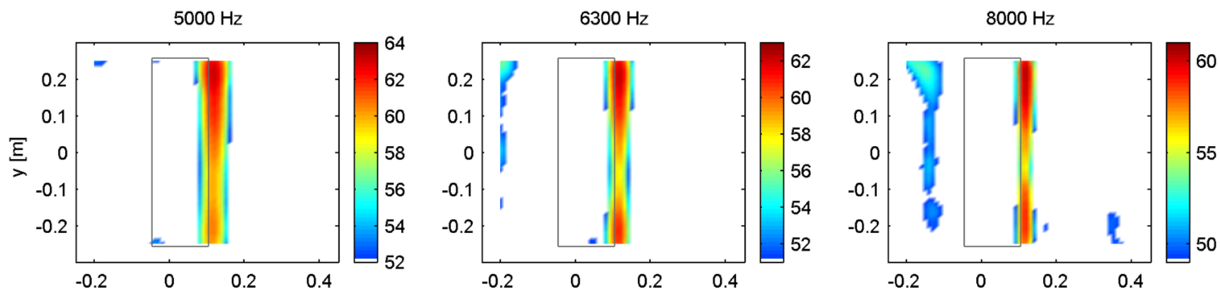

d) Flexible Serration

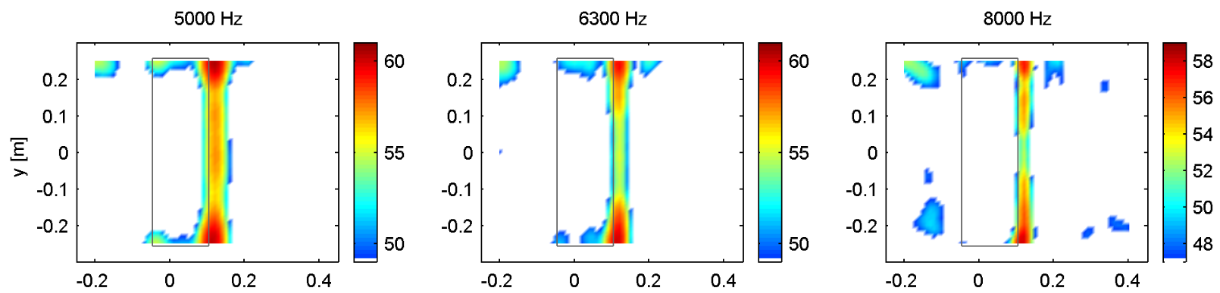

e) Cutted Serration

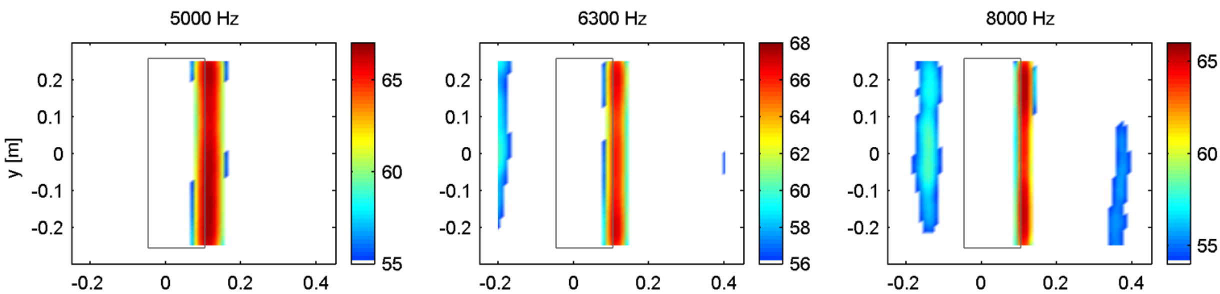

f) Serration with Cutted Plate

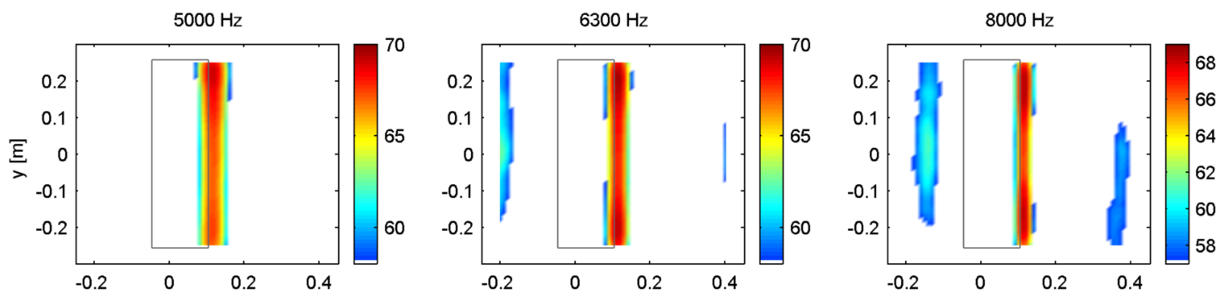

Figure 170 – **High Frequency Acoustic Maps – Free stream velocity 70 m/s; AoA = 0° (α_{eff} = 0°)**

a) Clean Configuration

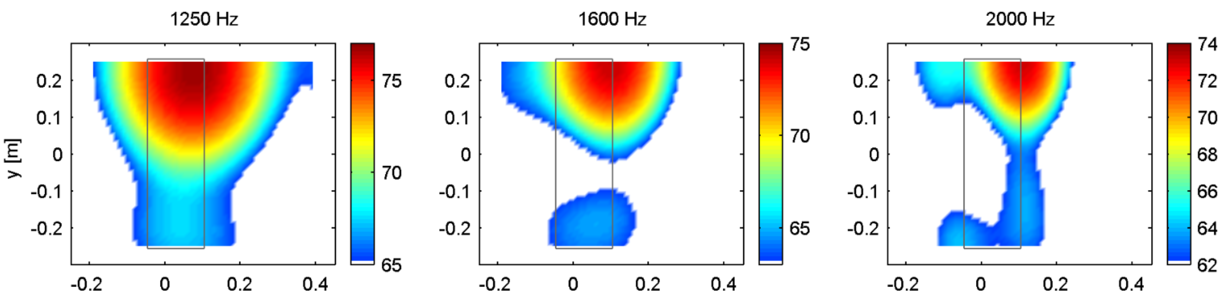

b) Serration Fixed on the Pressure Side

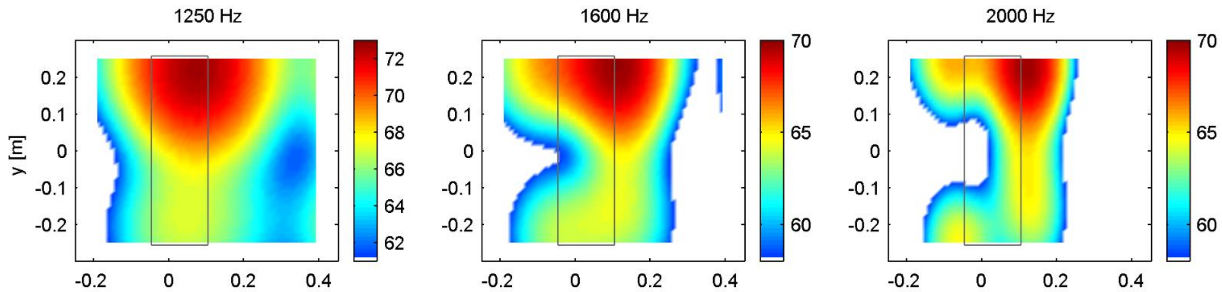

c) Serration Fixed on the Suction Side

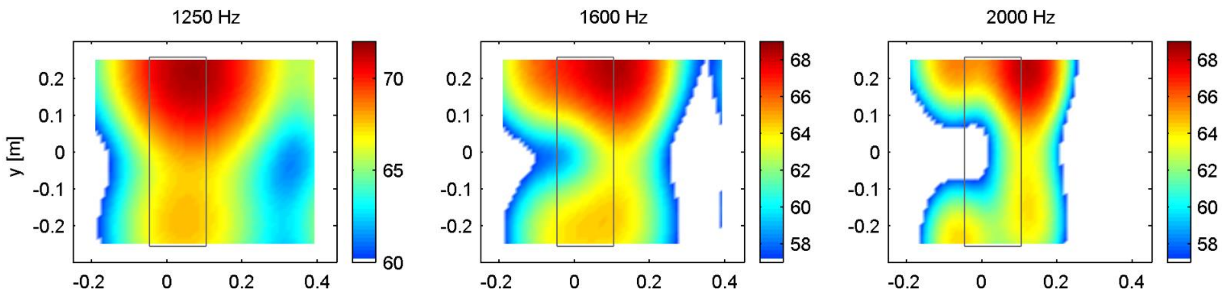

d) Flexible Serration

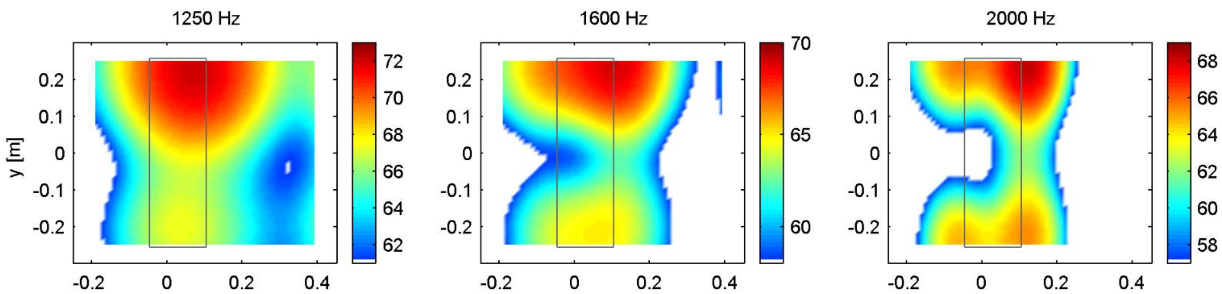

e) Cutted Serration

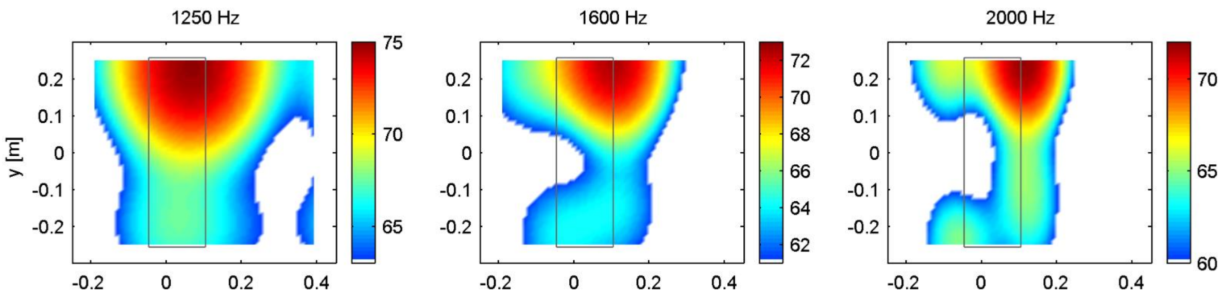

f) Serration with Cutted Plate

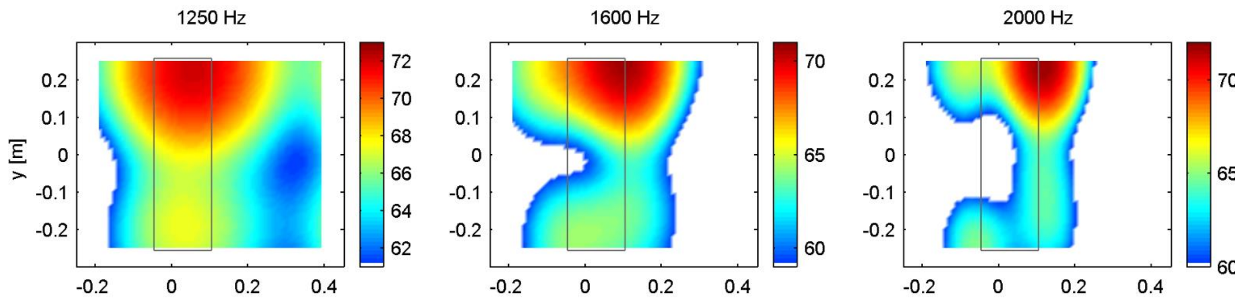

Figure 171 – **Low Frequency Acoustic Maps – Free stream velocity 70 m/s; AoA = 6° (α_{eff} = 3.4°)**

a) Clean Configuration

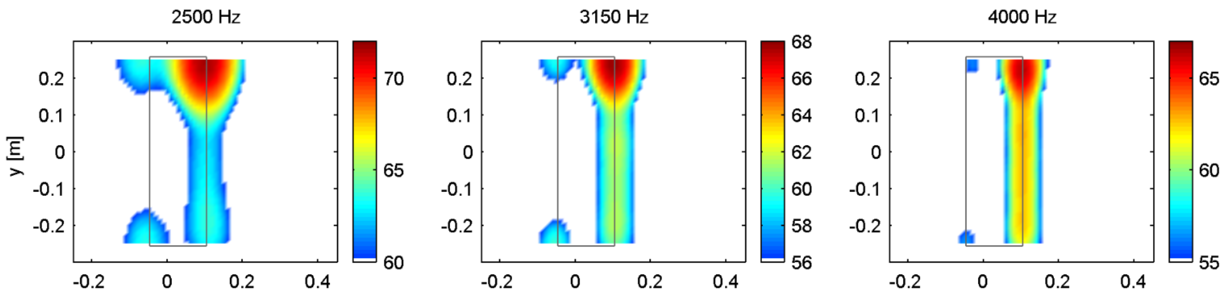

b) Serration Fixed on the Pressure Side

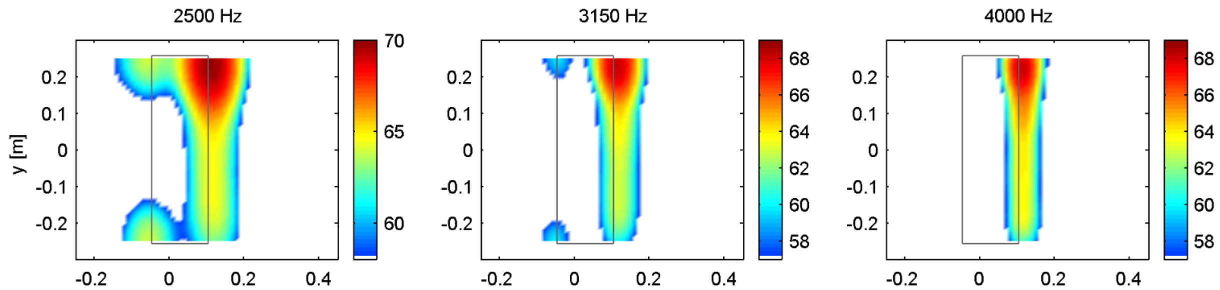

c) Serration Fixed on the Suction Side

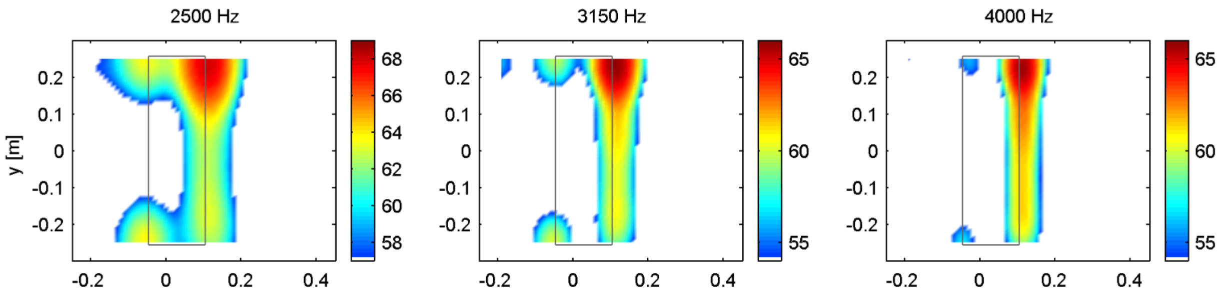

d) Flexible Serration

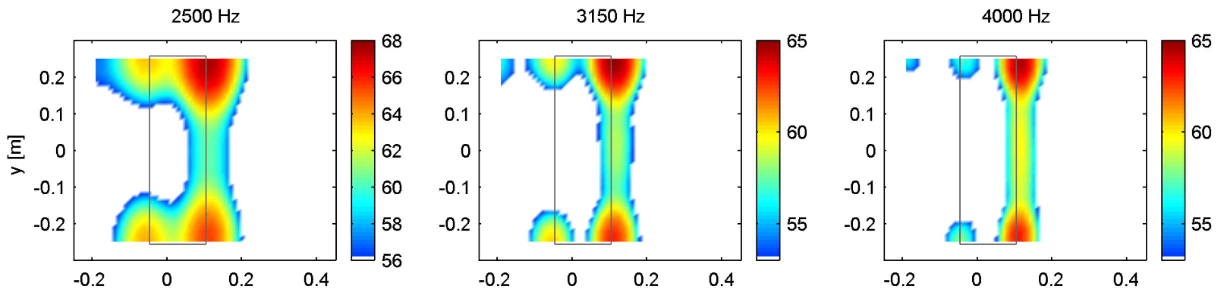

e) Cutted Serration

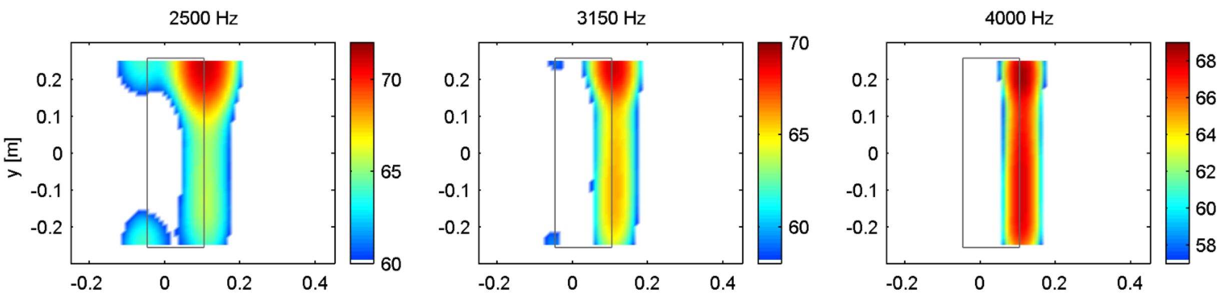

f) Serration with Cutted Plate

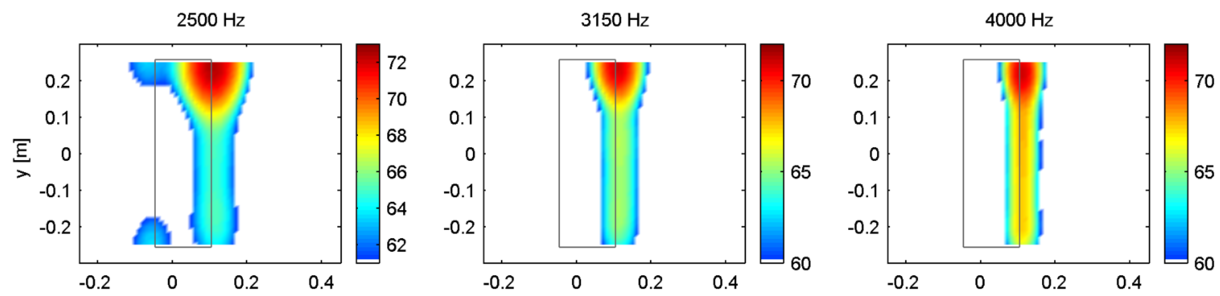

Figure 172 – **Medium Frequency Acoustic Maps – Free stream velocity 70 m/s; AoA = 6° (α_{eff} = 3.4°)**

a) Clean Configuration

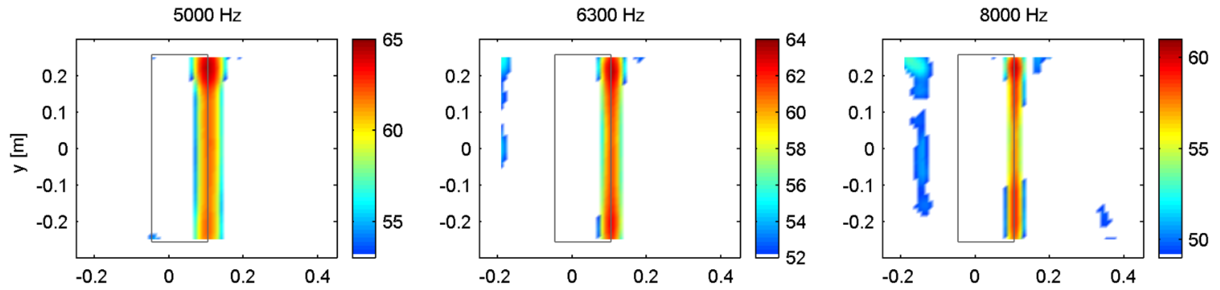

b) Serration Fixed on the Pressure Side

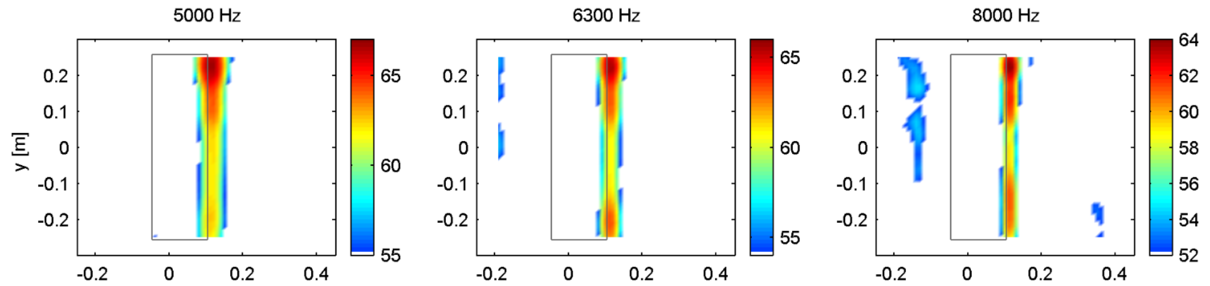

c) Serration Fixed on the Suction Side

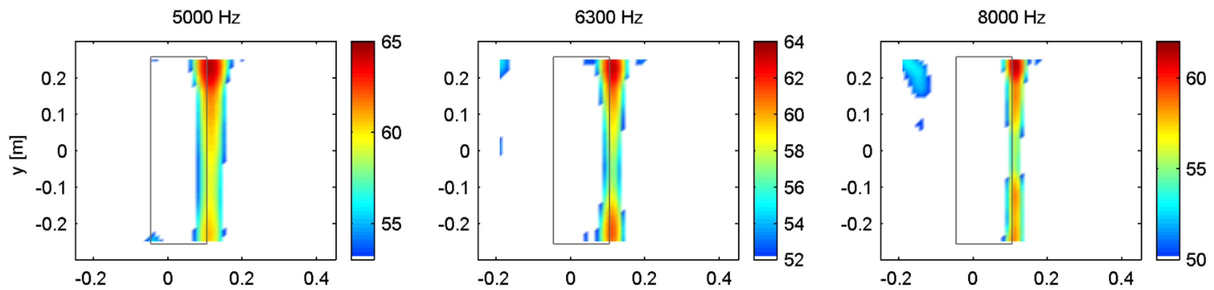

d) Flexible Serration

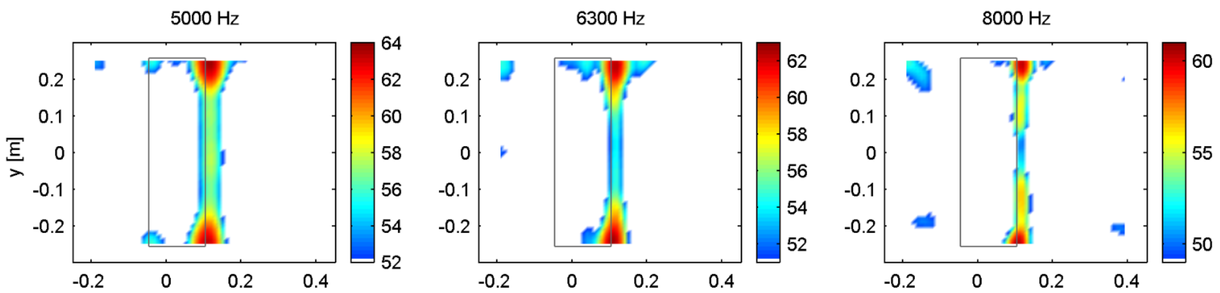

e) Cutted Serration

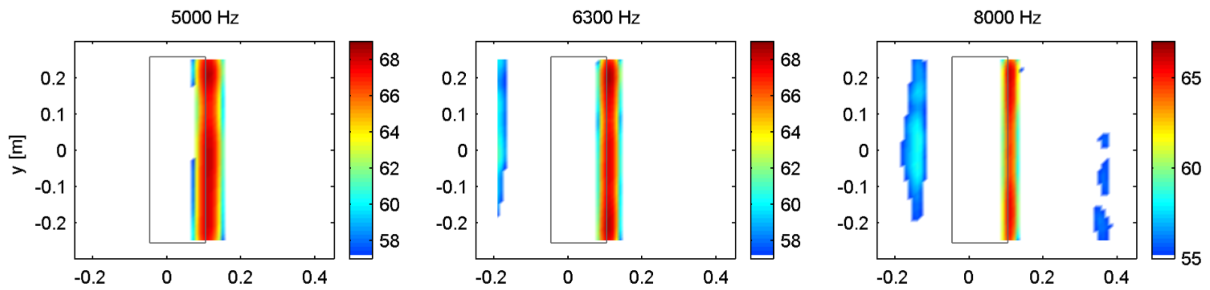

f) Serration with Cutted Plate

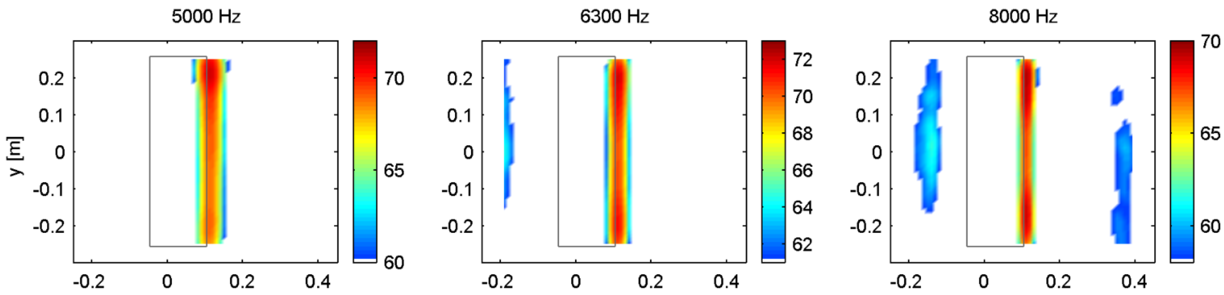

Figure 173 – **High Frequency Acoustic Maps – Free stream velocity 70 m/s; AoA = 6° (α_{eff} = 3.4°)**

a) Clean Configuration

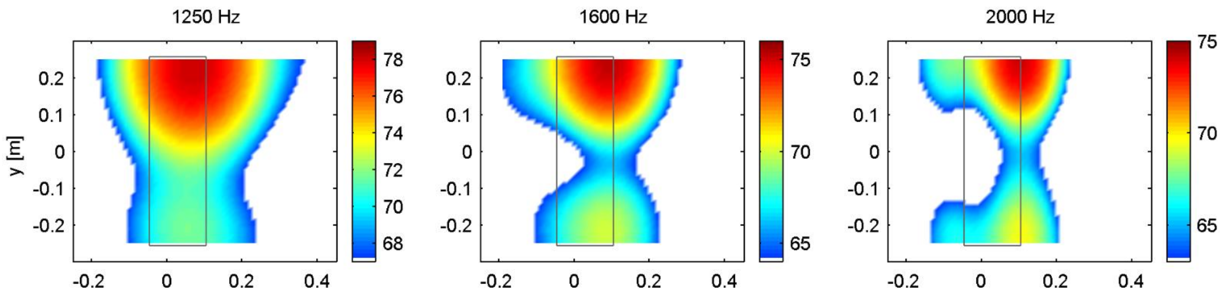

b) Serration Fixed on the Pressure Side

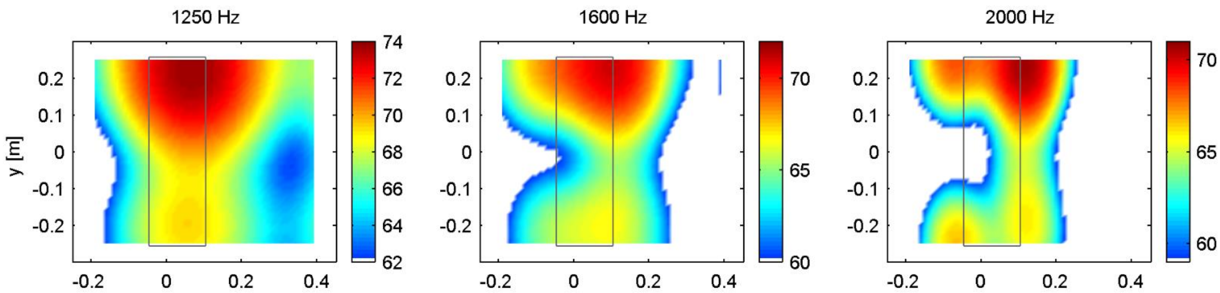

c) Serration Fixed on the Suction Side

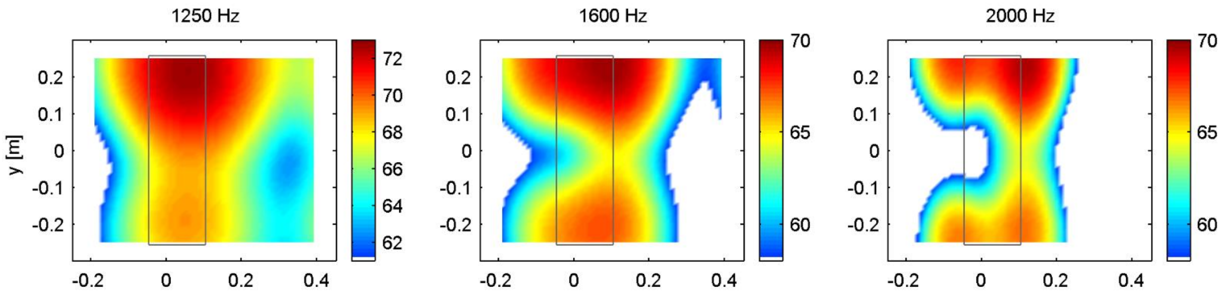

d) Flexible Serration

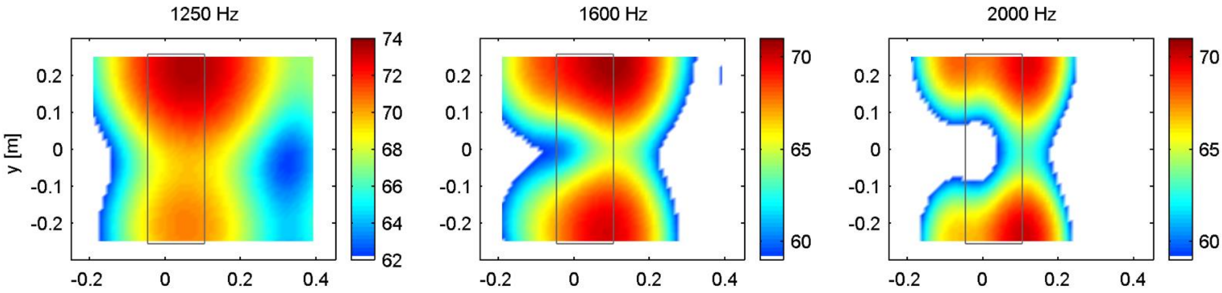

e) Cutted Serration

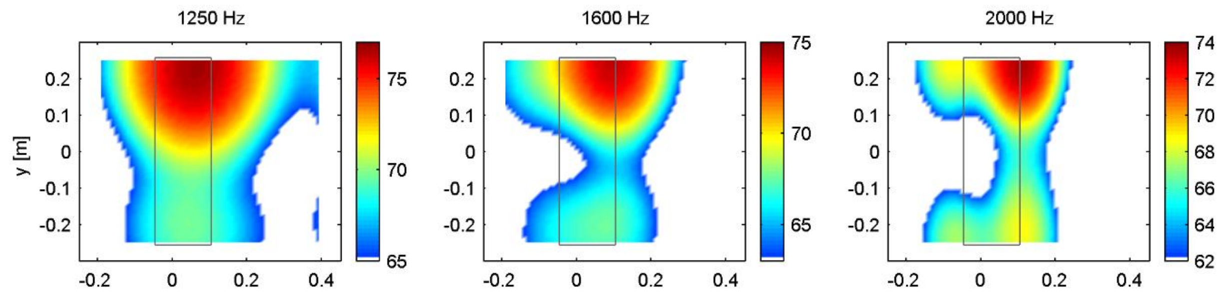

f) Serration with Cutted Plate

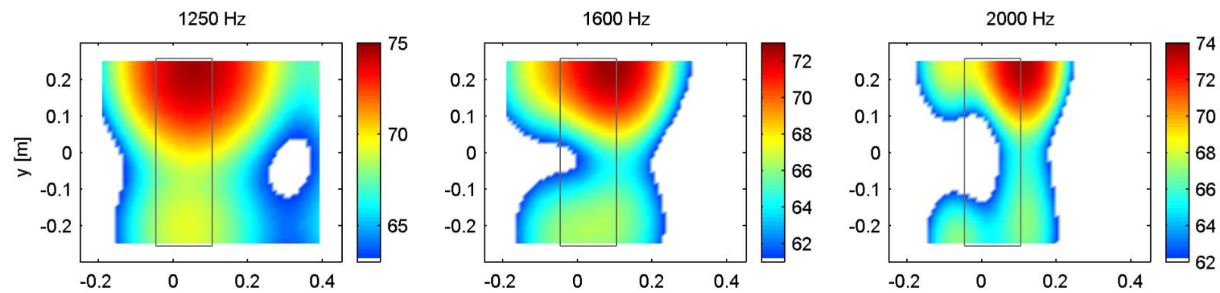

Figure 174 – **Low Frequency Acoustic Maps – Free stream velocity 70 m/s; AoA = 10.51° (α_{eff} = 6°)**

a) Clean Configuration

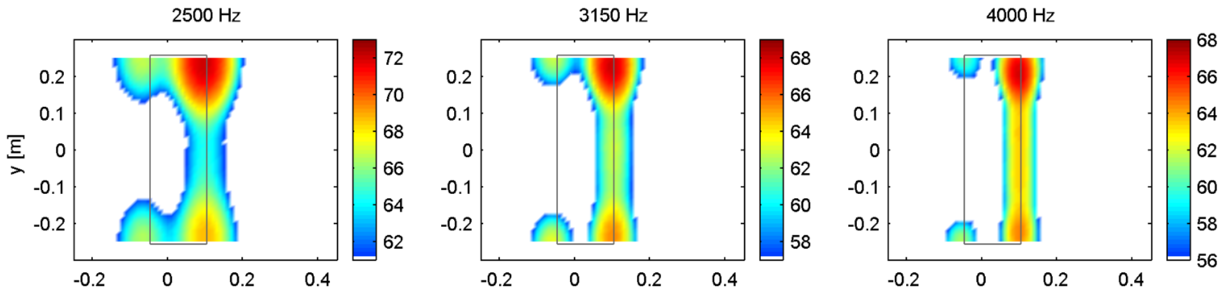

b) Serration Fixed on the Pressure Side

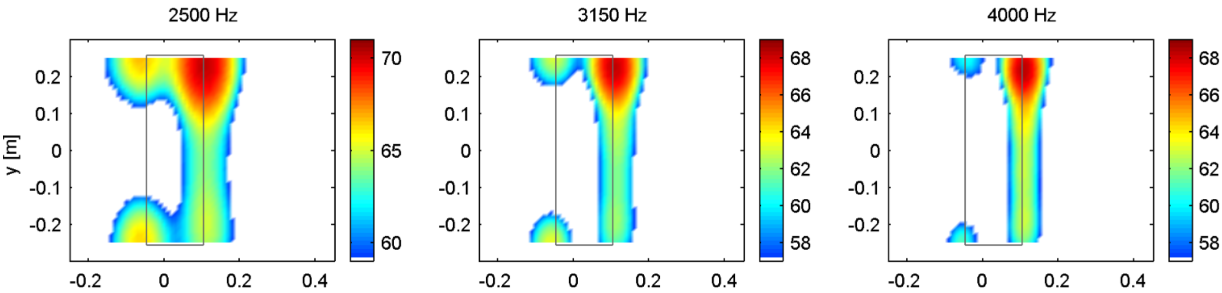

c) Serration Fixed on the Suction Side

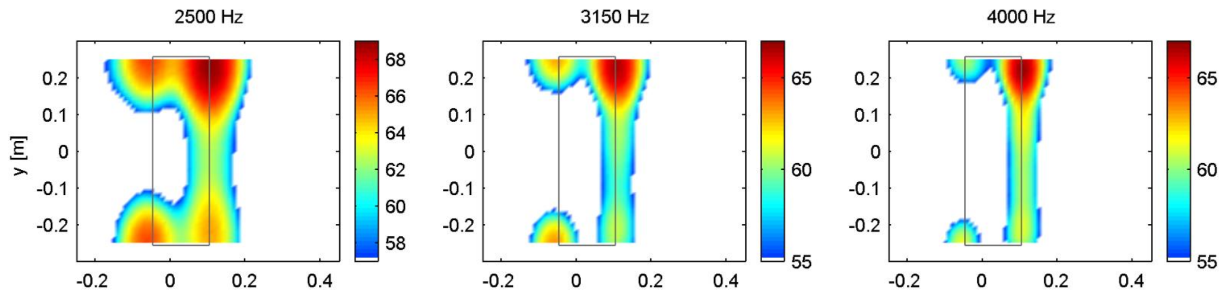

d) Flexible Serration

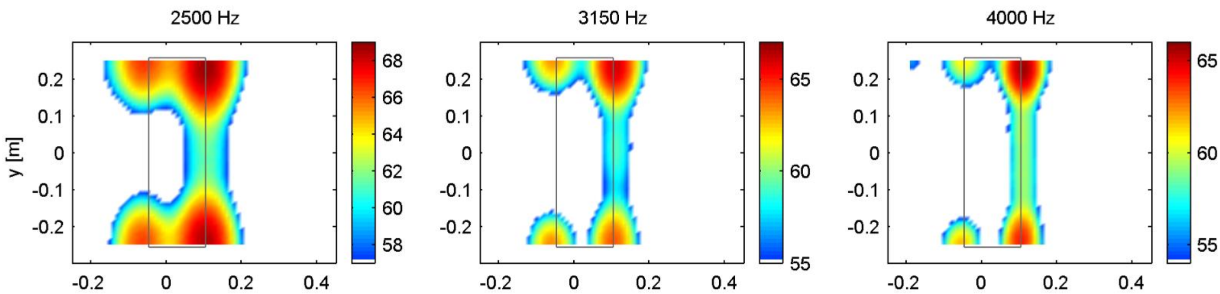

e) Cutted Serration

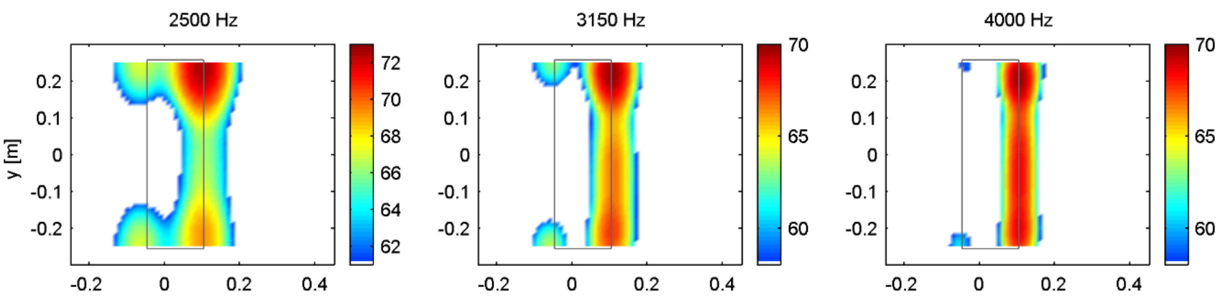

f) Serration with Cutted Plate

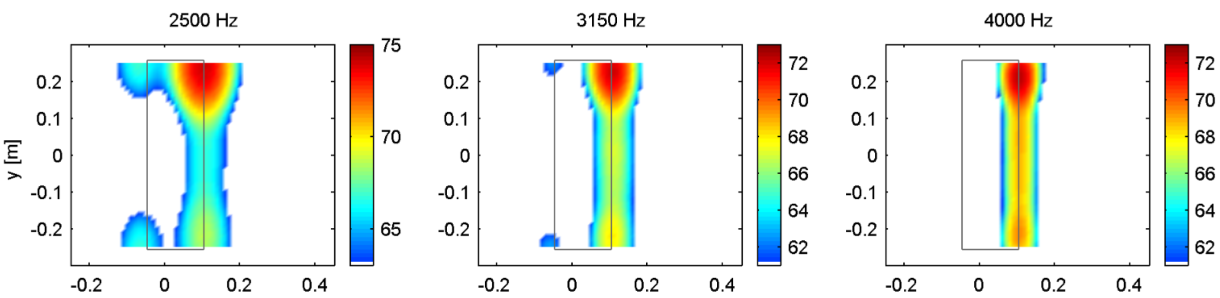

Figure 175 – **Medium Frequency Acoustic Maps – Free stream velocity 70 m/s; AoA = 10.51° (α_{eff} = 6°)**

a) Clean Configuration

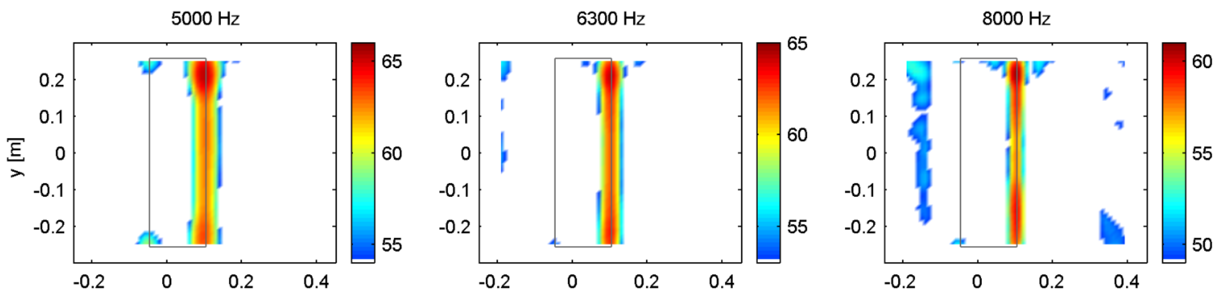

b) Serration Fixed on the Pressure Side

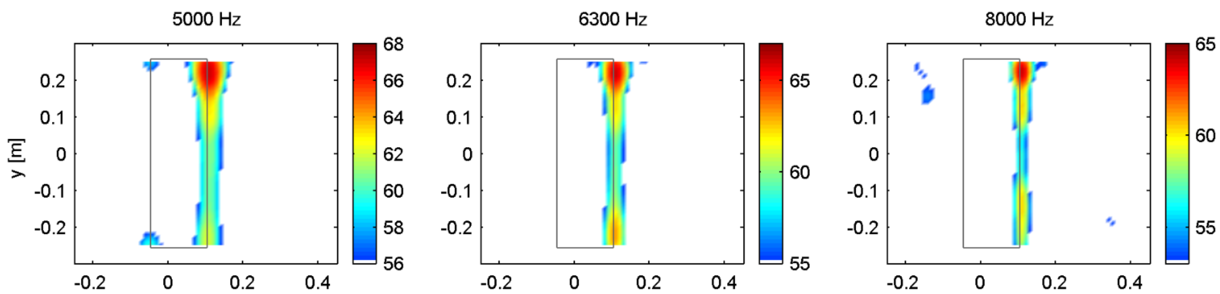

c) Serration Fixed on the Suction Side

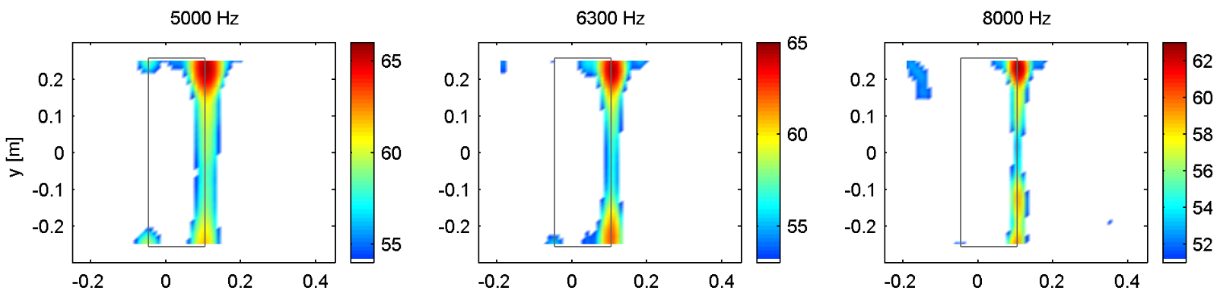

d) Flexible Serration

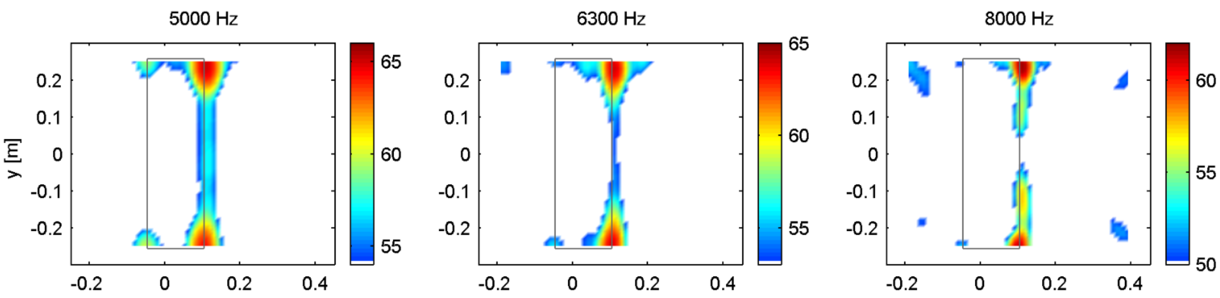

e) Cutted Serration

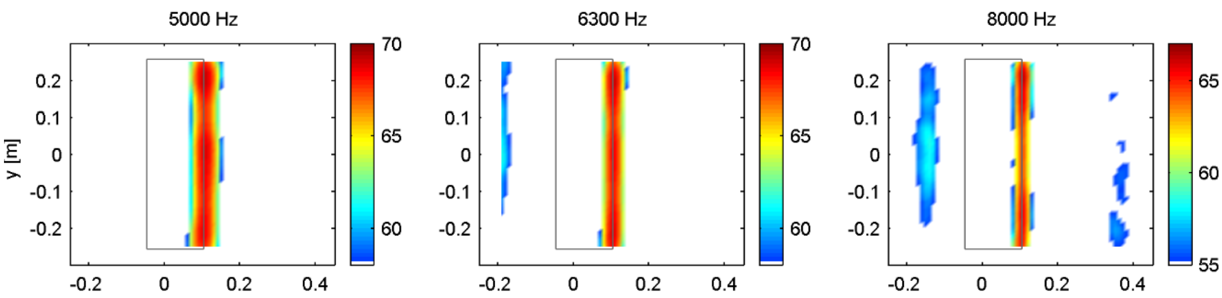

f) Serration with Cutted Plate

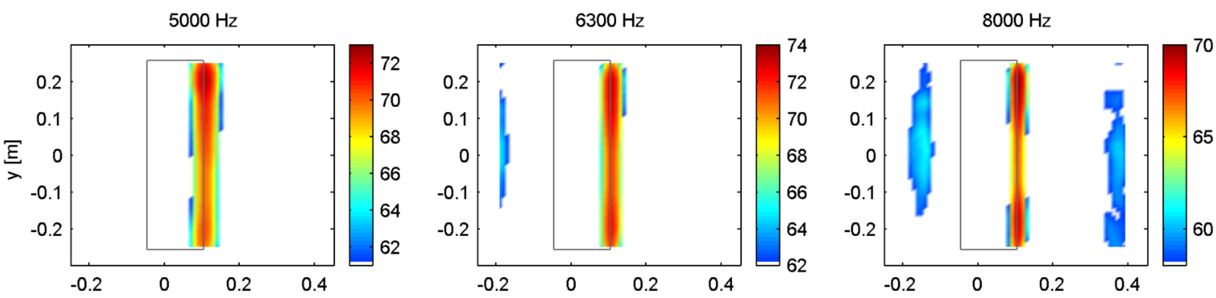

Figure 176 – **High Frequency Acoustic Maps – Free stream velocity 70 m/s; AoA = 10.51° (α_{eff} = 6°)**

a) Clean Configuration

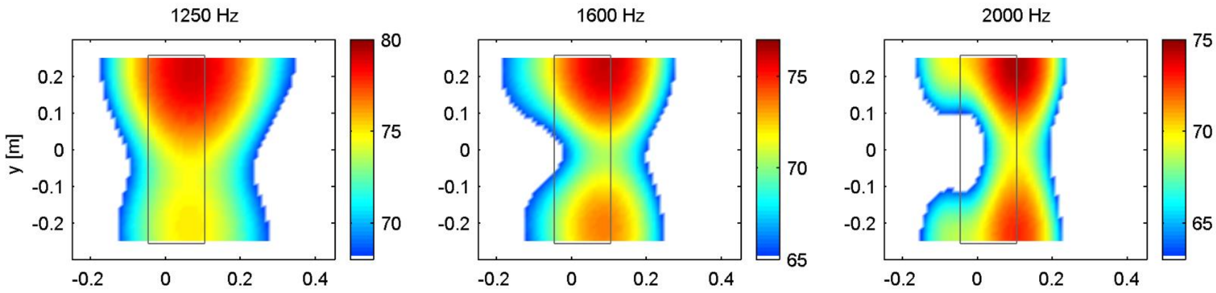

b) Serration Fixed on the Pressure Side

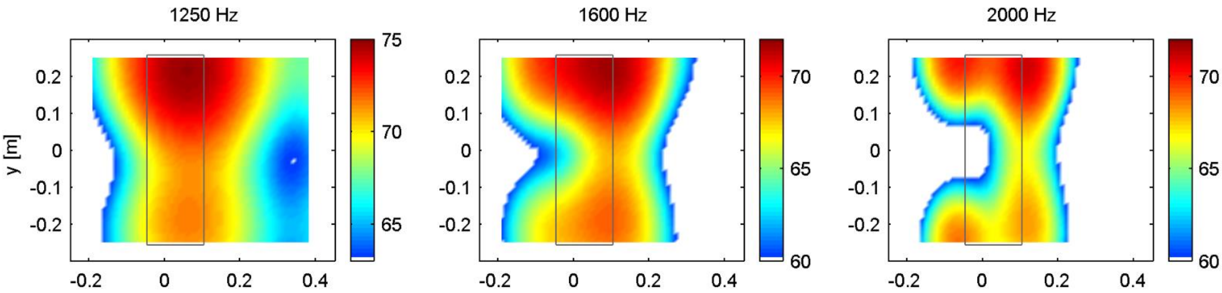

c) Serration Fixed on the Suction Side

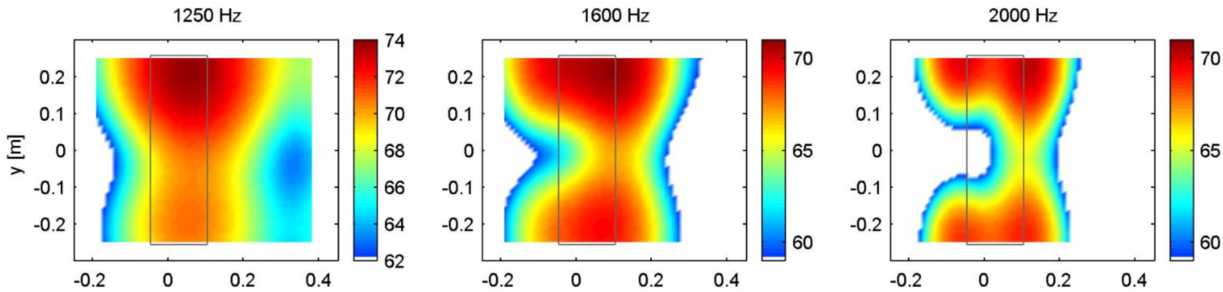

d) Flexible Serration

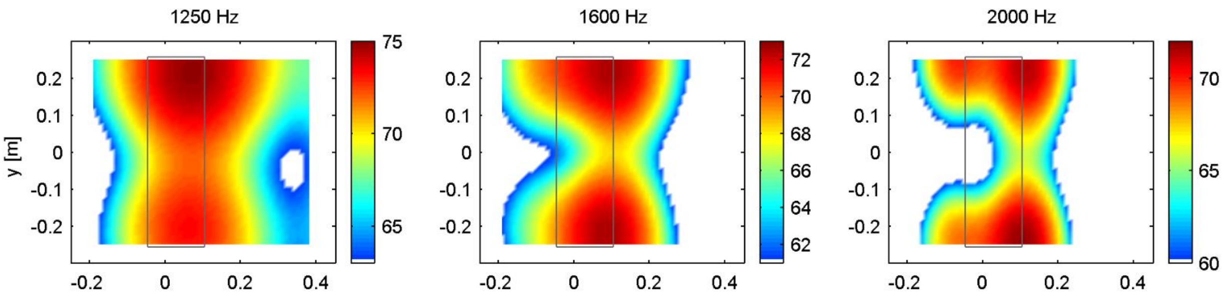

e) Cutted Serration

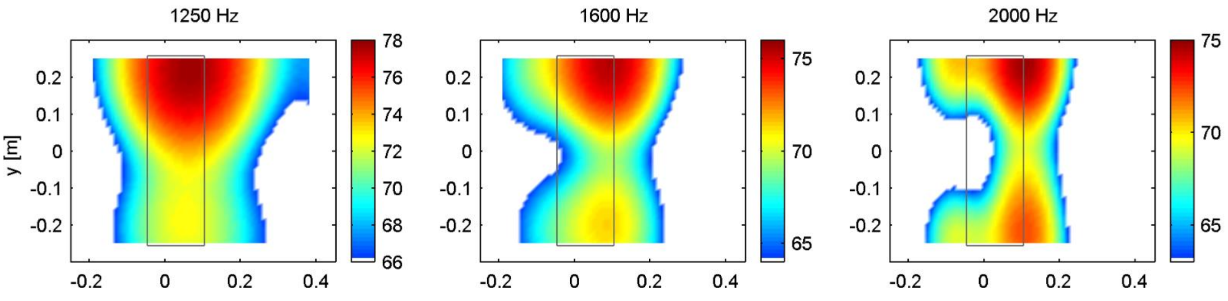

f) Serration with Cutted Plate

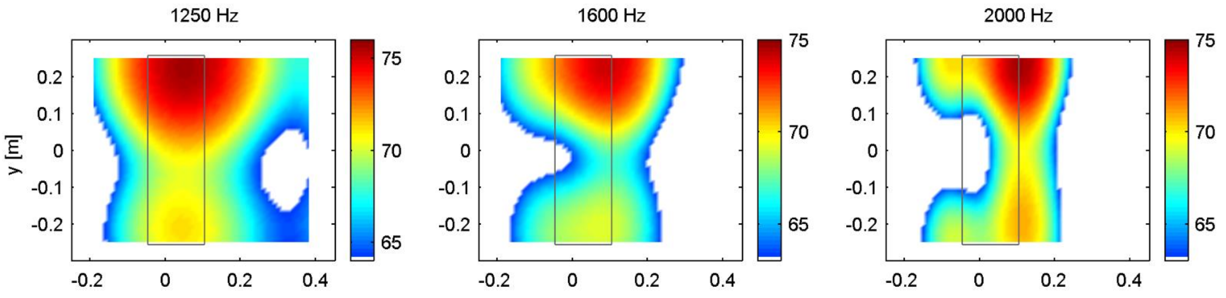

Figure 177 – **Low Frequency Acoustic Maps – Free stream velocity 70 m/s; AoA = 14.37° (α_{eff} = 8.2°)**

a) Clean Configuration

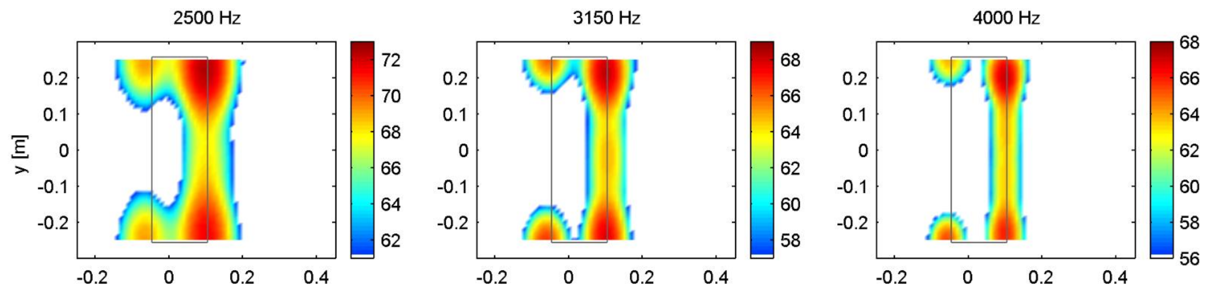

b) Serration Fixed on the Pressure Side

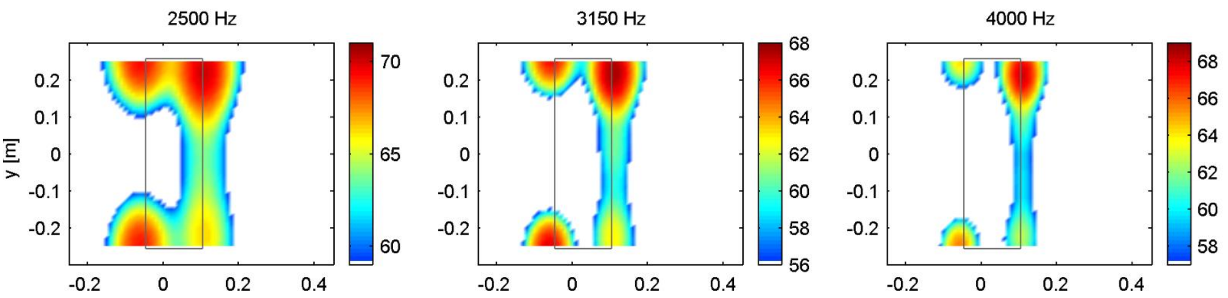

c) Serration Fixed on the Suction Side

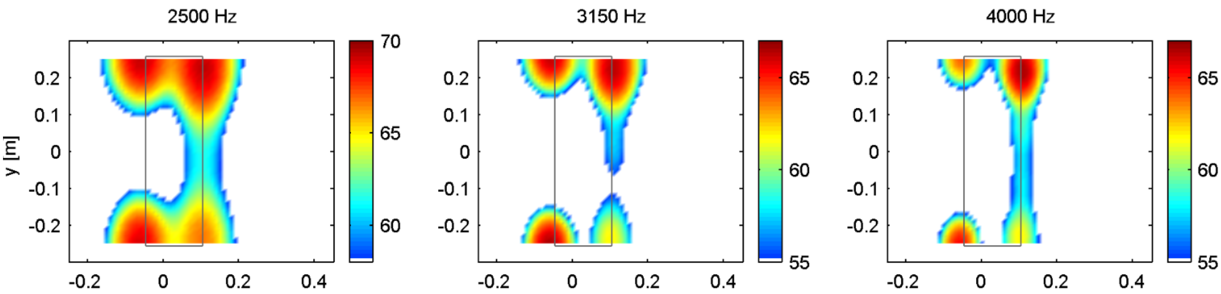

d) Flexible Serration

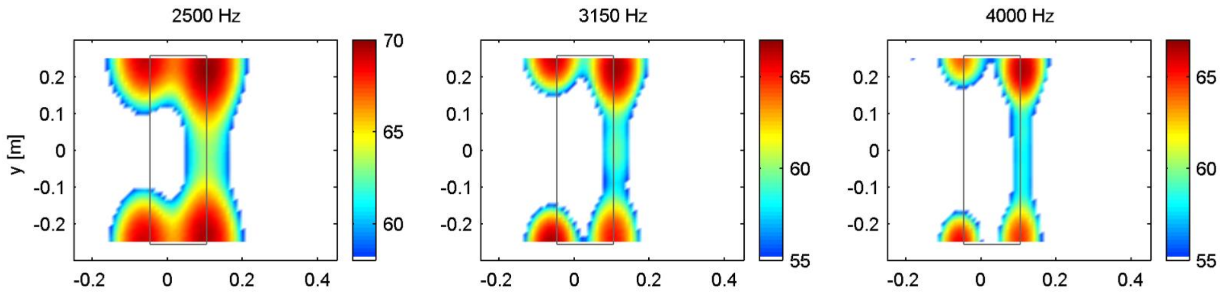

e) Cutted Serration

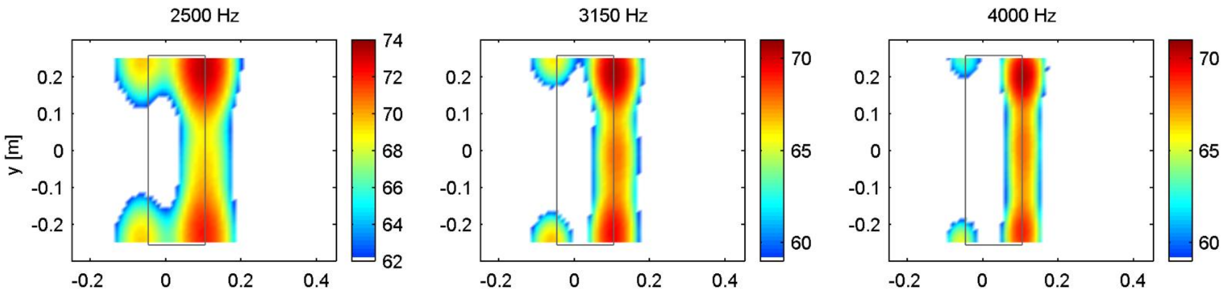

f) Serration with Cutted Plate

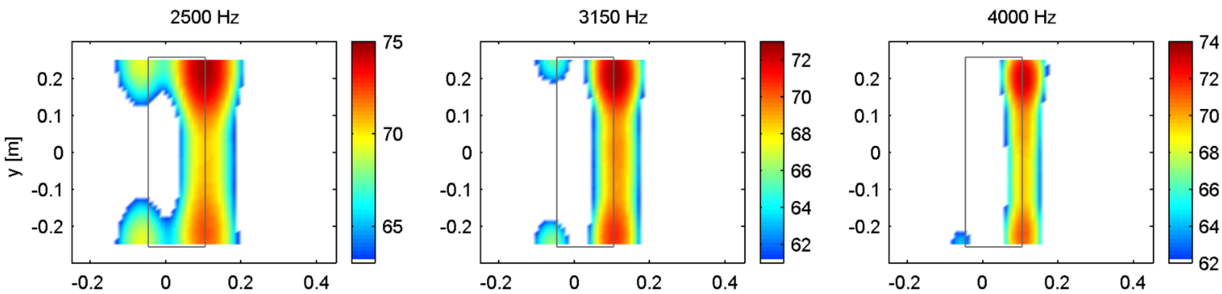

Figure 178 – **Medium Frequency Acoustic Maps – Free stream velocity 70 m/s; AoA = 14.37° (α_{eff} = 8.2°)**

a) Clean Configuration

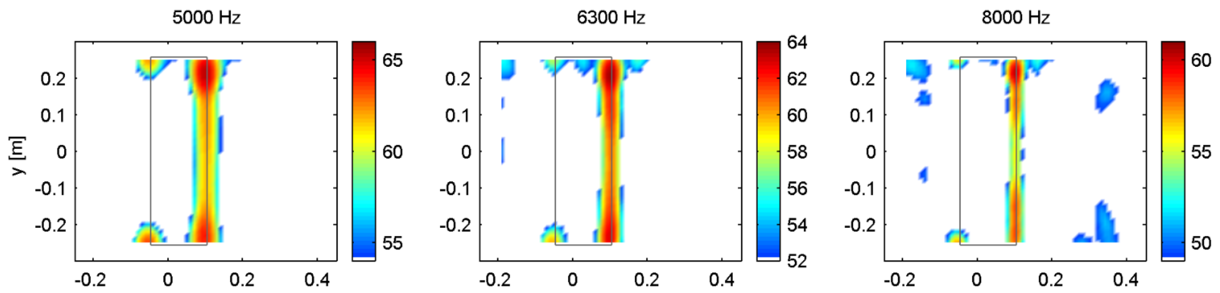

b) Serration Fixed on the Pressure Side

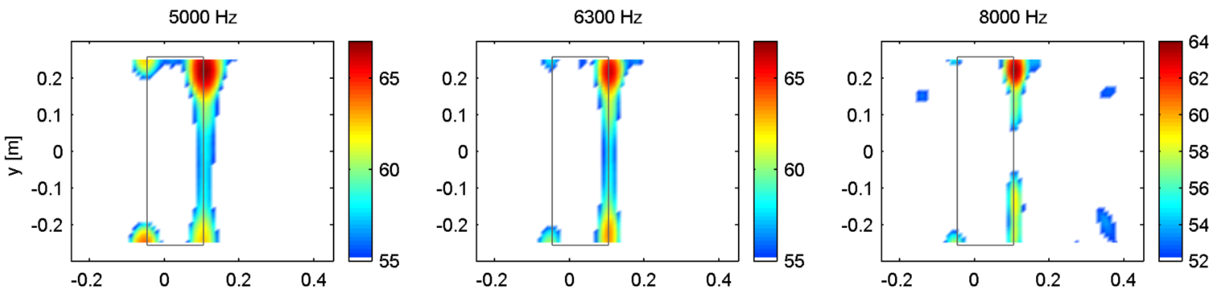

c) Serration Fixed on the Suction Side

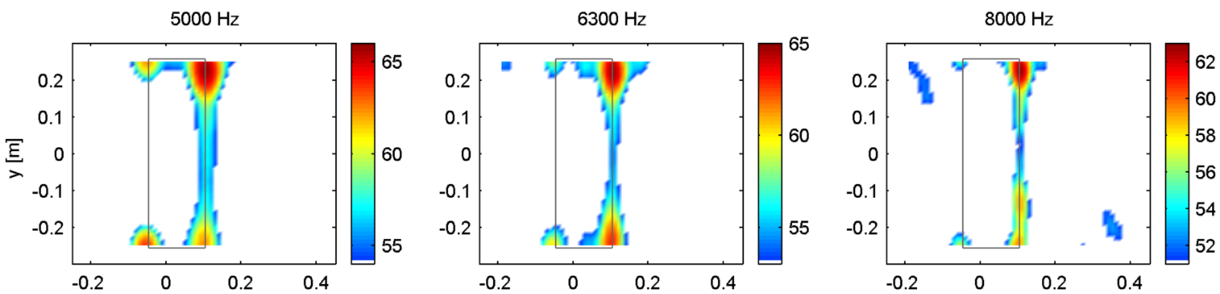

d) Flexible Serration

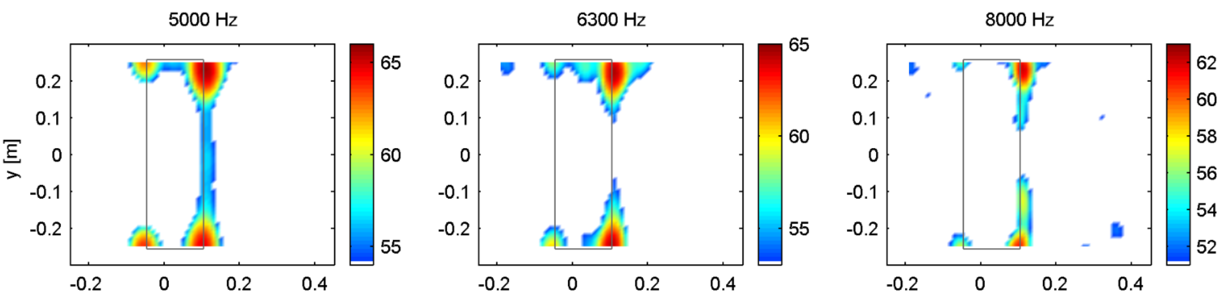

e) Cutted Serration

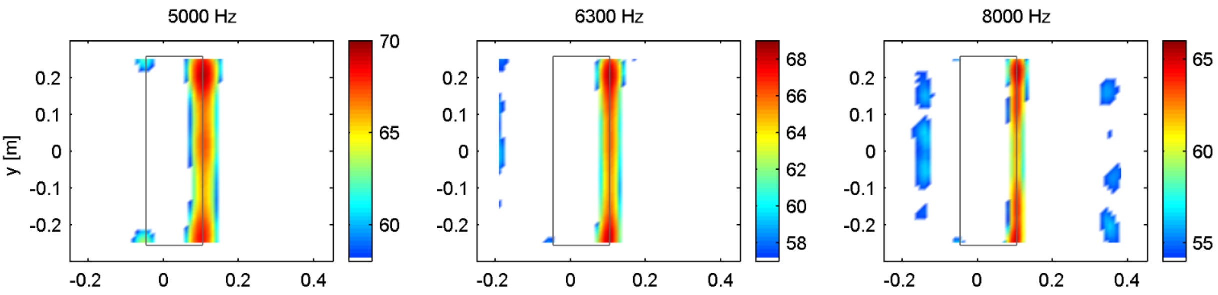

f) Serration with Cutted Plate

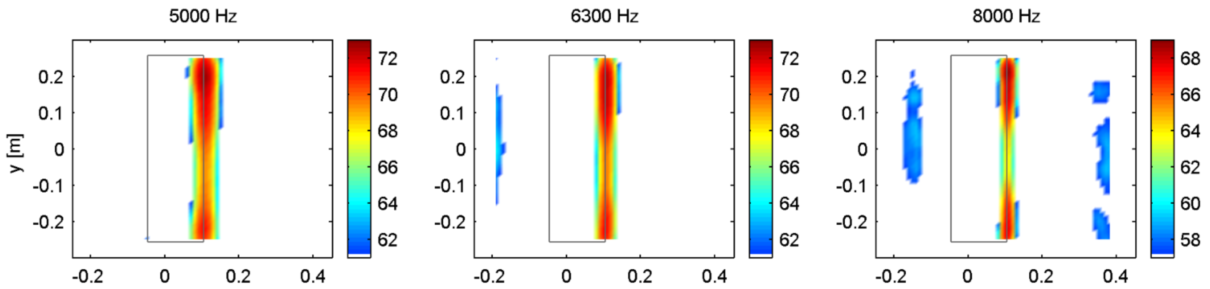

Figure 179 **– High Frequency Acoustic Maps – Free stream velocity 70 m/s; AoA = 14.37° (α_{eff} = 8.2°)**

www.nlr.nl